



Fault Analysis of Permanent Magnet Synchronous Machines for Safety Critical Applications

by

Yanwen Shi

A thesis submitted for the degree of Doctor of Philosophy

Department of Electronic and Electrical Engineering
The University of Sheffield

September 2019

ABSTRACT

This thesis is concerned with design and analysis of fault tolerant permanent magnet synchronous machines for safety critical applications. In addition to high performance under healthy operations, the fault tolerant machines under consideration should provide satisfactory performance under common faults, good demagnetisation withstand capability and thermal robustness.

Firstly, a novel triple redundant 9-phase (3x3-phase), 6-pole, 36-slot permanent magnet assisted synchronous reluctance machine (PMASynRM) with segregated delta-connected winding is proposed based on the same topology with segregated wye-connected winding. The performances of machines with these two winding configurations are comprehensively compared under healthy and fault conditions by finite element analysis (FEA) and equivalent models under various fault conditions, including inter-turn short circuit (SC). It is shown that the delta-connected winding has better fault tolerance due to higher output torque under one phase open-circuit fault and lower inter-turn SC current when the mitigation measure -- 3-phase terminal short-circuit is applied.

Subsequently, the demagnetisation withstand capability for the proposed PMASynRM with wye-connected winding is assessed by a continuous demagnetisation model under various critical faults at the peak torque and base speed. The dynamic response and the post demagnetisation performance have been obtained to demonstrate that the machines with both delta- and wye-connected windings have very strong demagnetisation withstand capability.

The thermal behaviour of the proposed PMASynRM with wye-connected winding under healthy and fault conditions with asymmetric temperature distribution have been investigated by established transient lumped parameter (LP) and 3-dimensional (3D) thermal models. Further, a directly coupled electromagnetic (EM)-thermal simulations based on 2-dimensional (2D) transient EM and 3D thermal model with aid of a scripting file are also performed to gain a deeper insight of the thermal behaviour of the proposed PMASynRM under various fault conditions, including inter-turn SC faults at different speeds and with different numbers of SC turns when considering 17 strands of the winding conductor as a whole as well as inter-strand SC fault when each strand is modelled separately. The temperature distributions which result with EM-thermal coupled simulations have been comprehensively compared with those under thermal-only simulation with constant losses to demonstrate the necessity of the EM-thermal coupled

simulation under various fault conditions. The EM and thermal behaviour of the proposed PMASynRM with wye-connected winding are also assessed against a more realistic insulation deterioration process leading to a full SC fault. In addition, the EM performance obtained by 2D FE model and thermal performance obtained by 3D thermal model have been validated experimentally.

Finally, electromagnetic and thermal behaviours of a 2.5 MW, dual 3-phase permanent magnet generator for E-Fan-X demonstrator are assessed by the developed EM-thermal coupled simulation technique to quantify fault severity against a number of potential electric failure modes resulting from insulation breakdown.

ACKNOWLEDGEMENT

Foremost, I would like to give my sincere gratitude to my supervisor, Prof. Jiabin Wang, for his continuous encouragement, support, and guidance on my research throughout 4-year PhD journey. I am motivated by his professional research attitude and learned a lot as he spent large time for guiding my research project and publications. I would also like to thank my 2nd supervisor, Dr. Antonio Griffo, for his encouragement.

I am also grateful to my colleagues who contribute to this thesis, Dr Liang Chen, Dr Xiao Chen, Dr Bo Wang, Dr Rongguang Hu, and Dr. Sreeju S Nair. I would also like to thank my colleagues for their help in my daily life, Dr Tianfu Sun, Dr Chaohui Liu, Shangjian Dai, Zhengmeng Liu and all my fellows from the Electrical Machine and Drives Group of the University of Sheffield.

My friends, particularly Na Zhan, Dr Shaosheng Xue, Shuru Zhang, Dr Liren Huang, Yan Zhou, Lu Wang, Dr Huayang Li, Dr Jie Ma and Dr Yanxin Li, also deserve my big thanks for their kindness and company during these years.

Last but not the least, special thanks and big hugs go to my family: my parents, my sister and my husband Yue Liu for their unconditional love and support.

TABLE OF CONTENTS

ABSTRACT	I
ACKNOWLEDGEMENT	III
TABLE OF CONTENTS	IV
NOMENCLATURES	VIII
ABBREVIATION	XIV
Chapter 1 Introduction	1
1.1 Introduction	1
1.2 Typical Faults of Electric Drive System	2
1.3 Current State-of-the-Art Fault Tolerant Electric Drive System	5
1.3.1 Design Requirements	5
1.3.2 Electrical Machine Candidates	7
1.3.3 Fault Tolerant Machine Topologies	8
1.4 Current State-of-the-Art Techniques of Fault Tolerant Analysis	16
1.4.1 Fault Modelling Techniques	16
1.4.2 Demagnetisation Analysis Techniques	19
1.4.3 Thermal Analysis Techniques	22
1.4.4 Summary	26
1.5 Scope of the Thesis	26
1.6 Contributions of the Thesis	29
1.7 Publications	30
Chapter 2 Winding Configuration Optimization of a Fault Tolerant Machine Drive Based on PMASynRM	32
2.1 Introduction	32
2.2 PMASynRM with Wye-Connected Winding Configuration	35
2.3 PMASynRM with Delta-Connected Winding Configuration	37
2.3.1 Design Specifications	37
2.3.2 Equivalent Inter-Turn Fault Model	38
2.4 Comparisons between Delta- and Wye-Connected Winding PMASynRM	45
2.4.1 Healthy Operation	45
2.4.2 Fault Operations	49
2.5 Summary	63
Chapter 3 Continuous Demagnetisation Assessment for PMASynRM	65
3.1 Introduction	65

3.2 Continuous Demagnetisation Assessment	67
3.3 Demagnetisation Assessment for Short Circuit Faults.....	73
3.4 Demagnetisation Assessment for Voltage-Reversal Faults	76
3.4.1 Fault Performance	76
3.4.2 Post-Fault Torque Harmonic Analysis	84
3.5 Summary	86
Chapter 4 Lumped Parameter and 3D Thermal Models of a PMASynRM.....	88
4.1 Introduction	88
4.2 Cooling Design.....	91
4.3 Transient Lumped Parameter Thermal Model	92
4.3.1 LP Thermal Model under Healthy Condition	92
4.3.2 LP Thermal Model under Short-Circuit Fault Conditions	99
4.4 3D Thermal Model.....	104
4.5 Thermal Performance Comparisons between LP and 3D Thermal Models.....	107
4.6 Experimental Validation of the Simulation of the PMASynRM	113
4.6.1 Comparisons of Measured and 2D Predicted EM Performance	114
4.6.2 Comparisons of Measured and 3D Predicted Thermal Performance.....	122
4.7 Thermal Performance of PMASynRM under Rated Operating Condition Based on the 3D Thermal Model	132
4.7.1 Thermal Behaviour under Healthy Condition.....	132
4.7.2 Thermal Behaviour under One Turn SC with Mitigation	134
4.8 Summary	136
Chapter 5 Electromagnetic-Thermal Coupled Simulation for the PMASynRM under Ideal Short-Circuit Fault Conditions	138
5.1 Introduction	138
5.2 Electromagnetic-Thermal Coupled Simulation.....	140
5.3 Thermal Behaviour of the PMASynRM under Various Fault Conditions.....	144
5.3.1 One Turn Short-Circuit at 500rpm	145
5.3.2 One Turn Short-Circuit at 4000rpm	148
5.3.3 Two Turns Short-Circuit at 4000rpm.....	152
5.3.4 Three Turns Short-Circuit at 4000rpm.....	154
5.3.5 One Turn Short-Circuit with 3-Phase Terminal SC at 4000rpm.....	156
5.4 Discussion	159
5.5 EM and Thermal Behaviours for the PMASynRM with Stranded Conductors	160
5.5.1 2D EM Model and 3D Thermal Model.....	160

5.5.2 EM Characteristics for the PMASynRM with Stranded Conductors.....	163
5.5.3 EM-thermal Coupled Simulation under Inter-Strand SC Conditions	171
5.6 Summary	175
Chapter 6 Electromagnetic and Thermal Behaviours of the PMASynRM with Insulation Deterioration Fault	177
6.1 Introduction	177
6.2 EM Behaviour under Insulation Deterioration Leading to SC Faults.....	178
6.2.1 Electromagnetic Behaviour	178
6.2.2 Critical Electrical Insulation Resistance	183
6.3 Thermal Model and Cut Through Resistances.....	184
6.3.1 3D Thermal Model.....	185
6.3.2 Boundary of Cut-Through Resistance.....	186
6.4 Fault Detection Threshold.....	188
6.4.1 Fault Detected and Mitigated when $R_{in} \geq R_{ct_l}$	189
6.4.2 Fault Detected and Mitigated when $R_{ct_l} > R_{in} \geq R_{ct2_s}$	191
6.4.3 Fault Detected and Mitigated when $R_{in} \approx R_{pmax}$	191
6.5 Transient Ageing Process with Insulation Deterioration Fault	191
6.6 Comparisons between Measured and 2D Predicted EM Performance with Different Insulation Resistances.....	194
6.6.1 Insulation Deterioration at 2000rpm with 40A Current	195
6.6.2 Insulation Deterioration at 1000rpm with 40A Current	199
6.7 Summary	200
Chapter 7 Case Study: Electromagnetic and Thermal Behaviours of a 2.5 MW Permanent Magnet Generator	202
7.1 Introduction	202
7.2 Critical Electrical Failure Modes	203
7.3 Turn-to-Turn Short Circuit.....	205
7.3.1 Influence of Number of Short-Circuited Turns.....	206
7.3.2 Influence of Short-Circuited Turn Fault in Different Phases.....	208
7.3.3 Influence of Short-Circuited Turn Fault Position in Slots	210
7.4 Phase-to-Phase Short Circuit within One 3-Phase Channel.....	213
7.5 Measures to Reduce Short-Circuit Current	216
7.5.1 Terminal Short-Circuit	216
7.5.2 Switch-off Engine (Generator Speed Reduced to 10% Rated Speed)	217
7.6 Influence of SC Contact Resistance on Fault Current.....	218

7.7 Thermal Impact of Short Circuit Fault.....	222
7.7.1 3D Thermal Model.....	222
7.7.2 Thermal Behaviours in Short-Circuit Fault Conditions	227
7.8 Summary	234
Chapter 8 Conclusions and Future Work.....	237
8.1 Summary	237
8.2 Future Work	242
REFERENCES.....	244
TABLE OF FIGURES.....	254
LIST OF TABLES	262
Appendix A Lumped Parameter Thermal Model in Matlab.....	265
Appendix B EM-Thermal Coupled Simulation Code.....	271

NOMENCLATURES

Symbol	Meaning	Unit
a	Length of the insulation volume	mm
A_{conv}	Surface area	m ²
b	Thickness of the insulation volume	mm
B_{max}	Initial value of each magnet element	T
B_{PXn}	Element flux density along the magnetising direction	T
B_{PYn}	Element flux density perpendicular to the magnetising direction	T
B_r	Pre-fault remanence of the permanent magnet	T
B_r'	Post-fault remanence of the permanent magnet	T
c	Height of the insulation volume	mm
c_c	Specific heat capacity of the copper	J/kg/C
C_C, C_c	Capacitance of the winding of whole slots/half slot	J/C
C_{ch}, C_{cf}	Capacitance of healthy/fault part of C_c	J/C
c_e	Equivalent specific heat capacity of the winding	J/kg/C
C_H	Capacitance of the housing	J/C
c_{mag}	Specific heat capacity of the magnet	J/kg/C
C_{MAG}	Capacitance of the magnet	J/C
c_p	Specific heat capacity of the impregnation	J/kg/C
c_{rotor}	Specific heat capacity of the rotor core	J/kg/C
C_{RY}, C_{RIR}	Capacitance of the rotor yoke/ rotor iron-ribs	J/C
c_{shaft}	Specific heat capacity of the shaft	J/kg/C
C_{SHAFT}	Capacitance of the shaft	J/C
c_{stator}	Heat capacity of the stator core	J/kg/C
C_{ST}, C_{st}	Capacitance of stator tooth of whole teeth/half tooth	J/C
C_{SY}, C_{sy}	Capacitance of stator yoke of whole/half tooth-slot sections	J/C
d_{mag}	Demagnetisation rate	
E_{fm}	Electromotive force of the faulted turns	V
F_s	Magneto-motive force of 3-phase set ABC	A
h_{airgap}	Heat convection transfer coefficient of the air-gap	W/m ² /C
h_{conv}	Heat convection coefficient	W/m ² /C
i_{AL}, i_{BL}, i_{CL}	Line A/B/C currents	A

i_{B_f}	Fault current in SC turns	
i_d, i_q, i_0	D-axis/ q-axis/ zero sequence current	A
i_f	Turn fault current	A
I_{fm}	Magnitude of fault current in SC turns	A
$i_k, k = A, B, \dots$	Current of phase k	A
I_m	Peak value of the line current	A
i_s^f	Current matrices of 3-phase set ABC under fault condition	A
I_{strand}	Magnitude of turn fault current in each strand	A
k_{air}	Thermal conductivity of the air	W/m/C
k_{axial}	Equivalent axial thermal conductivity of winding	W/m/C
k_c	Thermal conductivity of copper	W/m/C
k_{mag}	Thermal conductivity of the magnet	W/m/C
k_{mr}	Thermal conductivity of the interface between magnet and rotor	W/m/C
k_p	Thermal conductivity of impregnation	W/m/C
k_r	Thermal conductivity of the slot liner	W/m/C
$k_{rad/cir}$	Equivalent radial/circumferential thermal conductivity of winding	W/m/C
k_{rotor}	Thermal conductivity of the rotor core	W/m/C
k_{sh}	Thermal conductivity of the interface between stator and housing	W/m/C
k_{stator}	Thermal conductivity of the stator core	W/m/C
L_A	Axial length of the rotor/active winding	mm
L_{AA0}	Average inductance of phase A	H
L_{AA2}	Ripple inductance of phase A	H
L_{edw}	Length of the end winding of a quarter turn	mm
L_{fm}	Inductance of the faulted turns	H
L_{fs}	Inductance of the faulted turns in each strand	H
$L_{ij}, i, j = A, B, C, i \neq j$	Mutual inductance between phase i and phase j	H
$L_{jj}, j = A, B, C$	Self-inductances of the phase j	H
L_{ls}	Stator slot leakage	H
L_{md}, L_{mq}	D-axis/q-axis inductance	H

L_s^f	Inductance matrices of 3-phase set ABC under fault condition	H
n	Element number	
N_s	Slot number	
N_{sc}	Number of SC turns	
N_{strand}	Number of faulted parallel strands	
N_t	Number of turns in one phase	
N_{turn}	Number of SC turns in one strand	
N_u	Nusselt number	
P_C	Copper loss of all slots	W
P_{ch}, P_{cf}	Copper loss of healthy/fault part in one slot	W
P_{ct}	Cut-through loss	W
P_{ct1_s}	Cut-through loss of Case 1	W
P_{ct2_s}	Cut-through loss of Case 2	W
P_{fm}	Copper loss of all faulted turns	W
P_{ST}, P_{SY}	Stator iron loss in tooth region/yoke region	W
P_{strand}	Copper loss of faulted turn in each strand	W
P_{turn}	Copper loss of each SC turn in one strand	W
p_{12}, p_{22}	2nd IAP harmonics in channel 1/channel 2	W
q_{12}, q_{22}	2nd IPR harmonics in channel 1/channel 2	var
R_A	Measured resistance of phase A	Ω
R_{airgap}	Convection resistance of the air-gap	C/W
R_{air_H}	Internal convection resistance	C/W
R_B	Measured resistance of phase B	Ω
R_{Bf}	Measured resistance of SC turn of phase B	Ω
R_C	Measured resistance of phase C	Ω
R_{conv}	Convection thermal resistance	C/W
R_{ct}	Cut-through resistance	Ω
R_{ct_d}	Minimum threshold of the turn-to-turn insulation resistance	Ω
R_{ct1_l}	Cut-through resistance of Case 1	Ω
R_{ct2_l}	Cut-through resistance of Case 2	Ω
R_{C1}, R_{ct}	Thermal resistance of active winding C1 of whole slots/half slot	C/W

R_{C2}, R_{c2}	Thermal resistance of active winding C2 of whole slots/one slot	C/W
R_{C3}, R_{c3}	Thermal resistance of end winding C3 of whole slots/one slot	C/W
R_{c1h}, R_{c1f}	Thermal resistance of healthy/fault part of R_{c1}	C/W
R_{c2h}, R_{c2f}	Thermal resistance of healthy/fault part of R_{c2}	C/W
R_{c3h}, R_{c3f}	Thermal resistance of healthy/fault part of R_{c3}	C/W
R_{C_air}, R_{c_air}	Convection resistance between winding and airgap in whole/one tooth-slot sections	C/W
R_{c_airh}, R_{c_airf}	Convection resistance of healthy/fault part of R_{c_air}	C/W
R_{DE}	Measured resistance between phase D and E	Ω
R_{DF}	Measured resistance between phase D and F	Ω
R_{EF}	Measured resistance between phase E and F	Ω
R_f	External fault resistance of the SC path	Ω
R_{fm}	Resistance of the faulted turns	Ω
R_{fs}	Resistance of the one turn in each strand	Ω
R_{GH}	Measured resistance between phase G and H	Ω
R_{GI}	Measured resistance between phase G and I	Ω
R_H	Thermal resistance of housing	C/W
R_{HI}	Measured resistance between phase H and I	Ω
R_{in}	Insulation resistance across the associated number of turns	Ω
$R_k, k=0,1,10\dots$	Resistance is k times of one turn resistance	Ω
R_{MAG}	Thermal resistance of magnet	C/W
R_{MR}	Contact resistance between the magnet and rotor	C/W
R_{MAG_air}	Convection resistance between the magnet and air	C/W
R_{pmax}	Peak loss resistance	Ω
R_{RY}, R_{RIR}	Thermal resistance of rotor yoke/ rotor iron-rib	C/W
R_{R_air}	Convection resistance between the rotor and air	C/W
R_s	Phase resistance	Ω
R_s, R_{s0}	Phase resistance at winding temperature T_w/T_0	Ω
R_s^f	Resistance matrices of 3-phase set ABC under fault condition	Ω

R_{SH}, R_{sh}	Contact resistance between stator and housing in whole/half tooth-slot sections	C/W
R_{SHAFT}	Thermal resistance of shaft	C/W
R_{SHAFT_air}	Convection resistance between the shaft and air	C/W
R_{ST1}, R_{st1}	Thermal resistance of stator tooth part ST1 of whole /half tooth	C/W
R_{ST2}, R_{st2}	Thermal resistance of stator tooth part ST2 of whole /half tooth	C/W
R_{st3}	Thermal resistance of stator tooth part ST3 of half tooth	C/W
R_{SY}, R_{sy}	Thermal resistance of stator yoke of whole/ half tooth-slot sections	C/W
R_{s1}, R_{s1}	Thermal resistance of slot liner near stator tooth of whole/half slot	C/W
R_{s1h}, R_{s1f}	Thermal resistance of healthy/fault part of R_{s1}	C/W
R_{s2}, R_{s2}	Thermal resistance of slot liner near stator yoke of whole/one slot	C/W
t	Time	s
T_a	Taylor number	
t_{sh}	Contact thickness between the stator and housing	mm
T_w	Final temperature	°C
T_0	Initial temperature	°C
α_T	Temperature coefficient for copper	%/°C
v_c	Copper slot fill factor	
v_d, v_q, v_0	D-axis/ q-axis/ zero sequence voltage	V
$v_k, k = AS1, AS2, B, C$	Voltage of the winding part k	V
v_s^f	Voltage matrices of 3-phase set ABC under fault condition	V
γ_m	Radius in the middle of the air-gap	mm
δ	Air-gap length in the radial direction	mm
θ	Electrical rotor angle with respect to phase A winding	rad
θ_m	Mechanical angular position	rad
θ_n	Angle of magnetisation	rad
$\lambda_d, \lambda_q, \lambda_0$	D-axis/ q-axis/ zero sequence flux linkage	Wb

$\lambda_k, k=AS1, AS2, B, C$	Flux linkage of the winding part k	Wb
λ_m^f	Flux linkage matrices of permanent magnet under fault condition	Wb
λ_M	Peak permanent magnet flux linkage	Wb
$\lambda_{M,0}$	3 rd and its odd integer multiplies harmonic of PM flux linkage	Wb
λ_s^f	Flux linkage matrices of 3-phase set ABC under fault condition	Wb
μ	Fault ratio	
μ_v	Air dynamic viscosity	kg/m/s
ρ_a	Mass density of air	kg/m ³
ρ_c	Mass density of copper	kg/m ³
ρ_{ct1_s}	Insulation material resistivity of Case 1	$\Omega \cdot m$
ρ_{ct2_s}	Insulation material resistivity of Case 2	$\Omega \cdot m$
ρ_e	Mass density of the winding	kg/m ³
ρ_{mag}	Mass density of the magnet	kg/m ³
ρ_p	Mass density of the impregnation	kg/m ³
ρ_{rotor}	Mass density of the rotor core	kg/m ³
ρ_{shaft}	Mass density of the shaft	kg/m ³
ρ_{stator}	Mass density of the stator core	kg/m ³
ω	Electrical angular speed of the motor	rad/s
ω_r	Angular velocity of rotor	rad/s

ABBREVIATION

AC	Alternating current
AEA	All electric aircraft
AS1	Healthy part of phase A
AS2	Fault part of phase A
CFD	Computational fluid dynamics
DC	Direct current
emf	Electromotive force
FEA	Finite element analysis
FSCW	Fractional-slot concentrated winding
IAP	Instantaneous active power
IDG	Integrated drive generator
IGBT	Insulated gate bipolar transistor
IM	Induction machine
IPM	Interior permanent magnet
IRP	Instantaneous reactive power
LP	Lumped parameter
MEA	More Electric Aircraft
M_iN/P_j_k	Magnet in k^{th} layer of the i^{th} rotor pole with j magnetisation angle and N/P magnetised direction
MMF	Magneto-motive force
MTPA	Maximum torque per Ampere
OC	Open circuit
PM	Permanent magnet
PMASynRM	Permanent magnet-assisted synchronous reluctance motor
PMM	Permanent-magnet machine
PMSM	Permanent magnet synchronous machine
p.u.	Per unit
RMS	Root mean square

SC	Short circuit
SRM	Switched reluctance machine
SynRM	Synchronous reluctance machine
TEFC	Totally enclosed fan cooled
VA	Volt-ampere
2D	2-dimensional
3D	3-dimensional

Chapter 1 Introduction

1.1 Introduction

Air traffic has gained a worldwide growth in popularity in a last few decades. However, the resultant 2% of the man-made carbon dioxide emissions and fuel consumption by conventional aircraft propulsion system attract much attention on the need to improve fuel efficiency and reduce carbon footprint in the future aircraft [1]-[3].

As a result, the concept of replacing all the mechanical and pneumatic power systems with electrical power systems known as “All Electric Aircraft” (AEA) is proposed. The AEA is expected to reduce the weight by 10% and fuel consumption by 9% [4]. However, the key technologies, such as energy and power density of electrical energy storage has not reached maturity, and “More Electric Aircraft” (MEA) which utilises more electrical power system technologies represents an evolutionary process at this stage. Many subsystems of aircraft that previously used nonelectrical power systems have now been partially replaced with electrical power systems.

It has been reported in [3] that in recent commercial transport aircraft, such as the Boeing 787, many electrical power systems have been adopted, including the electric starter of the main engine, electric auxiliary power unit, environmental control system for regulating cabin temperature and pressure. National aeronautics and space administration has also developed a number of future goals for civilian transport aircraft.

Therefore, in order to offer continuous improvement on the future aircraft, electrical machine drives with high power density and high reliability is now a very attractive technology for research in academia and industry.

There has been extensive research on electric drive for safety critical applications. The essential requirements for the electric drive include low volume, weight and maintenance cost as well as the high availability and fault tolerant capability. Among them, the most important requirement of the electric drive is the high fault tolerance.

The concept of fault tolerance means the electric drive is capable of continuing operating in a satisfactory manner with a large range of principle faults [5] [6]. It is worth

noting that the electric drive for most safety critical applications is accepted to output the rated performance after any one fault [5], or at least is extremely unlikely to cause catastrophic damage, such as in-flight shut down or losing the control of the thrust [6].

1.2 Typical Faults of Electric Drive System

An electric drive system comprises sensors, electric motors, and power electronic converter [2] and each component may fail due to thermal, electrical, mechanical and environmental stresses [7]. These failures may lead to a complete system failure. Hence failure probabilities of different components of the electric drive have been widely studied.

The vulnerable components in electrical machines have been investigated in [8] and [9]. The dominant failure accounted for about 41%-51% occurs in bearings. The bearing fault is frequently initiated by mechanical breakage and overheating, and then reinforced by high vibration and persistent overloading, as well as underlying caused by the improper operation, defective components, and inadequate maintenance. From the survey, the second vulnerable component is the winding which accounts for around 15%-21% failure. The winding fault is frequently initiated by the overheating and other insulation breakdowns, and exacerbated by inadequate electrical protection. In induction machines (IMs), the other vulnerable components are rotor bars, end rings, and shaft. For permanent magnet (PM) machines, the permanent magnets are also a vulnerable component susceptible to mechanical stress and demagnetisation which results from overheating and excessive current.

Meanwhile, the vulnerable components in power electronic converters have been studied in [10] and [11]. The failure distribution of the converter shows that the most fragile component is the power device making up 38% failure in industry converters. The capacitors and gate drives are also considered to be fragile in many applications, while the resistors and inductors are barely observed with failures across all industry sectors.

From previous surveys, there is a considerable number of combination of faults. It is worth noting that no realistic system can be made to tolerant all possible combinations of faults. It is always that some combinations of failures will result in the catastrophic damage to the system [12]. In addition, it is well-known that the cost and complexity increase with the degree of fault tolerance. Consequently, reasonably additional cost and

complexity is acceptable for electric drives used in safety critical applications for the sake of higher degree of fault tolerance to protect against various principal failures.

The principal faults considered in the thesis are mainly on the machine and power converter of an electric drive. The faults within the drive are: 1) Switch open-circuit (OC), 2) Switch device short-circuit (SC), 3) Controller/sensor failure. The faults within the machine are: 1) Winding open-circuit, 2) Winding interphase or turn-to-turn short-circuit, 3) Winding intra-phase or phase-to-phase short-circuit, 4) Winding intra-strand and inter-strand short-circuit, 5) Demagnetisation, 6) Winding insulation deterioration.

On the drive side, the failures of insulated gate bipolar transistors (IGBT) which are adopted in most of converters as switches resulting from driver circuit fault, dv/dt disturbance, overvoltage/avalanche stress or temperature overshoot, would lead to the OC and SC faults [11]. The gate drive fault will also lead to the OC and SC faults because of excess electrical and thermal stress. Additionally, the position sensor and/or the controller failure may lead to voltage reversal fault when the voltage vector has erroneous 180 electrical degree offset with respect to the back electro-motive force (emf) of the machine.

A great deal of papers have investigated principal faults of permanent magnet machines in a drive and resultant fault behaviour [13]-[16]. Fig. 1-1 shows the schematic of a drive employing a voltage-source inverter and permanent magnet synchronous machine (PMSM) [13].

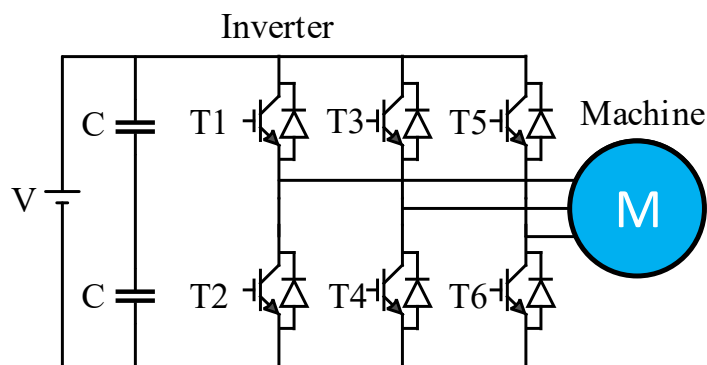


Fig. 1-1. PMSM voltage-source drive schematic[13]

Switch open-circuit fault occurs when the two switches of one phase are permanently turned off. The open-circuit fault is relatively less harmful compared to other faults because of small or zero phase currents [14].

Switch short-circuit faults are classified into symmetrical three-phase short-circuit fault and asymmetrical short-circuit fault. Symmetrical three-phase short-circuit fault may result from control error or be treated as a mitigation measure for some fault conditions. In this case, the entire top switches (T1, T3, T5) or the bottom switches (T2, T4, T6) are turned on. Asymmetrical short-circuit fault includes a single inverter switch short-circuit or a line-to-line short-circuit. Once a single inverter switch is short-circuited, such as T1, the complementary switch T4 should be turned off immediately to prevent a shoot-through. A line-to-line short-circuit fault happens when a top and bottom switch of two phase windings are turned on. In a symmetrical three-phase short-circuit fault, the steady-state phase current amplitudes are limited to the machine characteristic current. In contrast an asymmetrical short-circuit fault results in higher torque ripple and peak currents compared to the symmetrical three-phase short-circuit fault.

The position sensor and/or the controller failure may lead to the voltage reversal fault condition when the voltage vector applied to the machine has incorrect 180 electrical degree offset with respect to the machine back emf. Therefore, the phase current is produced by the sum of the applied voltage and the induced emf, and will be many times higher than the symmetric short-circuit current. It has been investigated in [15] and [16] that voltage reversal failure is more dangerous than the short-circuit faults, and will cause high levels of demagnetisation and significant deterioration in the performance. The severity of the fault under various operations is studied in [15] and [16] and it is shown that the transient current under peak torque operation is much larger than those under rated torque or peak power.

In electrical machines, the winding insulation suffers from various stresses, such as thermal overloading and stresses which accelerate thermal aging, electrical stresses which may lead to partial discharge and dielectric tracking, mechanical stresses on winding conductors, and environmental stresses such as dust and moisture. These stresses may result in deterioration of winding insulation and further lead to OC and SC faults. The SC faults could be classified to the intra-phase and inter-phase SC. In the intra-phase SC, the fault occurs between turns within a single phase, while in the inter-phase SC, the fault takes place between different phases. For permanent magnet machines, partial irreversible demagnetisation occurs when the flux density in the magnets is below its knee point.

Many papers have also investigated the principal faults of permanent magnet machines [13] [14]. Firstly, as the same with switch open-circuit fault, a winding open-circuit fault does not cause a catastrophic failure, but degrade its performance [11]. In addition, because only a few turns are entailed in the SC path in an intra-phase SC fault, an intra-phase SC fault is worse than the inter-phase SC fault due to much great fault current.

Furthermore, the worst fault scenario of an intra-phase short-circuit fault has also been studied in [17]. The effect of the number of short-circuited turns, as well as their location in a slot on the magnitude of the circulating current is investigated. It is shown that one-turn short-circuit fault leads to the lowest inductance and impedance of the faulty part, resulting in the highest fault current. If a short-circuited turn is located near the slot opening, the resultant fault current will be the highest due to large flux leakage and hence low impedance. The significantly large fault current may produce excessive heating, and subsequently lead to a local hotspot and further insulation deterioration or insulation failure in other part of the winding [7]. The fault current may also cause irreversible demagnetisation of the magnets [8].

Irreversible demagnetisation poses a certain safety risk because it can severely reduce the back emf and output torque, and increase the acoustic noise and vibrations [15] [16].

1.3 Current State-of-the-Art Fault Tolerant Electric Drive System

In order to achieve an electric drive with high fault tolerance, a considerable number of papers have investigated the requirements of the fault tolerant electric drive system used in safety critical applications. Subsequently, many papers have studied fault tolerant machine topologies based on these requirements.

1.3.1 Design Requirements

The requirements for a fault tolerant electric drive system are extensively discussed in [12] and they are summarised as follows [6]:

- 1) Redundancy and partitioning: The concept of redundancy is the system utilising one or more units operating in parallel which significantly reduces

the system down time and could still meet the output requirement [12]. However, the balance between the redundancy and the complexity also needs to be considered. Partitioning means that the system could be partitioned into several subunits, and each subunit is independent. Consequently, the output will be degraded whereas the whole system will not be completely disrupted.

- 2) Fault isolation: The redundancy and partitioning are not sufficient to protect the system from breakdown if the fault in one unit could affect other healthy units or even further propagate to the whole system. It is necessary that the fault must be contained, or isolated, to the failure unit. Specially, the electrical, magnetic, physical and thermal isolations between phases are essential in an electric drive system [5]. The electrical isolation, such as driving each phase from a separate single-phase bridge, is quite essential under fault conditions, especially under switch or winding short-circuit faults. Moreover, this will improve the voltage withstand ability of each device and marginally increases the total power electronic device volt-ampere rating although the number of power devices is increased. The magnetic isolation for reducing the effect of the mutual coupling between phases could prevent the fault currents in one phase from inducing large voltages in other phases and further cause the malfunction on the whole system. The physical isolation between phases, such as placing each winding round a single tooth so that all phase windings (including the end windings) are physically separated, will significantly eliminate the possibility of a phase-to-phase fault. If the stator outer surface is adequately cooled, the dominant temperature rise in the machine is confined within individual slots. The electrical and magnetic isolations together with the physical isolation between phases will lead to effective thermal isolation between phases.
- 3) Fault detection and mitigation: Even though the system satisfies all above requirements, the electric drive system is not yet sufficient for safety critical application without the fault detection and mitigation. The fault detection must respond quickly to enable the appropriate mitigation measure taken to prevent fault propagation before causing damage to the whole system [18].

- 4) Continued operation until the next service opportunity: This is the basic requirement for the fault tolerance that the electric drive should continue operating under fault conditions with acceptable output performance.

This thesis primarily focuses on fault tolerant electrical machines for aerospace application. Based on the above discussion, the basic requirements for fault tolerant electrical machines are:

- 1) Electrical, thermal and magnetic isolations between the phases
- 2) One per unit (p.u.) phase inductance
- 3) Fault tolerant operation
- 4) Quick fault detection and mitigation

Apart from these requirements, the electrical machines adopted for aerospace application also need the following characteristics:

- 1) High torque density
- 2) High efficiency over wide torque and speed ranges
- 3) Thermal overloading capability
- 4) High reliability
- 5) Low maintenance cost

The thesis will address a number of issues pertinent to fault tolerant machines for the safety critical applications.

1.3.2 Electrical Machine Candidates

Potential candidates of fault tolerant electrical machines are induction machine, synchronous reluctance machine (SynRM), switched reluctance machine (SRM), as well as permanent magnet machine (PMM) [5].

IMs have lots advantages, such as low cost, rugged rotor structure and simple manufacturing techniques. However, they have lower efficiency, lower torque density and lower power factor compared to PM machine due to their high copper loss. Moreover, IM has a narrow constant-power range which is usually 2-3 times of the base speed and requires complex control schemes due to motor parameter variations. Most critically, the

mutual coupling between all phases and rotor cages or rotor windings is strong, which makes IM less fault tolerant.

SynRMs have neither PMs nor windings in their rotor, resulting in a low cost, robust rotor structure capable of withstanding large thermal or mechanical stresses and wide speed operation. On the other hand, they are inferior in torque density, power factor, torque ripple and efficiency compared to PM machines.

SRMs are advantageous in terms of inherent fault tolerance, rugged and simple rotor structure with no PMs nor windings and low mutual coupling between phases. Besides, each phase winding can be electrically, thermally and magnetically isolated. However, SRMs have a very large inherent torque ripple due to the doubly salient rotor and stator, and sequential phase excitation, etc. This, in turn, results in the significant vibration, acoustic noise in general and also lower torque density compared with PM machines.

PMMs are very popular because of lighter weight, small volume, high power and torque density, high efficiency, and improved reliability. The main disadvantage is intrinsically less fault-tolerant because the PM flux cannot be turned off in case of a fault, and the conflicts between demagnetisation withstand capability and field weakening capability. Besides, high cost and volatile supply of rare-earth magnets has led to developing motors with less rare-earth PMs or the use of ferrite PMs.

1.3.3 Fault Tolerant Machine Topologies

A great deal of fault tolerant machine topologies have been investigated and reported in existing literatures.

The most classical and straightforward method is to employ redundant motor-drive systems assembled either in series or in parallel. The authors in [19] reported a redundant system adopted in the electric power steering with two electrical motors placed on the same shaft in series. In contrast, two electrical motors in a drive can be mechanically connected in parallel and fed by two separate inverters and power supplies as described in [20] and shown in Fig. 1-2. It is shown that even in the worst case in which one motor-drive system is completely failed, the remaining healthy motor-drive system can still operate albeit the torque capability is halved. However, adopting redundant motor-drives

requires large space and extra accessories under healthy and fault conditions, leading to low power density, low torque density and high cost.

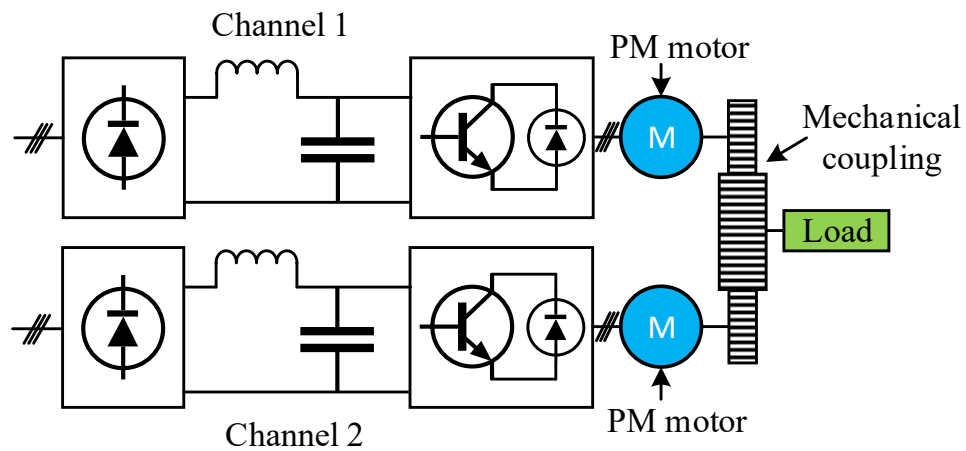
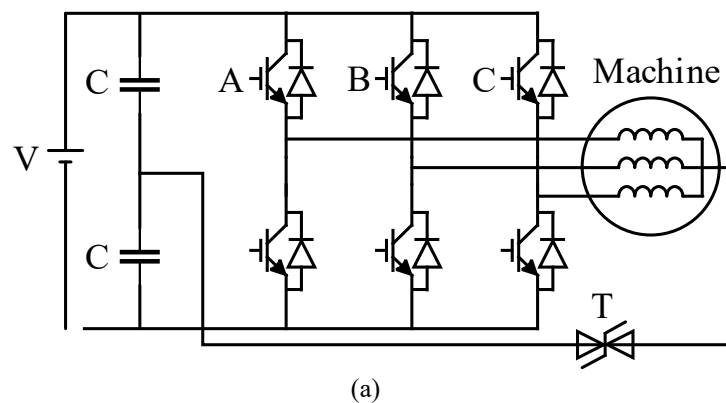
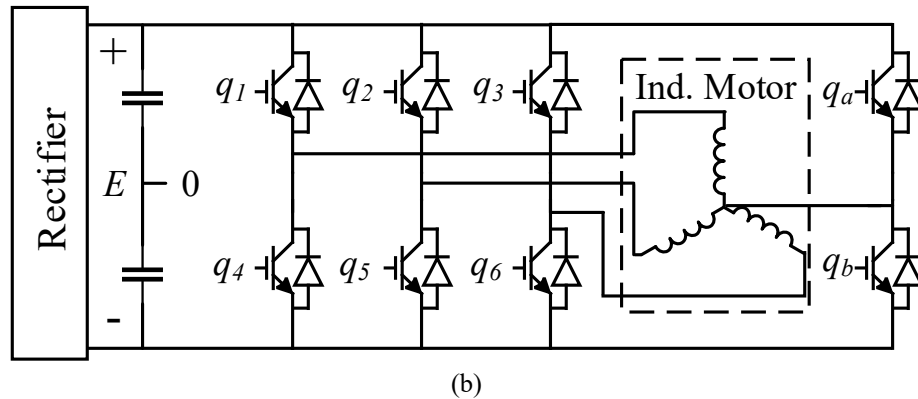


Fig. 1-2. Schematic of two redundant motor actuators.

Alternatively, fault-tolerant operation of a three-phase motor-drive system in an event of open circuit fault may be facilitated by connecting the neutral to the middle point of the direct current (DC) link as shown in Fig. 1-3 (a) or to a converter fourth leg as illustrated in Fig. 1-3 (b) [21]. It has been investigated that when one of the main inverter legs is lost, this machine can operate with only two remaining stator windings with a suitable control scheme as the zero sequence current could generate rotating magnetomotive force (MMF) in the airgap.





(b)
Fig. 1-3. 3-phase motor-drive system configurations. (a) Middle point of the DC link. (b) Converter fourth leg. [21]

The neutral connection which increases the system cost and reduces the reliability of the overall system can be eliminated by changing the wye connected winding to delta connected winding. It is shown in [22] that an induction machine with delta-connected three-phase stator winding as depicted in Fig. 1-4 can inherently operate in the one-phase open-circuit fault condition because the remaining two active phases can be independently controlled. The concept is applicable to PM machines.

However, because of the triplen harmonic components in the phase currents under healthy condition, delta-connected machines are less employed in industrial fields and studied in literatures. The major work reported in literatures is only concerned with the one-phase open-circuit fault of delta-connected induction machine. No comprehensive comparisons of the performance under healthy and various fault conditions between delta-connected and wye-connected PM machines have been made.

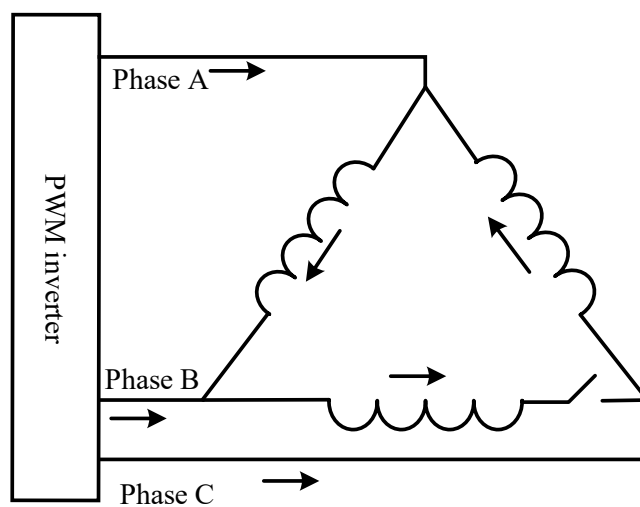


Fig. 1-4. Delta-connected three-phase stator winding with one phase open-circuit fault. [22]

Another common method which could eliminate the neutral connection is adopting the multiple phase (phase number > 3) machines. The authors in [23]-[26] have investigated the servo characteristics and fault tolerant capability of four-phase, five-phase, and six-phase machines. Fig. 1-5 presents an example of a five-phase half-bridge converters of a five-phase fault tolerant machine [23]. It has been concluded that the multiple phase machine could yield near-sinusoidal or quasi-rectangular MMF distribution, enhancing the average torque and reducing the torque ripple. Further, the semiconductor switches of the multiple phase machine have lower volt-ampere (VA) rating because the power is split across the larger number of the inverter legs. Evidently, the multiple phase machine drive has much better fault tolerance than the three-phase machines that it could continuously operate under one or more than one phase OC fault with appropriate current control strategies.

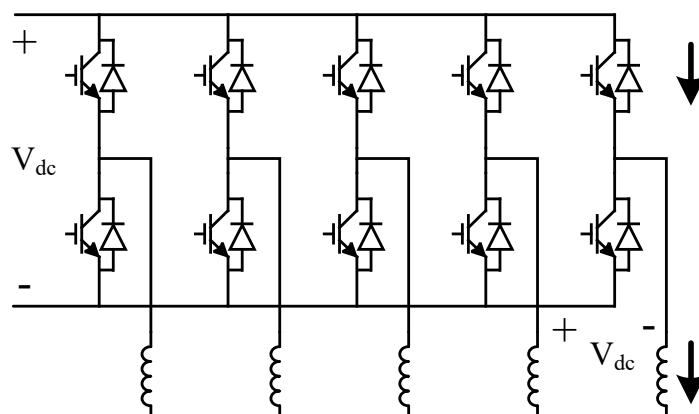


Fig. 1-5. Five-phase half-bridge converters of a five-phase fault tolerant machine. [23]

However, special current control strategies are required in 3-phase or multiple phase fault tolerant machines under fault conditions which will increase the cost and complexity. Additionally, the majority of the reported papers are concentrated on the phase OC fault of the 3-phase or multiple phase machines. The other more likely faults, such as short-circuit faults, have not been comprehensively dealt with.

Therefore, PM machines with multiple three-phase windings with inherently fault tolerant capability and reconfigurable control systems are investigated in many papers.

As the electrical motor is less likely to break down than the inverter, a double-wye connected winding PM motor is adopted in [20] for a fault-tolerant actuator, shown in Fig. 1-6, instead of two PM motors, shown in Fig. 1-2 to reduce the unnecessary

accessories. Moreover, the authors in [27] investigated a dual three-phase induction motor drive while those in [28], [29] and [30] investigated the PM machines with a segregated dual and triple three-phase windings, respectively. The schematic of the dual three-phase machine is shown in Fig. 1-7. Each three-phase set is supplied by independent electrical source through independent inverters.

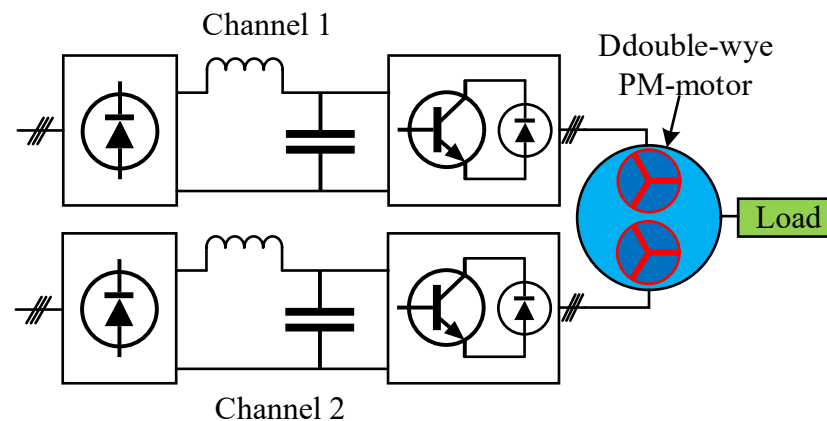


Fig. 1-6. Schematic of a double-wye PM motor architecture [20]

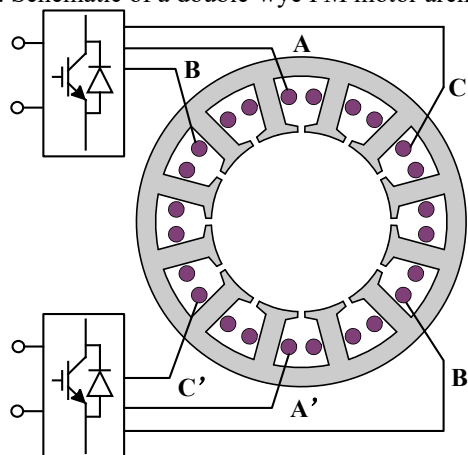


Fig. 1-7. Schematic of the dual three-phase motor drive [29]

In the multiple 3-phase machines, conventional current control strategies for 3-phase machines can be adopted under healthy condition and remain unchanged under fault conditions. Moreover, when a fault occurs in one winding set, this winding set will be taken out of service by a mitigation measure. The remaining healthy winding sets will operate normally and hence the output torque is reduced and the torque ripple is moderately increased. For some multiple 3-phase winding layouts, such as shown in Fig. 1-6 and Fig. 1-7, the different winding sets are electrically and magnetically decoupled to reduce the mutual coupling between different winding sets. However, for many other multiple 3-phase winding layouts, such as the overlapped triple three-phase winding as

shown in Fig. 1-8 [30], the fault propagation and mutual coupling of different 3-phase windings are quite strong, which increases the short circuit current and the torque ripple.

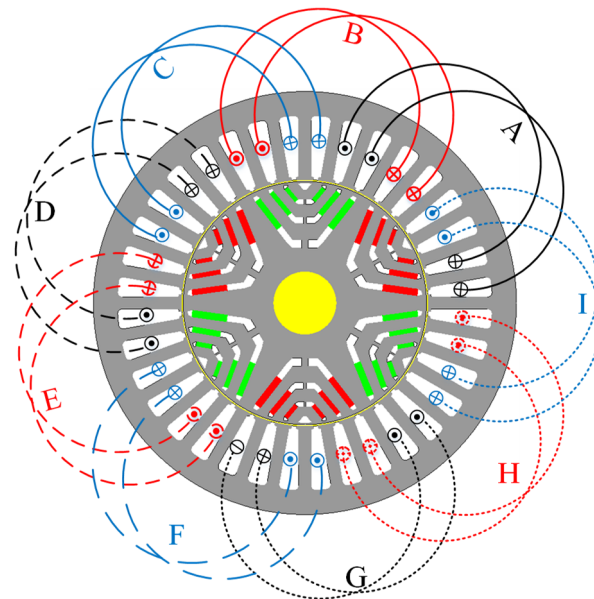


Fig. 1-8. Schematic of the triple three-phase motor winding layout. [30]

In addition, as previously introduced, because short circuit failures in the winding or power device sides are more severe than the open circuit failures, FSCW machines are focused in many literatures to address them. FSCW machines allow the short end windings, high fill factor (0.6) coils and stator modularity leading to increase in torque density and efficiency, improvement in thermal capability, while having high inductance which could limit the short-circuit current [30].

The SRM with the drive topology as shown in Fig. 1-9 [5] [31] and the FSCW SynRM with the drive topology as shown in Fig. 1-10 [32] [33] have been extensively studied. Both the SRMs and the FSCW SynRMs have highly inherent fault tolerance due to simple rotor structure with no PMs nor windings, magnetically and thermally isolated winding layout, high inductance, low cost, and high temperature withstand ability. Though, as observed, each phase of the SRM is driven by an asymmetric half bridge converter, while the 3-phase set of the FSCW SynRM is driven by the normal three-phase voltage source inverter. Therefore, the SRM has better fault tolerance than the FSCW SynRM due to the electrical isolation in the inverter drive. If a fault occurs in the winding or the drive of one phase, the total phase will be taken out of service without affecting the remaining healthy phases[34]. However, the relatively lower torque density, lower power density, lower

efficiency, and excessive torque ripple (44%) [33] make the SRMs and the FSCW SynRMs less attractive in the high performance application compared to the PM machines.

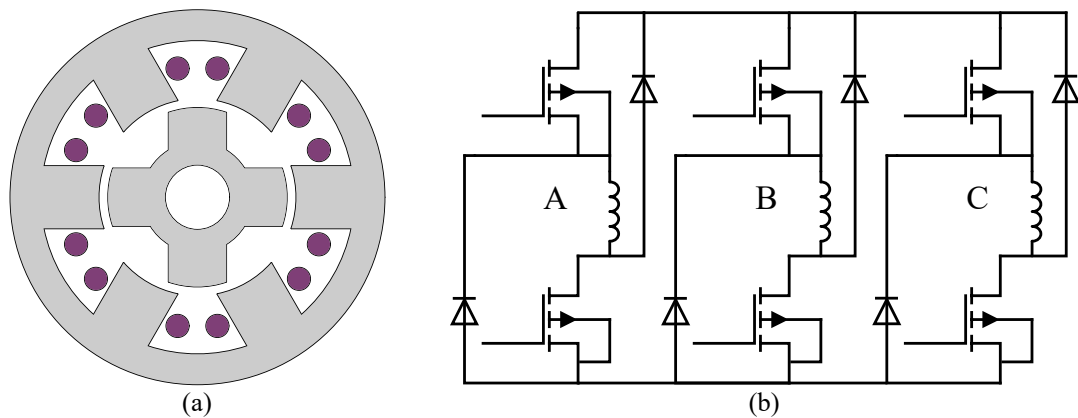


Fig. 1-9. Switched reluctance motor. (a) Cross section. (b) Three-phase asymmetric half bridge converter.

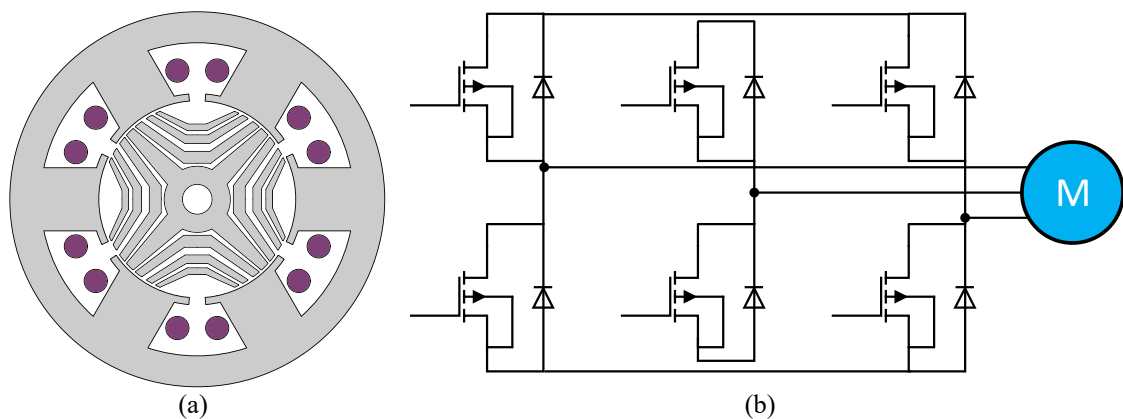


Fig. 1-10. FSCW synchronous reluctance motor. (a) Cross section. (b) Three-phase voltage source inverter. [34]

The FSCW PM machine can achieve a similar degree of fault tolerance to the SRMs and the FSCW SynRMs with higher power density and efficiency. Each stator phase is wound either on adjacent teeth as shown in Fig. 1-11 (a) or even on alternate teeth as shown in Fig. 1-11 (b) to facilitate magnetic and thermal isolations. Each single phase is controlled by an H-bridge PWM converter resulting in electrical isolation [35]-[37]. These advantages make it eminently suitable for high performance safety critical applications. However, the disadvantages are still obvious.

The FSCW yields high MMF space harmonic contents which give rise to high eddy current loss and torque ripple [35]. Some topologies utilise coils wound on alternate teeth with the width approximately equal to the rotor pole-pitch which are wider than the unwound teeth as shown in Fig. 1-12 for maximizing the torque and reducing the torque ripple compared with the original design as shown in Fig. 1-11 (b) [38]. Further, methods,

such as optimising the tooth span and slot opening size, increasing the airgap length, choosing appropriate slot and pole combinations, are proposed in [39] for reducing eddy current loss. Moreover, a FSCW machine has very small reluctance torque, so it needs strong permanent magnet field to attain high torque capability. This may further result in large back emf and fault current. Thus, it is a challenge to obtain appropriate trade-off between high torque capability and low back emf in this type of machines.

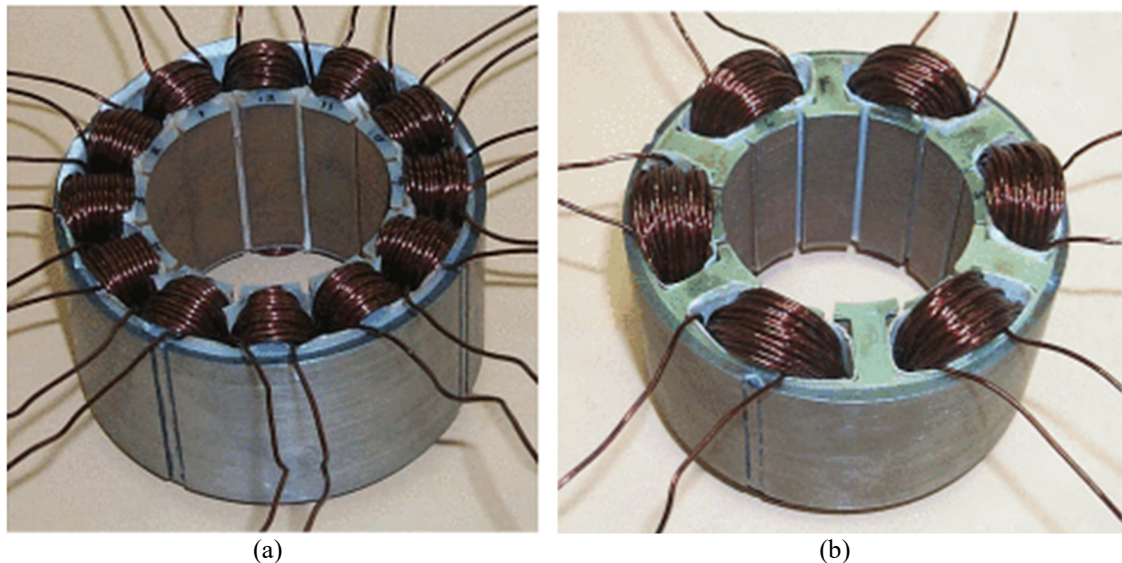


Fig. 1-11. The PM machine with 12 slots and 10 poles. (a) Stator with coils on adjacent teeth. (b) Stator with coils on alternate teeth. [38]

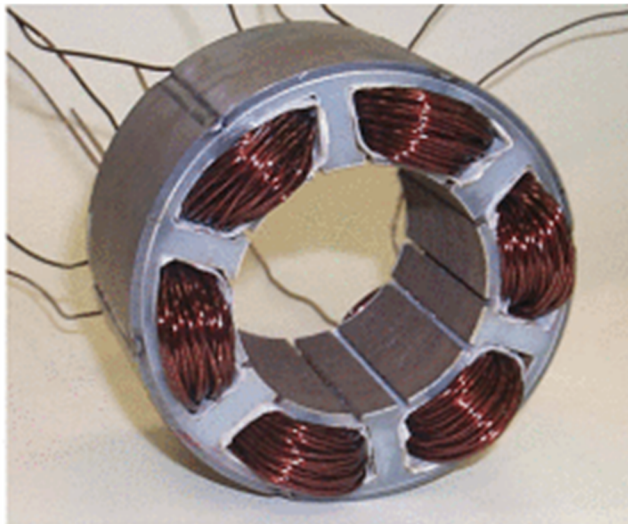


Fig. 1-12. Alternative design for 12-slot 10-pole machine with alternate teeth wound on wider teeth. [38]

No machine topologies reviewed previously could achieve high fault tolerance while maintain high performance in a cost-effective manner.

The author in [40] proposed a triple redundant, 9-phase (3x3-phase) permanent magnet-assisted synchronous reluctance motor (PMASynRM) with wye-connected winding configuration. The machine has physical and thermal isolations between different 3-phase sets. Further, each 3-phase set is controlled by an independent inverter to have the electrical isolation. The performances of the drive under healthy condition and various fault conditions, including open circuit, one 3-phase short circuit, and inter-turn short circuit, etc., have been assessed. The results show that this machine has high saliency which leads to low permanent magnet usage, inherent large reluctance torque, high efficiency and high torque density. All above features are conducive for high performance and fault tolerance, making this machine a promising solution for the safety-critical applications. This thesis will focus on this topology for extensive design, such as a novel triple redundant 3x3-phase PMASynRM with delta-connected winding providing a path for zero sequence current, and fault tolerant study.

1.4 Current State-of-the-Art Techniques of Fault Tolerant Analysis

In order to design a fault tolerant machine and assess its performance, the following techniques, such as the fault modelling technique, demagnetisation analysis technique and thermal analysis technique, can be adopted. Therefore, the current state-of-the-art in these three techniques for fault tolerant analysis are reviewed.

1.4.1 Fault Modelling Techniques

As introduced above, stator winding failure is the second major faults in electrical machines. Specially, inter-turn SC resulted from insulation degradation between the turns is one of the leading causes of winding failures and particularly critical. An inter-turn SC leads to a significantly large circulating current in the faulted turns which may produce excessive heat in the surrounding insulations. This further results in local hotspot and degrades the insulation and ultimately leads to catastrophic failure, such as phase-to-ground or phase-to-phase faults. The significant fault current and high temperature can also produce irreversible demagnetisation of the magnets. Therefore, sensitive fault detection, and effective fault mitigation and fault-tolerant control strategies are essential for fault tolerant machines in safety critical application. Because the fault modelling is the first step for the development of fault detection techniques, an accurate transient

model of inter-turn SC fault at design stage is essential [41] [42]. Additionally, fault modelling which could locate an inter-turn SC fault in large rating machines is cost effective as removing the complete winding is costly and the downtime of the machine is long.

Many reported literatures have developed inter-turn fault models based on various techniques. The analytical modelling is the most commonly used and is presented in [42]-[44] for computational efficiency and ease of use in system simulation studies.

Firstly, the classical reference frames theory is investigated for fault modelling [44]-[47]. A simplified mathematical d-q-0 model with no need of any geometry information for induction machines is presented in [46] and [47]. However, the simplified d-q-0 model cannot identify the fault location.

Then, a new approach considering machine geometry and the physical winding layout based on the multiple-coupled-circuit modelling is introduced in [48] and [49] which could inherently identify the fault location in the model. Moreover, the winding function approach considering asymmetries in the stator windings and space harmonics is adopted in [50]-[52] for accurate estimation of the inductances. On the basis of winding function approach, the models with inter-turn SC of delta-connected induction machine and wye-connected synchronous machine are established in [51] and [52], respectively. The equivalent circuits of 3-phase delta- and wye-connected windings with an inter-turn SC fault also known as turn fault on single phase are presented in Fig. 1-13 and Fig. 1-14, respectively. However, some simplifications adopted for the machine together with the neglect of the saturation lead to inaccuracy.

Subsequently, the authors in [53] developed a simplified mathematical model which includes the zero sequence voltage components in the wye-connected PMSM and zero sequence current component in the delta-connected PMSM which could help identify the faulty phase. However, the mathematical model of the PMSM with inter-turn fault neglects the high-order harmonic components in the fault current and saturation. A common weakness in analytical modelling is that magnetic saturation cannot be adequately represented.

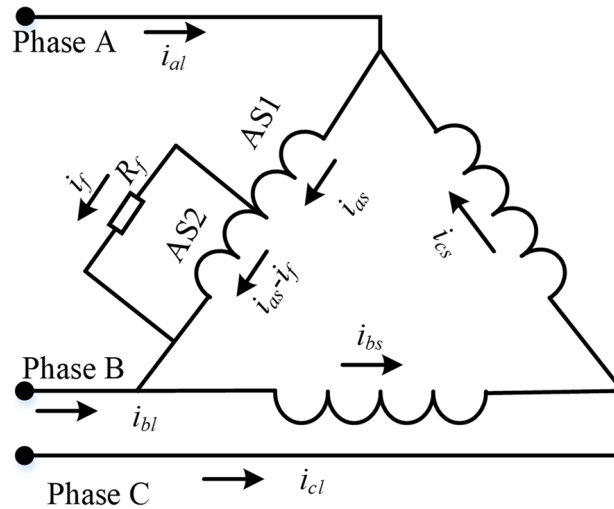


Fig. 1-13. The equivalent circuit of 3-phase delta connected machine windings with turn fault on single phase.

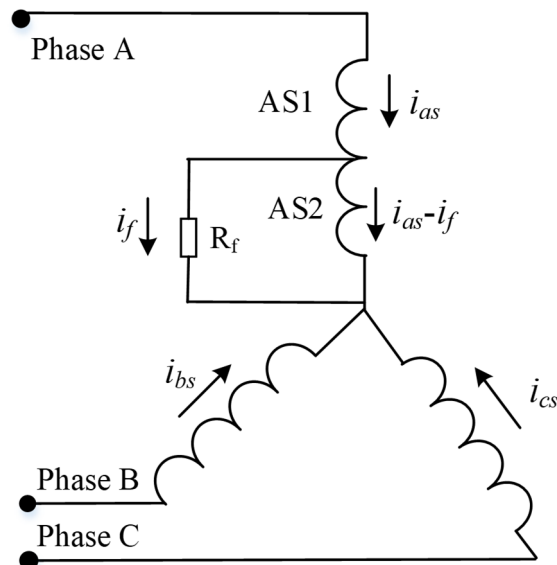


Fig. 1-14. The equivalent circuit of 3-phase wye connected machine windings with turn fault on single phase.

Hence, numerical modelling techniques such as the finite element (FE) method are adopted to increase modelling accuracy. The author in [54] established an accurate semi-analytical model of interior permanent magnet (IPM) motor under stator turn fault considering magnetic saturation. The analytical equations of an IPM motor with a turn fault in the dq frame are derived based on the dq flux-linkage map of the healthy motor computed from its FE model with due accounting of saturation. Therefore, the combined transient model has more accuracy when predicting the peak currents and current waveforms compared to the pure analytical models. However, the self- and mutual inductances of the healthy and faulted turns are assumed to be proportional to their

number of turns. This assumption is not strictly correct, especially at high saturation condition or for most FSCW PM machines in which a significant part of the inductances are contributed by the slot leakage. Moreover, the use of fault ratio for simple scaling of leakage inductance is also not suitable since the leakage inductance is dependent on the location of faulted turns in the slot [55].

Therefore, the authors in [41] established an accurate and computationally efficient fault model of an IPM motor in which the nonlinear mapping of the flux linkages to currents and rotor position θ_m (mechanical angular position) are obtained from FE method. This approach is the most accurate fault model apart from a time-stepped transient FE-circuit coupled analysis because it could represent full spatial harmonics and magnetic saturation under inter-turn fault as well as all load conditions. The effects of rotor skew are also accounted. The method can also be used for surface PMMs, SRMs, switched flux machines, etc. However, the method in [41] is more computationally expensive than the method in [54]. Besides, it does not provide insight into the key factors affecting fault currents.

Many inter-turn SC models have been investigated with different accuracies. Selection of an appropriate modelling method depends on requirements for accuracy and available computational resources.

In this thesis, the equivalent model of delta connected PMASynRM with inter-turn fault in one phase which has not been comprehensively reported in the literature before will be established. Moreover, the modelling method introduced in [54] is adopted as it can explain the effect of the zero sequence current on the fault current with reasonable accuracy.

1.4.2 Demagnetisation Analysis Techniques

PM machines are widely adopted in many applications due to their high power and torque density, high power factor over wide torque-speed operating region and good controllability. However, demagnetisation in a permanent magnet machine is a potential risk.

It is well known that if machines operate in harsh environment or under high temperature and/or heavy loads, the possibility of irreversible demagnetisation is

increased. High mechanical vibration may also lead to cracks in the magnets and make them more vulnerable to demagnetisation field. Besides, peak transient current in fault conditions can be extremely high and causes irreversible demagnetisation in magnets [56] [57].

Irreversible demagnetised regions may be partial or over wide areas of magnets. Both demagnetisation faults will severely reduce the emf and output torque of a machine and hence degrading PM machine performance and efficiency. In addition, the fault may lead to excessive harmonics in the airgap flux density, stator currents, voltages and output torque, and consequently significant increase in acoustic noise and vibrations. Furthermore, the input current will be increased for the same load torque when the magnets are partially demagnetised. This would give rise to further increase in magnet temperature, and result in more severe demagnetisation in the machine [57]. Therefore, demagnetisation withstand capability is critical for fault tolerant machines in safety critical applications while maintaining the appropriate trade-off between the demagnetisation withstand capability and the cost of increased volume and mass of magnets.

A number of papers have compared rotor types and winding configurations in terms of their demagnetising withstand capability. It can be concluded that V-shaped and VU-shaped IPM rotor configurations in which the magnets are buried deep in the rotor core have a lower demagnetisation risk compared to SPM and spoke-type alternatives [58] [59]. Furthermore, the distributed winding configurations are generally less vulnerable to demagnetisation than the FSCW machines

In addition, another major challenge in design stage is the accurate assessment of demagnetisation against extreme operating conditions, including fault.

The analytical techniques [60]-[62] are fast to diagnose and assess the risk of demagnetisation at the design stage. However, the analytical approach neither is applicable to machines with complex rotor structure nor considers effects of saturation and stator slotting. This method can only provide an approximate result. Therefore, FE-based approach is studied to assess the risk of demagnetisation. Both the 2-dimensional (2D) and 3-dimensional (3D) FE-based approaches are adopted in [63]-[65] for demagnetisation assessment of machines with complex rotor structure with high accuracy,

and can also give the details of local demagnetisation in different sections of the magnet albeit they require long computation time.

Moreover, the work in [66]-[68] considered the direction of magnetisation in a magnet instead of only using the magnitude of flux density and consequently further increase the accuracy in the demagnetisation assessment. Unfortunately, most above assessments could not give a clear insight of the severity of demagnetisation behaviour as they are not capable of predicting the post-demagnetisation performances of the PM machine. To address this problem, various assessments capable of predicting the post-demagnetisation performance have been reported in [69]-[71]. The authors in [69] adopted a history-dependent hysteresis model to predict the reduction of back-emf, while the authors in [70] [71] calculated the remanence ratio which is defined as the reduction of post-fault remanence flux density of permanent magnets with respect to the pre-fault values. However, as these demagnetisation models do not consider the continuing accumulation of demagnetisation, they could only present the demagnetised region in which the operating point is below the knee point flux density at the present time and could not track the history of demagnetised regions, causing errors in the post-demagnetisation performance assessment. Accordingly, the demagnetisation models which can track the history of partial demagnetisation have been offered in some literatures [72]-[74].

The authors in [74] provided a continuous demagnetisation performance assessment which utilises the recoil line, considers the direction of flux density and tracks the history of partial demagnetisation. The remanence of each magnet element is updated in the case of partial demagnetisation, and the new value in the subsequent step of the analysis will not replace the previous values. It also evaluates post-demagnetisation performance, such as the reduction in back-emf and output torque, under various fault conditions, especially the voltage reversal fault which is the worst case. The model has been validated by experimental measurements on the post-demagnetisation performance of a prototype machine.

Hence the technique described in [74] could be utilised at the design stage to check whether the proposed triple 3-phase machine has high demagnetisation withstand capability under various fault conditions, particularly under the voltage reversal fault.

1.4.3 Thermal Analysis Techniques

The comprehensive thermal analysis was not performed along with electromagnetic (EM) analysis of electrical machines in the past. Instead, limiting values of magnetic and electric loadings and/or current density were used at the design stage for preventing the motors from overheating. However, there is a growing need for electrical machines with high power density in various fields in recent years. It is well known that the high power density can be achieved by applying high current densities to the electrical machine windings which may result in large copper losses and, in turn, high hotspot temperatures [75]. Meanwhile, the high power density can also be achieved by operation at high speeds, leading to high current and frequencies and then increasing the iron losses in the stator and rotor laminations, and eddy current loss in the permanent magnets. Hence thermal analysis is indispensable in order to avoid premature failure due to overheating. Furthermore, since the losses are critically dependent on the temperature and vice versa, EM and thermal analysis need to be performed together for accurate prediction of the motor behaviour [76].

Since temperature is one of the key limiting factors for fault tolerant machines, accurate thermal analysis is particularly important at design stage for such machines. The winding hotspot temperature under healthy and fault conditions should be below the maximum permissible temperature to ensure required insulation life. This is significantly vital under the inter-turn SC fault condition because the very large circulating current may flow in the faulted turns and produce large heat and rapid increase in winding temperature.

A variety of techniques have been published on thermal analysis in electrical machines. They can be broadly classified as lumped parameter (LP) based and numerical based approaches.

1.4.3.1 Lumped-Parameter Thermal Network

The analytical method based on a LP thermal model has been developed to estimate the temperature distribution. The components that have similar temperatures will be lumped together and represented as a single node in the LP thermal model. The thermal transfers between these nodes are represented by thermal impedances connecting these nodes.

As well known, the LP thermal model describes the relationship of the temperature and heat flow (power) over a thermal resistance, which is analogy to the voltage, current, and electrical resistance in an electrical network, respectively. Therefore, the LP thermal model could predict the temperatures of the main components within the machine for a given loss distribution.

An early attempt is to use simple thermal networks with few thermal resistances, capacitances, and heat sources to implement a functioning thermal analysis because of the limited computational capabilities [77]. Nowadays, much more complex thermal networks with a high number of thermal elements have been extensively investigated with the introduction of computers. Moreover, the transient LP thermal models can be applied to a variety of machine types, such as induction machines in [78]-[80] and PM machines in [81]-[83].

Furthermore, the LP network structure and the number of nodes in each section of critical components should be carefully selected to represent heat transfers in both axial and radial directions to improve prediction accuracy. For example, the author in [84] developed a LP thermal network to model a tooth-slot section of a water cooled tubular linear PM machine for predicting hotspot temperature in the phase windings. However, excessively large number of nodes in a LP network will increase the complexity of the thermal model. It is important to obtain the trade-off between the prediction accuracy and thermal model complexity.

Since heat can be transferred through conduction, convection and radiation, a LP thermal model contains thermal impedance components representing the three heat transfer mechanisms for different parts of the motor construction [85]. Extensive work has been undertaken to develop methods for computing critical thermal parameters [85]-[88].

Conduction thermal resistance represents the main heat-transfer paths in a machine, such as from the winding to the stator tooth and back iron, from the tooth and stator back iron to the stator bore and housing interface, etc. The conduction resistance can be obtained by the path length divided by the product of the path area and the materials' thermal conductivity. Convection is the heat transfer process due to fluid motion in natural or forced convection. Radiation is the heat transfer process from a surface by

electromagnetic waves [89]. Internal convection and radiation resistances are usually used for heat transfer across the airgap and from the end windings to the endcaps and housing. External convection and radiation resistances are used for heat transfer from the outside of the machine to the ambient. The convection resistance is equal to one divided by the product of the surface area and the convection-heat-transfer coefficient. The convection-heat-transfer coefficient can be predicted by proven empirical formulations based on convection correlations for most of the basic geometric shapes in electrical machines [90]. The radiation resistance is equal to one divided by the product of the surface area and the radiation-heat-transfer coefficient. The radiation-heat-transfer coefficient depends on the emissivity, the view factor and temperatures of the surface. The emissivity depends on the surface material and finish, while the view factor can be obtained according to different geometric surfaces.

In summary, the LP thermal model is highly effective and computationally efficient for predicting both steady-state and transient temperatures of the critical regions in a wide range of machines. However, because the complex thermal phenomena in electrical machines are often simplified based empirical data in the LP model, prediction accuracy will be limited.

1.4.3.2 Numerical Approaches

Numerical approaches mainly consist of finite element analysis and computational fluid dynamics (CFD) for thermal analysis of electrical machines.

FEA can be subdivided into 2D and 3D models of electrical machines. Compared to the LP thermal model, FEA alone suffers from the same problems that convection and radiation are approximated based on empirical formulations [90]. However, FEA can accurately model the solid elements of complex geometric shapes with specified conductivities and hence accurately predict temperature distribution in a complex geometry. It is commonly used in predicting winding temperature distribution which is of great importance in the thermal analysis of electrical machines.

Additionally, the accuracy of losses, including harmonic losses in the rotor, air friction loss on the rotor surface, stator core loss and copper loss, etc., predicted in the FEA is critical for the final temperature distribution. [91]. To improve prediction accurate, the

author in [92] utilised the non-symmetrical operational iron loss distribution in a FE thermal model of a salient machine.

With great flexibility in modelling complex geometry and heat transfers thermal FEA methods are applicable to different electrical machine topologies, such as TEFC induction motors [93], naturally cooled synchronous machine [89], air-cooled IPM [94], etc. albeit the FEA approach is time-consuming. However, it is a widely accepted approach to thermal analysis for very complex geometry which is may not be dealt with by the LP thermal method. Additionally, FEA could provide a clear and detailed insight of the temperature distribution in various components of an electrical machine.

As pointed out previously, convective heat transfer and fluid flows of the coolant in electrical machines with different cooling systems cannot be predicted by LP and FEA thermal models. Therefore, CFD has been employed recently to study fluids dynamics and heat transfer of electrical machines using various well established discretization methods. As a result, the thermal design of machines can be optimised at an early stage without the need for extensive and costly experimentation [95].

It has been shown that CFD is attractive for the thermal-flow analysis of the complex air flow in the end regions of TEFC induction machines and the knowledge gained from such analysis could help modify cooling design to improve cooling efficiency [96] [97]. Moreover, the CFD predictions have been compared with experimental measurements in [95] [98] to demonstrate that the commercial CFD can provide valuable insight into air flow and heat transfer with reasonable accuracy.

Although CFD has become an effective tool for modelling convective heat transfer and fluid flows of the coolant in electrical machines, implementing CFD models of electrical machines is very time-consuming and needs high computational resources [95]-[99].

However, it is found that most published papers concentrate on the thermal analysis under healthy condition and only few papers consider the thermal analysis under fault conditions with asymmetric temperature distribution. Seldom have considered coupled electromagnetic-thermal simulations under fault conditions. Therefore, this thesis will establish a LP thermal model, a 3D FEA thermal model and a directly coupled

electromagnetic-thermal simulation based on the FE transient models for accurately predicting asymmetric temperature distribution of a fault tolerant machine under common fault conditions.

1.4.4 Summary

Fault tolerance means the machine has the ability to operate continuously under fault conditions with satisfactory performance. Therefore, the ‘bench marks’ of the post-fault performance of the PMASynRM under study are set to determine whether the PMASynRM is “fault tolerant” or not in Chapters 2 to 7. Firstly, the types of faults to be tolerated include demagnetisation, switch and winding open-circuit fault, switch and winding short-circuit fault, inter-turn short-circuit with mitigation measure. Then the satisfactory performance indicators under fault conditions conclude: 1) Mean torque under fault condition is larger than 50% rated torque; 2) Torque ripple is smaller than 40%; 3) Average temperature is smaller than 200°C and hotspot temperature is smaller than 220°C. In addition, the switch and winding open-circuit fault can be remediated by opening all the switches of the faulty set, while the switch and winding short-circuit fault can be remediated by closing all the top or the bottom switches of the faulty 3-phase inverter. The open-circuit and short-circuit faults can be easily detected by eliminating voltage sensors [100]. Moreover, in case of the worst fault which is inter-turn fault, it can be detected by the 2nd harmonic in instantaneous active power (IAP) and reactive power (IRP) produced by an SC fault, and then mitigated by applying a 3-phase terminal short circuit to the faulty set [101].

1.5 Scope of the Thesis

The thesis is organised in eight chapters on design, optimisation and multi-physics fault analysis of fault tolerant machines for safety-critical application. Then it provides the suggestion on which analysis and modelling techniques are necessary to evaluate the fault tolerant, detection and mitigation capabilities of permanent magnet electrical machines in aerospace applications. The main contents are summarised as follows:

Chapter 1 introduces the background of the safety critical applications for fault tolerant machine drives. In addition, the typical fault conditions and the design requirements for dealing with these faults of the machine drive system are explained.

Moreover, the fault tolerant machine topologies and techniques for fault tolerant analysis are comparatively reviewed, including the current state-of-art electrical machine candidates and current state-of-art fault modelling, demagnetisation analysis, thermal analysis techniques.

Chapter 2 proposes a novel triple redundant 9 phase (3x3-phase), 6-pole, 36-slot PMASynRM with segregated delta-connected winding. It also investigates the impacts of zero sequence current on the performance by comparing delta- and wye-connected winding configurations. Firstly, equivalent models of delta- and wye-connected winding with inter-turn SC have been established to assess whether the zero sequence current could reduce the significant inter-turn fault current with the aid of FE analysis. Subsequently, the healthy and various fault behaviours of the PMASynRM with delta- and wye-connected windings are comprehensively compared to show that the delta-connected PMASynRM has better fault tolerance.

Chapter 3 assesses the demagnetisation withstand capability for the proposed PMASynRM with wye-connected winding by employing a continuous demagnetisation model. The dynamic response during fault transients, the demagnetised regions in the magnets and the post demagnetisation performance under various critical faults at the peak torque and base speed have been comprehensively assessed. The comparisons of transient responses of the wye- and delta-connected winding under critical fault condition demonstrate that the machines with both windings have very strong demagnetisation withstand capability.

Chapter 4 establishes transient LP and 3D thermal models to assess the thermal behaviour of the proposed PMASynRM with the wye-connected winding under healthy and fault conditions with asymmetric temperature distribution. Firstly, the cooling design with a spiral cooling jacket of the machine is introduced. The transient LP and 3D thermal models are modelled in detail and compared for predicting the temperature distributions under typical fault conditions. Subsequently, a machine prototype has been tested to validate the losses predicted by the 2D electromagnetic model and the transient as well as the steady-state temperatures predicted by the 3D thermal model considering specific experimental conditions. The merits of the two thermal models are also evaluated. The LP model would be more suitable for thermal assessment of the fault tolerant machine in

design stages while the 3D model will be more accurate for thermal assessments in real operations.

Chapter 5 proposes a directly coupled EM-thermal simulation based on 2D transient EM and 3D thermal model with aid of a scripting file to gain a deeper insight of the thermal behaviour under various fault conditions of the proposed PMASynRM with wye-connected winding. These faults include different speeds, different number of SC turns, with and without remedial action, with non-stranded and stranded coils. The transient temperature results under EM-thermal coupled simulation have been comprehensively compared with those under thermal-only simulation. The comparison shows the necessity of the EM-thermal coupled simulation against different fault conditions. Moreover, the most severe faults are given.

Chapter 6 assesses the EM and thermal behaviour of the proposed PMASynRM with wye-connected winding under insulation deterioration leading to SC faults. Cut-through resistance is defined as the minimum resistance across faulted turns before irreversible damage of insulation due to heat would take place. The range of the cut-through resistances for all possible faulty insulation volumes under turn-to-turn insulation deterioration leading to SC fault are quantified by 3D thermal analysis and the insulation resistance thresholds for fault detection and mitigation to prevent the catastrophic failure have been estimated. Moreover, an example with particular insulation volume has been analysed with an EM-thermal model to show the aging process when the electrical resistance decreases with increase in temperature. Finally, tests on the prototype machine drive have validated the predicted EM behaviour under turn-to-turn insulation deterioration leading to SC faults.

Chapter 7 analyses potential electric failure modes resulting from insulation breakdown and quantifies their severity and consequences of a 2.5 MW, two 3-phase permanent magnet generator operating at +/- 1.5kV DC for E-Fan-X demonstrator by employing 2D FE model and 3D thermal model. The impacts of worst case faults are assessed and the limitation on existing measures for fault mitigation is highlighted. It has been concluded that there is no effective means to manage the worst case short circuit fault other than mechanical disconnection of the generator from the engine. Moreover,

the fault can only be managed if an insulation break down can be detected at very early stage before an avalanche effect is triggered. Recommendations are made for future work.

Chapter 8 summarises the findings of the study on the fault tolerant machines for safety-critical application described in the thesis and also outlines the future scope of the research for enhancement of the fault tolerant machine.

1.6 Contributions of the Thesis

The major contributions of this thesis on design and analysis of the fault tolerant machines for safety-critical application are outlined as follows:

1. The triple redundant, 9-phase PMASynRM with delta-connected winding is proposed and compared with the same PMASynRM with wye-connected winding under healthy and fault conditions. It has been shown that the zero sequence current in the delta-connected machine significantly reduces the turn fault current and hotspot temperature compared with the wye-connected PMASynRM, leading to better fault tolerance.
2. A continuous demagnetisation model is adopted to assess the risk of partial irreversible demagnetisation for the fault tolerant PMASynRM. It has been shown that the machine has very strong demagnetisation withstand capability under short-circuit faults. The output torque only reduces modestly under the most severe voltage reversal fault.
3. The transient LP thermal models and a 3D thermal model for thermal analysis under healthy and fault conditions of the triple redundant, 9-phase PMASynRM with spiral cooling jacket system have been established. These two models could predict the transient and steady-state asymmetric temperature distributions under fault conditions and the 3D thermal model can better represent loss distribution in the end winding.
4. A directly coupled EM-thermal simulation based on 2D transient EM and 3D thermal model with aid of a scripting file is established to assess the thermal behaviour as a result of the interaction of electromagnetic and thermal behaviours under various fault conditions of the proposed PMASynRM. It has been demonstrated that EM-thermal coupled simulation is necessary for accurate

prediction of temperature rise when the copper loss of the faulted turns or strands is quite large.

5. The EM and thermal behaviour of the PMASynRM under insulation deterioration leading to SC faults have been comprehensively assessed. Based on this, the range of the cut-through resistances for all possible faulty insulation volumes as well as the insulation resistance thresholds for fault detection and mitigation to prevent the catastrophic failure have been estimated under turn-to-turn insulation deterioration leading to SC faults. It has been shown that when the insulation material resistivity decreases with the increase in temperature, the insulation deterioration is accelerated or even triggers an avalanche effect.
6. The potential electric failure modes resulting from insulation breakdown, and their severity and consequences of a 2.5 MW permanent magnet generator operating at +/- 1.5kV DC for E-Fan-X demonstrator are analysed by employing simulation techniques described in the thesis. The worst case faults are assessed and the limitation on existing measures for fault mitigation is highlighted.
7. The necessary analysis and modelling techniques for evaluating the fault tolerant, detection and mitigation capabilities of permanent magnet electrical machines in aerospace applications are suggested.

1.7 Publications

Journal papers:

[J1] **Y. Shi** and J. Wang, “Continuous demagnetisation assessment for triple redundant nine-phase fault-tolerant permanent magnet machine,” *J. Eng.*, vol. 2019, no. 17, pp. 4359–4363, 2019.

[J2] **Y. Shi**, J. Wang, and B. Wang, “Performance assessment of triple redundant nine-phase delta- and wye-connected permanent magnet-assisted synchronous reluctance motor under healthy and fault conditions,” *J. Eng.*, vol. 2019, no. 17, pp. 3563–3567, 2019.

[J3] **Y. Shi**, J. Wang, and B. Wang, “Electromagnetic-thermal Coupled Simulation under Various Fault Conditions of a Triple Redundant 9-phase PMASynRM,” *IEEE Trans. Ind. Appl.*, is accepted.

[J4] Bo Wang, J. Wang, A. Griffo and **Y. Shi**, “Investigation into Fault Tolerant Capability of a Triple Redundant PMA SynRM Drive,” *IEEE Trans. Power Electron*, vol. 34, no. 2, pp. 1611-1621, 2019.

Conference papers:

[C1] **Y. Shi**, J. Wang, and B. Wang, “Lumped-Parameter and 3D Thermal Model of a PMASynRM under Fault Conditions with Asymmetric Temperature Distribution,” *2018 IEEE Energy Convers. Congr. Expo. ECCE 2018*, pp. 6521–6528, 2018.

[C2] **Y. Shi**, J. Wang, and B. Wang, “EM-Thermal Coupled Simulation under Various Fault Conditions of a Triple Redundant 9-Phase PMASynRM,” *2018 IEEE Energy Convers. Congr. Expo. ECCE 2018*, pp. 5757–5764, 2018.

[C3] **Y. Shi**, J. Wang, R. Hu, and B. Wang, “Electromagnetic and thermal behavior of a triple redundant 9-phase PMASynRM with insulation deterioration fault,” *2019 IEEE Energy Convers. Congr. Expo. ECCE 2019*.

Chapter 2 Winding Configuration Optimization of a Fault Tolerant Machine Drive Based on PMASynRM

2.1 Introduction

Fault tolerant drive which can continue operating in a satisfactory manner with a number of potential faults have attracted increasing attention in safety critical applications.

It is well known that compared to IMs, SRMs, and SynRMs, the PM machine is an attractive candidate because of high torque and power density, high efficiency and low maintenance cost. However, the presence of PM field in a PM machine under fault conditions is of major concern. Therefore, PMASynRM which using low cost PM (such as ferrite and bonded NdFeB) or small amount of PM has gained increasing attention recently. PMASynRM has high-saliency, wide flux-weakening region, competitive torque density and efficiency with PM machines, and improved fault-tolerant capability due to low back emf. The main disadvantage is that it usually utilises distributed windings to generate large reluctance torque but also results in strong inter-phase coupling.

Additionally, a number of fault tolerant machine topologies have been introduced. The most simple method is to employ redundant machine-drive systems assembled either in series or in parallel [19] [20]. However, they usually have low power density and torque density due to large space and extra accessories. The alternative method is wye-connected three-phase motor-drive system in which the neutral point is accessible and connected to the middle point of the DC link or to a converter fourth leg [21], while another method is the delta connected motor drive [22]. Both the two above methods could inherently work under one-phase open-circuit fault condition because the remaining two active phases can be independently controlled. However, the additional connection from the neutral point to the middle point of the DC link or the fourth leg increases the system cost and reduces the reliability of the overall system. Moreover, the delta-connected winding is less adopted in industrial applications due to presence of the triplen emf harmonics and resultant zero sequence current under healthy condition. Multiple phase (>3) machines have much better fault tolerance than three-phase machines since they can continuously

operate at the loss of more than one phase with an appropriate control algorithm [23]-[26]. However, the required special current control strategies increase the cost and complexity. Furthermore, in order to improve the fault tolerance at SC faults, PM machines with multiple three-phase winding with reconfigurable control systems having inherently fault tolerant capability since the fault set can be taken out of service are proposed [27]-[30]. However, the strong mutual coupling of different 3-phase windings will increase the SC current and the torque ripple. The FSCW SynRM [32]-[33] are similar to SRMs, having inherent fault tolerance but low torque density, efficiency, and excessive torque ripple. Compared with FSCW SynRM, FSCW PM machines with each stator phase wound either on adjacent teeth or on alternate teeth also have inherent fault tolerant capability due to magnetic, thermal and electrical isolations but with high power density and efficiency. However, the high eddy current loss, high torque ripple combined with the inherent small reluctance torque introduce challenges of FSCW PM machines in the safety critical applications with high performance [36]-[39]. Because the torque in such machines is produced by PM field only, increase in torque leads to large back-emf at high speed. Uncontrollable regeneration, which is not permitted in some applications, may take place when the converter fails.

Since none of the above machine topologies could achieve high fault tolerance while maintain high performance in a cost-effective manner, [40] proposed a triple redundant, 9-phase (3x3-phase) PMASynRM with wye-connected winding configuration. This machine has been demonstrated to have inherent high reluctance torque and torque density, high efficiency and high fault tolerant ability under various fault conditions.

As introduced, typical fault conditions contain open circuit, short circuit and turn fault conditions, etc. Among these faults, inter-turn short-circuit fault is particularly critical since it leads to a large circulating current many times greater than the rated current in the faulted turns. This may give rise to a local hotspot and ultimately cause a complete insulation failure of the winding as well as irreversible demagnetisation of magnets. Therefore, in order to realise fault-tolerant operation it is essential to effectively mitigate the inter-turn SC fault. Multiple inter-turn SC fault mitigations are reviewed in [102], such as terminal short circuit, phase current injection and mechanical shunts, etc. Among these strategies, terminal SC is easily applied on the fault phase or a total 3-phase set via

power electronic converters to reduce the flux linkage of the faulted turns and further reduce the turn fault current.

As well known, machines operating in unbalanced modes under fault conditions usually lead to significant zero sequence flux linkage in the faulted turn. Consequently, a novel triple redundant 9-phase (3x3-phase) PMASynRM with delta-connected winding based on the machine topology in [40] is proposed in this chapter for further reducing the excessive turn fault current. The delta-connected winding provides a path for zero sequence current in the fault 3-phase set, resulting in lower residual flux linkage in the faulted turns and lower turn fault current. However, the majority of work reported in literatures only deals with the one-phase open-circuit fault of delta-connected induction machine. There is no comprehensive comparisons of the performance under healthy and various fault conditions between delta- and wye-connected PM machines in terms of performances in both healthy and fault conditions.

Moreover, the influence of the zero sequence current on the flux linkage in the faulted turns will be analysed in detail by the equivalent model of delta-connected PMASynRM with inter-turn fault. As introduced, many inter-turn SC models have been investigated with different accuracies on different machine topologies. However, the equivalent model of delta connected PMASynRM with inter-turn fault in one phase has not been comprehensively reported in the literature before.

This chapter will investigate the triple redundant 3x3-phase PMASynRM with delta-connected winding based on the machine topology in [40]. Firstly, an equivalent model of delta-connected winding with inter-turn short-circuit will be established for better insight of the fault behaviour. The performances of the triple redundant PMASynRM with delta- and wye-connected windings will be comprehensively compared under healthy and various fault conditions, including open circuit, inter-turn short-circuit and terminal short-circuit. Additionally, because temperature is a key limiting factor for post fault operation, the hotspot temperatures under fault conditions will be analysed and compared.

2.2 PMASynRM with Wye-Connected Winding Configuration

The triple redundant, 9-phase (3x3-phase), 36-slot, 6-pole PMASynRM with wye-connected winding as shown in Fig. 2-1 is designed by Vipulkumar I. Patel and Bo Wang. The output torque of PMASynRM is a combination of PM torque and reluctance torque. The high saliency results in large inherent reluctance torque and further reduces the permanent magnet usage without decreasing the torque capability. Therefore, it exhibits comparable performance with conventional PM machines in terms of efficiency and torque density. Moreover, the low PM field results in low back-emf and low SC current. It also eliminates the risk of uncontrolled generation at high speed and largely reduces the possibility of the demagnetisation under fault conditions. All these advantages together improve the fault tolerance of the proposed PMASynRM.

Additionally, as shown in Fig. 2-1, the machine employs three 3-phase sets denoted as ABC, DEF and GHI, each forming a balanced wye-connected 3-phase set that does not overlap with the other 3-phase sets. Compared with the conventional overlapped distributed windings, this winding layout improves the physical and thermal isolations between different 3-phase sets while with the exactly same MMF distribution as well as the performances under healthy conditions. Moreover, each 3-phase set is controlled by an independent 3-phase inverter for electrical isolation. Thus, fault propagation between different 3-phase sets is minimised and the three modules provide redundancy for many common faults. It has been demonstrated that this triple redundant, 9-phase PMASynRM has high performance with excellent fault tolerant capability with no additional cost compared to the conventional overlapped distributed PMASynRM.

In case of an open-circuit fault or a short circuit fault in one 3-phase set either in the inverter switch or the winding, the fault 3-phase set can be simply taken out of service by deactivating all the fault set switches or applying terminal SC on the fault windings. Moreover, if the worst scenario that an inter-turn SC occurs, the mitigation measure of 3-phase terminal SC will be applied to the fault set which will nullify the flux linkage of the faulted turns and reduce the SC current. Due to the physical, thermal and electrical isolation between three 3-phase sets, the remaining two healthy 3-phase sets can continue operating to generate about $2/3$ torque.

However, it is noting that magnetic coupling still exists between three 3-phase sets via MMF distribution. Therefore, the fault performance in one 3-phase set will be influenced by others under fault conditions. It is shown in [40] that the high MMF offset component exists in case of one 3-phase set SC due to mutual coupling between different sets leading to 2nd harmonic torque ripple. Additionally, a combination of the MMF with alternating current (AC) component and offset component exists in case of SC fault leading to positive, negative and zero sequence components of flux linkage because of mutual coupling of different 3-phase windings. For the wye-connected winding, the positive and negative sequence components of flux linkages in the fault set can effectively be reduced by terminal SC in the fault 3-phase set. However, the zero sequence flux linkage cannot be nullified since there is no path for the zero sequence current. Thus, at the worst scenario of inter-turn SC, the remaining zero sequence flux linkage of the SC turns might result in significant fault current.

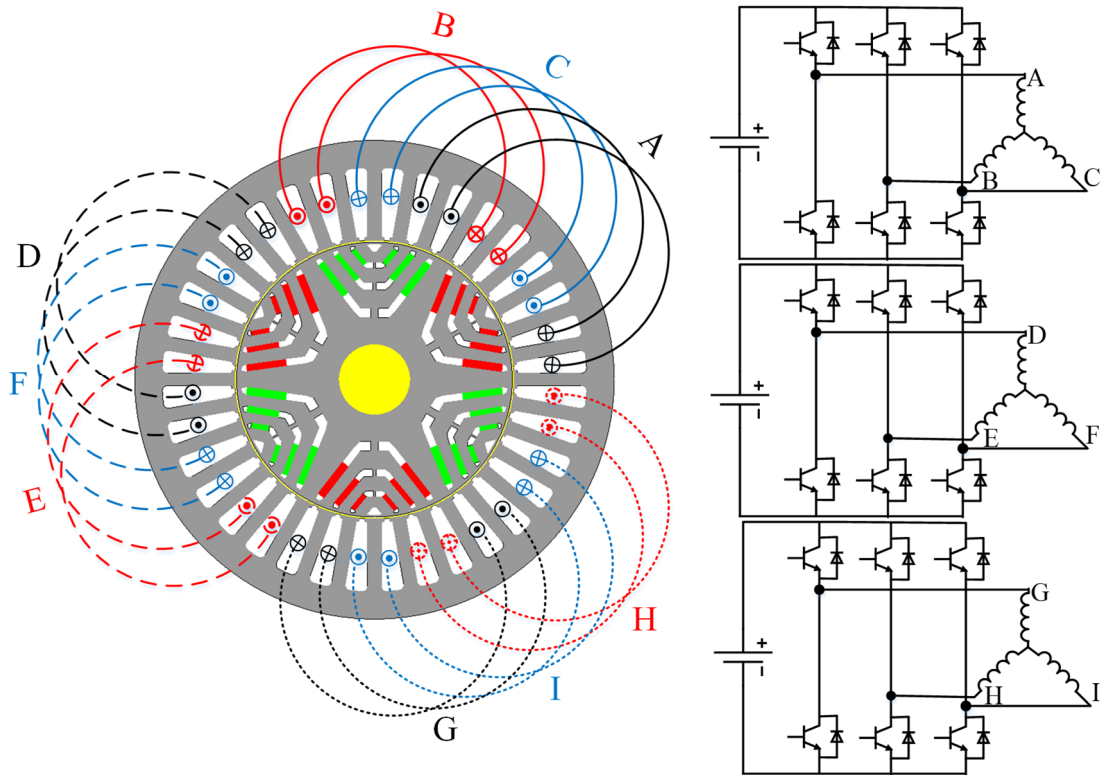


Fig. 2-1. PMASynRM with segregated triple wye-connected 3-phase windings.

2.3 PMASynRM with Delta-Connected Winding Configuration

In order to reduce the damage of excessive turn fault current, a new triple redundant 3x3-phase PMASynRM with delta-connected winding with the same machine topology as in Fig. 2-1 is proposed. The design specifications are introduced and the effect of the zero sequence current on the fault current is explained in the subsequent section by equivalent inter-turn fault model.

2.3.1 Design Specifications

The design specifications of wye- and delta-connected triple redundant, 9-phase PMASynRM are listed in Table 2-1.

Table 2-1. Design specifications of the machine

Quantity	Unit	Value
Rated continuous power	kW	40
Base speed	rpm	4000
Peak power	kW	50
Maximum operation speed	rpm	19200
DC-link voltage(Line-to-line voltage limit)	V	270

Fig. 2-2 shows the triple redundant 3x3-phase PMASynRM with delta-connected windings. The three delta-connected 3-phase sets are still be driven by three standard inverters. The two prototypes are designed to have the same fundamental MMF, the line currents and the slot fill factor. Hence, the number of turns per coil and the phase resistance in the delta-connected PMASynRM are proportionally increased, while the conductor size and the fundamental phase current is decreased.

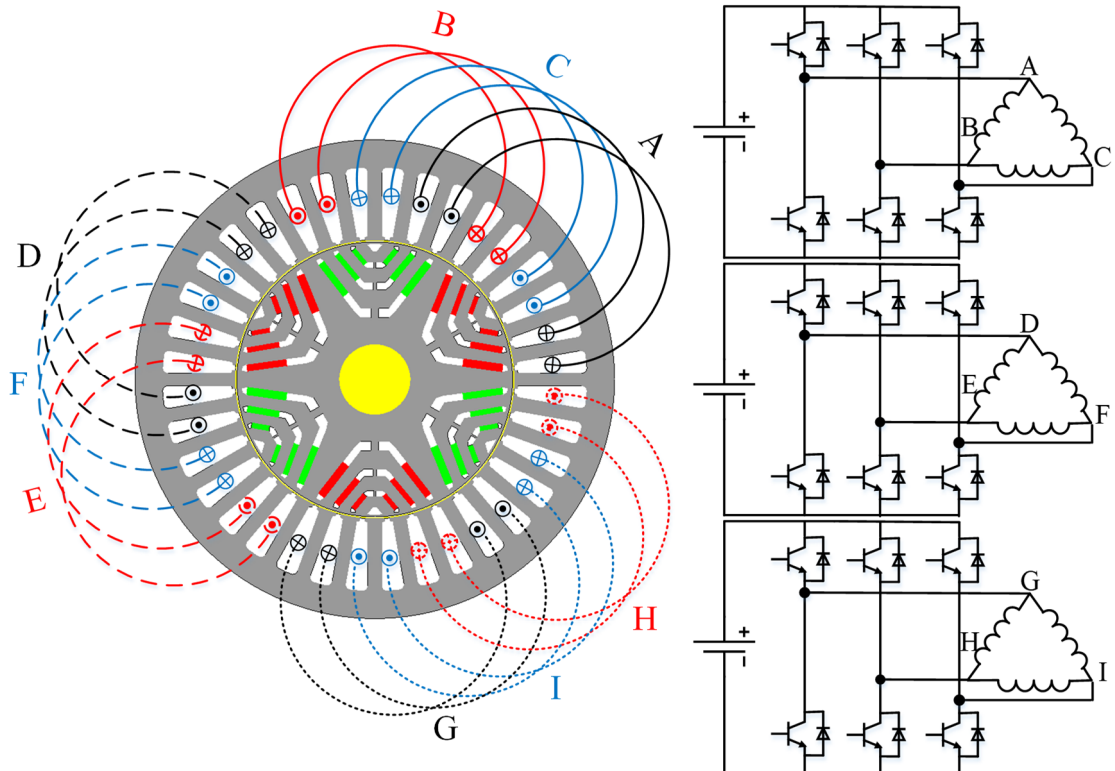


Fig. 2-2. PMASynRM with segregated triple delta-connected 3-phase windings.

2.3.2 Equivalent Inter-Turn Fault Model

An accurate transient model of the delta-connected PMASynRM with inter-turn fault is not only essential for rapid detection and fault-tolerant control strategies, but also useful for explaining the effect of the zero sequence current on the fault current.

Without loss of generality, a turn fault is assumed to occur in phase A of ABC set, and the influence between different 3-phase sets is neglected. Therefore, only one 3-phase under the fault condition needs to be considered. The circuit schematic of the delta-connected 3-phase set ABC with a turn fault in phase A is shown in Fig. 2-3. Phase A is divided into two sub-windings denoted by AS1 (healthy part) and AS2 (fault part). Some further simplifications are made for derivation of the influence of key parameters on the inter-turn fault current. (1) The stator cores are infinitely permeable and magnetic saturation is neglected; (2) Stator slotting effect is ignored. The fault ratio μ is defined as the ratio of the number of SC turns (N_{sc}) to the total number of turns in phase A (N_i).

The theoretical analysis for establishing the equivalent model for the delta-connected PMASynRM with inter-turn fault in one phase is based on the method described in [54].

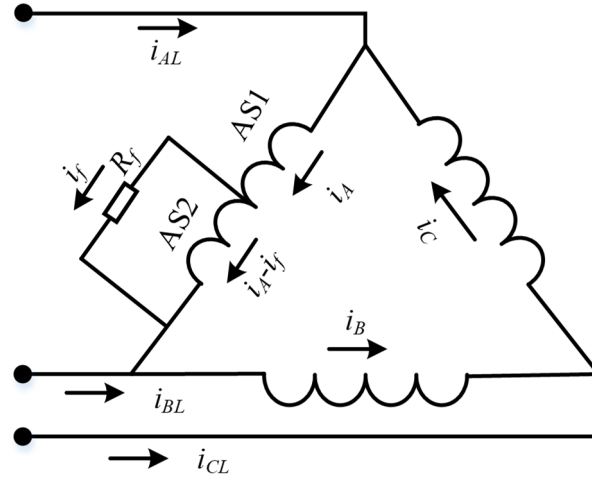


Fig. 2-3. Schematic of the delta-connected PMASynRM with turn fault in single phase.

The stator equations for the delta-connected PMASynRM machine with inter-turn fault can be expressed in abc stationary frame as,

$$v_s^f = R_s^f i_s^f + \frac{d\lambda_s^f}{dt} \quad (2-1)$$

$$\lambda_s^f = L_s^f i_s^f + \lambda_m^f \quad (2-2)$$

where v_s^f , i_s^f , λ_s^f , λ_m^f , R_s^f , L_s^f , denotes the voltage, current, flux linkage, flux linkage of permanent magnet, resistance and inductance matrices of the 3-phase system, respectively. Moreover, the superscript f denotes fault condition. According to Fig. 2-3, the fault part AS2 is considered as a separate winding in fault modelling. Therefore, subscript A, B, and C denotes phase A, B, and C, respectively and subscript AS1 and AS2 denotes healthy part AS1 and fault part AS2, respectively. Besides, as machine cores are assumed infinitely permeable and the magnetic saturation is neglected, the self-inductances are assumed to be proportional to turn number squares and mutual inductances to the product of turn numbers associated with two parts under the fault condition. Thus, the above matrices can be expressed by (2-3)-(2-8):

$$v_s^f = [v_{AS1} \quad v_{AS2} \quad v_B \quad v_C]^T \quad (2-3)$$

$$i_s^f = [i_A \quad i_A - i_f \quad i_B \quad i_C]^T \quad (2-4)$$

$$\lambda_s^f = [\lambda_{AS1} \quad \lambda_{AS2} \quad \lambda_B \quad \lambda_C]^T \quad (2-5)$$

$$R_s^f = R_s \text{diag}[1 - \mu \quad \mu \quad 1 \quad 1] \quad (2-6)$$

$$L_s^f = L_{ls} \text{diag}[1-\mu \quad \mu \quad 1 \quad 1] + \begin{bmatrix} (1-\mu)^2 L_{AA} & \mu(1-\mu)L_{AA} & (1-\mu)L_{AB} & (1-\mu)L_{AC} \\ \mu(1-\mu)L_{AA} & \mu^2 L_{AA} & \mu L_{AB} & \mu L_{AC} \\ (1-\mu)L_{BA} & \mu L_{BA} & L_{BB} & L_{BC} \\ (1-\mu)L_{CA} & \mu L_{CA} & L_{CB} & L_{CC} \end{bmatrix} \quad (2-7)$$

$$\lambda_m^f = \left[(1-\mu)\lambda_M \cos\theta \quad \mu\lambda_M \cos\theta \quad \lambda_M \cos\left(\theta - \frac{2}{3}\pi\right) \quad \lambda_M \cos\left(\theta + \frac{2}{3}\pi\right) \right]^T \quad (2-8)$$

$$\mu = \frac{N_{sc}}{N_t} \quad (2-9)$$

where i_j and L_{jj} ($j=A, B, C$) denotes the current and self-inductances of the phase j ; v_k and λ_k ($k=AS1, AS2, B, C$) denotes the voltage and flux linkage of the winding part k ; L_{ij} ($i, j=A, B, C, i \neq j$) denotes the mutual inductance between phase i and phase j ; i_f is the fault current; R_s is the phase resistance; L_{ls} is the stator slot leakage; λ_M is the peak magnitude of phase flux linkage generated by the permanent magnet; θ is rotor angle (electrical) with respect to phase A winding. Additionally, since the terminal voltage of phase A is the sum of voltages of AS1 and AS2, the voltage equation in (2-1) can be rearranged to (2-10)-(2-14).

$$v_s = R_s i_s + \frac{d\lambda_s}{dt} + \mu A_1 i_f \quad (2-10)$$

where

$$v_s = [(v_{AS1} + v_{AS2}) \quad v_B \quad v_C]^T \quad (2-11)$$

$$i_s = [i_A \quad i_B \quad i_C]^T \quad (2-12)$$

$$\lambda_s = [(\lambda_{AS1} + \lambda_{AS2}) \quad \lambda_B \quad \lambda_C]^T \quad (2-13)$$

$$A_1 = -[R_s \quad 0 \quad 0]^T \quad (2-14)$$

Therefore, the flux vector may be rewritten as,

$$\lambda_s = L_s i_s + \lambda_m - \mu i_f A_2 \quad (2-15)$$

$$L_s = \begin{bmatrix} L_{ls} + L_{AA} & L_{AB} & L_{AC} \\ L_{BA} & L_{ls} + L_{BB} & L_{BC} \\ L_{CA} & L_{CB} & L_{ls} + L_{CC} \end{bmatrix} \quad (2-16)$$

$$A_2 = \begin{bmatrix} L_{ls} + L_{AA} \\ L_{BA} \\ L_{CA} \end{bmatrix} = \begin{bmatrix} L_{ls} + L_{AA0} + L_{AA2} \cos(2\theta) \\ -\frac{1}{2}L_{AA0} + L_{AA2} \cos(2\theta - \frac{2}{3}\pi) \\ -\frac{1}{2}L_{AA0} + L_{AA2} \cos(2\theta + \frac{2}{3}\pi) \end{bmatrix} \quad (2-17)$$

where L_{AA0} and L_{AA2} are the constants for the average and ripple inductance, respectively.

The voltage and flux linkage of the fault winding part AS2 can be written separately as,

$$v_{AS2} = R_f i_f = \mu R_s (i_A - i_f) + \frac{d\lambda_{AS2}}{dt} \quad (2-18)$$

$$\lambda_{AS2} = \mu A_2^T i_s + \mu \lambda_m \cos \theta - \mu i_f [L_{ls} + \mu(L_{AA0} + L_{AA2} \cos 2\theta)] \quad (2-19)$$

where R_f is the external fault resistance of the SC path. By performing ABC to dq synchronous frame transformation, the stator voltage and flux linkage equations can be transformed to the dq frame as given in (2-20)-(2-21),

$$\begin{bmatrix} v_d \\ v_q \\ v_0 \end{bmatrix} = R_s \begin{bmatrix} i_d \\ i_q \\ i_0 \end{bmatrix} + \frac{d}{dt} \begin{bmatrix} \lambda_d \\ \lambda_q \\ \lambda_0 \end{bmatrix} + \omega \begin{bmatrix} -\lambda_q \\ \lambda_d \\ 0 \end{bmatrix} + \frac{1}{3} \mu R_s \begin{bmatrix} -2 \cos \theta \\ 2 \sin \theta \\ -1 \end{bmatrix} i_f \quad (2-20)$$

$$\begin{bmatrix} \lambda_d \\ \lambda_q \\ \lambda_0 \end{bmatrix} = \begin{bmatrix} L_{ls} + L_{md} & 0 & 0 \\ 0 & L_{ls} + L_{mq} & 0 \\ 0 & 0 & L_{ls} \end{bmatrix} \begin{bmatrix} i_d \\ i_q \\ i_0 \end{bmatrix} + \frac{1}{3} \mu \begin{bmatrix} -2(L_{ls} + L_{md}) \cos \theta \\ 2(L_{ls} + L_{mq}) \sin \theta \\ -L_{ls} \end{bmatrix} i_f + \begin{bmatrix} \lambda_M \\ 0 \\ \lambda_{M,0} \end{bmatrix} \quad (2-21)$$

where i_d , i_q , i_0 are the d-axis, q-axis and zero sequence currents; v_d , v_q , v_0 are the d-axis, q-axis and zero sequence voltages; λ_d , λ_q , λ_0 are the d-axis, q-axis and zero sequence flux linkages; L_{md} , L_{mq} are the main d- and q-axes inductances; $\lambda_{M,0}$ is only composed of the triplen harmonics (3rd harmonic component and its odd integer multiplies harmonic components of the λ_M).

Furthermore, v_{AS2} , and the flux linkage, λ_{AS2} , of the fault winding part AS2 for the delta-connected PMASynRM in the dq frame are given by,

$$v_{AS2} = R_f i_f = \mu R_s (i_d \cos \theta - i_q \sin \theta + i_0 - i_f) + \frac{d\lambda_{AS2}}{dt} \quad (2-22)$$

$$\lambda_{AS2} = \mu(L_{ls} + L_{md})i_d \cos \theta - \mu(L_{ls} + L_{mq})i_q \sin \theta + \mu L_{ls}i_0 + \mu\lambda_m \cos \theta - \mu[L_{ls} + \mu(L_{AA0} + L_{AA2} \cos 2\theta)]i_f \quad (2-23)$$

Similarly, the voltage and flux linkage of the fault winding part AS2 for the wye-connected machine in the dq frame are obtained by [54]:

$$v_{AS2} = R_f i_f = \mu R_s (i_d \cos \theta - i_q \sin \theta - i_f) + \frac{d\lambda_{AS2}}{dt} \quad (2-24)$$

$$\lambda_{AS2} = \mu(L_{ls} + L_{md})i_d \cos \theta - \mu(L_{ls} + L_{mq})i_q \sin \theta + \mu\lambda_m \cos \theta - \mu[L_{ls} + \mu(L_{AA0} + L_{AA2} \cos 2\theta)]i_f \quad (2-25)$$

It can be observed from equations (2-22) and (2-23) of the delta-connected winding and equations (2-24) and (2-25) of the wye-connected winding that the only difference is the zero sequence current i_0 . FE analysis implemented in Altair Flux will be used to assess the influence of zero sequence current on the flux linkage λ_{AS2} .

Firstly, a PMASynRM with wye-connected winding configuration as shown in Fig. 2-4 is built in FEA. The 3-phase set ABC is in terminal SC, while the other two 3-phase sets DEF and GHI operate in the healthy condition with the rated current excited at the phase angle for maximum torque per Ampere (MTPA) condition. The phase flux linkages of 3-phase set ABC with terminal SC are presented in Fig. 2-5. It is clear that these 3 phases have similar waveforms and phase shifts of flux linkages which are mainly contributed by the zero sequence component as a result of unbalance operation.

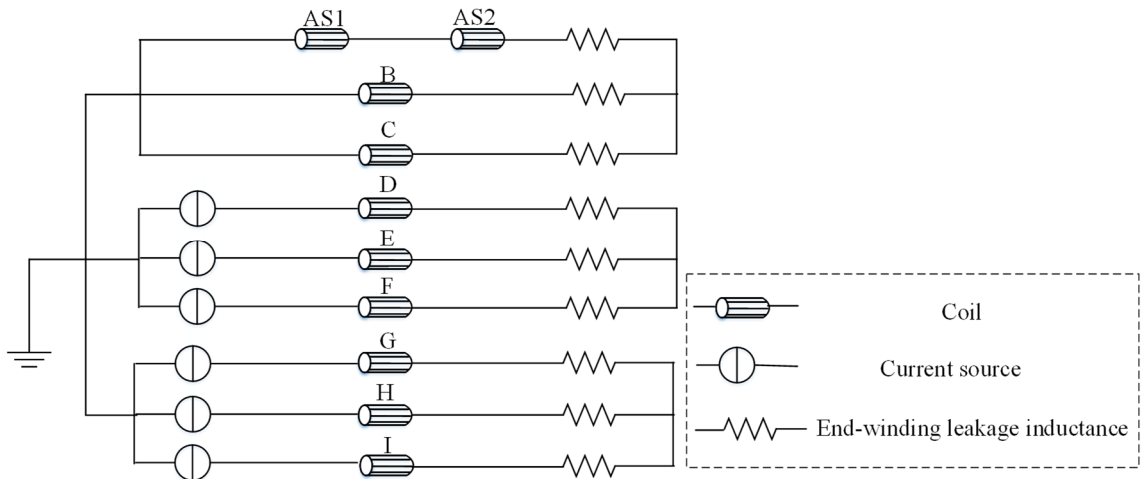


Fig. 2-4. Schematic circuit simulated for PMASynRM with wye-connected winding configuration when set ABC is in terminal SC.

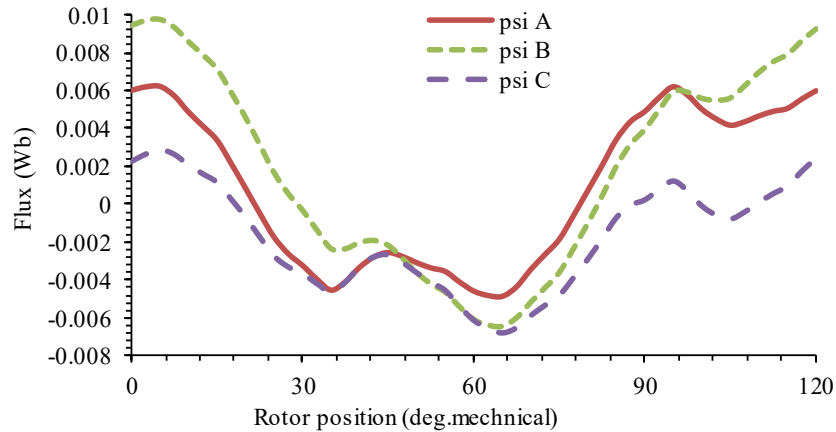


Fig. 2-5. Phase flux linkages of wye-connected 3-phase set ABC with terminal SC without neutral line.

Afterwards, the PMASynRM with a different winding configuration as shown in Fig. 2-6 is also simulated in FEA. The DEF and GHI 3-phase sets are still wye-connected and operate in the healthy condition and a terminal SC is applied to the wye-connected 3-phase set ABC. However, Fig. 2-6 differs from Fig. 2-4 in that the ABC set has a neutral line. This provides a path for zero sequence current, which is equivalent to that of Fig. 2-7 in which the terminal SC is applied to 3-phase set ABC with the delta-connection.

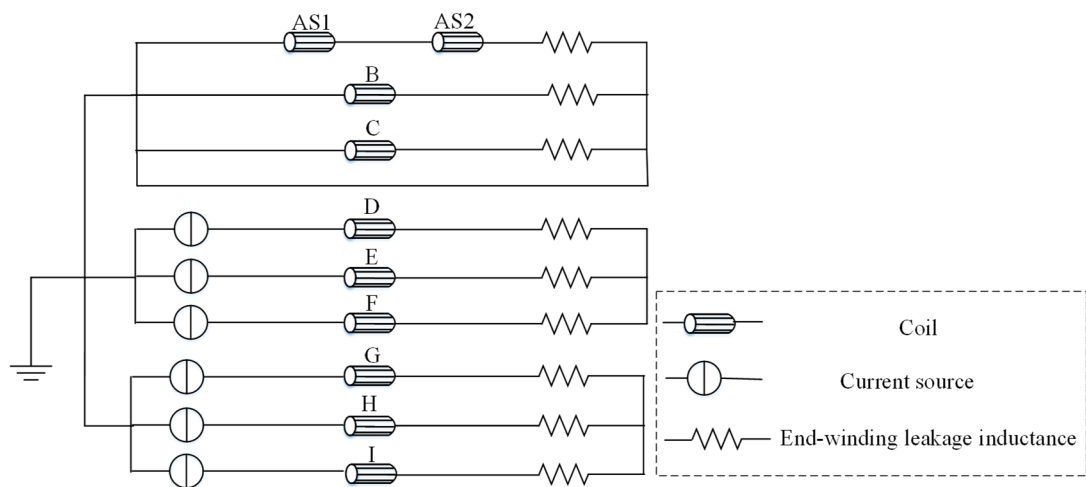


Fig. 2-6. Schematic circuit simulated for PMASynRM with wye-connected winding with neutral line when set ABC is in terminal SC.

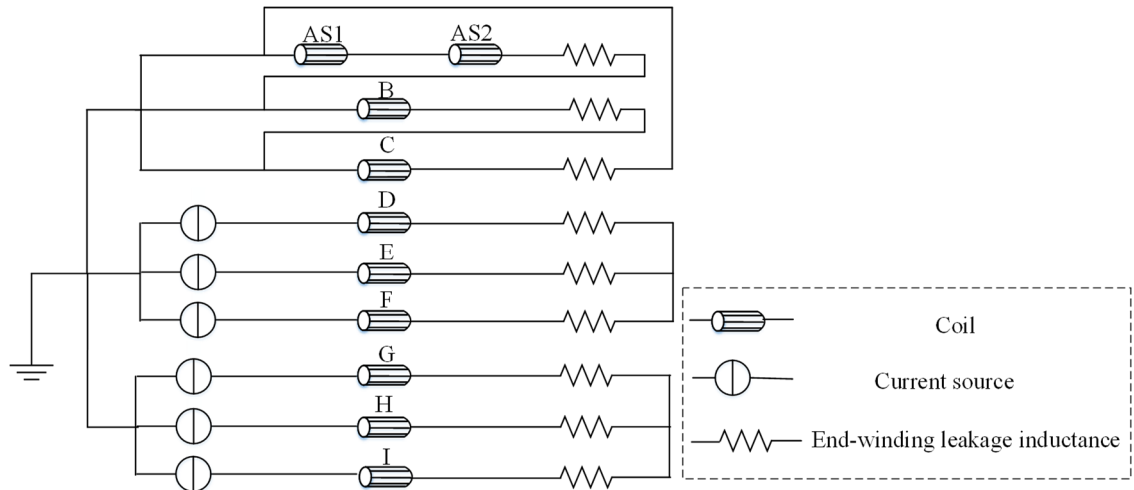


Fig. 2-7. Schematic circuit simulated for PMASynRM with delta-connected set ABC in terminal SC and other two healthy wye-connected sets.

In the simulations, no fault is assumed in the AS2 part both in Fig. 2-4 and Fig. 2-6, so the turn-fault current i_f is zero. The other two healthy 3-phase sets have the same mutual coupling effect on the ABC set. Hence, the difference of the flux linkages in the 3-phase set ABC and the flux linkage of AS2, λ_{AS2} , between the two winding configurations is mainly due to the zero sequence current according to equations (2-22)-(2-25). Fig. 2-8 shows the flux linkages of 3-phase set ABC with terminal SC, while the flux linkages λ_{AS2} under the two winding configurations are compared in Fig. 2-9. The zero sequence current simulated for the PMASynRM with neutral line is 13.6A. As observed from Fig. 2-8, the flux linkages of 3-phase set ABC are quite different from that shown in Fig. 2-5 and exhibit much lower magnitudes and large phase shift between the phases. It follows that the zero sequence flux linkage in the Fig. 2-5 are effectively reduced by the zero sequence current. Additionally, from Fig. 2-9, the flux linkage λ_{AS2} of the machine with the neutral line is much smaller than that of the machine without the neutral line. It follows that the zero sequence current helps lower the turn flux linkage λ_{AS2} and hence will further reduce the fault current in the faulted turns.

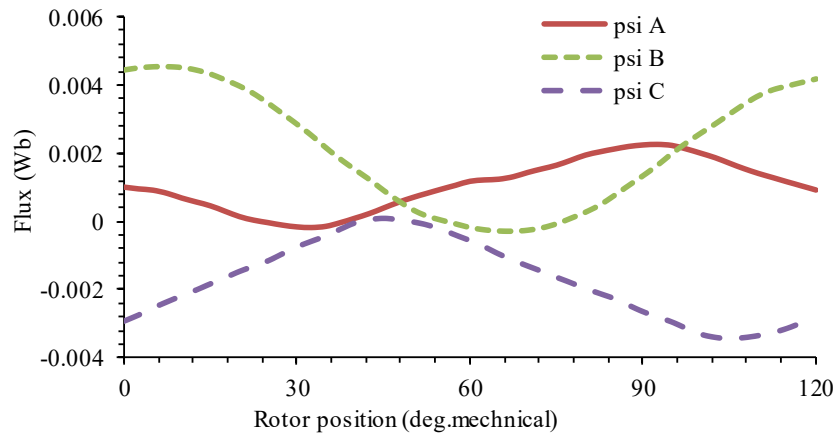


Fig. 2-8. Phase flux linkages of 3-phase set ABC with terminal SC with neutral line.

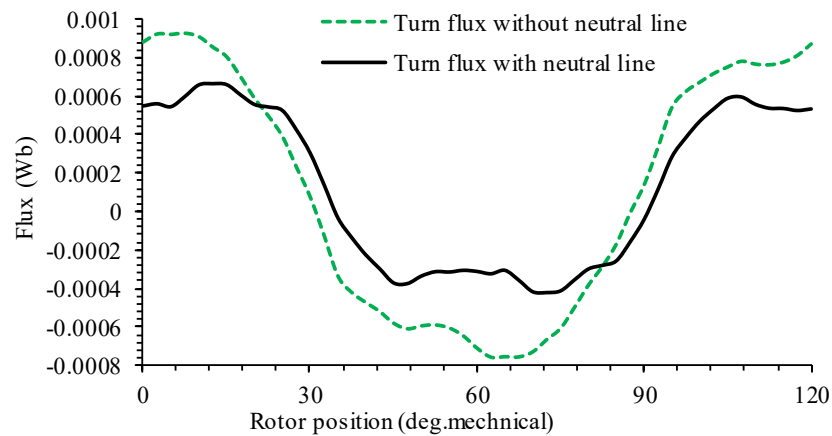


Fig. 2-9. Comparison of turn flux linkages with or without neutral line.

2.4 Comparisons between Delta- and Wye-Connected Winding PMASynRM

From the above analysis, presence of a zero sequence current path could help reduce the turn flux linkage and turn fault current. To exploit this feature, the characteristics of the delta- and wye-connected triple redundant 3x3-phase PMASynRM under healthy and various fault conditions are evaluated and compared via FE simulation in Altair Flux in the following section.

2.4.1 Healthy Operation

The performances under healthy conditions in all three 3-phase sets are identical in the triple redundant 3x3-phase PMASynRM, so only the performance of the 3-phase set ABC are shown below.

Under no-load condition, the no-load line-to-line back emf waveforms and their spectra of 3-phase set ABC of the delta- and wye-connected machines are compared in

Fig. 2-10 (a) and (b), respectively. As observed, the delta-connected PMASynRM has extra triplen harmonic components in the line-to-line back emf compared with the wye-connected PMASynRM.

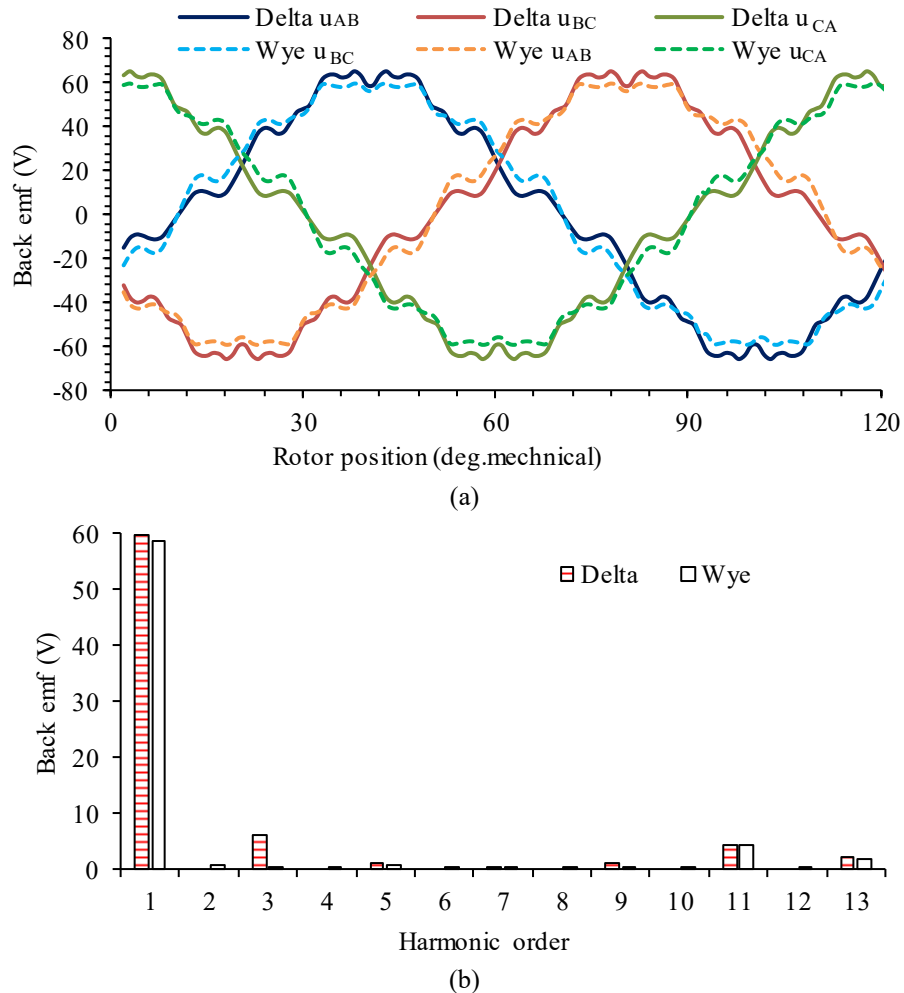


Fig. 2-10. Comparison of no-load line-to-line back emf between delta- and wye-connected machines. (a) Back emf. (b) Harmonic.

In the rated operation (rated torque at the base speed), the line currents are excited with the rated value 118A and the optimal gamma angle of 51° for MTPA is evaluated both in the delta- and wye-connected machines. The resultant waveforms of the phase currents between delta- and wye-connected PMASynRMs are plotted in Fig. 2-11. Obviously, the phase currents of the wye-connected PMASynRM are sinusoidal assuming perfect inverter control, while the phase current of the delta-connected PMASynRM has distortions since it contains the fundamental and triplen harmonics. The amplitude of the fundamental phase current of delta-connected PMASynRM (68.04A) is approximately 1.732 times lower than that of wye-connected PMASynRM (118.32A).

Additionally, the 3rd harmonic component in the phase currents of the delta-connected PMASynRM, also known as zero sequence current, is plotted in Fig. 2-12. It is clear that the zero sequence current is identical in phases A, B and C with the magnitude calculated around 10% of the fundamental current. It results from the triplen harmonics in the line-to-line back emf as well as the interaction of the rotor saliency with the fundamental component of phase currents.

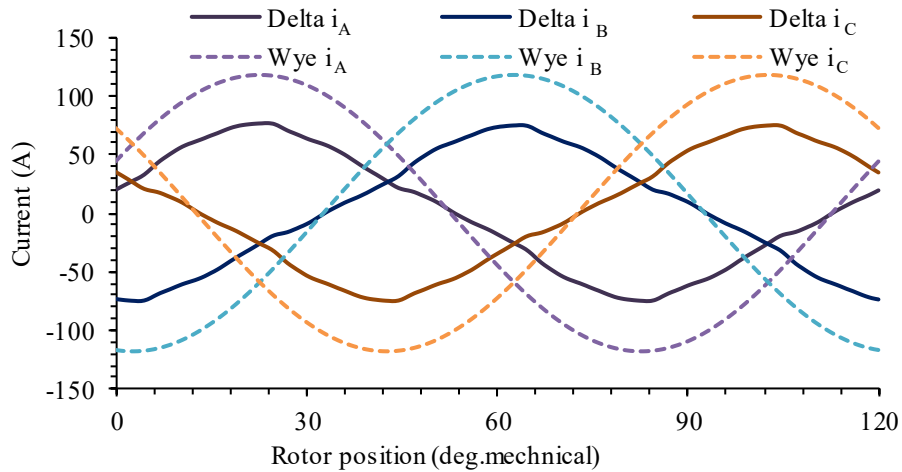


Fig. 2-11. Comparison of phase currents between delta- and wye-connected machines at rated operation.

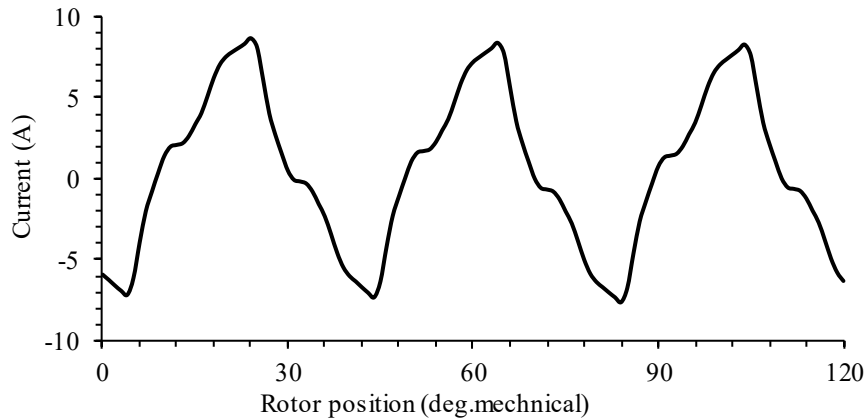


Fig. 2-12. Zero sequence current of delta-connected machine at rated operation.

In the wye-connected PMASynRM, as the phase current is ideally sinusoidal, output torque ripples mainly result from the interaction between fundamental currents and the harmonic distortion in the emf as well as cogging. In the delta-connected PMASynRM, apart from the same torque ripple as those with the wye-connected PMASynRM, the 3rd harmonic phase current (neglecting higher order triplen harmonics) will interact with the emf harmonic to generate extra torque ripples. However, only triplen emf harmonics will

interact with the 3rd order zero sequence current, generating triplen orders of torque ripples.

The torque waveforms and their spectra of the delta- and wye-connected machines at the rated torque and base speed are compared in Fig. 2-13 and the key performance indicators in Table 2-2 where the built factor (1.2) of an iron loss is considered. The torque ripple is defined as the ratio of peak-to-peak torque fluctuation to the average torque over a fundamental period. As can be seen, the fundamental torque of the delta-connected PMASynRM (95.23 Nm) is 0.45% lower than that of the wye-connected PMASynRM (95.66Nm). Main torque ripple harmonics of the two machines are 6th and 12th. There is very little increase of the triplen order torque ripples of the delta-connected PMASynRM because of relatively small triplen emf harmonics. Hence, the zero sequence current of the delta-connected PMASynRM has little effect on the output torque, albeit it will increase the copper loss by ~1% as in Table 2-2.

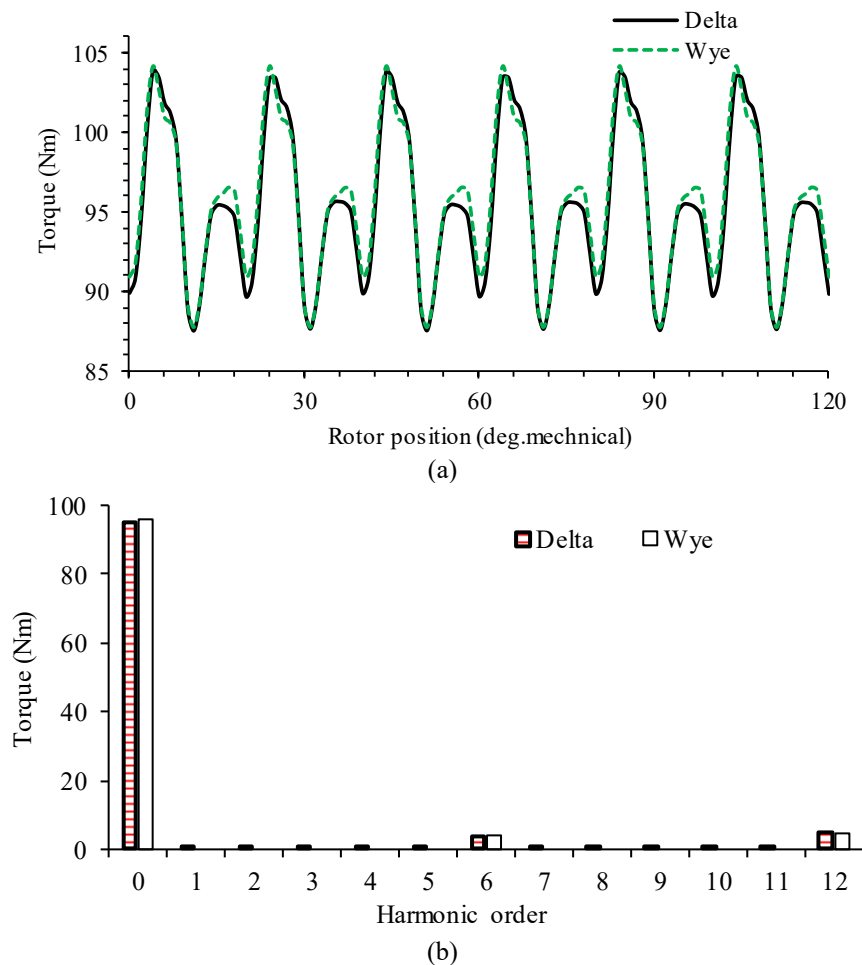


Fig. 2-13. Comparison of torques between delta- and wye-connected PMASynRMs at rated torque and base speed. (a) Torque. (b) Harmonic.

Table 2-2. Comparison of performances between delta- and wye-connected PMASynRMs at rated torque and base speed

Winding configuration	Wye	Delta	Difference (%)
Average torque (Nm)	95.66	95.23	-0.45
Torque ripple (%)	17.19	17.12	-0.41
Copper loss (W)	1228.62	1241.37	1.04
Total iron loss 1.2*(W)	324.07	320.77	-1.02
Efficiency (%)	96.89	96.84	-0.05

Moreover, the key performance indicators under peak torque and base speed between the delta- and wye-connected PMASynRMs are compared in Table 2-3.

Table 2-3. Comparison of performances between delta- and wye-connected PMASynRMs at peak torque at base speed

Winding configuration	Wye	Delta	Difference (%)
Average torque (Nm)	115.61	115.34	-0.23
Torque ripple (%)	16.13	15.05	-6.70
Copper loss (W)	1885.08	1906.65	1.14
Total iron loss 1.2*(W)	342.25	343.06	0.24
Efficiency (%)	96.13	96.08	-0.05

2.4.2 Fault Operations

The performances of the two winding configurations under various fault conditions at the rated torque and base speed are also compared. Fault conditions considered in this study are listed in Table 2-4, including F1: one-phase open-circuit, F2: one 3-phase open-circuit, F3: one-turn short-circuit, F4: one-turn short-circuit with 3-phase terminal short-circuit. One 3-phase terminal short-circuit fault is not considered separately because it has very similar steady-state performances to F4. One-phase open-circuit (F1) is considered because the delta-connected machine has advantageous and quite different performance than the wye-connected machine under this fault condition. Moreover, F2 (one 3-phase open-circuit) is a typical fault condition, while F3 (one-turn short-circuit) is not only typical but also critical due to the excessive SC current. F4 (one-turn short-circuit with 3-phase terminal short-circuit) is a measure of fault mitigation of F3. All simulations are conducted at the rated torque and base speed. Moreover, for the sake of discussion, all the faults are assumed to occur in the 3-phase winding ABC.

Table 2-4. Fault Conditions under Consideration

Fault	Pre-fault operation
F1 One-phase open-circuit	Rated torque and base speed
F2 One 3-phase open-circuit	Rated torque and base speed
F3 One-turn short-circuit	Rated torque and base speed
F4 One-turn short-circuit with 3-phase terminal short-circuit	Rated torque and base speed

2.4.2.1 One-Phase Open-Circuit Fault

It has been known that in the wye-connected machine, a 3-phase set cannot produce continuous torque when one phase is open-circuited. For the delta-connected PMASynRM, if one connection to the inverter leg is open-circuited, the fault 3-phase set cannot operate either. Therefore, this scenario is not considered here. However, if an OC occurs in the phase connection as shown in Fig. 2-14. Without loss of generality, the open-circuit phase is assumed to be in phase C, so the phase current of phase C is zero. The phasor diagram of the line currents (i_{AL} , i_{BL} , i_{CL}) and phase currents (i_A , i_B , i_C) for a balanced operation in one 3-phase set under one-phase open-circuit fault is shown in Fig. 2-15.

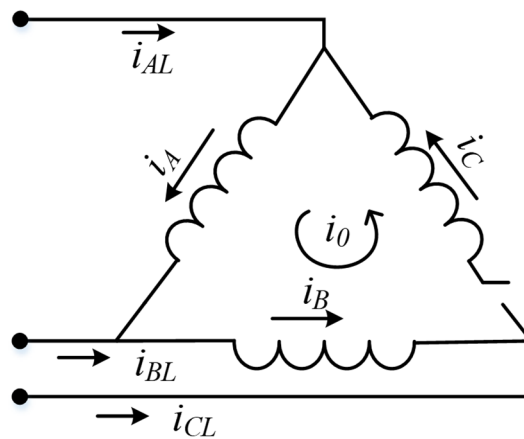


Fig. 2-14. Schematic of one phase winding OC in delta connected winding.

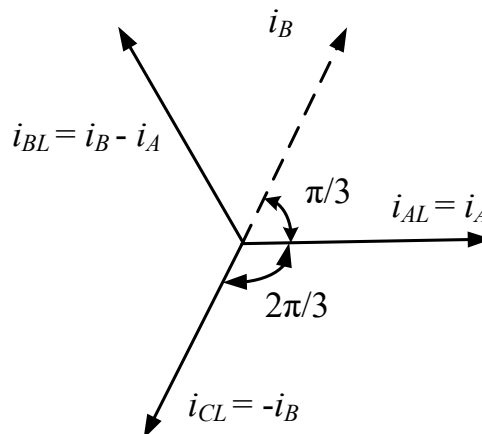


Fig. 2-15. Phasor diagram of currents in one-phase open-circuit fault for a balanced operation
According to Fig. 2-14, the relationship between line currents $i_{AL}(t)$, $i_{BL}(t)$, $i_{CL}(t)$ and phase currents $i_A(t)$, $i_B(t)$, $i_C(t)$ are expressed,

$$\begin{bmatrix} i_{AL}(t) \\ i_{BL}(t) \\ i_{CL}(t) \end{bmatrix} = \begin{bmatrix} 1 & 0 & -1 \\ -1 & 1 & 0 \\ 0 & -1 & 1 \end{bmatrix} \begin{bmatrix} i_A(t) \\ i_B(t) \\ i_C(t) = 0 \end{bmatrix} \quad (2-26)$$

where the line currents of one 3-phase set are controlled by the current source through inverters and the angular phase shift between the line currents is 120 electrical degrees. Thus the following equations are obtained from (2-26) as shown in Fig. 2-15.

$$i_{AL}(t) = i_A(t) = I_m \cos(\omega t) \quad (2-27)$$

$$i_{BL}(t) = i_B(t) - i_A(t) = I_m \cos(\omega t - \frac{2}{3}\pi) \quad (2-28)$$

$$i_{CL}(t) = -i_B(t) = I_m \cos(\omega t - \frac{4}{3}\pi) \quad (2-29)$$

where I_m is the peak magnitude of the line current, ω is the electrical angular speed of the motor. The phase currents of phase A and B are obtained from (2-27) to (2-29),

$$i_A(t) = I_m \cos(\omega t) \quad (2-30)$$

$$i_B(t) = -I_m \cos(\omega t - \frac{4}{3}\pi) \quad (2-31)$$

It can be observed that the phase currents of phase A and B are independent. Therefore, the resultant MMF $F_s(t)$ of this 3-phase set can be expressed as,

$$F_s(t) = N_t [i_A \cos \theta + i_B \cos(\theta - 2\pi / 3)] \quad (2-32)$$

Rearrange (2-32) with (2-30) and (2-31), then $F_s(t)$ becomes,

$$\begin{aligned} F_s(t) &= N_t I_m [\cos \theta \cos(\omega t) - \cos(\theta - 2\pi / 3) \cos(\omega t - 4\pi / 3)] \\ &= \frac{N_t I_m}{2} [\cos(\omega t + \theta) + \cos(\omega t - \theta) - \cos(\omega t + \theta) - \cos(\omega t - \theta - \frac{2}{3}\pi)] \\ &= \frac{\sqrt{3} N_t I_m}{2} \cos(\omega t - \theta + \frac{1}{6}\pi) \end{aligned} \quad (2-33)$$

To summary, when phase C is open-circuited, the currents in phases A and B can still be controlled by the inverter to produce continuous torque. Additionally, as known, the negative-sequence MMF usually appears in the fault condition and further produces significant torque oscillation. However, as observed from (2-33), when the angular phase shift between the line currents is 120 electrical degrees in the delta-connected machine, the negative-sequence MMF will be eliminated. Therefore, the resultant MMF only

contains the positive-sequence component which will largely reduce the torque ripple under one-phase open-circuit fault condition.

Under one-phase OC fault of delta-connected machine, the remaining two active phase currents are equal to their line currents as shown in (2-30) and (2-31). Therefore, for the same line currents with the pre-fault condition, the magnitude of phase currents i_A , i_B will be 1.732 times. This is denoted as Delta_S1. The alternative scenario is denoted as Delta_S2 in which the magnitude of phase currents i_A , i_B are kept the same with the pre-fault condition, so the line currents will be 1.732 times lower than these under pre-fault condition as shown in Fig. 2-16 (a). Fig. 2-16 (b) illustrates the phase currents of the fault 3-phase set ABC under Delta_S2 which matches well with the equations (2-27)-(2-30), validating the correction of the theoretical analysis.

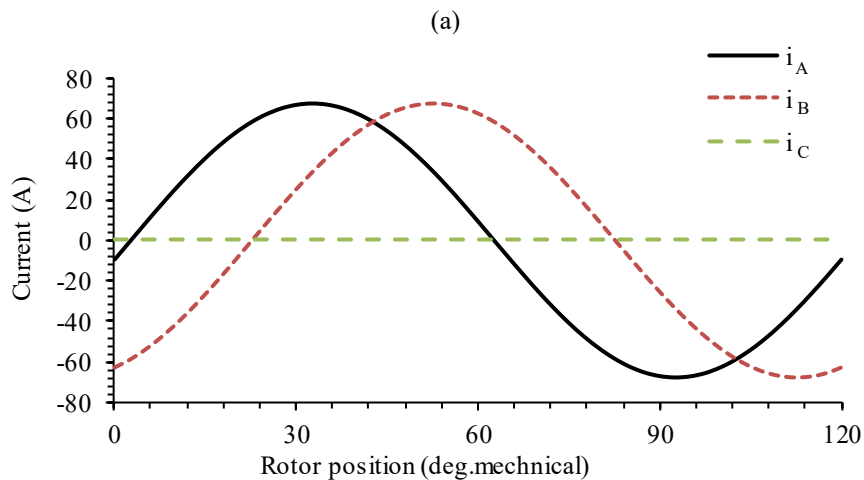
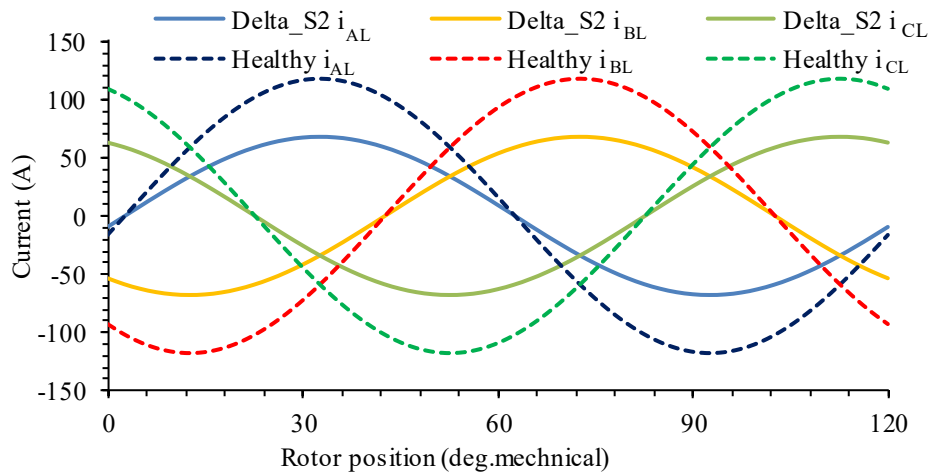


Fig. 2-16. Line and phase currents of the fault set ABC under Delta_S2. (a) Line currents between healthy condition and Delta_S2. (b) Phase currents under Delta_S2.

The remaining two 3-phase sets of the wye- and delta-connected machines are excited by the same currents under healthy condition. The resultant torque waveforms and characteristics under one-phase open-circuit fault between the wye- and delta-connected PMASynRMs with the remedial actions Delta_S1 and Delta_S2 are compared in Fig. 2-17 and Table 2-5.

The average torques of Delta_S1 and Delta_S2 which only reduce 9% and 19% of rated torque, respectively, are both larger than that of the wye-connected PMASynRM in which the reduction is slightly higher than 1/3 of the rated torque. This is because the remaining two active phases of the fault 3-phase set in the delta-connected machine can be independently controlled and used to produce torque. Additionally, as observed from Fig. 2-17, apart from the 6th and 12th harmonic torque ripples, the 2nd harmonic torque ripple is visible in all the torque waveforms due to the electromagnetic unbalance. However, with the remedial action Delta_S2, the torque ripple, especially the 2nd harmonic torque ripple, is significantly smaller than that in the wye connected PMASynRM as in Fig. 2-17 and Table 2-5. This is because the negative-sequence rotating component of MMF has been eliminated.

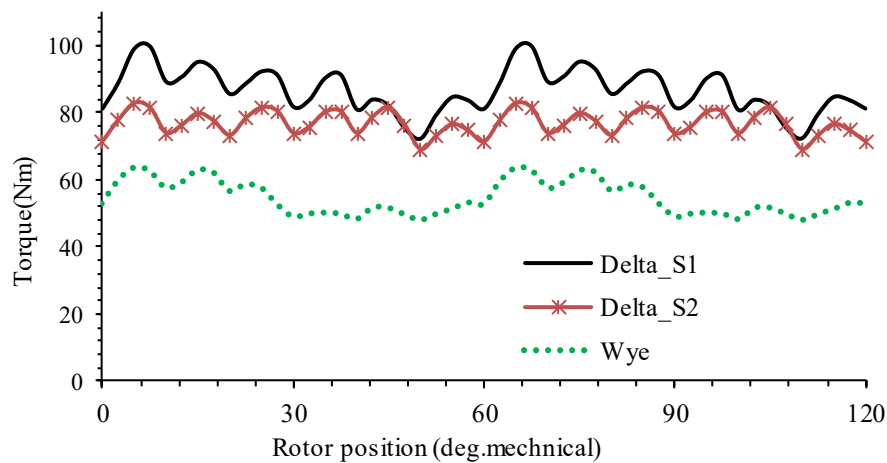


Fig. 2-17. Comparison of torque waveforms between wye-connected machine and Delta_S1 and Delta_S2 under F1

Table 2-5. Comparison of performances under F1

Winding configuration	Wye	Delta_S1	Delta_S2
Average torque (Nm)	54.57	86.85	76.96
Average torque normalised to/rated (p.u.)	0.57	0.91	0.81
Torque ripple (%)	28.09	31.69	17.96

2.4.2.2 One 3-Phase Open-Circuit Fault

There are two possible cases of the delta-connected PMASynRM under one 3-phase open-circuit fault. One is named as Delta_C1 in which the 3-phase inverter is disconnected as illustrated in Fig. 2-18 (a), and the other is denoted as Delta_C2 in which three stator phases are disconnected as illustrated in Fig. 2-18 (b). The remaining two 3-phase sets are excited as usual and capable of continuous operation to generate torque.

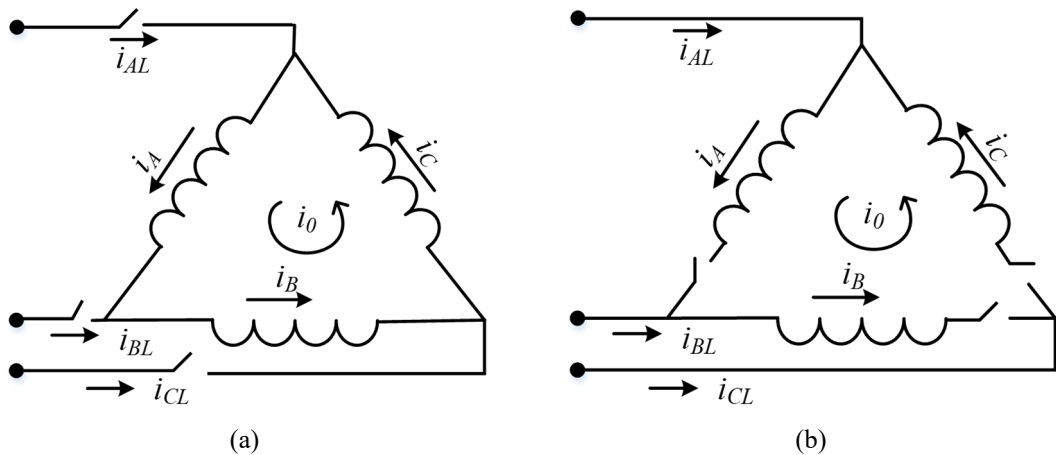


Fig. 2-18. One 3-phase open-circuit fault at rated torque and base speed of delta-connected machine. (a) Inverter OC (Delta_C1). (b) Winding OC (Delta_C2).

Because of the unbalance, the remaining two healthy 3-phase sets will generate a MMF offset over the fault 3-phase set region. This generates a fundamental current, while the triplen harmonics in the line-to-line back emf generates harmonic currents in the fault 3-phase set in Delta_C1 as shown in Fig. 2-19. However, as there is no zero sequence current path in Delta_C2 and in the wye-connected PMASynRM, the phase currents of the faulted 3-phase set are both zero.

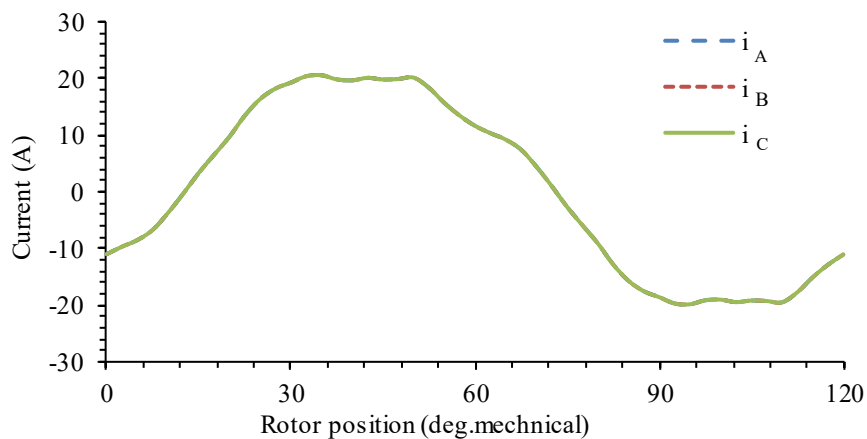


Fig. 2-19. Phase currents of 3-phase set ABC under one 3-phase open-circuit fault in Delta_C1.

Under one 3-phase open-circuit fault of the delta-connected PMASynRM, however, although the line currents of the remaining two 3-phase sets are kept the same by the inverter control, the phase currents are much distorted due to the unbalance and mutual coupling. This can be obviously observed in Fig. 2-20 which illustrates the phase currents of 3-phase set DEF in Delta_C1 and Delta_C2. The distortion of phase currents leads to increased copper loss and torque ripple compared with the wye-connected PMASynRM under one 3-phase open-circuit fault. The resultant torque waveforms and steady-state characteristics under one 3-phase set OC fault between the wye-connected PMASynRM and Delta_C1 and Delta_C2 are compared in Fig. 2-21 and Table 2-6. As observed, 2nd harmonic torque ripple is obviously visible in all torque waveforms due to electromagnetic unbalance. The steady-state performance of the wye-connected PMASynRM under F2 is the same as that under F1. The delta-connected PMASynRMs with Delta_C1 and Delta_C2 have similar average torque but with larger torque ripple, higher copper loss, and slightly lower efficiency compared with the wye-connected PMASynRM under F2.

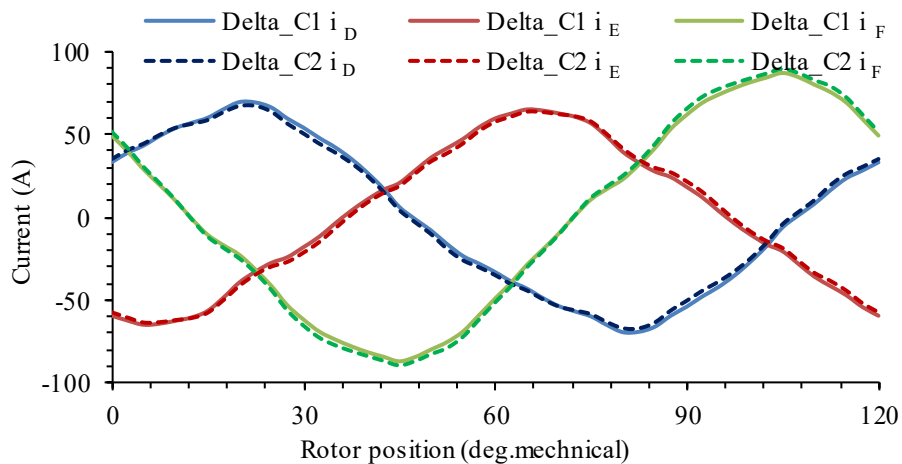


Fig. 2-20. Phase currents of 3-phase set DEF in Delta_C1 and Delta_C2 under F2.

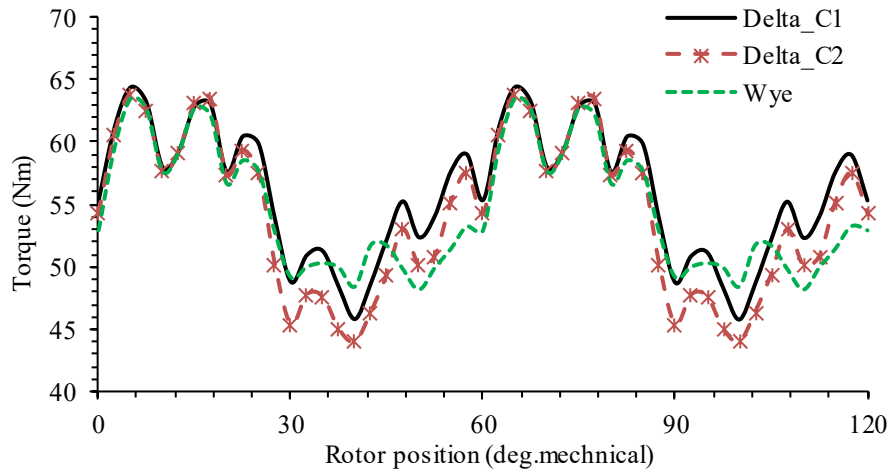


Fig. 2-21. Comparison of output torques between wye-connected PMASynRM and Delta_C1 and Delta_C2 under F2

Table 2-6. Comparison of performances under F2

Winding configuration	Wye	Delta_C1	Delta_C2
Average torque (Nm)	54.57	55.90	54.19
Torque ripple (%)	28.09	33.32	36.68
Copper loss (W)	819.08	977.22	925.45
Total iron loss (W)	56.93	51.61	52.43
Efficiency (%)	96.31	95.79	95.87

2.4.2.3 One-Turn Short-Circuit Fault

One-turn short-circuit fault is quite critical as it will generate significant circulating current in the fault turn which might result in complete insulation failures.

Without loss of generality, one turn short-circuit is assumed to occur in phase B. Moreover, the line currents of the three 3-phase sets of wye- and delta-connected machines are both excited as usual by the inverter control. Therefore, the phase currents of set ABC of wye-connected machine are sinusoidal and the same as the rated currents. However, the phase currents of set ABC of delta-connected machine are heavily distorted from rated currents because of the unbalance and mutual coupling as shown in Fig. 2-22.

The fault current waveforms in the fault turn, the resultant torque waveforms and the steady-state performance indicators under one turn short-circuit fault of the wye- and delta-connected PMASynRM are shown in Fig. 2-23, Fig. 2-24, and Table 2-7, respectively. It can be observed that the normalised root mean square (RMS) turn fault current and the resultant copper loss in the fault turns of the delta-connected PMASynRM are much higher than those of the wye-connected PMASynRM. Additionally, the average

torques between two winding configurations are similar while the torque ripple of the delta-connected machine is slightly lower.

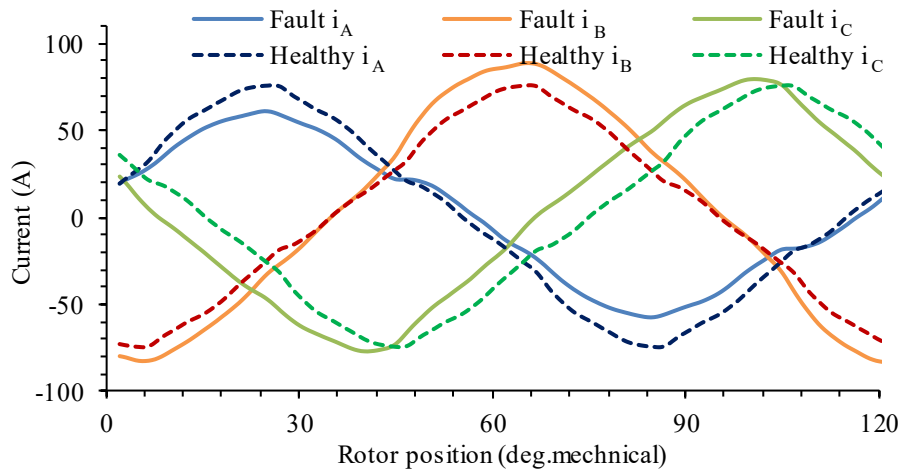


Fig. 2-22. Comparison of phase currents of set ABC of delta-connected machine under healthy condition and F3.

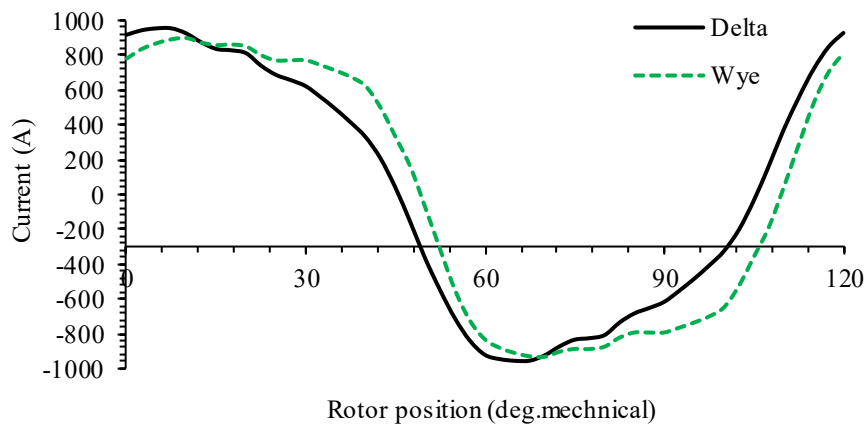


Fig. 2-23. Comparison of turn fault currents between delta- and wye-connected machines under F3.

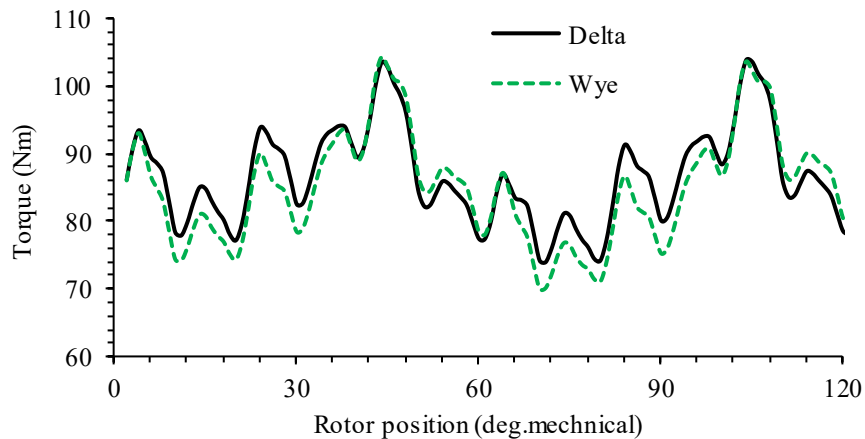


Fig. 2-24. Comparison of output torques between delta- and wye-connected PMASynRMs under F3.

Table 2-7. Comparison of performances under F3

Winding configuration	Wye	Delta
RMS of turn current (A)	726.70	694.43
RMS turn fault current normalised to/ rated (p.u.)	8.71	14.44
Turn loss (W)	857.63	1354.82
Average torque (Nm)	84.64	85.89
Torque ripple (%)	37.03	33.50

2.4.2.4 One-Turn Short-Circuit with 3-Phase Terminal Short-Circuit

The extremely large turn fault current in F3 is unsustainable. However, upon detection of the fault, 3-phase terminal short-circuit should be applied by turning on the entire bottom or the top switches of the 3-phase inverter to nullify the flux linkage in the fault turn and hence reducing the fault current. This is referred to as F4. Thus, performances under F4 are most critical for post fault operation and the resultant maximum temperatures under F4 between the wye- and delta-connected PMASynRMs will be assessed and compared.

Due to the mutual coupling between the two healthy 3-phase sets and the fault 3-phase set, the fault current is dependent on the location of the fault in the six possible coils A1, A2, B1, B2, C1 and C2 as illustrated in Fig. 2-25. It has been shown in [30], when the SC turn is located in B2 coil marked by the black squares as in Fig. 2-25, the resultant current of the wye-connected PMASynRM is the highest. Similar scan of the turn fault current when the fault occurs in six coils of the delta-connected PMASynRM is performed by FEA. For each fault location, the amplitude and gamma (torque) angle of the current vector in the two healthy 3-phase sets are varied over [0A, 150A] and [40°, 80°], respectively. The RMS fault current variations with the amplitude and gamma angle of the currents in the two healthy 3-phase sets in the six coils are shown in Fig. 2-26. It has been found that the RMS turn fault current normalised to rated current is the largest around 2-2.8 p.u. when the fault is located at B2 coil, while no more than 2 p.u. in the other coils. Therefore, the fault in B2 coil is also the worst in this delta-connected machine.

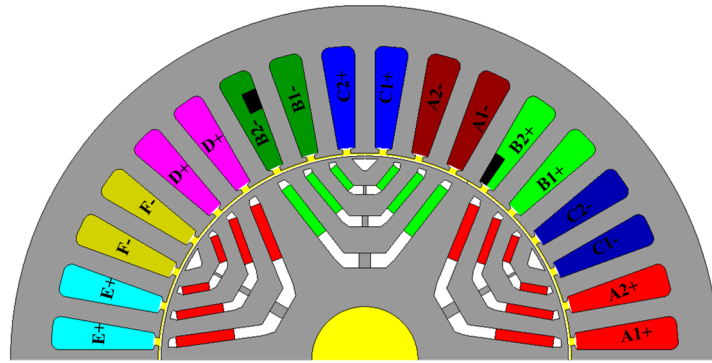


Fig. 2-25. Cross section of SC turn in B2 coil of PMASynRM

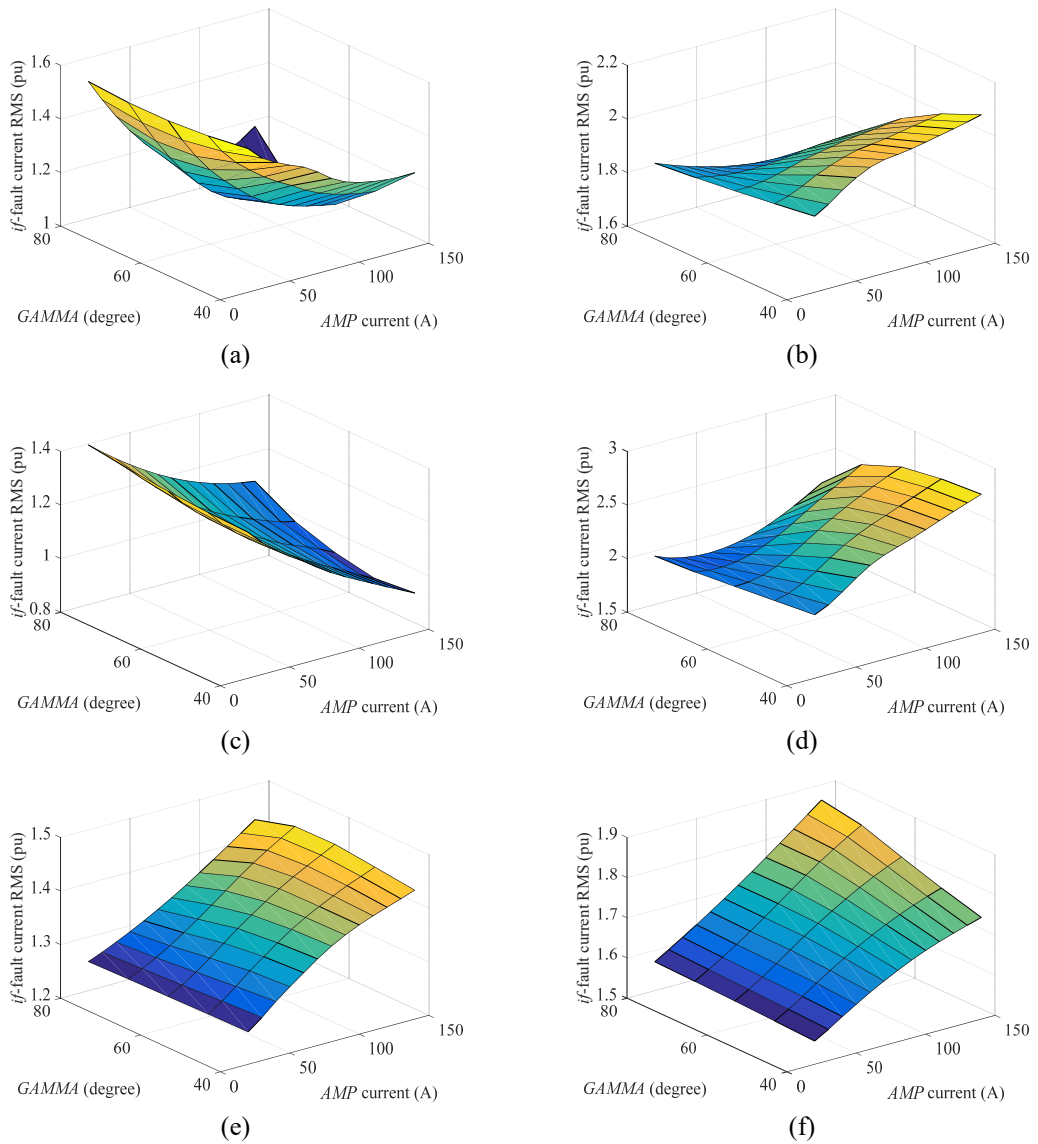


Fig. 2-26. Variations of turn fault current in coils with amplitude and gamma angle of currents in healthy sets (a) A1. (b) A2. (c) B1. (d) B2. (e) C1. (f) C2.

Fig. 2-27 and Fig. 2-28 compare the phase currents of the 3-phase set ABC in the healthy and F4 conditions of the wye- and delta-connected PMAynRMs, respectively. The terminal SC phase currents in the fault 3-phase set are all lower than the rated values

both in two winding configurations. This effect is beneficial for reduction of winding hotspot temperature. It has been calculated that the RMS currents in phases A, B and C under the 3-phase terminal SC of the wye-connected machine are 49.16%, 68.13% and 69.21% of the rated RMS current, respectively, while those of the delta-connected machine 44.88%, 83.02% and 64.57% of the rated RMS current, respectively. As can be inferred from equations (2-15) to (2-17), the influence of the turn fault current on the flux linkage in the fault phase (phase B) is proportional to the self-inductance, while the influence on the flux linkages in other two phases is proportional to the mutual-inductances. As the self-inductance is larger than the mutual-inductances, the turn fault current has much greater influence on the flux linkage in phase B than in the other two phases. Therefore, the reduction of current in phase B of the delta-connected machine is smaller than that of the wye-connected winding due to the difference in the turn fault currents. Namely, the turn fault current in the delta-connected machine under the influence of the zero sequence current is much lower than that in the wye-connected machine.

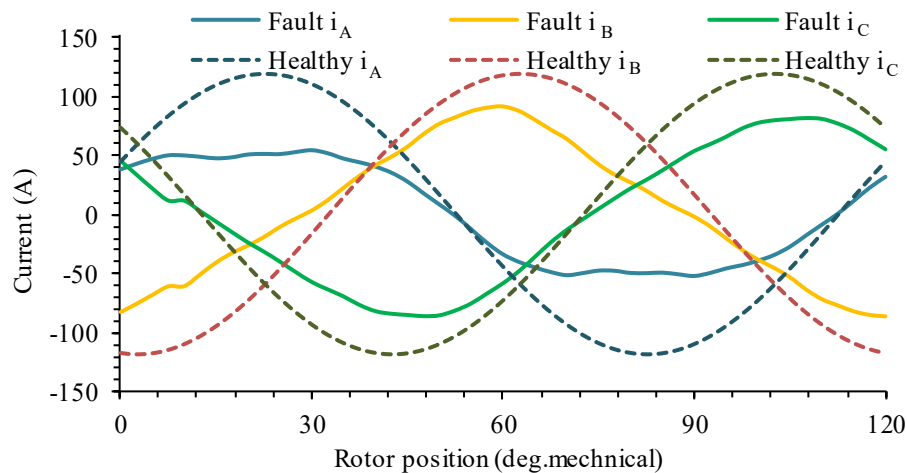


Fig. 2-27. Comparison of phase currents of set ABC of wye-connected machine under healthy condition and F4.

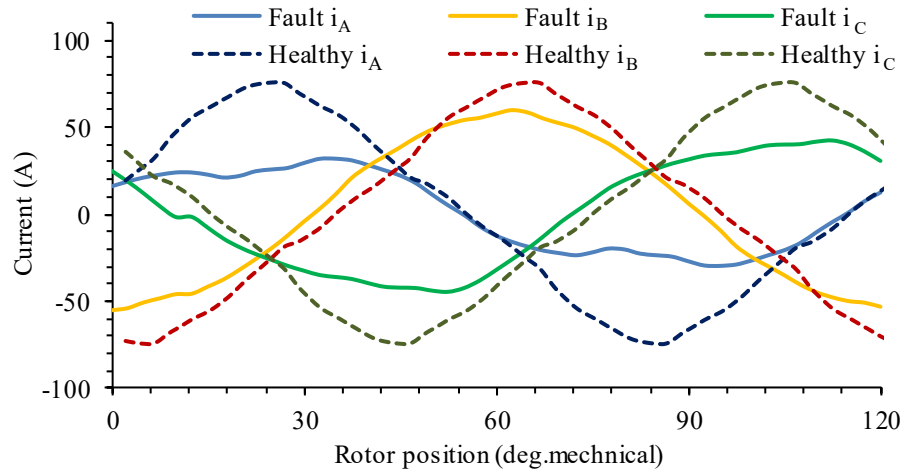


Fig. 2-28. Comparison of phase currents of set ABC of delta-connected machine under healthy condition and F4.

The resultant turn fault current waveforms, torque waveforms and performance indicators of the wye- and delta-connected PMASynRMs under F4 are shown in Fig. 2-29, Fig. 2-30 and Table 2-8, respectively. In addition, Table 2-9 compares the average temperatures of different parts and hotspot temperature under one-turn short-circuit with 3-phase terminal short-circuit fault for the two winding configurations. These temperatures are predicted by the lumped parameter thermal model of the machine which is applicable to assessing asymmetric temperature distribution under fault conditions. The LP thermal model will be established and detailed introduced in Chapter 4 section 4.3.2. Both thermal models of two winding configurations have the same initial and ambient temperatures.

It can be observed that the average torques and torque ripples of the wye- and delta-connected PMASynRMs are very similar. However, the RMS turn fault current of the delta-connected machine (122.26A, 2.54 p.u.) is significantly lower than that of the wye-connected machine (266.25A, 3.20 p.u.). This is because the zero sequence tends to reduce the zero sequence flux linkage of the fault turn in the delta-connected PMASynRM. It results in 64% reduction in the copper loss of the fault turn. Thus, although the two design variants have close temperatures of different parts under F4, the hotspot temperature of the delta-connected PMASynRM (188°C) is much lower than that of the wye-connected PMASynRM (214°C) as in Table 2-9. Both two hotspot temperatures of wye- and delta-connected PMASynRM are below the maximum permissible temperature of the insulation (220°C).

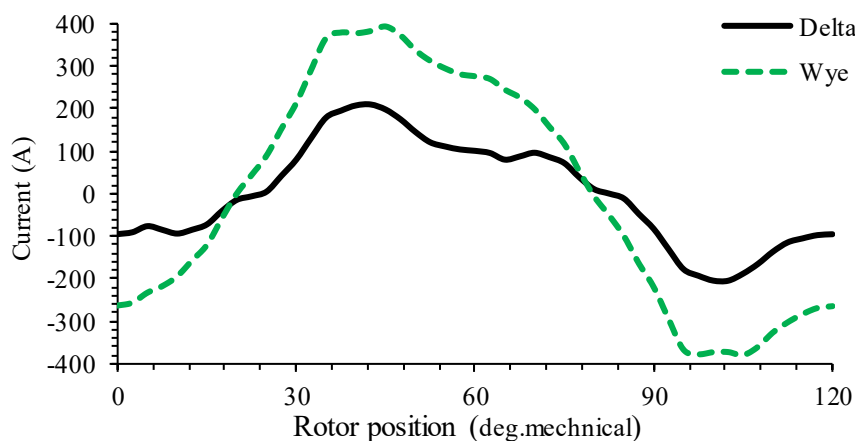


Fig. 2-29. Comparison of turn fault currents in the fault turn between wye- and delta-connected machines under F4.

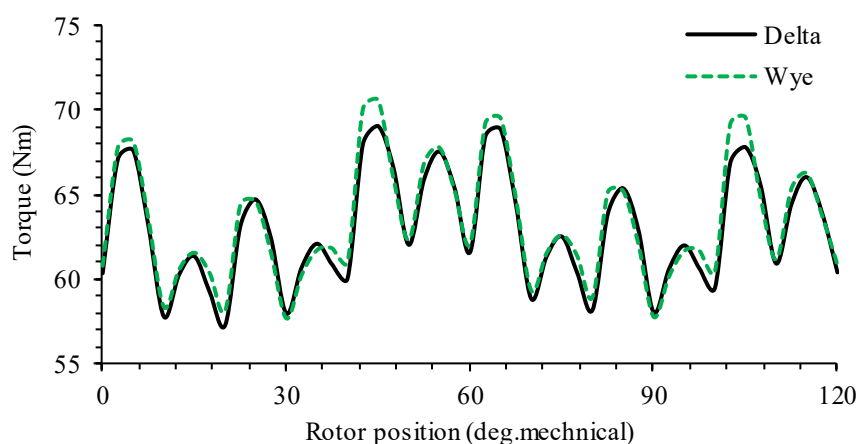


Fig. 2-30. Comparison of output torques between wye- and delta-connected machines under F4.

Table 2-8. Comparison of performances under F4

Winding configuration	Wye	Delta
RMS of turn current (A)	266.62	122.26
RMS turn fault current normalised to/rated (p.u.)	3.20	2.54
Turn loss (W)	115.44	41.99
Average torque (Nm)	63.37	62.92
Torque ripple (%)	20.45	18.76

Table 2-9. Comparison of temperatures under F4 predicted by LP model between wye- and delta-connected machines.

Component	Wye (°C)	Delta (°C)	Difference (°C)
Rotor	188	186	-2
Magnet	189	187	-2
Stator tooth	167	165	-2
Stator yoke	155	154	-1
Healthy winding	161	160	-2
B2 coil	181	175	-7
B2 coil hotspot	214	188	-26

The comparisons of the post-fault performances including average torque and torque ripple between wye- and delta-connected machines under F1 to F4 are summarised in

Table 2-10. According to the ‘bench marks’ of the post-fault performance of the PMASynRM in Chapter 1, the mean torques under faults are all larger than 50% rated torque and the torque ripples are all smaller than 40% for both wye- and delta-connected machines. Moreover, all the faults could be detected and mitigated. Additionally, under the most critical fault condition in respect of thermal behaviour which is F4 as a mitigation measure of F3, two hotspot temperatures of wye- and delta-connected PMASynRM are below the maximum permissible temperature of the insulation (220°C). Therefore, both two machines have fault tolerance as they have satisfactory performances under switch and winding open-circuit fault, switch and winding short-circuit fault, inter-turn short-circuit with mitigation measure.

Table 2-10. Comparison of performances under fault conditions between wye- and delta-connected machines

Faults Winding	F1		F2		F3		F4			
	Delta		Delta		Wye	Delta	Wye	Delta		
	Wye	S1	S2	Wye					C1	C2
Average torque (Nm)	54.57	86.85	76.96	54.57	55.90	54.19	84.64	85.89	63.37	62.92
Torque ripple (%)	28.09	31.69	17.96	28.09	33.32	36.68	37.03	33.50	20.45	18.76

2.5 Summary

This chapter establishes an equivalent model of the delta-connected PMASynRM with inter-turn fault for better insight into the influence of the zero sequence current on the turn fault current. Subsequently, it compares the performances of a triple redundant, 9-phase PMASynRM with wye- or delta-connected windings under healthy and fault conditions. It has been shown that they have very similar performances in healthy operations, although the delta-connected PMASynRM has extra zero sequence current which leads to increase in the copper loss by 1%. The steady-state performance of the delta-connected PMASynRM is slightly worse than that of the wye-connected PMASynRM under 3-phase open-circuit and one-turn short-circuit fault. However, it has much higher average torque and smaller torque ripple compared with the wye-connected PMASynRM under one-phase open-circuit fault. It is also shown that the zero sequence current in the delta-connected machine reduces the flux linkage of the fault turns, resulting in significantly lower turn fault current and lower hotspot temperature compared with the wye-connected PMASynRM. PMASynRMs with both two winding configurations have fault tolerance, but delta-connected PMASynRM has better fault tolerance.

Additionally, this chapter shows that in order to evaluate the capability of fault tolerant operation and effective fault mitigation, the electromagnetic analysis under principal faults either in the drive side or in the machine is essential. Moreover, a thermal model is also essential to determine fault tolerance. In addition, although the PMASynRM with electrical and thermal insulation has the magnetic coupling between different phase sets, it achieves high fault tolerance which indicates that magnetic isolation may not be strictly needed for fault tolerance. Subsequently, in order to improve the fault tolerance, the phase inductance should be large for having effective mitigation measure (F4) for critical fault (F3) in which the terminal SC current is similar to rated current. Then, the delta-connected winding which could decrease the zero sequence flux linkage, the turn fault current and hotspot temperature under inter-turn SC fault with mitigation measure is also recommended for fault tolerant machine.

Chapter 3 Continuous Demagnetisation Assessment for PMASynRM

3.1 Introduction

It has been known that permanent magnet-assisted synchronous reluctance machine is quite attractive in safety critical applications because of its high performance as well as improved fault-tolerant capability. However, the permanent magnet is vulnerable to demagnetisation resulting from the overheating, large current and heavy load. Demagnetisation of magnets will reduce electromotive force and output torque, as well as increase acoustic noise and vibrations. All these pose a particular safety risk of PMASynRM. Since machines used in safety critical applications require high reliability, it is essential to accurately assess the risk of irreversible demagnetisation of the proposed PMASynRM under various fault conditions.

As well known, permanent magnets are quite vulnerable to large d-axis current. Therefore, investigations have been made to identify the worst fault condition which may produce the most significant demagnetising current and cause severe demagnetisation. Firstly, the transient SC current under SC faults is significant which is always several times larger than the rated current and may produce excessive heating and irreversible demagnetisation [8]. Additionally, SC faults under the peak torque operation is much more severe than those under the rated torque or peak power [15] [16]. Moreover, voltage reversal failure occurs when the voltage vector has incorrect 180 electrical degree offset with reference to the back emf due to position sensor and/or controller failures, producing much higher demagnetising current than any short-circuit faults [15] [16].

Demagnetisation assessment has been studied in many publications. The authors in [60]-[62] employed fast analytical techniques for assessing and preventing demagnetisation of PM machines during operations. The model in [60] estimated the magnetic flux operating point of the magnets to predict the partial PM demagnetisation. Moreover, the analytical model established in [62] superposed the armature reaction fields in the magnets to determine the extent to which the magnets are irreversibly demagnetised. The analytical technique is computationally efficient at the design stage

for assessing the risk of demagnetisation. However, the analytical technique is not applicable to machines with complex rotor structure and is less accurate than FE based approach due to neglecting saturation and stator slotting. The 2D demagnetisation models are carried out in [63] [64] to identify the demagnetisation risk and then mitigate the demagnetisation by optimisation of the design topology. Further, a 3D FE simulation for demagnetisation assessment of a ferrite based spoke type motor is utilised in [65]. 3D FE analysis needs a large amount of computation time.

However, most above approaches only use the magnitude of flux density instead of considering the direction of magnetisation of flux density as in [66]-[68], hence resulting in inaccuracy in the demagnetisation analysis. The author in [66] utilised a 2D FEM method to calculate the max partial demagnetisation operating point which is equal to the quotient between the minimum flux density along the magnet surface and the remanence flux density of the magnet material. Then, the author in [67] predicted the demagnetisation characteristics of IPM machines by using the flux density vector plots to account for the direction of the magnetisation at various time instants during fault conditions. The author in [68] decomposed the flux density of all nodes in each magnet into two components, including along and perpendicular to the magnetising direction. The flux density along the magnetising direction is utilised to assess the partial irreversible demagnetisation under various fault conditions by 2D transient FEA with improved accuracy.

Unfortunately, most above assessments cannot evaluate post-demagnetisation performances to give a clear insight of the severity of demagnetisation behaviour. Therefore, a set of different simple analytical demagnetisation models adopting the history-dependent hysteresis model considering both the magnitude and direction of magnetisation are established in [69] to predict the reduction of emf of an overloaded and overheated SPM machine. However, this analytical model does not provide a comprehensive assessment of demagnetisation in the magnets. The authors in [70] defined the pre- and post remanence ratio of PMs to quantify the PM demagnetisation state of a distributed wound IPM machine under various fault conditions. Further, the authors in [59] and [71] utilised the data extracted at the peak demagnetising moment to evaluate the post-demagnetisation performances of PM machines with different rotors and winding configurations.

However, these demagnetisation models only present the demagnetised region in which the operating point is below the knee point flux density at a specific time instant, such as the peak demagnetising instant, and do not consider the continuous accumulation of demagnetisation, causing prediction errors in the post-demagnetisation performance. Thus, demagnetisation models using recoil lines which can track the history of partial demagnetisation have been proposed in [72]-[74]. The authors in [72] proposed a model employing recoil lines to calculate the magnetisation vector when the operating points have fallen below the knee of the BH curve. The recoil line is also adopted of an efficient searching algorithm in [73] to iteratively find and update the new worst operating point below the knee point. The authors in [74] provided a continuous demagnetisation performance assessment which utilises the recoil line, considers the direction of flux density, tracks the history of partial demagnetisation, and evaluates post-demagnetisation performance.

The basic aims of this chapter are to assess the demagnetisation withstand capability for the proposed triple redundant, 9-phase (3x3-phase) fault machine based on PMASynRM topology. The risk of partial irreversible demagnetisation under various critical faults of the PMASynRM with wye-connected windings will be comprehensively assessed by employing a continuous demagnetisation model. Additionally, the dynamic response during fault transients and the post demagnetisation performance, such as the demagnetisation distribution, reduction in back emf and torque, will also be evaluated. Furthermore, a discussion has been made to compare the transient responses of the wye- and delta-connected winding under critical fault conditions.

3.2 Continuous Demagnetisation Assessment

The triple redundant, 9-phase, 36-slot, 6-pole PMASynRM with wye-connected windings is shown in Fig. 3-1 with the winding and magnet layouts. In Fig. 3-1 (b), the magnets are shown in red and green as indicated by M_iN/P_j_k , where $k = 1, 2, 3$, denotes the k^{th} layer, $j = 1, 2$, denotes two different magnetisation angles of the i^{th} rotor pole ($i = 1$ to 6), and N and P denotes the polarity of magnetised directions. Moreover, every magnet is divided into a number of elements for accurate assessment which is not shown in Fig. 3-1 (b).

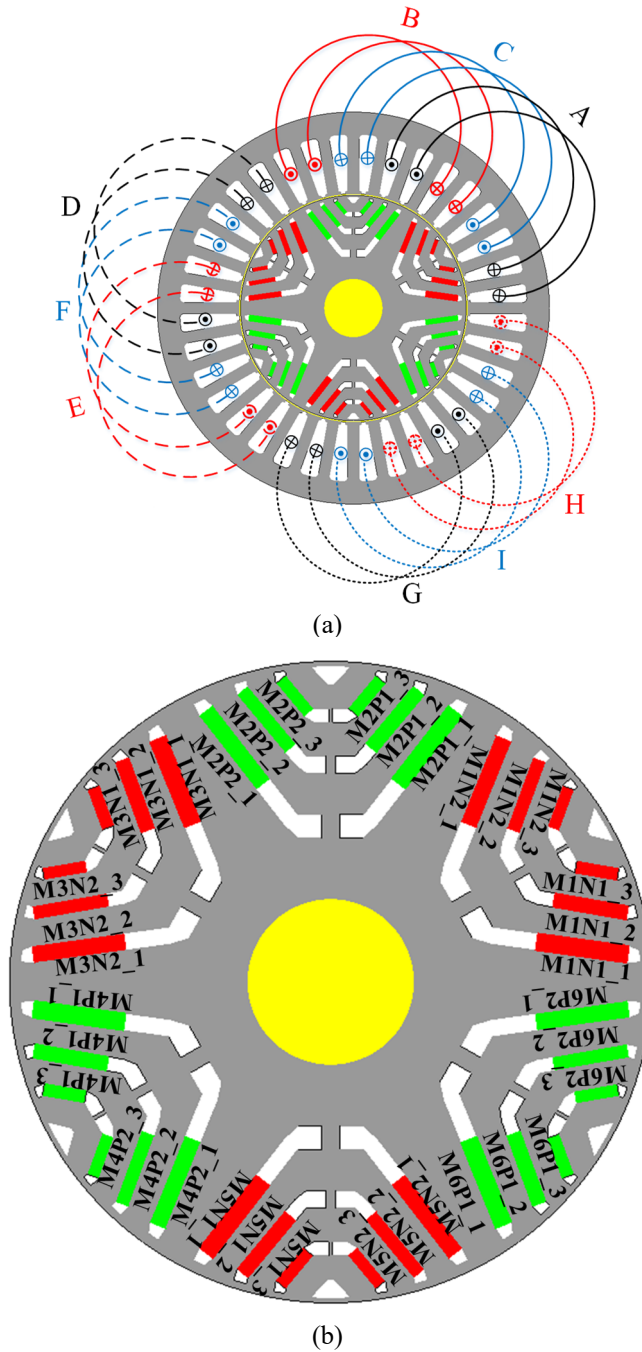


Fig. 3-1. Cross-section of 9-phase, 36-slot, 6-pole PMASynRM. (a) Winding layout. (b) Magnet layout.

The flux density in each magnet element is decomposed into two parts which are along and perpendicular to the magnetising direction [15]. Fig. 3-2 shows the schematic of flux density in one element of M1N1_1 and M1N2_1 along and perpendicular to the magnetising direction.

$$B_{Px_n} = B_{x_n} \cos(\theta_n) + B_{y_n} \sin(\theta_n) \quad (3-1)$$

$$B_{PYn} = -B_{Xn} \sin(\theta_n) + B_{Yn} \cos(\theta_n) \quad (3-2)$$

where n is the element number; θ_n is the angle of magnetisation; B_{PXn} is the element flux density along the magnetising direction; B_{PYn} is the element flux density perpendicular to the magnetising direction. To prevent partial irreversible demagnetisation at a given element in a magnet, the flux density in the direction of magnetisation (B_{PXn}) must be larger than the value at the knee point.

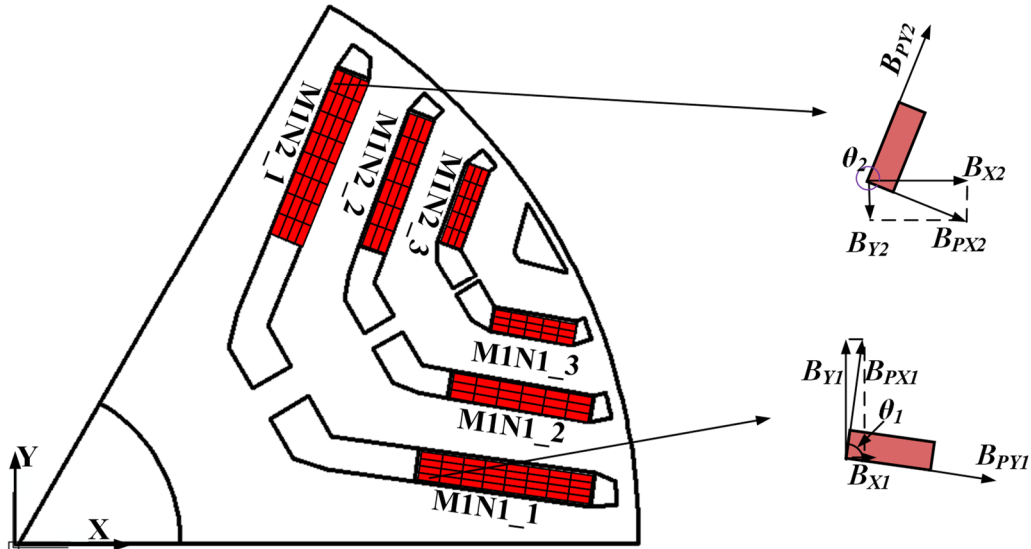


Fig. 3-2. Decomposition of flux density of M1N1_1 and M1N2_1

The material of VACOMAX 225 HR is used for magnets in the machine. Fig. 3-3 shows the demagnetisation curves of the VACOMAX 225 HR for various operating temperatures. It is evident that the knee points for 200°C and 250 °C are around -0.5T, while the knee point for 300°C is slightly lower than 0T. In this study, magnets are considered to be operated at 300°C and the knee point is set to be 0T, viz., if the flux density in the direction of magnetisation goes below 0T, partial irreversible demagnetisation will occur. Since the temperature coefficient of the magnets is very small and 300°C working temperature is exaggerated, the influence of temperature changing is not considered in the study.

Fig. 3-4 illustrates the flow chart of the continuous demagnetisation analysis described in [74]. The continuous demagnetisation analysis is based on continuous prediction of magnitude and direction of flux density in each element and uses the BH curve and recoil line of magnets and direction of the magnetisation to determine the remanence of magnets in each element in the next step.

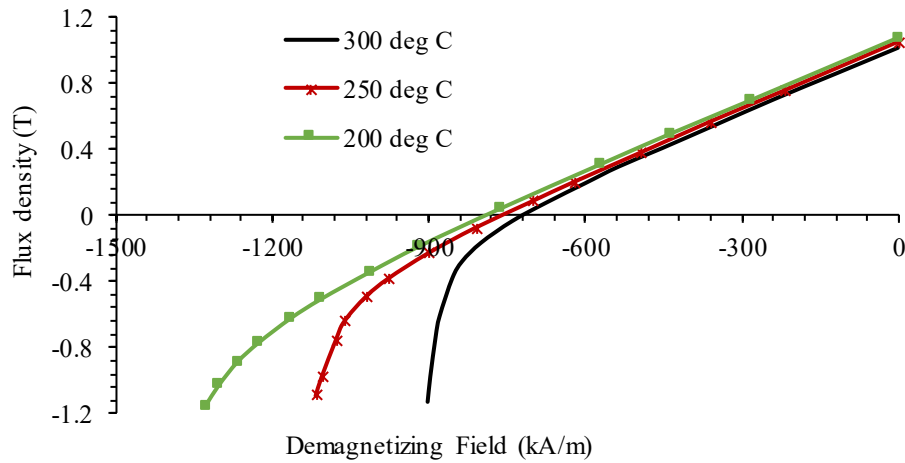


Fig. 3-3. Demagnetisation characteristics of VACOMAX 225 HR

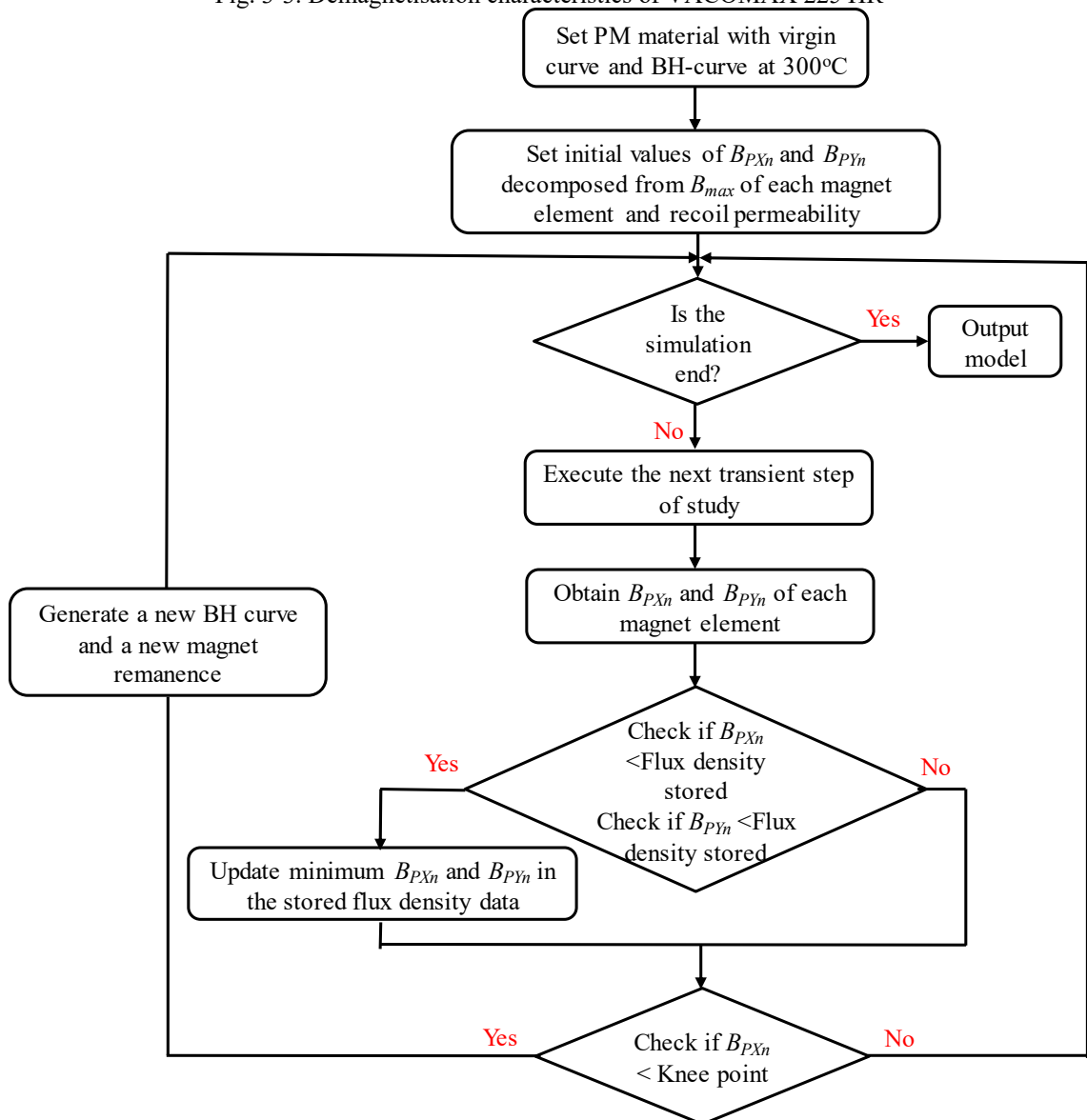


Fig. 3-4. Flow chart of continuous demagnetisation analysis.

As observed, the PM material with demagnetisation BH curve together with the virgin curve at 300°C shown in Fig. 3-5 is first set in the machine model. The virgin curve determines the initial material magnetisation without external fields. Hence, the model can be used to study magnetisation or re-magnetisation process as well. The BH curve in the second and third quadrants is used for considering demagnetisation. The B_{max} of each magnet element is decomposed into components along and perpendicular to the magnetising direction which are the initial values of B_{PXn} and B_{PYn} . Afterwards, every new obtained flux density of each magnet element will also be decomposed into B_{PXn} and B_{PYn} which will be compared with the previous stored flux density values. Once the new obtained values are smaller, they will be updated and stored as the minimum flux densities in the element. Then, if the B_{PXn} which is in the direction of magnetisation is above the knee point, the remanence in the subsequent step keeps the same. Otherwise, if the B_{PXn} is below its knee point, a new BH curve (knee point with recoil line) in each element identified as dotted line in Fig. 3-5 is generated and will intersect with the vertical axis to determine the new magnet remanence in each element in the subsequent step. The process is implemented in 2D Opera, and can track the history of partial demagnetisation accurately. Hence, this method records the minimum flux density during the fault transient which can be used to assess partial demagnetisation. In addition, every first, second and third layer magnet are divided into 90, 78 and 42 elements, respectively. As every magnet element is calculated separately, different elements operate on different magnetisation levels. Therefore, it can evaluate post-demagnetisation performance, such as the demagnetisation distribution, and the reduction in back emf and output torque.

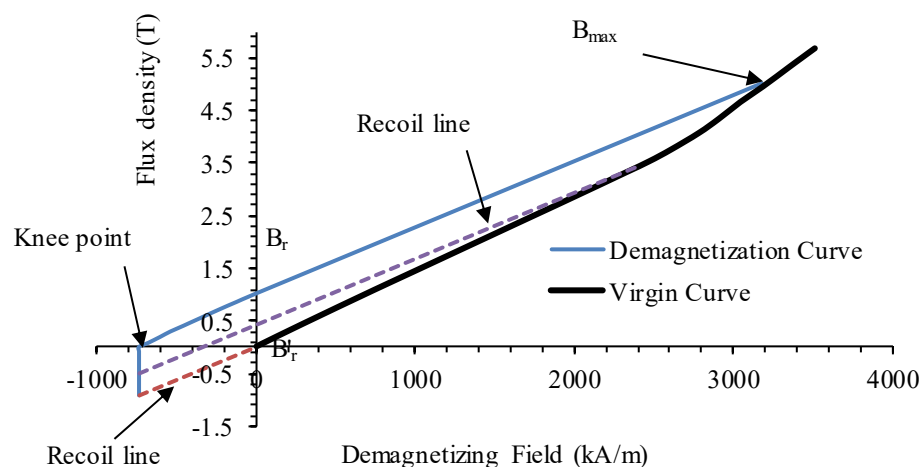


Fig. 3-5. Demagnetisation BH curve with virgin curve at 300°C explaining partial demagnetisation.

Fault conditions which are very critical with respect to partial irreversible demagnetisation considered in this chapter are listed in Table 3-1. All these faults are injected at the peak torque (114Nm) and base speed (4000rpm). This operating condition has been shown to cause more severe consequences than the rated torque or peak power operating conditions.

F1 to F4 are various short-circuit fault conditions induced by machine. F1 and F2 which are 3-phase SC and 9-phase SC faults will generate large demagnetising current which may cause demagnetisation. F4 (one turn SC) is considered as it will produce significant SC current during fault condition which may have effect on the demagnetisation, while F3 (turn fault with 3-phase terminal SC) which is a measure of fault mitigation of F4 is also considered. F5, F6 and F7 which are 3-phase, 6-phase and 9-phase voltage-reversal faults, respectively, are induced from inverter drive. The voltage-reversal fault is the worst scenario because of much higher current than those of short-circuit conditions F1 to F4. This is because under short-circuit conditions, the full inverter voltage of winding is zero, so the fault current is only generated by the induced emf. However, under voltage-reversal conditions, the inverter loses its synchronization with the induced emf, resulting in a sudden surge of currents in the phases which are produced by the sum of the full inverter voltage and the induced emf. Without loss of generality, one turn short-circuit is assumed to occur in phase B and 3-phase fault is assumed to occur in 3-phase set ABC.

Table 3-1. Fault conditions under consideration.

	Fault	Pre-fault operation
F1	3-phase short-circuit	Peak torque and base speed
F2	9-phase short-circuit	Peak torque and base speed
F3	Turn fault with 3-phase terminal SC	Peak torque and base speed
F4	Turn fault	Peak torque and base speed
F5	3-phase voltage reversal	Peak torque and base speed
F6	6-phase voltage reversal	Peak torque and base speed
F7	9-phase voltage reversal	Peak torque and base speed

In 2D Opera, the switches are in parallel connection with the current sources and windings. The switches can be turned on at any rotor position to simulate a SC fault because it is verified in [15] that the instant of short circuit will not change the maximum demagnetising current. To simulate a voltage reversal fault, voltage sources are connected in parallel with the current sources, and both of them have separate switches for fault

injection. Switches can be turned on without affecting each other when assessing the voltage reversal faults.

3.3 Demagnetisation Assessment for Short Circuit Faults

Faults F1, F2, F3 and F4 listed in Table 3-1 which are 3-phase short-circuit, 9-phase short-circuit, turn fault with 3-phase terminal short-circuit and turn fault, respectively, have been carried out at the peak torque and the base speed.

Firstly, the dynamic characteristics of F1 (3-phase short-circuit) fault condition are shown in Fig. 3-6. Fig. 3-6 (a) and (b) plot the transient phase currents and the current trajectory in d-q axis plane of 3-phase set ABC, respectively, for better insight of dynamic response.

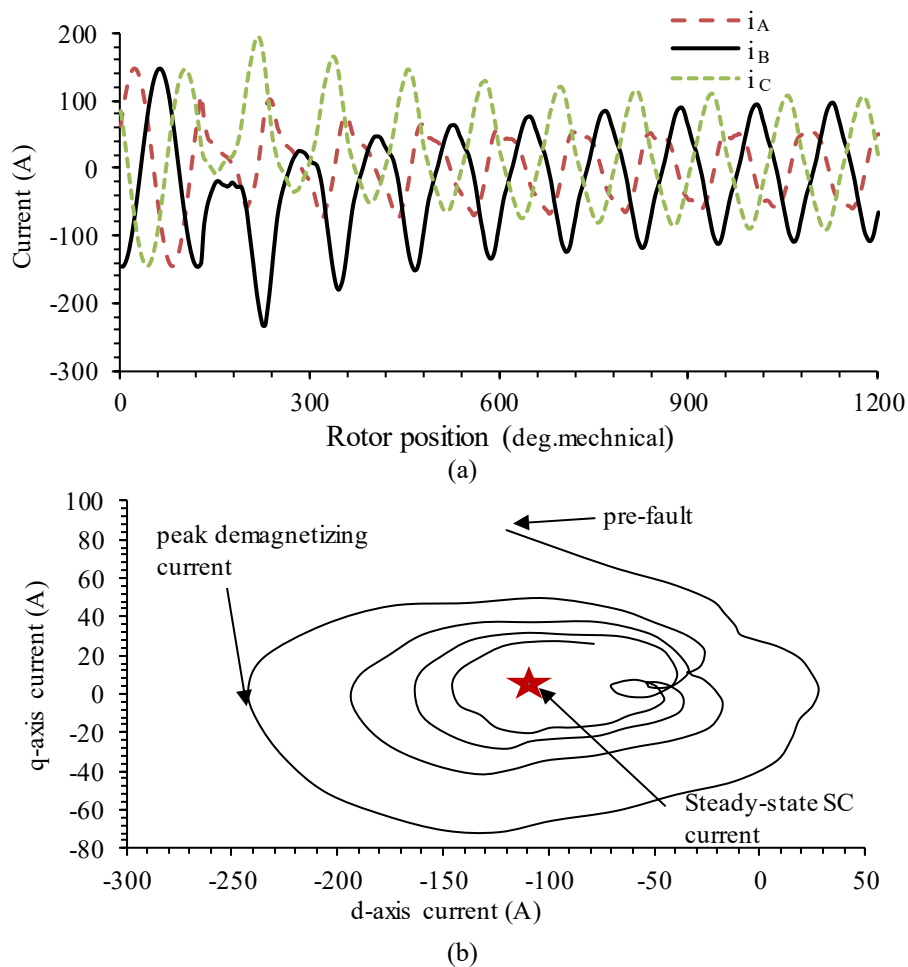


Fig. 3-6. Characteristics under 3-phase short-circuit condition. (a) Transient phase currents of phase A, B, C. (b) D-q axis current trajectory.

As observed in Fig. 3-6 (b), failure is applied at the pre-fault operation and the trajectory passes through the peak demagnetising current identified by an arrow. The steady-state short-circuit current is marked as star. The maximum d-axis current is -242A which is 2.0 p.u. normalised to peak magnitude of the rated current.

The analysis is repeated for F2, F3 and F4 and the performance indicators during transient process and after demagnetisation, including peak phase current, peak d-axis current, peak turn-fault current, steady-state short-circuit current, reduction in back emf and output torque, of the PMASynRM under F1 to F4 have been compared in Table 3-2. As for F1 and F2, there are no turn fault currents, while for F3 and F4, the large turn fault current is emerged and Fig. 3-7 illustrates the transient current of phase B and fault turn during fault transient process under F4 (one turn SC). Additionally, the lowest flux density along the magnetising direction of all magnets during the transient fault for evaluating the severity of the demagnetisation are also listed in Table 3-3. Following observations can be obtained from the comparisons of the above four fault conditions at the peak torque and base speed.

Table 3-2 Comparison of currents and post demagnetisation performances under Faults F1 to F4.

Fault	Peak phase current (A)	Peak d-axis current (A)	Steady-state short circuit current (A)	Peak turn-fault current (A)	% Reduction in Back emf	% Reduction in Torque
F1	-233.60	-242	-85.43	--	0	0
F2	-218.77	-240	-85.43	--	0	0
F3	-140.82	-175	-85.43	-1664.45	0	0
F4	-146.70	-120	--	-1664.50	0	0

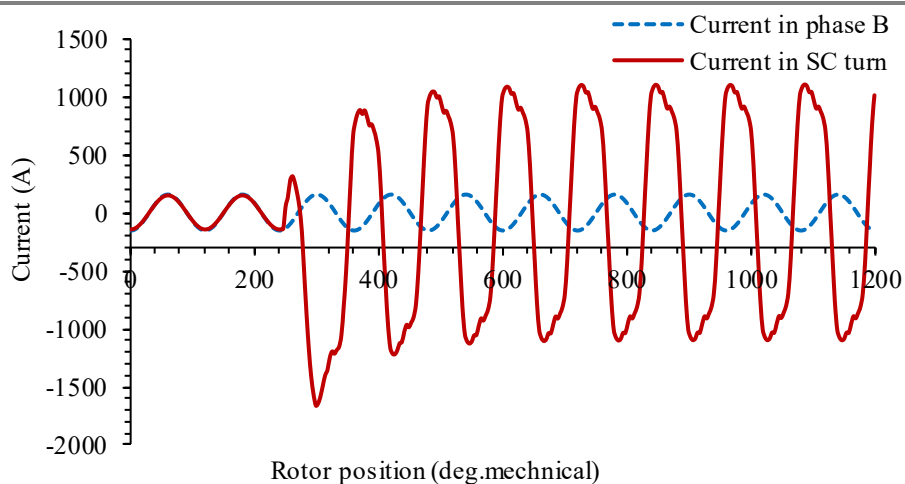


Fig. 3-7. Transient currents of phase B and fault turn during fault transient process under F4.

Table 3-3 Comparison of the lowest flux density along the magnetising direction of all magnets during fault transient.

Flux density (T)t	F1	F2	F3	F4
M1N1_1	0.50	0.43	0.53	0.64
M1N1_2	0.43	0.28	0.48	0.55
M1N1_3	0.40	0.28	0.45	0.49
M1N2_1	0.51	0.42	0.54	0.67
M1N2_2	0.37	0.27	0.42	0.45
M1N2_3	0.44	0.32	0.47	0.49
M2P1_1	0.40	0.43	0.52	0.64
M2P1_2	0.25	0.29	0.37	0.56
M2P1_3	0.29	0.28	0.31	0.47
M2P2_1	0.39	0.42	0.53	0.67
M2P2_2	0.28	0.27	0.34	0.45
M2P2_3	0.33	0.32	0.34	0.49
M3N1_1	0.53	0.43	0.53	0.64
M3N1_2	0.51	0.29	0.48	0.55
M3N1_3	0.43	0.28	0.45	0.48
M3N2_1	0.53	0.42	0.54	0.68
M3N2_2	0.43	0.28	0.42	0.45
M3N2_3	0.47	0.32	0.47	0.50
M4P1_1	0.60	0.43	0.41	0.64
M4P1_2	0.49	0.29	0.26	0.55
M4P1_3	0.54	0.28	0.29	0.47
M4P2_1	0.62	0.42	0.40	0.67
M4P2_2	0.47	0.28	0.25	0.46
M4P2_3	0.57	0.32	0.33	0.48
M5N1_1	0.52	0.43	0.53	0.62
M5N1_2	0.50	0.29	0.49	0.55
M5N1_3	0.46	0.28	0.43	0.49
M5N2_1	0.53	0.42	0.54	0.66
M5N2_2	0.44	0.28	0.42	0.45
M5N2_3	0.48	0.32	0.47	0.50
M6P1_1	0.53	0.43	0.52	0.63
M6P1_2	0.39	0.29	0.39	0.51
M6P1_3	0.45	0.28	0.31	0.45
M6P2_1	0.53	0.42	0.54	0.64
M6P2_2	0.37	0.28	0.34	0.42
M6P2_3	0.49	0.32	0.34	0.47

- (1) Since none of the flux density in magnets goes down 0T after faults as seen in Table 3-3, as well as no reduction in the back emf and output torque are seen in Table 3-2, F1, F2, F3 and F4 do not result in any degree of partial irreversible demagnetisation at the peak torque and base speed condition.
- (2) Although the 3-phase short-circuit fault results into higher peak demagnetising current (-233.6A) compared with 9-phase symmetrical short-circuit fault (-218.8A), the overall minimum flux density along the

magnetising direction of 9-phase short-circuit fault shown in Table 3-3 is lower.

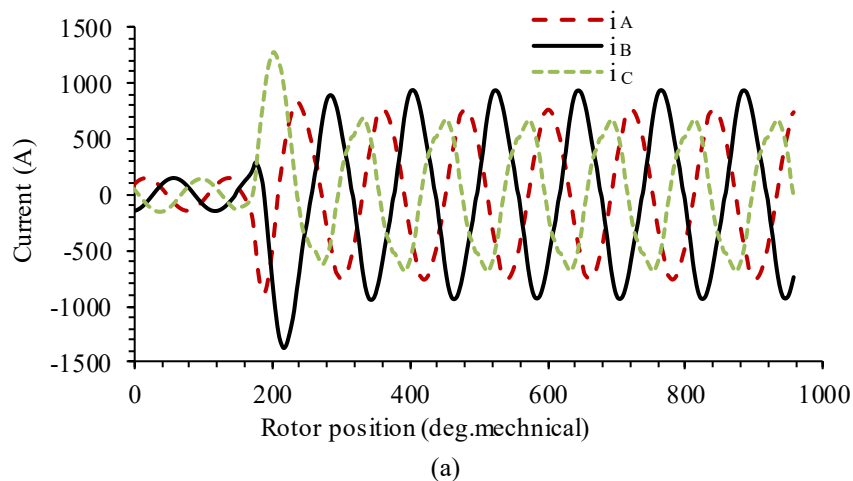
- (3) Faults F3 and F4 generate huge circulating current in the fault turn which is 13.9 p.u. normalised to the peak magnitude of the rated current as in Fig. 3-7 and Table 3-2, however, because of the small inductance, the turn-fault current has little effect on the demagnetising flux. Hence, the turn-fault condition is less significant than the terminal short-circuit fault in respect of irreversible demagnetisation of this machine as seen in Table 3-3.

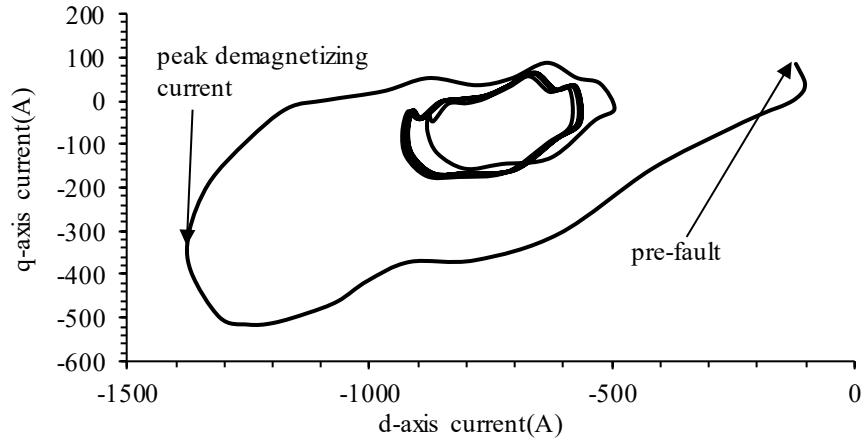
3.4 Demagnetisation Assessment for Voltage-Reversal Faults

Afterwards, Faults F5, F6 and F7 listed in Table 3-1 associated with the 3-phase, 6-phase and 9-phase voltage-reversal faults which are quite critical have been analysed at the peak torque and the base speed in the following section.

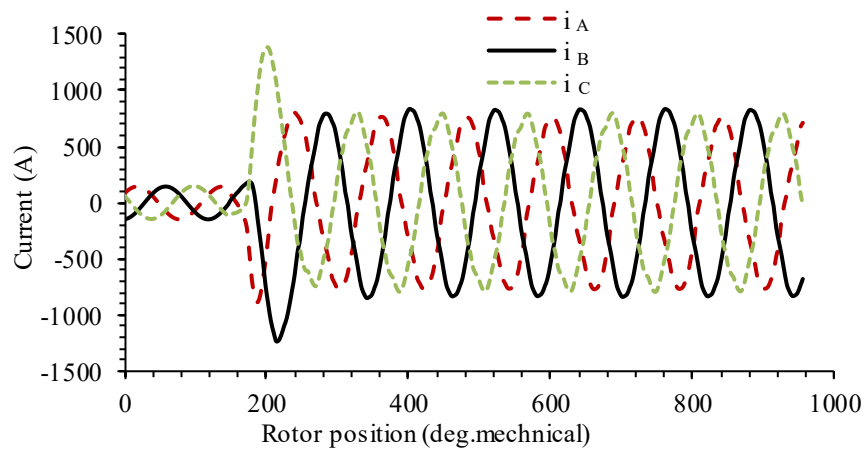
3.4.1 Fault Performance

The transient phase currents and the current trajectories in the d-q axis plane of 3-phase set ABC under F5, F6 and F7 fault conditions are shown in Fig. 3-8, while the back emf and the output torque before and after faults F5, F6 and F7 are illustrated in Fig. 3-9 and Fig. 3-10, respectively. The performance indicators during the transient process and after demagnetisation of the PMASynRM under F5 to F7 are shown in Table 3-4.

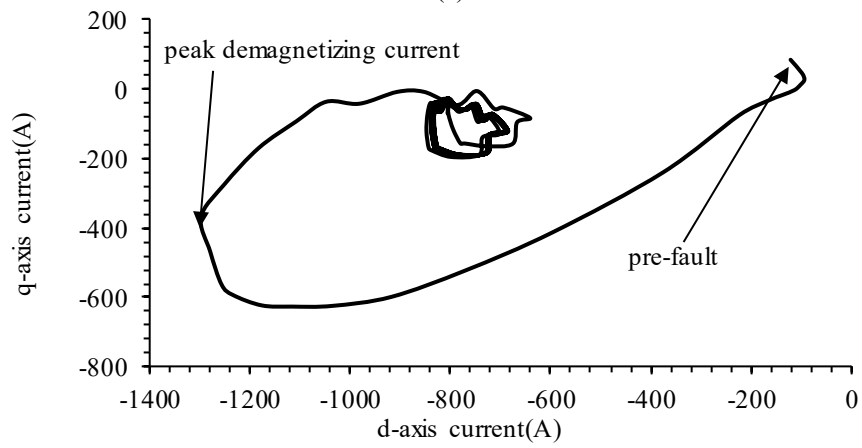




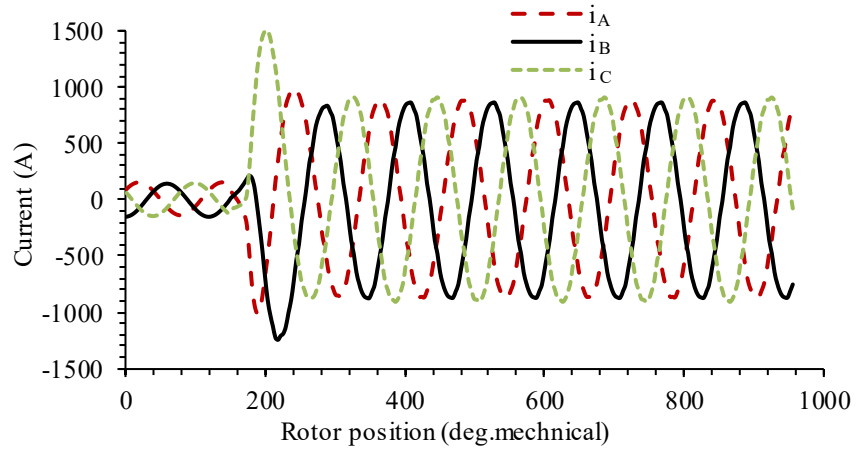
(b)



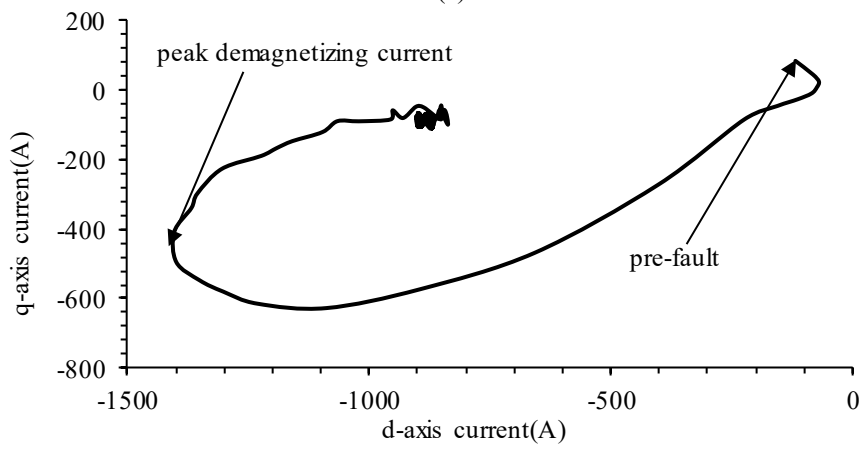
(c)



(d)

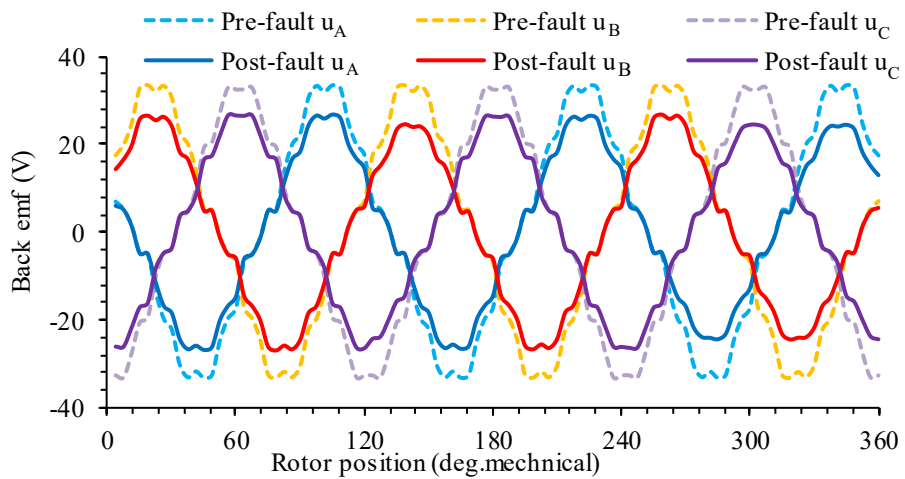


(e)



(f)

Fig. 3-8. Transient phase currents and current trajectories in the d-q axis plane under various voltage-reversal conditions. (a) Transient phase currents of phase A, B, C under F5. (b) D-q axis current trajectory under F5. (c) Transient phase currents of phase A, B, C under F6. (d) D-q axis current trajectory under F6. (e) Transient phase currents of phase A, B, C under F7. (f) D-q axis current trajectory under F7.



(a)

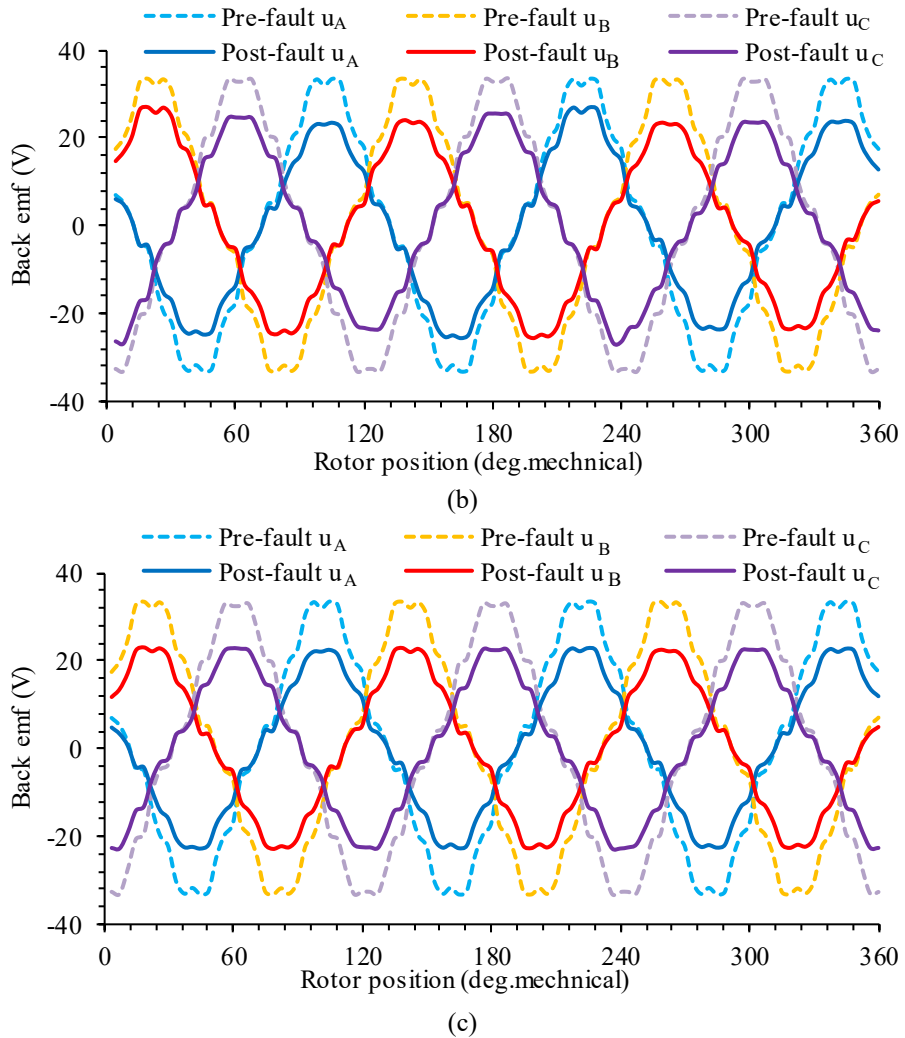


Fig. 3-9. Comparison of the back emfs before and after faults. (a) F5. (b) F6. (c) F7.

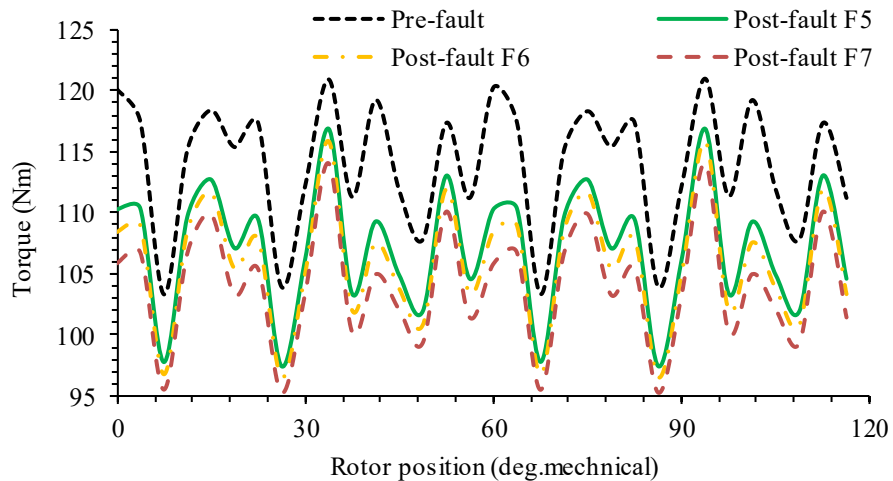


Fig. 3-10. Comparison of the output torques before and after faults F5, F6, F7.

Table 3-4 Comparison of transient currents and post demagnetisation performances under Faults F5 to F7.

Fault	Peak phase current (A)	Peak d-axis current (A)	Peak breaking torque (Nm)	% Reduction in Back emf	% Reduction in Torque	Torque ripple (%)
F5	-1366	-1370	3.74	20.91	5.93	17.92
F6	-1299	-1300	-120	25.01	7.02	17.77
F7	-1237	-1400	-282	31.34	8.72	17.86

It can be observed from Fig. 3-8 and Table 3-4 that the peak transient current is an order of magnitude higher than the rated when the combined effect of the back emf and full inverter voltage is only limited by the machine inductance under the voltage-reversal faults. It is also seen that the 3-phase voltage-reversal fault generates the largest peak phase current (1366A), while those of the 6-phase (1299A) and 9-phase (1237A) voltage-reversals are slightly lower. However, 9-phase voltage-reversal condition yields the highest peak d-axis current (1400A) and largest negative torque during transient process. Additionally, as observed in Fig. 3-9, Fig. 3-10 and Table 3-4, the back emf and output torque after all three voltage-reversal faults have been reduced compared with the original value under healthy condition. This indicates that the magnets have suffered from significant partial irreversible demagnetisation under F5 to F7. Moreover, the post-fault back emf waveforms of 3-phase and 6-phase voltage-reversals as shown in Fig. 3-9 (a) and (b) are asymmetric indicating that the demagnetisation levels in all magnets are not the same under F5 and F6, while the symmetric post-fault back emf waveform of the 9-phase voltage-reversal as shown in Fig. 3-9 (c) indicates the symmetric demagnetisation under F7. Among all voltage-reversal faults, the 3-phase voltage-reversal fault has the least irreversible demagnetisation while the 9-phase voltage reversal results in the most severe partial irreversible demagnetisation with 31.1% and 8.72% reductions in the back emf and output torque, respectively. Moreover, the torque ripple increases from 15.40% to 17.86%.

However, even though the reductions in the back emf under these faults are quite large, torque reduction only reaches 8.72% under the worst case. This is because the relatively small percentage (30%) of the alignment (PM) torque in the total output torque of the machine.

Additionally, in order to evaluate the extent of the partial irreversible demagnetisation in every magnet, demagnetisation rate d_{mag} is introduced. It is defined by,

$$d_{mag} = \frac{B_r - B_r'}{B_r} * 100\% \quad (3-3)$$

where B_r is the pre-fault remanence and B_r' is the post-fault remanence of the permanent magnet of VACOMAX 225 HR at 300°C. According to this definition, d_{mag} will be zero if no irreversible demagnetisation takes place and increase with the severity of demagnetisation.

The demagnetisation rate of every magnet element under F5, F6, and F7 is obtained and presented in Fig. 3-12 (a), Fig. 3-13 (a), and Fig. 3-14 (a), respectively. Fig. 3-11 shows the corresponding position of all the magnets of the machine. The white area inside a magnet has no partial irreversible demagnetisation, while the colorful areas are covered by demagnetised nodes with the colour from red to blue indicating the increased extent of demagnetisation. It can be observed from Fig. 3-12 (a) that the demagnetisation of the 3-phase voltage-reversal condition is asymmetric and the worst demagnetised magnets which are marked with a red circle are M2P. This can also be verified by the post-fault no-load flux density waveform in Fig. 3-12 (b) in which the flux density generated by M5N, M6P, M1N, M3N and M4P are almost the same, while the flux density generated by M2P is smaller. As observed from Fig. 3-13 (a), the demagnetisation of 6-phase voltage-reversal condition is also asymmetric, and the worst demagnetised magnets are marked with red circles which are M1N, M2P, M3N, and M4P. It can also be verified in Fig. 3-13 (b) that flux density produced by M5N and M6P are larger than others. Moreover, from Fig. 3-14 (a) and (b), both the demagnetisation area and no-load flux density of 9-phase voltage-reversal condition are almost symmetric. These figures also approve that the demagnetisation is worst under 9-phase voltage-reversal condition. Additionally, from the transient responses, it can be concluded that the most severe demagnetisation instant is when the negative d-axis current reaches the maximum value and the rotor magnets aligned with the d-axis of the fault windings at this instant of time are most vulnerable.

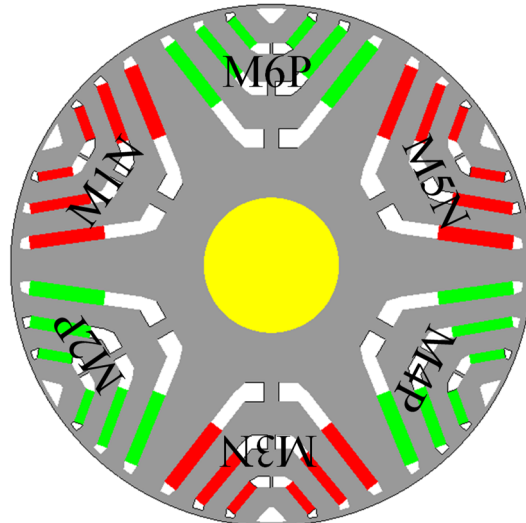


Fig. 3-11. Corresponding position of all the magnets of the machine with partial demagnetised area.

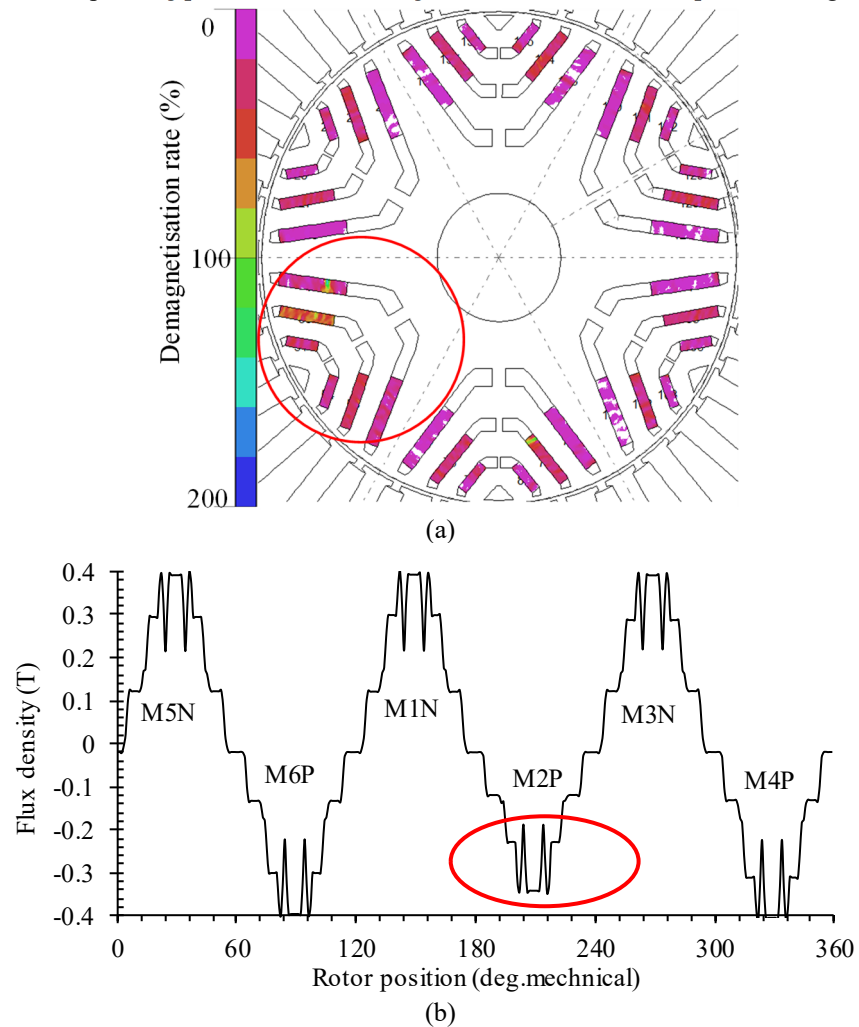


Fig. 3-12. Partial demagnetised area and no-load flux density waveform after F5 (a) Demagnetised area. (b) Post-fault no-load flux density.

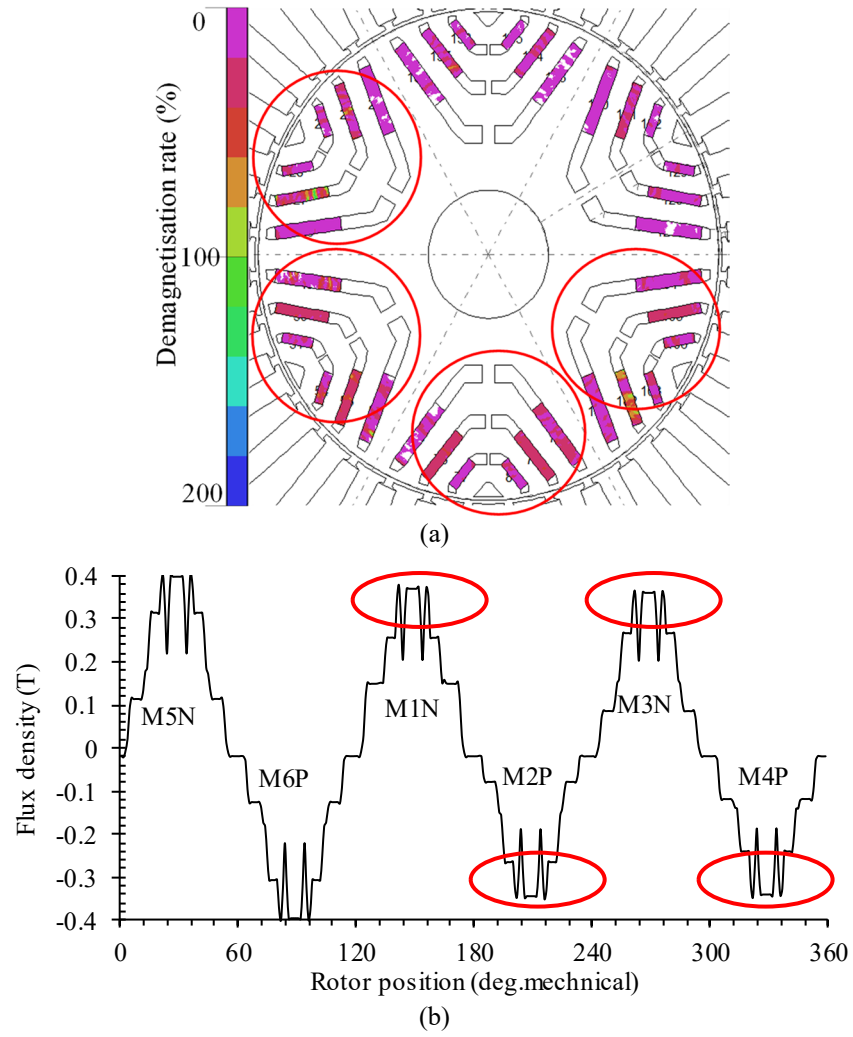
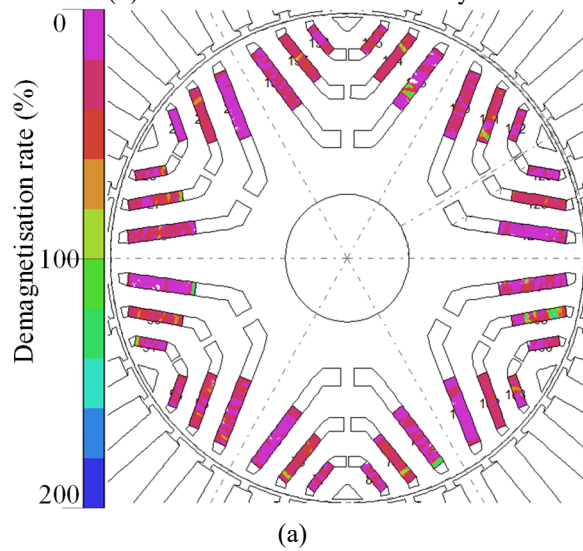


Fig. 3-13. Partial demagnetised area and no-load flux density waveform after F6 (a) Demagnetised area. (b) Post-fault no-load flux density.



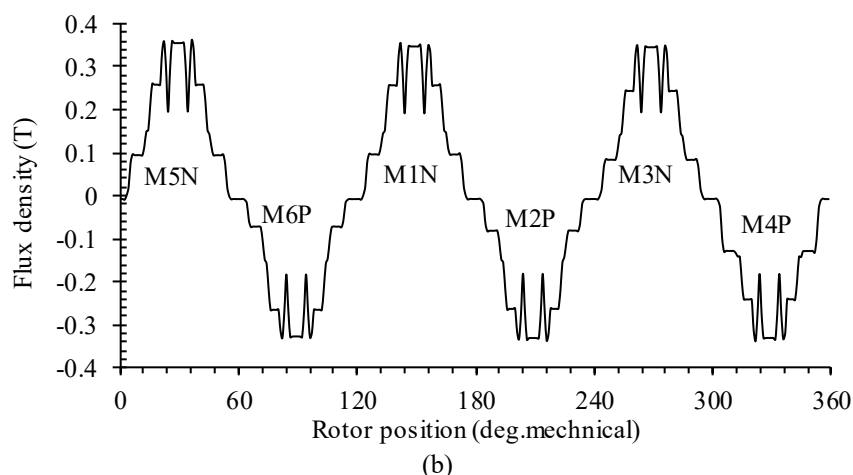


Fig. 3-14. Partial demagnetised area and no-load flux density waveform after F7 (a) Demagnetised area.
(b) Post-fault no-load flux density.

3.4.2 Post-Fault Torque Harmonic Analysis

As is well known, if partial irreversible demagnetisation in a PM machine is not symmetric, the output torque may have specific fault harmonic frequencies. Therefore, as 3- and 6-phase voltage-reversal faults have generated asymmetric partial irreversible demagnetisation, the post-fault output torque of 3-phase voltage-reversal fault is analysed below for better insight of this phenomena.

Firstly, the flux density waveforms before and after 3-phase voltage-reversal fault are presented in Fig. 3-15 and Fig. 3-12 (b). The flux density under healthy condition is symmetric as seen in Fig. 3-15 and hence the harmonic contents of the airgap flux density distribution generated by each pole-pair is the same, while the post-fault flux density as shown in Fig. 3-12 (b) is obviously asymmetric. Therefore, harmonic contents of airgap flux density distribution in space over one pole-pair by the pre-fault M1N and M2P, post-fault M1N and M2P, post-fault M3N and M4P, post-fault M5N and M6P, are compared in Fig. 3-16. It can be observed from Fig. 3-16 that all three pole-pairs are irreversible demagnetised with the lower magnitude of fundamental flux density compared to that of the pre-fault flux density and the pair consisting of M1N and M2P has the lowest value. Moreover, the 2nd order harmonic is present as a result of the asymmetric demagnetisation in the post-fault flux density over the M1N and M2P pole-pair.

However, because this machine employs integer-slot full-pitched distributed winding, the winding factor associated with even harmonics are zero. Thus, the additional even space harmonics of the airgap flux density have no effect on the harmonic content of the

back emf as shown in Fig. 3-18. Fig. 3-18 illustrates harmonic content of pre-fault and post-fault back emfs of phase A generated by pole-pair M1N and M2P which is presented in Fig. 3-17. Additionally, with symmetric and balanced 3-phase currents, no additional harmonics, especially 2nd order harmonic, will appear in the output torque after the asymmetric partial irreversible demagnetisation. This is indeed shown in Fig. 3-19. Hence, it follows that with integer-slot full-pitch distributed windings, the asymmetric demagnetisation will not result in additional harmonic frequencies in the output torque.

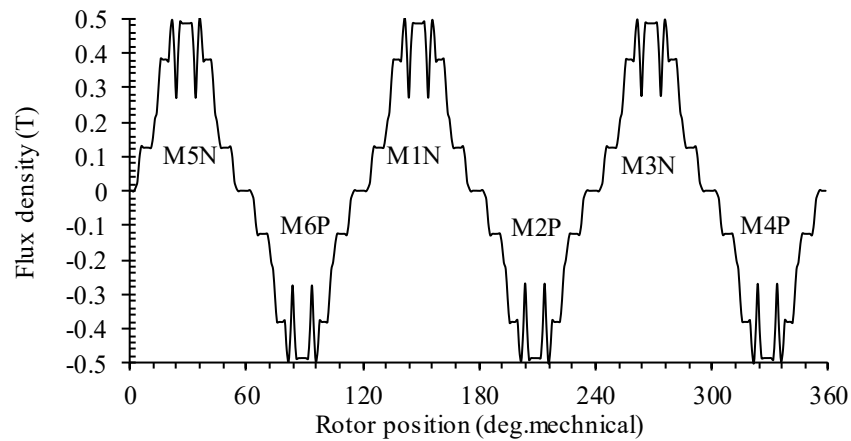


Fig. 3-15. Pre-fault no-load flux density.

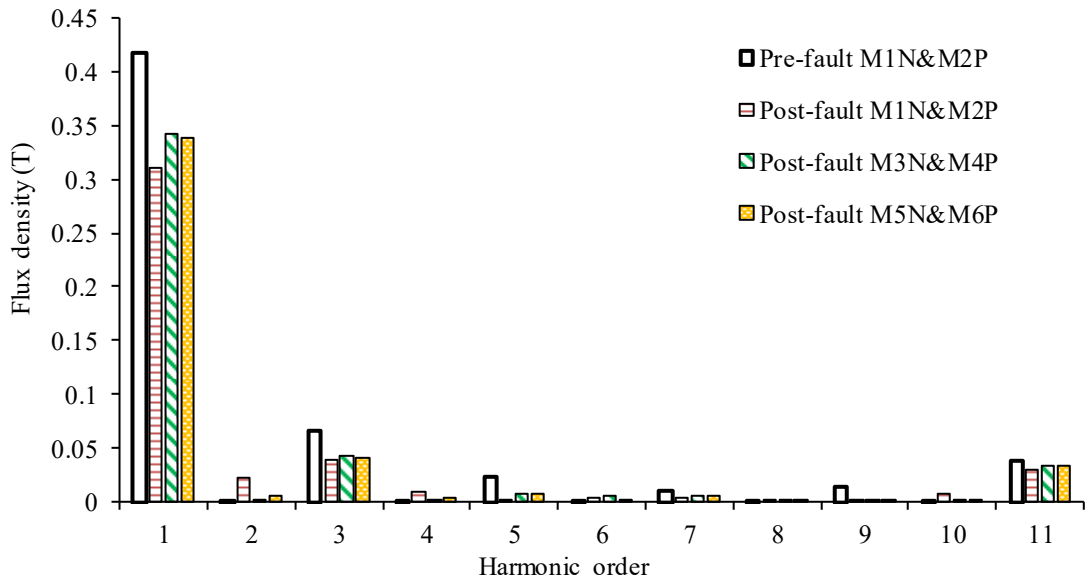


Fig. 3-16. Space harmonic distribution of airgap flux density before and after 3-phase voltage-reversal fault.

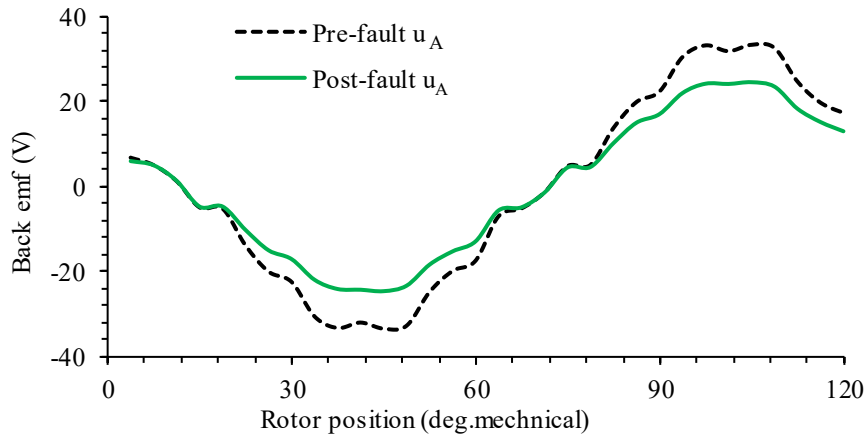


Fig. 3-17. Comparison of the pre-fault and post-fault back emf of phase A generated by pole-pair M1N and M2P.

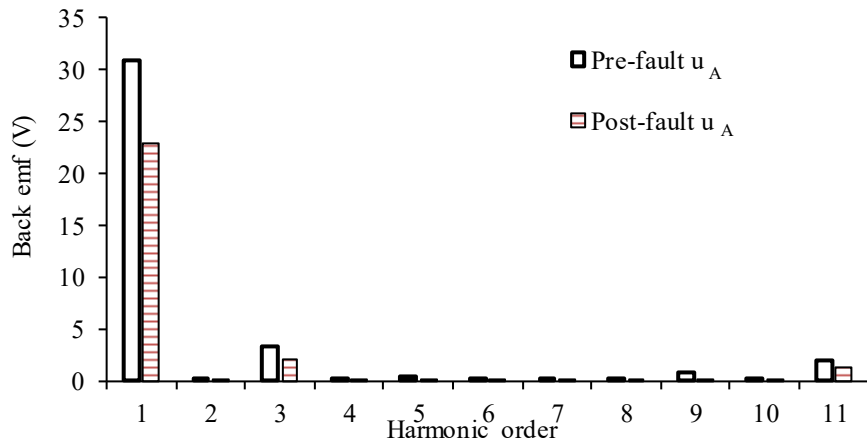


Fig. 3-18. Space harmonic distribution of back emf before and after 3-phase voltage-reversal fault.

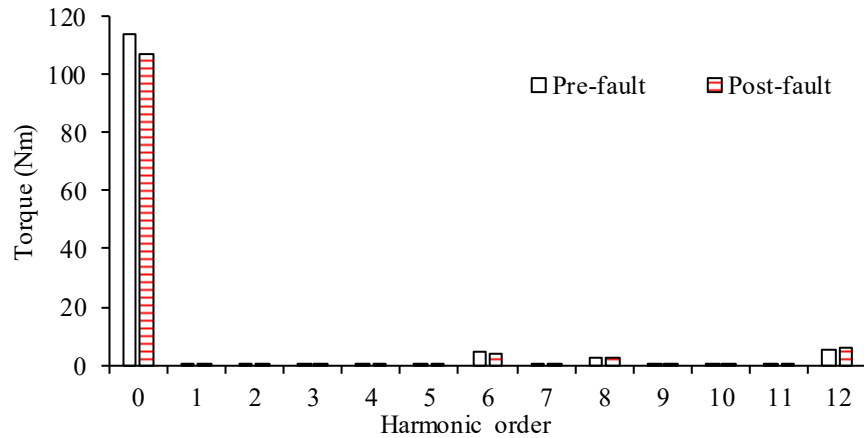


Fig. 3-19. Torque harmonic distribution before and after 3-phase voltage-reversal fault.

3.5 Summary

In this chapter, the risk of partial irreversible demagnetisation for the triple redundant, fault tolerant PMASynRM with wye-connected winding under various faults at the peak torque and base speed has been comprehensively assessed by employing a continuous demagnetisation model. Because of the advanced design features employed for the

permanent magnet rotor, terminal and inter-turn short-circuit faults will not produce any degree of partial irreversible demagnetisation. However, all the voltage-reversal faults result in significant partial irreversible demagnetisation. Among them, 9-phase voltage-reversal fault causes the symmetric and most severe partial irreversible demagnetisation and the resultant reduction in back emf is 31.34%, but the reduction in output torque is only 8.72% which is modest. Further, the asymmetric demagnetisation will not lead to the additional harmonics in the output torque. It shows that the wye-connected PMASynRM has very strong demagnetisation withstand capability.

In summary, it can be seen that the continuous demagnetisation assessment is essential to be included in fault analysis for fault tolerance. Moreover, as the average torque decreases only by 8.72% and the torque ripple only increases from 15.40% to 17.86% under the worst fault condition, the machine has fault tolerance according to bench marks. The faults are detectable by the 2nd harmonic in IAP and IRP produced by large SC fault. Besides, the IPM rotor configurations in which the magnets are buried in the rotor core with advanced PM material has large alignment torque and can further improve the demagnetisation capability.

Chapter 4 Lumped Parameter and 3D Thermal Models of a PMASynRM

4.1 Introduction

As previously introduced, the most important requirement of the fault tolerant machine for safety critical applications is its ability to manage and mitigate faults. It has been reported that winding failure resulting from insulation break-down is one of the dominant failure modes within the machine. Since insulation life decreases significantly when winding temperature increases, temperature is one of the key limiting factors for fault tolerant machines. Therefore, accurately predicting the temperature distribution and hotspot temperature under various conditions, especially some typical fault conditions, is vital at design stage.

There has been extensive research on thermal analysis of electrical machines under healthy condition by LP thermal models, commercial software packages, and finite-element analysis [103]-[107].

The analytical LP thermal models have been applied to a variety of machine types. The authors in [78] and [79] introduced LP thermal models of totally enclosed fan cooled (TEFC) induction machines for predicting both steady-state and transient temperatures. The author in [80] proposed a simplified thermal model for self-cooled induction motors. The author in [82] developed a LP thermal model for a multi-barrier IPM synchronous machines which could predict the temperatures of key points in the stator windings and the rotor magnets. To account for a more complex heat dissipation process, the author in [83] established a 3D equivalent thermal network model of the PM spherical motor. The LP thermal model is fast for predicting both steady-state and transient temperatures in a wide range of machines. However, it usually adopts simplifications based on empirical data in electrical machines which reduces accuracy.

The commercial software packages based on the LP thermal network method are widely used in thermal analysis of electrical machines. Motor-CAD [108] is one of the most widely used commercial software package. It is quite convenient that the users only need to input geometric data, winding information, used materials, loss distribution and

the cooling systems. Further, it could help users set mechanical interface gaps according to roughness and manufacturing techniques of various components. Afterwards, the software will automatically build a thermal model and compute thermal parameters by selecting the most appropriate analytical formulations. However, only a set of fixed machine topologies are embedded in the software. Therefore, any topology which is different from those built-in topologies cannot be analysed by Motor-CAD. Additionally, the software cannot predict asymmetric temperature distribution of the electrical machines under fault conditions.

Both 2D and 3D FEA can accurately model complex geometry of different electrical machine topologies compared with LP model and predict asymmetric temperature distribution of various electrical machines under fault conditions compared with Motor-CAD but more time-consuming. Furthermore, it can be used in predicting winding temperature distribution which is of great importance. It is well known that wire conductors of most mush windings are random placed in a slot, which makes it impossible to model each individual conductor with the precise position inside the slots in thermal analysis.

Two alternative approaches both adopt FEA to calculate the equivalent thermal conductivity of a stranded winding in a slot. They can be easily employed for windings with a known conductor placement. Otherwise, the random conductor placement and the impregnation together with the gaps between the slot liner and the stator lamination need some assumptions to be made for calculation.

The first approach is that a set of rectangular-shaped copper conductors in a slot are modelled in the 2D FEA [90]. Additionally, a simple boundary condition is applied in the model for setting a fixed temperature boundary to the outer surface of the stator lamination, and a fixed copper loss to the conductors. This can obtain the temperature difference between the hotspot in the winding and stator. Moreover, the layered winding model is reported as an alternative method to predict the temperature rise in a slot [90]. A set of thermal resistances associated with the volume and placement of the different materials are placed in series from the slot wall to the centre of the slot. Each thermal resistance is represented as a layer, and the volume of each material in the model is the same as that in the actual machine

However, this thesis will adopt the most simple and widely acceptable approach to analytically calculate an equivalent thermal conductivity based on the correlation reported in [88] of the winding combining all materials, such as copper conductors, impregnation and slot line insulation, which can be utilised both in LP thermal model and FEA.

However, few papers have considered the thermal analysis under fault conditions with asymmetric temperature distribution. A thermal network is used in [109] for an inter-turn short circuit fault detection in PMSM. An EM-thermal coupled model based on a LP network is reported in [110] to obtain fault diagnosis of winding open-circuit or an inter-turn fault in DC motor. Simulink-MATLAB-based fault (short-circuit fault) model and 2D FEM magnetic model are employed in [111] to predicate copper and iron losses under SC condition of a dual-star flux-switching permanent magnet motor. LP and 3D FEM steady state thermal models are subsequently used to calculate the temperatures of different machine components. In general, it is important to establish a thermal model for accurately predicting the asymmetric temperature distribution of a fault tolerant machine under common fault conditions. However, systematic approaches are currently lacking.

Among all the common faults, inter-turn SC fault is one of the leading causes of winding failures and it is particularly critical since only a few turns are in the SC path. Consequently, the excessive fault current several times greater than rated may give rise to a local hotspot and ultimately cause a complete insulation failure of the winding. It is important to quantify the rate of temperature rise and the permissible maximum time duration in which the fault should be detected and an appropriate mitigation action is taken before causing further damage. Usually for the triple redundant fault tolerant machine under study, terminal SC is applied on the faulted 3-phase as a fault mitigation measure upon detection of an inter-turn SC fault. Thus, thermal modelling and analysis of these two fault conditions are the main focus in this chapter.

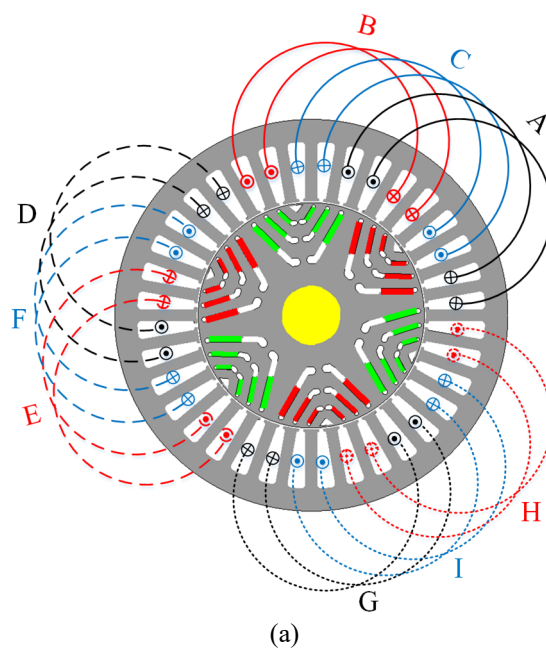
This chapter will establish transient LP thermal models and a 3D thermal model for thermal analysis under healthy and fault conditions of the triple redundant, 9-phase PMASynRM. Firstly, the cooling design of the machine is introduced. Then, the detailed modelling of the transient LP models under healthy and fault conditions with all the thermal parameters are described. The 3D thermal model is also built in detail. Subsequently the temperatures predicted by the two models under the same conditions

have be compared. Moreover, the losses in the thermal models under fault conditions are predicted by the 2D electromagnetic model. The predicted fault currents by 2D EM model are compared with the test results. The transient and steady-state temperatures predicted by the 3D thermal model considering more realistic issues will be comprehensively compared with the experimental results under healthy and SC fault conditions. The merits of the two thermal models are also assessed.

4.2 Cooling Design

The fault tolerant triple redundant, 9-phase PMASynRM with wye-connected windings is illustrated in Fig. 4-1. The ambient and coolant oil temperatures are 100°C and 110°C, respectively. Therefore, the spiral cooling jacket which is one of the most commonly used liquid cooling designs is adopted for effective heat dissipation. Besides, the windings are potted with Stycast 2676FT which is a high thermal conductivity material (1.3W*m/K) to improve the heat dissipation of the windings, especially the end winding regions.

The machine with the spiral cooling jacket is modelled in Motor-CAD [108] and illustrated in Fig. 4-2. The cooling jacket is integrated in the housing in which the coolant oil circulates in the grooves through an external pump and heat exchange to remove the heat inside the machine.



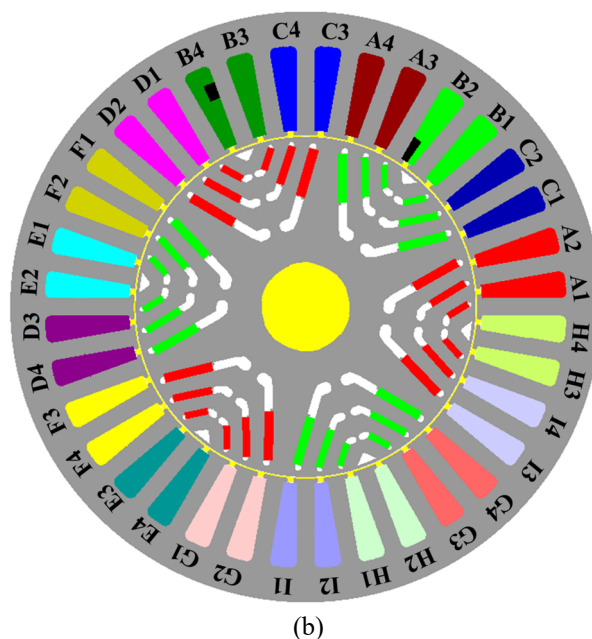


Fig. 4-1. Cross section of a triple redundant, 9-phase PMASynRM. (a) Winding Layout. (b) Named slots and short-circuit turn.

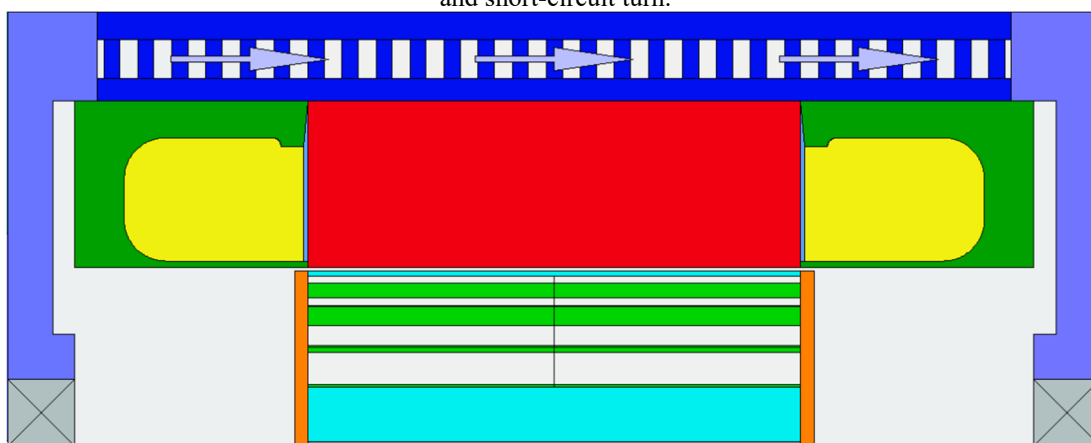


Fig. 4-2. Illustration of the spiral cooling jacket system of machine.

4.3 Transient Lumped Parameter Thermal Model

In order to facilitate fast prediction of thermal behaviour of the machine, transient LP thermal models are built under healthy and various fault conditions.

4.3.1 LP Thermal Model under Healthy Condition

For derivation of the transient LP thermal model of the 36-slot PMASynRM under healthy condition, some assumptions are made. The thermal dissipation in the rotor part and stator core is mainly in the radial direction while the thermal dissipation in the winding area considers the radial and axial directions. The commercial software package, such as Motor-CAD as well as empirical equations presented in [76], are used to help develop the model. Additionally, the losses, mainly including the copper loss and iron

loss are predicted by the 2D EM model. The iron loss is calculated by Bertottie loss model via FE analysis. Moreover, PM eddy current loss is also quantified and included in the thermal models.

As the LP thermal model is symmetric under healthy condition, only half of the tooth pitch is modeled. Fig. 4-3 and Fig. 4-4 show the schematic of 1/6 rotor part with key dimensions and the LP thermal model of the rotor part, respectively. The rotor iron loss is divided into yoke and iron-rib parts, and the eddy current loss in magnets is inputted into the magnet node. The main heat dissipation path in the radial direction includes the shaft R_{SHAFT} , the rotor yoke R_{RY} , the magnet R_{MAG} , the contact thermal resistance R_{MR} between the magnet and rotor, and the rotor iron-rib R_{RIR} . Furthermore, convective heat transfer at the end region of the shaft, rotor and magnet with the end cap air is also accounted by three thermal resistances R_{SHAFT_air} , R_{R_air} , and R_{MAG_air} shown in Fig. 4-4. Moreover, C_{SHAFT} , C_{RY} , C_{MAG} , and C_{RIR} denote capacitances of the shaft, rotor yoke, magnets and rotor iron-ribs, respectively. The convective resistances are evaluated in Motor-CAD considering the natural air convection. The other thermal resistances and capacitances can be obtained by adopting the governing principle of the heat conduction [103]. Because of the complexity, some simplifications have been made, then the thermal resistances and capacitances are given in (4-1) to (4-5) and in (4-6) to (4-9), respectively.

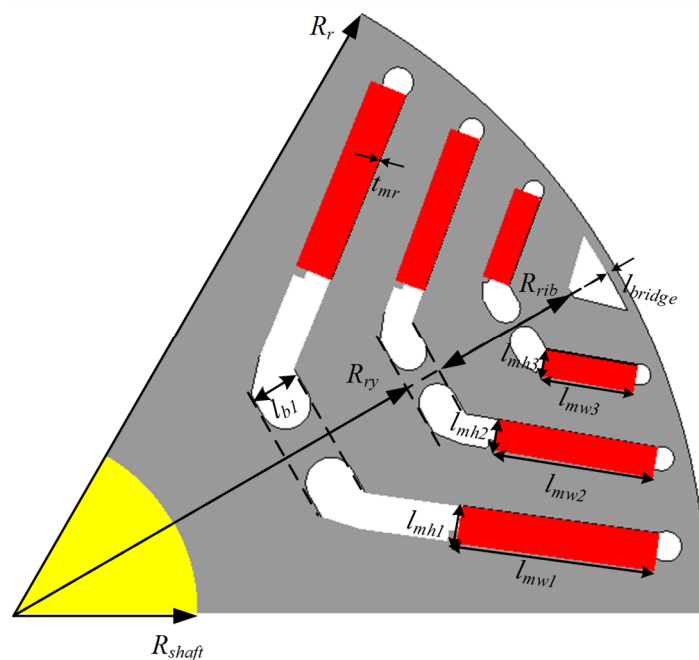


Fig. 4-3. The schematic of 1/6 rotor part.

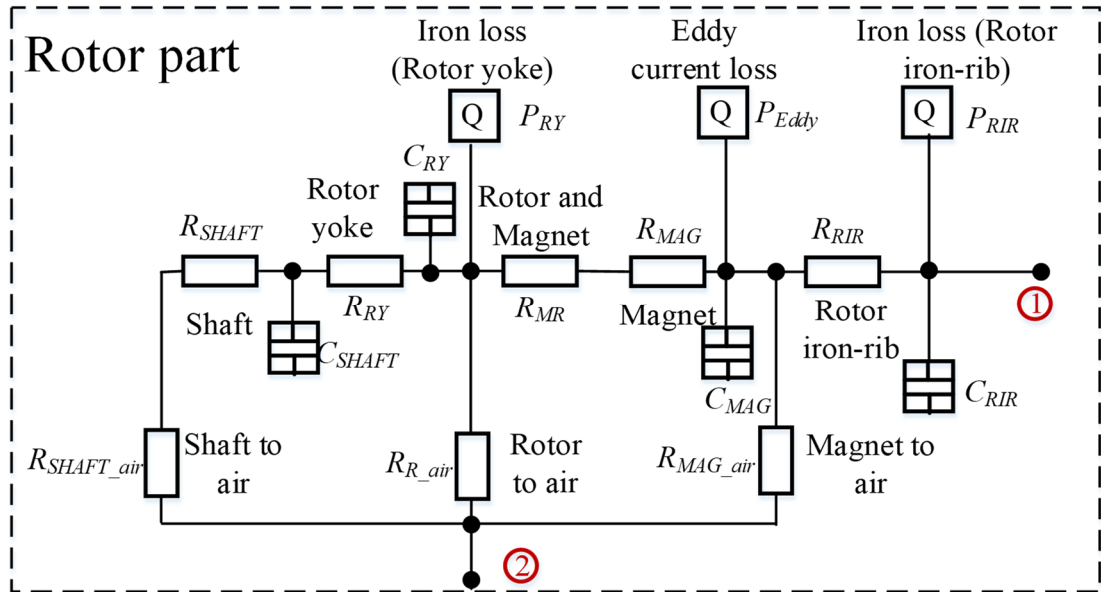


Fig. 4-4. LP thermal model of the rotor part.

$$R_{SHAFT} = \frac{L_A}{4\pi k_{shaft} R_{shaft}^2} + \frac{1}{\pi k_{shaft} L_A} \quad (4-1)$$

$$R_{RY} = \frac{\ln[(R_{ry} - l_{b1}) / R_{shaft}]}{2\pi k_{rotor} L_A} \quad (4-2)$$

$$R_{MR} = \frac{t_{mr}}{4pk_{mr} L_A (l_{mw1} + l_{mw2} + l_{mw3})} \quad (4-3)$$

$$R_{MAG} = \frac{1}{4pk_{mag} L_A} \left(\frac{l_{mh1}}{l_{mw1}} + \frac{l_{mh2}}{l_{mw2}} + \frac{l_{mh3}}{l_{mw3}} \right) \quad (4-4)$$

$$R_{RIR} = \frac{R_{rir}}{8pk_{rotor} L_A l_{mw2}} + \frac{l_{bridge}}{2\pi k_{rotor} L_A (R_r - l_{bridge})} \quad (4-5)$$

$$C_{SHAFT} = \pi R_{shaft}^2 L_A \rho_{shaft} c_{shaft} \quad (4-6)$$

$$C_{RY} = \pi [(R_{ry} - l_{b1})^2 - R_{shaft}^2] L_A \rho_{rotor} c_{rotor} \quad (4-7)$$

$$C_{MAG} = 4p[l_{mh1}l_{mw1} + l_{mh2}l_{mw2} + l_{mh3}l_{mw3}] L_A \rho_{mag} c_{mag} \quad (4-8)$$

$$C_{RIR} = [2\pi(R_r - l_{bridge})l_{bridge} + 8pR_{rir}l_{mw2}] L_A \rho_{rotor} c_{rotor} \quad (4-9)$$

where L_A is the axial length of the rotor and active winding; k_{shaft} , c_{shaft} and ρ_{shaft} are the thermal conductivity, specific heat capacity and mass density of the shaft; k_{rotor} , c_{rotor} and ρ_{rotor} are the thermal conductivity, specific heat capacity and mass density of the rotor core; k_{mag} , c_{mag} and ρ_{mag} are the thermal conductivity, specific heat capacity and mass density of

the magnet; k_{mr} is the thermal conductivity of the interface between the magnet and rotor. All the other dimensional parameters are illustrated in Fig. 4-3.

Afterwards, Fig. 4-5 shows the schematic of a half slot and tooth with key dimensions indicated, while Fig. 4-6 shows the LP thermal model of the stator part. It can be seen that the thermal resistance of the winding is divided into the active parts R_{C1} , R_{C2} and the end-winding part R_{C3} . Part of the heat in the winding is transferred to the stator tooth via R_{C1} and slot liner R_{S1} , and to the stator yoke via R_{C2} and slot liner R_{S2} . The remaining part of the heat in the winding is transferred through the end winding R_{C3} to the housing directly. The heat in the stator core mainly dissipates radially through the tooth parts R_{ST1} , R_{ST2} , and the yoke part R_{SY} to the housing via the contact thermal resistance R_{SH} between the stator and housing. Moreover, the inner bore of the stator is in contact with the airgap and the heat transfer between the slot winding and the airgap is represented by the thermal resistance R_{C_air} which is evaluated in Motor-CAD. All the other thermal resistances and capacitances can be derived using the governing principle of the heat conduction.

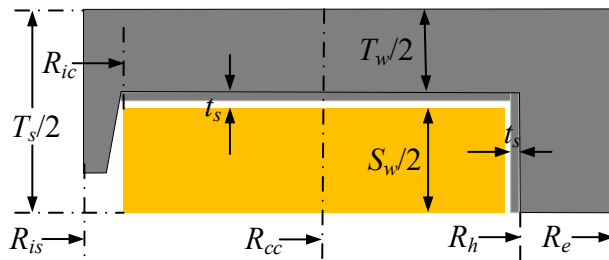


Fig. 4-5. The schematic of a half slot and tooth.

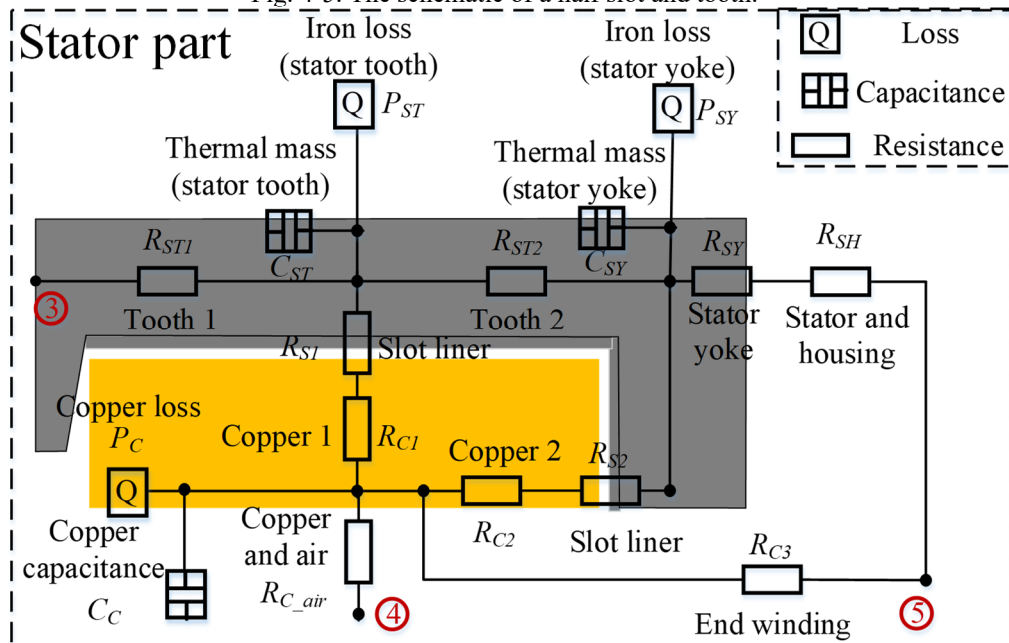


Fig. 4-6. LP thermal model of the stator part.

It is well known that the winding region is of great thermal significance and has to be analysed with care because of high copper loss and great heat intensity. The winding usually consists of conductors, wire insulations and impregnations, so the equivalent thermal conductivity based on analytical homogenization [112] [113] is employed. It is worth noting that the axial thermal conductivity of windings is commonly far larger than the cross-sectional thermal conductivity.

As the volume of the wire insulation is much smaller than that of the impregnation, it can be assumed that the winding only consists of two materials which is copper and Stycast 2676FT in this machine. Thus, the Hashin and Shtrickman approximation [112] can be used to estimate the radial/circumferential equivalent thermal conductivity $k_{rad/cir}$ in (4-10):

$$k_{rad/cir} = k_p \frac{(1+v_c)k_c + (1-v_c)k_p}{(1-v_c)k_c + (1+v_c)k_p} \quad (4-10)$$

where k_c is the copper thermal conductivity; k_p is the impregnation thermal conductivity and v_c is the copper slot fill factor.

The axial equivalent thermal conductivity k_{axial} is simply calculated from the parallel model [18] for the two materials and is given by:

$$k_{axial} = v_c k_c + (1-v_c)k_p \quad (4-11)$$

The equivalent conductivities in (4-10) and (4-11) for multi-strand windings with impregnation have been validated by experiments reported in [113] and [114].

The equivalent mass density ρ_e and equivalent specific heat capacity c_e of the winding also combines the effect of conductors and impregnations as given by [113]:

$$\rho_e = v_c \rho_c + (1-v_c)\rho_p \quad (4-12)$$

$$c_e = \frac{v_c \rho_c c_c + (1-v_c)\rho_p c_p}{\rho_e} \quad (4-13)$$

where c_c and ρ_c are the specific heat capacity and mass density of the copper, respectively; c_p and ρ_p are the specific heat capacity and mass density of the impregnation, respectively.

Based on the foregoing discussions, the thermal resistances and capacitances are given in (4-14) to (4-22) and in (4-23) to (4-25), respectively.

$$R_{C1} = \frac{S_w}{8N_s k_{rad/cir} L_A (R_h - R_{ic})} \quad (4-14)$$

$$R_{C2} = \frac{R_h - R_{cc}}{N_s k_{rad/cir} L_A S_w} \quad (4-15)$$

$$R_{C3} = \frac{L_A + L_{edw}}{8N_s k_{axial} S_w (R_h - R_{ic})} + \frac{\ln(R_e / R_{cc})}{4\pi k_{rad/cir} L_{edw}} \quad (4-16)$$

$$R_{S1} = \frac{t_s}{2N_s k_r L_A (R_h - R_{is})} \quad (4-17)$$

$$R_{S2} = \frac{t_s}{N_s k_r L_A S_w} \quad (4-18)$$

$$R_{ST1} = \frac{R_{cc} - R_{is}}{N_s k_{stator} L_A T_w} \quad (4-19)$$

$$R_{ST2} = \frac{R_h - R_{cc}}{N_s k_{stator} L_A T_w} \quad (4-20)$$

$$R_{SY} = \frac{\ln(R_e / R_h)}{2\pi k_{stator} L_A} \quad (4-21)$$

$$R_{SH} = \frac{t_{sh}}{2\pi k_{sh} L_A R_e} \quad (4-22)$$

where L_{edw} is the length of the end winding of a quarter turn; k_{stator} , k_r and k_{sh} are the thermal conductivities of the stator core, slot liner and interface between the stator and housing, respectively; N_s is the slot number; t_{sh} is the contact thickness between the stator and housing. All the other dimensional parameters are illustrated in Fig. 4-5. The stator iron loss is separated into the loss in tooth region, P_{ST} , and the loss in yoke, P_{SY} , while the stator core capacitance is similarly separated into C_{ST} and C_{SY} , which are inputted to the stator tooth and yoke nodes, respectively. Under healthy condition, the winding temperature is represented by that in one node to which the copper loss P_C and winding thermal capacitance C_C are connected. The thermal capacitances are given in (4-23) to (4-25).

$$C_{ST} = N_s(R_h - R_{is})L_A T_w \rho_{stator} c_{stator} \quad (4-23)$$

$$C_{SY} = 2\pi(R_e^2 - R_h^2)L_A \rho_{stator} c_{stator} \quad (4-24)$$

$$C_C = [N_s(R_h - R_{ic})L_A S_w + 2\pi(R_e^2 - R_{is}^2)L_{edw}] \rho_e c_e \quad (4-25)$$

where c_{stator} and ρ_{stator} are the heat capacity and mass density of the stator core, respectively.

Fig. 4-7 shows the LP thermal model of the whole motor, in which the rotor part and stator part represented by their block names are connected by the thermal resistance of the airgap R_{airgap} and the air in the rotor end region and the stator housing. Internal convection resistance R_{air_H} representing the thermal resistance between the shaft, magnet, rotor, end-winding to the housing via air is estimated by Motor-CAD.

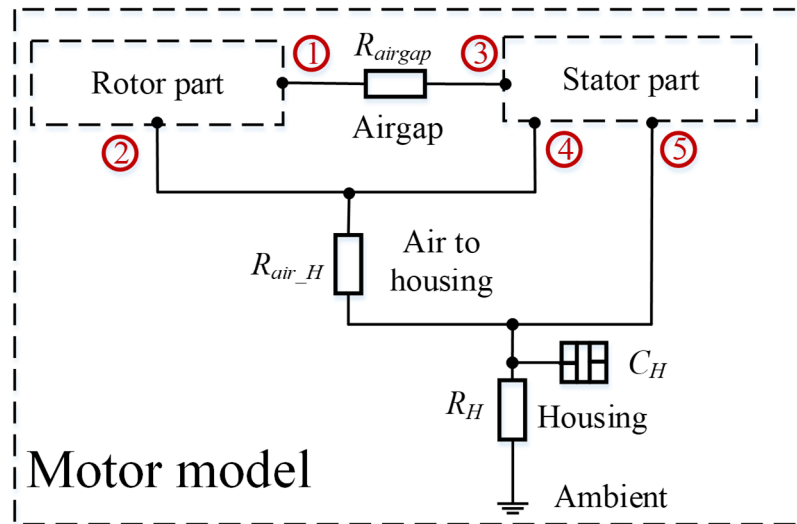


Fig. 4-7. LP thermal model of the whole motor.

Because most losses generated in the rotor are transferred to the stator by the airgap, the convective resistance R_{airgap} between the rotor and the stator via the air-gap is important. The convective resistance R_{airgap} can be evaluated from Motor-CAD or by the empirical equations given in [104] [107].

Because of the rotor rotation, the flow in the airgap is forced to be tangential flow known as Taylor vortex flow. In order to describe this phenomenon, the Taylor number T_a given in (4-26) should be evaluated,

$$T_a = \frac{\rho_a^2 \omega_r^2 \gamma_m \delta^3}{\mu_v^2} \quad (4-26)$$

where μ_v is the air dynamic viscosity; ρ_a is the air density; ω_r is the angular velocity of rotor; γ_m is the radius in the middle of the air-gap and δ is the air-gap length in the radial direction.

The Nusselt number N_u which depends on the Taylor number is shown in (4-27),

$$\begin{cases} N_u = 2 & (T_a < 1700) \\ N_u = 0.128T_a^{0.367} & (1700 < T_a < 10^4) \\ N_u = 0.409T_a^{0.241} & (10^4 < T_a < 10^7) \end{cases} \quad (4-27)$$

The convection heat transfer coefficient of the airgap h_{airgap} can be predicted by the following equation,

$$h_{airgap} = \frac{N_u k_{air}}{\delta} \quad (4-28)$$

where k_{air} is the thermal conductivity of the air. The heat transfer coefficient of stator-to-airgap and rotor-to-airgap is the same. Therefore, the convective resistance R_{airgap} can be obtained by,

$$R_{airgap} = \frac{1}{\pi h_{airgap} \gamma_m L_A} \quad (4-29)$$

Additionally, as the ambient temperature is only a few degrees Celsius different with the temperature of the cooling oil in the housing oil jacket, all the heat of the motor is assumed to transfer to the cooling oil. The housing thermal resistance R_H and the capacitance C_H are evaluated in Motor-CAD. R_H combines the housing conduction resistance and the convection resistance of the spiral housing cooling jacket. Further, the ambient temperature is set as the oil temperature.

4.3.2 LP Thermal Model under Short-Circuit Fault Conditions

It should be noted that the above LP thermal model cannot predict asymmetric temperature distributions in the circumferential direction which usually appear under fault conditions. Therefore, this section is focused on establishing a LP thermal model which is applicable to assessing asymmetric temperature distribution under fault conditions.

Since an inter-turn SC with the least number of short-circuited turns, i.e., one turn, leads to the highest SC current and most rapid temperature rise in the faulted region, the LP thermal model focuses on the prediction of the thermal behaviours of this machine under one turn SC and one turn SC with 3-phase terminal SC as a mitigation measure. This knowledge is important to ensure fault tolerant ability of the machine in the worst case because experimental measurements of the hotspot temperature in such conditions are not always possible.

Without loss of generality, it is assumed that the worst case one turn SC occurs in phase B and terminal SC will be applied to 3-phase set ABC when the fault is detected. As introduced in Chapter 2 section 2.4.2, when the SC turn is located at the two black quadrangles shown in Fig. 4-1 (b) of slots B2 and B4, the SC current and copper loss are the highest due to resultant MMF offset component resulting from mutual coupling between the two healthy 3-phase sets and the faulty 3-phase set. The subsequent analysis is focused on this worst case.

Compared to the transient LP thermal model under healthy condition, the rotor model and the schematic diagram of the transient LP thermal model of the 36-slot PMASynRM under fault conditions are the same as those shown in Fig. 4-4 and Fig. 4-7, respectively, while the stator LP model is quite different. Firstly, the thermal dissipation in the winding area must consider the radial, axial and circumferential directions. Additionally, the thermal dissipation in the stator core is not only in the radial direction but also in the circumferential direction via the stator teeth because it may have large effect under fault condition when the losses in slots are no longer symmetric. Because of the difference in loss distributions, the thermal model for a healthy slot and a fault slot must be considered separately.

Therefore, the LP thermal model of one healthy slot and tooth is first presented in Fig. 4-8. Similar to Fig. 4-6, part of heat in the winding is transferred to the stator tooth via R_{c1} and slot liner R_{s1} , part is transferred to the stator yoke via R_{c2} and slot liner R_{s2} , while the remaining part is transferred through the end winding R_{c3} to the housing directly. However, the heat in the stator core can not only be dissipated radially through the tooth part R_{st1} , R_{st2} , and the yoke part R_{sy} to housing via the contact thermal resistance R_{sh} between stator and housing, but also circumferentially through tooth part R_{st3} to the

adjacent tooth. Additionally, R_{c1} , R_{s1} , R_{st1} , R_{st2} , R_{sy} , R_{sh} , C_{st} , and C_{sy} which represent half slot and tooth can be obtained by multiplying R_{C1} , R_{S1} , R_{ST1} , R_{ST2} , R_{SY} , R_{SH} , C_{ST} , and C_{SY} calculated above in Fig. 4-6, respectively, by $2N_s$. Further, R_{c2} , R_{c3} , R_{s2} , and C_c which represent one slot and tooth can be obtained by multiplying R_{C2} , R_{C3} , R_{S2} , and C_C calculated above, respectively, by N_s . These resistances and capacitances are given in (4-30) to (4-41). The extra thermal resistance R_{st3} can be obtained by (4-42).

$$R_{c1} = 2N_s R_{C1} \quad (4-30)$$

$$R_{c2} = N_s R_{C2} \quad (4-31)$$

$$R_{c3} = N_s R_{C3} \quad (4-32)$$

$$R_{s1} = 2N_s R_{S1} \quad (4-33)$$

$$R_{s2} = N_s R_{S2} \quad (4-34)$$

$$R_{st1} = 2N_s R_{ST1} \quad (4-35)$$

$$R_{st2} = 2N_s R_{ST2} \quad (4-36)$$

$$R_{sy} = 2N_s R_{SY} \quad (4-37)$$

$$R_{sh} = 2N_s R_{SH} \quad (4-38)$$

$$C_{st} = 2N_s C_{ST} \quad (4-39)$$

$$C_{sy} = 2N_s C_{SY} \quad (4-40)$$

$$C_c = N_s C_C \quad (4-41)$$

$$R_{st3} = \frac{T_w}{4k_{stator} L_A (R_h - R_{is})} \quad (4-42)$$

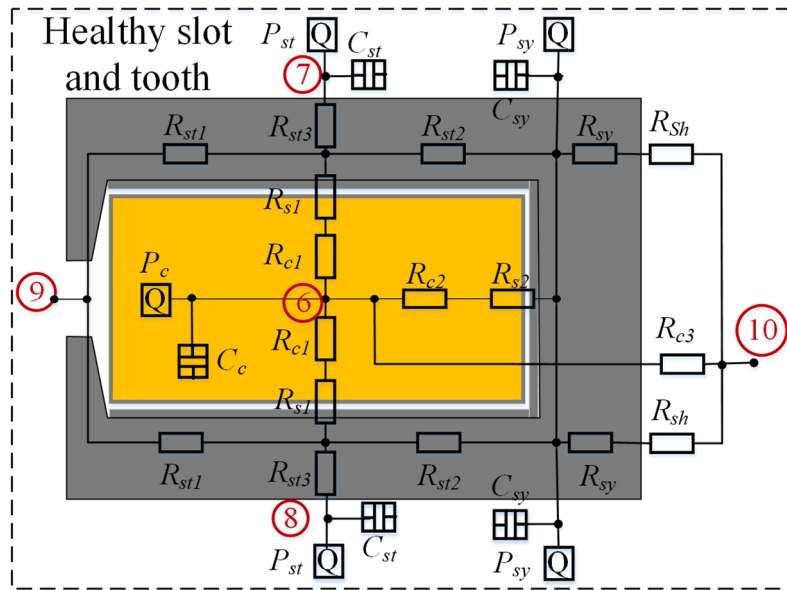


Fig. 4-8. LP thermal model of the healthy slot and tooth.

Fig. 4-9 shows the LP thermal model of the fault slot and tooth containing an inter-turn short-circuit fault close to the slot opening, such as B2 slot as shown in Fig. 4-1 (b). Compared with Fig. 4-8, the winding is divided into healthy part and fault part.

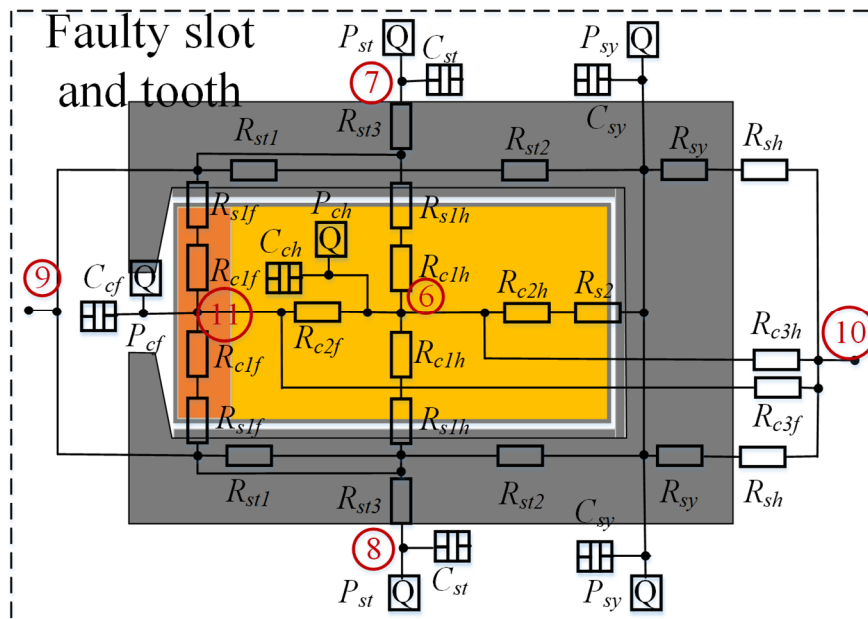


Fig. 4-9. LP thermal model of the fault slot and tooth with inter-turn SC.

Thus, the thermal resistances R_{c1} , R_{c2} , R_{c3} and R_{sl} , and the thermal capacitance C_c are also divided into healthy parts (R_{c1h} , R_{c2h} , R_{c3h} , R_{slh} , and C_{ch}) and fault parts (R_{c1f} , R_{c2f} , R_{c3f} , R_{slf} , and C_{cf}). Their values are given in (4-42) to (4-51). The fault ratio μ is previously defined in Chapter 2 section 2.3.2 as the ratio of the number of SC turns (N_{sc}) to the total

number of turns in one phase (N_i). As observed, the values in healthy and fault parts of R_{c1} , R_{c3} , R_{s1} and C_c are determined by the associated number of turns.

$$R_{c1h} = \frac{R_{c1}}{1-\mu} \quad (4-42)$$

$$R_{c1f} = \frac{R_{c1}}{\mu} \quad (4-43)$$

$$R_{c2h} = R_{c2} \quad (4-44)$$

$$R_{c2f} = \frac{R_{cc} - R_{ic}}{k_{rad/cir} L_A S_w} \quad (4-45)$$

$$R_{c3h} = \frac{R_{c3}}{1-\mu} \quad (4-46)$$

$$R_{c3f} = \frac{R_{c3}}{\mu} \quad (4-47)$$

$$R_{s1h} = \frac{R_{s1}}{1-\mu} \quad (4-48)$$

$$R_{s1f} = \frac{R_{s1}}{\mu} \quad (4-49)$$

$$C_{ch} = \frac{C_c}{1-\mu} \quad (4-50)$$

$$C_{cf} = \frac{C_c}{\mu} \quad (4-51)$$

Likewise, the copper losses of the SC turn P_{cf} and the healthy part P_{ch} are inputted to the two associated nodes. For the fault slot and tooth containing an inter-turn SC fault in the middle of the slot, such as B4 slot shown in Fig. 4-1 (b), the LP thermal model is similar to Fig. 4-9 except changing the positions of healthy part and fault part.

The two thermal networks in Fig. 4-8 and Fig. 4-9 form the building blocks for the LP thermal model of the machine with fault turn in slots B2 and B4. Fig. 4-10 shows the LP thermal model of the stator containing all the slots, in which the building block for each slot is identified by the slot name with the numbered nodes for connection to other parts of the stator. Node 7 in each stator slot model is connected node 8 of the adjacent

slot model for the thermal dissipation in the circumferential direction. The inner bore of the stator is in contact with the airgap and the heat transfer between the slot winding and the airgap is represented by the thermal resistance R_{c_air} for healthy slots and by R_{c_airh} and R_{c_airf} for the fault slots.

Additionally, the LP thermal models of the rotor part and the schematic connections between the rotor, stator and housing under fault conditions are the same as those under healthy condition which are illustrated in Fig. 4-4 and Fig. 4-7, respectively.

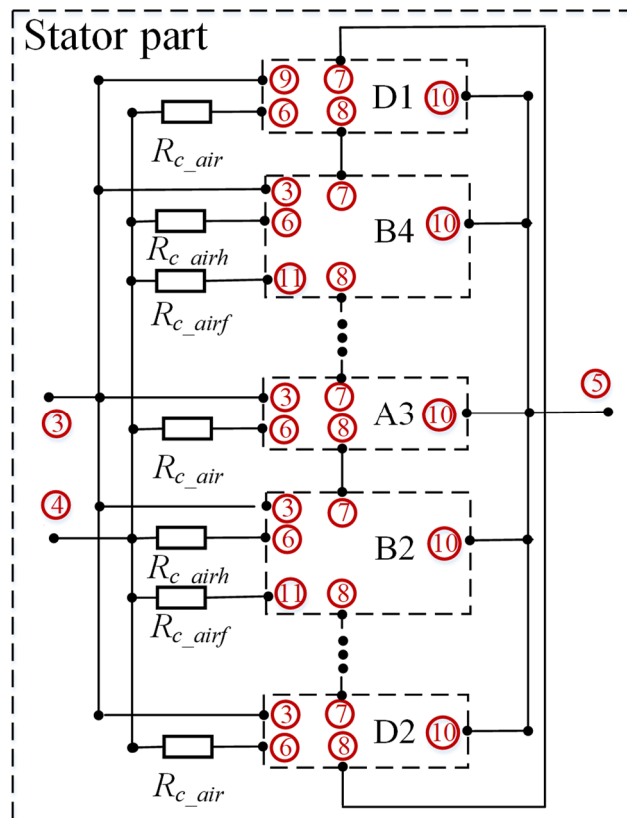


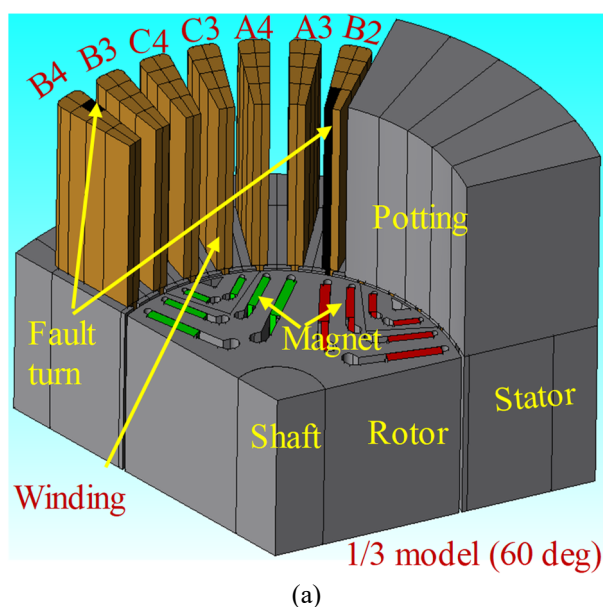
Fig. 4-10. LP thermal model of the stator part.

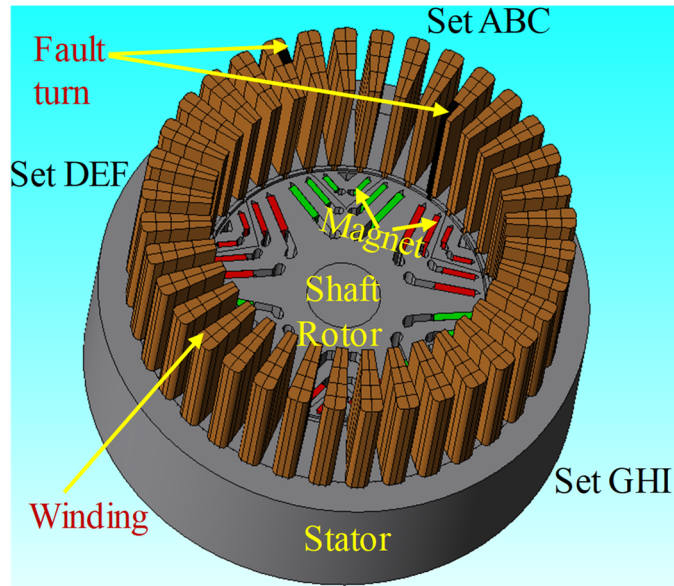
4.4 3D Thermal Model

The 3D thermal model for numerical simulation by finite element analysis is shown in Fig. 4-11 where different components are indicated. Fig. 4-11 (a) shows the 1/3 3D model encompassing 12 slots and half of the machine axial length, while Fig. 4-11 (b) shows the full 3D thermal model containing 36 slots and half the axial length. The full 3D thermal model is more accurate than the 1/3 model for thermal analysis when the heating effect and temperature distribution in the three 3-phase winding sets are quite asymmetric, such as those under one turn SC and one turn SC with 3-phase terminal SC.

By contrast, the 1/3 model may be adopted when the machine is healthy or when the heating effect of the fault is localized and is less significant compared to the total of the machine under a given load condition, or over a short duration in which the heat is more likely to be stored in the materials than dissipated to other regions. It has advantages of smaller size and computationally less demanding with reasonable accuracy.

From Fig. 4-1, the end winding layout is quite complex to represent in the 3D model. It is quite time consuming and computationally expensive to model each individual turn. Further, because the copper loss and temperature distribution in the healthy and faulted turns are different, the end winding part cannot be simplified as a homogeneous ring. Thus, the end winding is simplified in the 3D thermal model as straight winding segments with the same equivalent length as those in the prototype machine as in Fig. 4-11. The windings are potted and composed of conductor and Stycast 2676FT. Different with the real world that the heat is directly transferred via end winding of the same turn, the thermal coupling between the end winding of the turn is transferred by covered potting composed of pure Stycast 2676FT as in Fig. 4-11 (a). This may produce slight inaccuracy of the temperature predictions of the end winding. However, this model will be calibrated and validated by test results. The schematic diagram of heat equivalent circuit shown in Fig. 4-12 explains the heat transfer network of the 3D thermal model of this motor in JMAG [115].





(b)
Fig. 4-11. 3D thermal model. (a) 1/3 model. (b) Whole model.

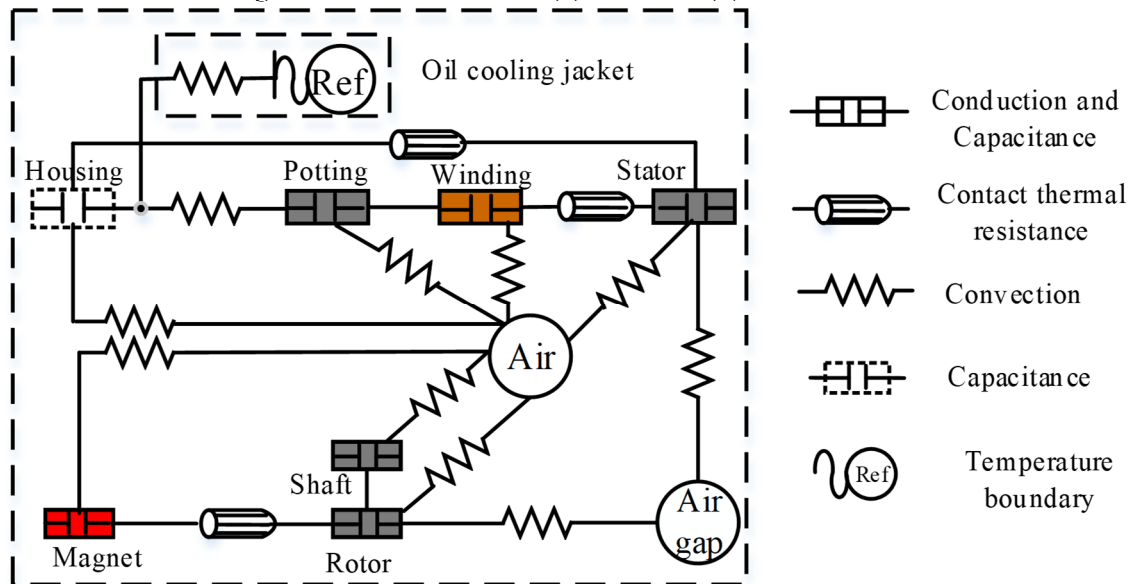


Fig. 4-12. Schematic diagram of heat equivalent circuit of this motor.

As observed from Fig. 4-12, the radiation heat transfer is negligible in the study because of the small temperature difference between the machine surfaces and ambient air. The heat conductions and thermal mass accounted automatically in the 3D FE thermal model when the thermal conductivities and heat capacities of various components are appropriately set, such as potting, winding, stator core, rotor core, magnets and shaft, etc. The equivalent radial/circumferential and axial conductivities in (4-10) and (4-11), and the equivalent heat capacity in (4-13) of the winding are also used in the 3D model.

The slot liners and thermal contact resistances between two constituent regions, such as the magnet and rotor core, and the stator core and housing, are modelled in the 3D thermal model by setting appropriate gap thickness and the thermal conductivity of the interface materials.

All the internal convection thermal resistances between the various parts and air have been obtained in the LP thermal model. Since convection thermal resistance, R_{conv} , is related to heat convection coefficient h_{conv} and surface area A_{conv} by [90]:

$$R_{conv} = \frac{1}{k_{conv} A_{conv}} \quad (4-52)$$

The heat convection coefficient of a surface can be calculated by (4-52) when its area is known in the 3D model. These values are used for setting up convection boundary conditions in the 3D thermal model [107].

The oil cooling jacket can be represented as a temperature boundary with a thermal convection resistance between the stator cooling channels and cooling oil in the 3D thermal model [116] shown in Fig. 4-12.

4.5 Thermal Performance Comparisons between LP and 3D Thermal Models

The LP model in section 4.3.1 and the 1/3 3D thermal model as shown in Fig. 4-11 (a) are compared with Motor-CAD under healthy condition for predicting the steady-state and transient temperatures when the machine operates at 4000 rpm with the rated current of 120A in all phases. The inlet temperature and flowrate of coolant oil are assumed to be 50°C and at 7 litre/min.

Additionally, as the rated speed and electric frequency are not very high, the effect of the skin effect and proximity loss on the copper loss are negligible. However, the winding resistance changing with temperature is considered in the copper loss calculation.

$$R_s = R_{s0} [1 + \alpha_T (T_w - T_0)] \quad (4-53)$$

where R_s and R_{s0} are the phase resistances at winding temperature T_w and T_0 , respectively. α_T (0.393%/°C) is the temperature coefficient for copper.

Therefore, the copper loss variation with winding temperature is accounted through iteration until convergence with the predicted temperature. The temperature distributions predicted by the 3D model and Motor-CAD are illustrated in Fig. 4-13 and Fig. 4-14, respectively. Moreover, the predicted steady-state and transient temperature results are compared in Table 4-1 and Fig. 4-15, respectively. As observed from Fig. 4-13, Fig. 4-14 and Table 4-1, the predicted temperatures of different components by the three methods are quite close. Additionally, the hotspot temperatures and their locations at the end winding part predicted by the 3D model and Motor-CAD match quite well. However, the LP thermal model can only predict average temperatures in the winding region. Moreover, the predicted transient average temperatures in the magnet region by the three models agree well and the similar agreement is seen for the transient average temperatures in the winding region.

Therefore, the comparisons show that the LP thermal model and 3D thermal model are correctly performed.

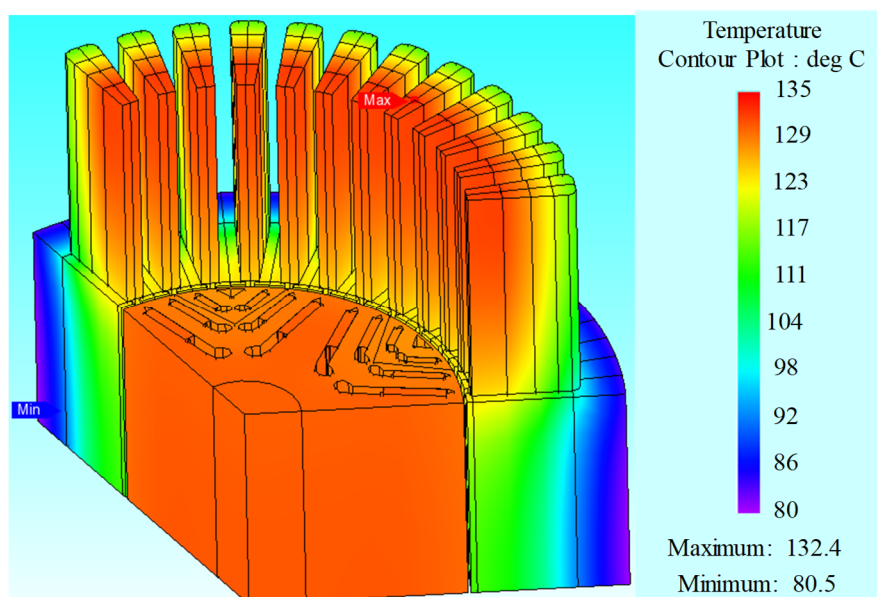


Fig. 4-13. Temperature distribution of 3D thermal model under healthy condition.

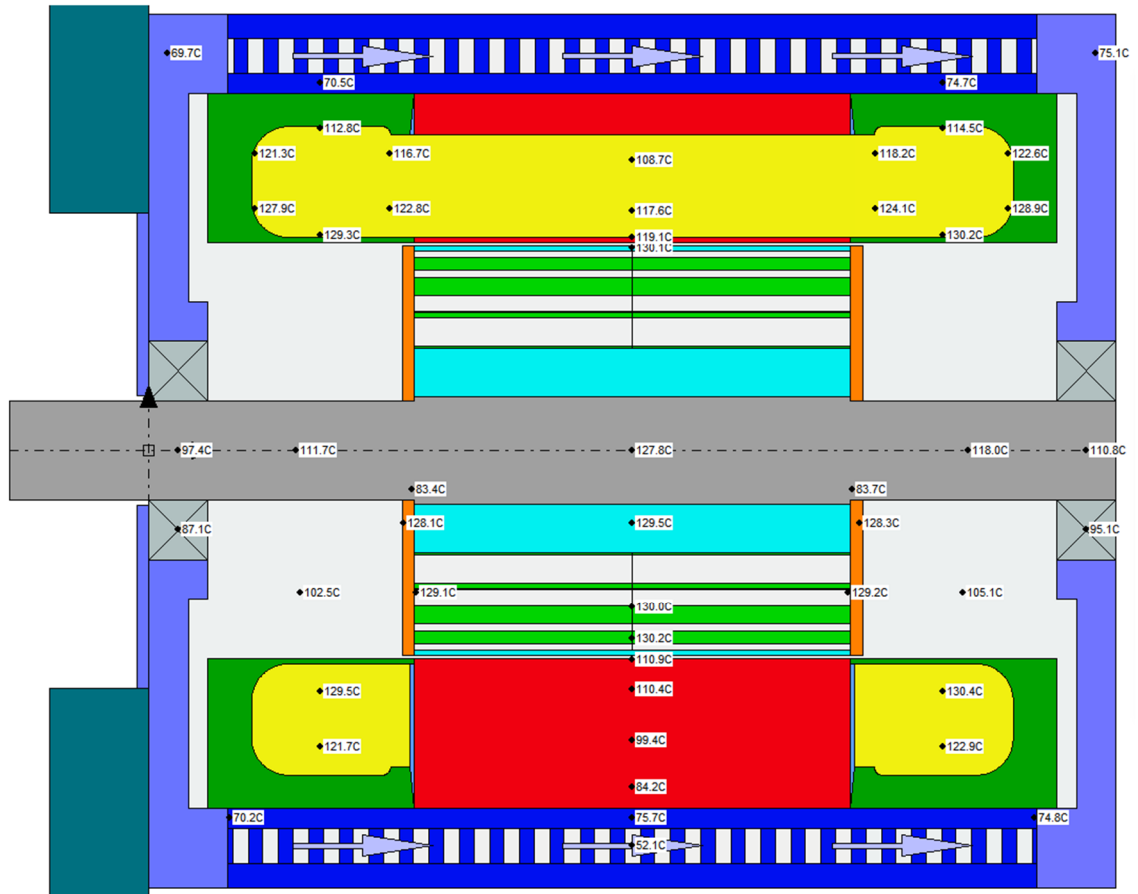
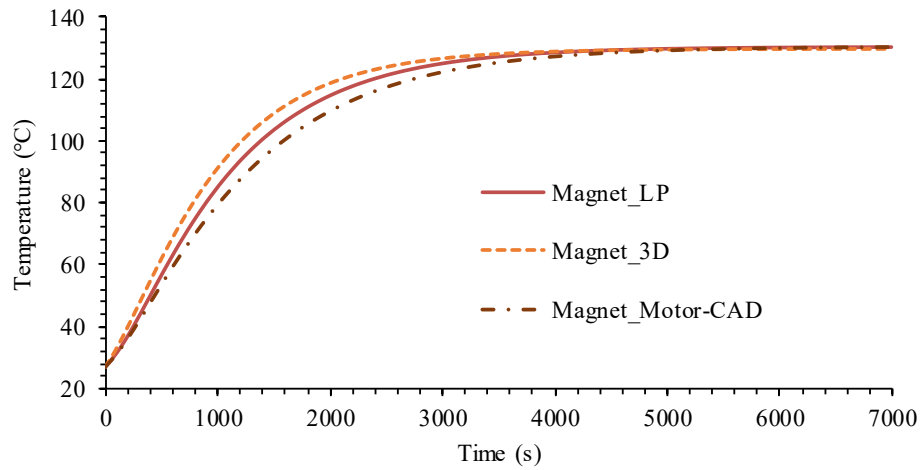


Fig. 4-14. Temperature distribution of Motor-CAD under healthy condition.

Table 4-1 Comparison of temperatures under healthy condition predicted by LP model, 3D model and Motor-CAD.

Component	LP thermal (°C)	3D thermal (°C)	Motor-CAD (°C)
Rotor yoke	130	129	129
Magnet	130	130	130
Rotor iron-rib	129	131	130
Stator	101	104	98
Winding	118	118	120
Hotspot	--	132	134



(a)

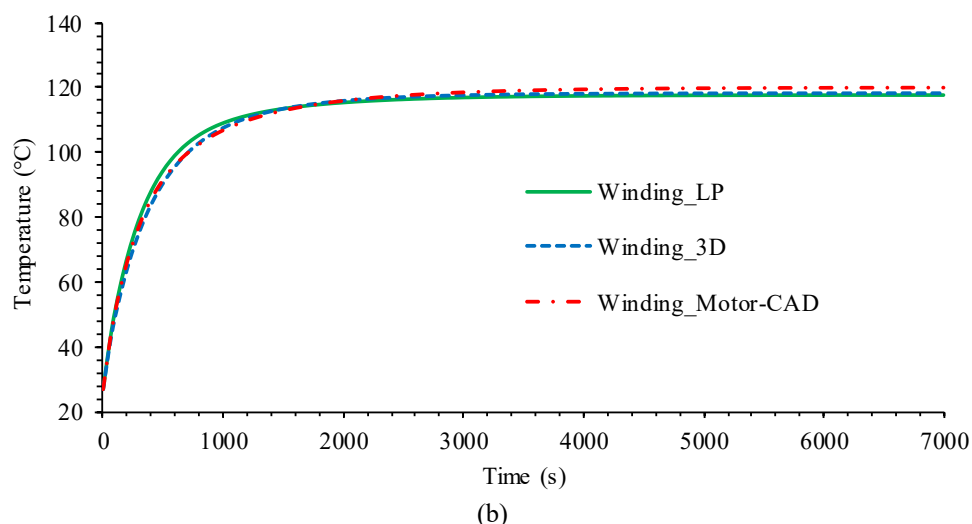


Fig. 4-15. Transient average temperatures between LP model, 3D model and Motor-CAD under healthy condition. (a) Magnet. (b) Winding.

As the Motor-CAD cannot predict asymmetric temperature distributions under fault conditions, only the LP model in section 4.3.2 and the full 3D thermal model as shown in Fig. 4-11 (b) are used to predict the thermal behaviour of the PMASynRM under one turn SC and one turn SC with 3-phase terminal SC conditions when the machine operates at 4000 rpm with the rated current of 120A excited in the health phases. The inlet temperature and flowrate of the coolant oil are also assumed to be 50°C and at 7 litre/min.

Both of these two models contain 36 slots. The steady-state average temperatures of different parts, such as the rotor, magnet, stator tooth, stator yoke, healthy winding, the healthy part of slot B2 (B2_h) and the healthy part of slot B4 (B4_h) as well as the hotspot temperatures of the SC turn in slot B2 (B2 hotspot) and slot B4 (B4 hotspot) are extracted and compared. The comparisons of temperatures under one turn SC and one turn SC with 3-phase terminal SC predicted by the two models are given in Table 4-2 and Table 4-3, respectively.

Table 4-2 Comparison of temperatures under one turn SC fault predicted by LP and 3D models.

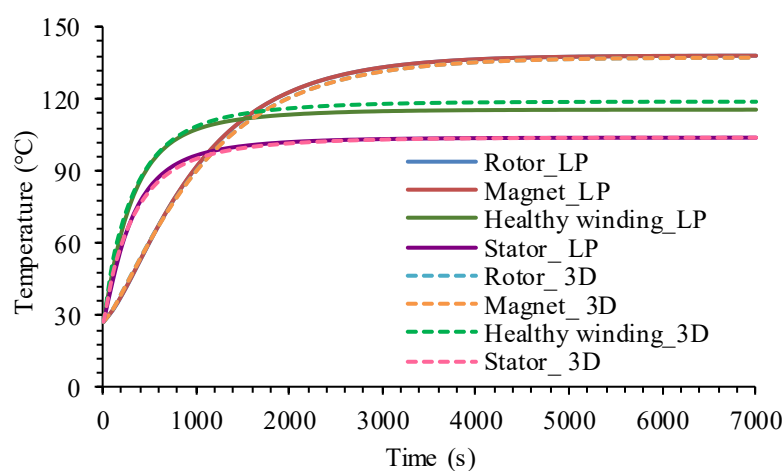
Component	LP thermal (°C)	3D thermal (°C)	Difference (°C)
Rotor	138	137	-1
Magnet	138	138	0
Stator tooth	113	119	6
Stator yoke	95	89	-6
Healthy winding	113	117	3
B2_h	190	199	9
B2 hotspot	373	381	8
B4_h	193	204	11
B4 hotspot	303	302	-1

Table 4-3 Comparison of temperatures under one turn SC fault with 3-phase terminal SC for fault mitigation predicted by LP and 3D models.

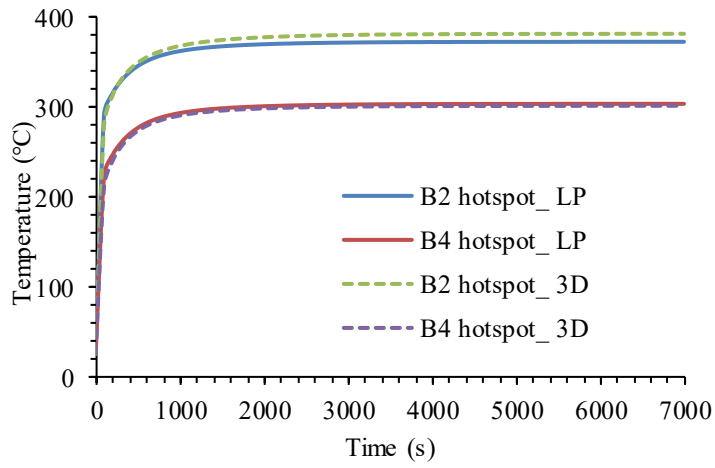
Component	LP thermal (°C)	3D thermal (°C)	Difference (°C)
Rotor	113	114	1
Magnet	114	114	0
Stator tooth	91	94	3
Stator yoke	80	76	-4
Healthy winding	90	91	1
B2_h	101	96	-5
B2 hotspot	121	122	1
B4_h	101	103	2
B4 hotspot	113	116	3

It can be seen that the differences predicted by the LP and 3D thermal models under one turn SC with 3-phase terminal SC are smaller than those under one turn SC. However, all the temperature differences predicted by the two models are within $\pm 11^{\circ}\text{C}$ while the differences of the predicted steady-state hotspot temperatures are less than 8°C . It is seen that the LP thermal model is sufficiently accurate to predict temperature distribution under fault conditions, especially to predict the hotspot temperature of the fault turn.

The transient temperatures of the rotor, magnet, stator, healthy winding, B2 hotspot and B4 hotspot predicted by the LP and 3D thermal models under one turn SC fault and one turn SC fault with 3-phase terminal SC applied for fault mitigation are compared in Fig. 4-16 and Fig. 4-17, respectively. It can be concluded that the transient and steady-state results predicted by the two models match well.

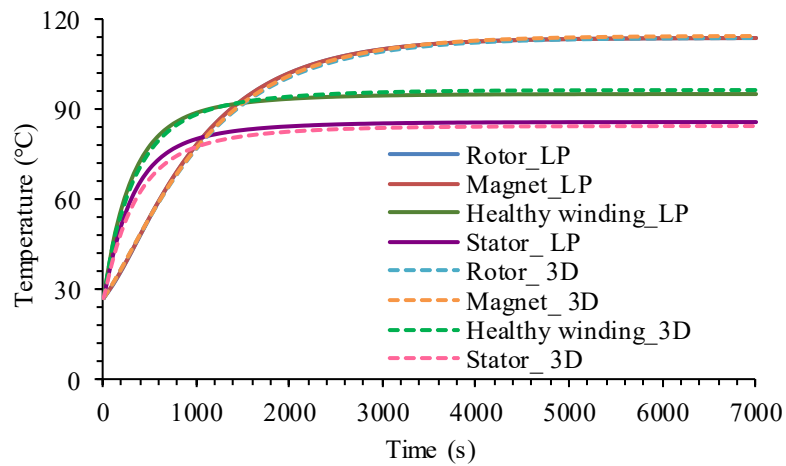


(a)

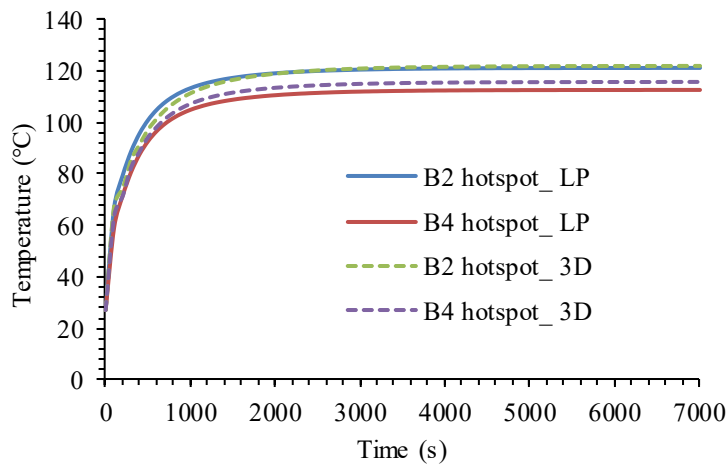


(b)

Fig. 4-16. Transient temperatures between LP and 3D models under one turn SC fault. (a). Average temperatures. (b). Hotspot temperatures.



(a)



(b)

Fig. 4-17. Transient temperatures between LP and 3D models under one turn SC fault with 3-phase terminal SC applied for fault mitigation. (a). Average temperatures. (b). Hotspot temperatures.

It can be seen that the hotspot temperature under one turn SC condition predicted by both models reaches $\sim 380^{\circ}\text{C}$. The machine will be completely damaged if the fault is not dealt with in a timely manner. In contrast, by application of terminal SC of the fault 3-phase through inverter once the fault is detected, the hotspot temperature is managed below 125°C . The machine drive can continue to operate with the two remaining healthy 3-phase sets albeit the torque capability is reduced to $\sim 2/3$ under the working condition.

The 3D thermal model needs 2Gb memory and 18 minutes to compute while the LP thermal model requires 25 times less memory and can be solved 12 times faster. The LP model shows good accuracy for predicting the transient and steady-state temperature distribution under fault conditions. However, because of the limited nodes in the LP model, the 3D FE model can provide more detailed temperature distribution with better accuracy and cope with more practical issues as will be discussed subsequently.

4.6 Experimental Validation of the Simulation of the PMASynRM

The triple redundant 3x3-phase PMASynRM has been built according to the design. The permanent magnet material is VACOMAX 225 HR, while the stator and rotor materials are 0.2mm Vacoflux 50 and Vacodur 50, respectively. The stator stack is skewed by 10 degrees which is one slot to reduce the slotting effect. Each turn of the winding consists of 17 strands of 0.8mm varnished Polyester C200 copper wire from PAR Ltd to reduce AC losses in the winding. Moreover, the Stycast 2762 with Catalyst 17 is adopted as the potting material for the winding.

The prototype PMASynRM is mounted on the test rig shown in Fig. 4-18. The machine is connected to the AVL dynamometer operated in speed control mode via couplings and inline torque transducer. The machine is driven by a DSP based three 3-phase inverters. A single turn tap is brought out from phase B winding to emulate one-turn short circuit via a controlled relay.



Fig. 4-18. The prototype on the test rig with oil cooling system.

The short-circuit currents under fault conditions predicted by the 2D EM model and temperatures predicted by the 3D thermal model will be compared with the test results to validate these two models, respectively, in this section.

4.6.1 Comparisons of Measured and 2D Predicted EM Performance

Firstly, the tests were performed to validate the losses adopted in the thermal models predicted by the 2D EM model. The loss of a machine is mainly contributed by iron loss and copper loss.

First, no-load loss was measured by rotating the rotor at various speeds while the stator windings are not excited. The no-load mechanical loss was estimated from the machine with similar dimensions and bearings. Therefore, the no-load iron loss was separated from the measured no-load loss and estimated no-load mechanical loss. By introducing a built factor of 1.2 for accounting the effect of core manufacture process and assembly, the predicted no-load iron load is reasonably close to the measured values as shown in [16]. Therefore, the same built factor is used to scale FE predicted iron losses used in the thermal model in various operating conditions with reasonable accuracy.

The copper loss is determined by the winding resistance and the square of current. Therefore, it is critically dependent on current, so the accuracy of predicted phase current and fault current is assessed under one turn SC and one turn SC with 3-phase terminal SC conditions. To measure the fault current, a single tap in phase B2 coil is brought out from

the winding by the thick cables as shown in Fig. 4-19 (a), while the fault emulation cables are connected to a high current relay shown in Fig. 4-19 (b) to control the inter-turn fault.

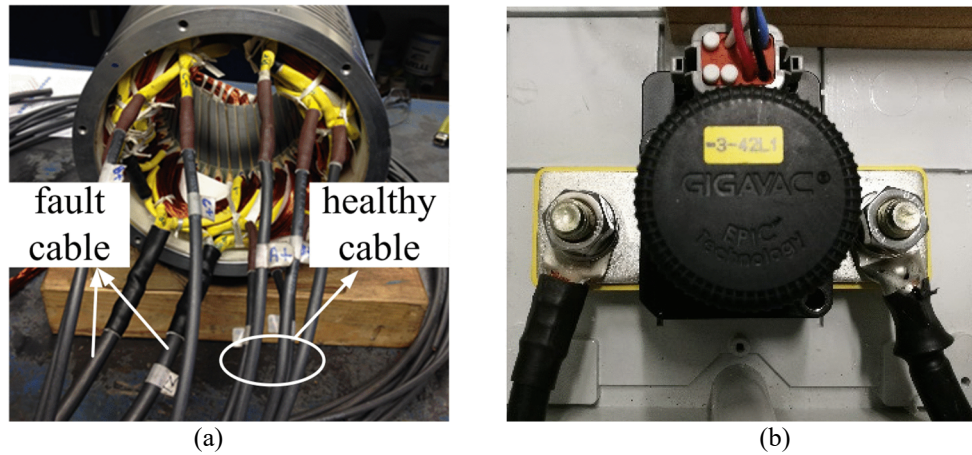


Fig. 4-19. Motor winding leads and relay for turn fault. (a) Leads. (b) Relay.

The terminal connections of each 3-phase set are illustrated in Fig. 4-20. It is clear in Fig. 4-20 (a) that two extra terminals for the SC turn B_f are added in phase B2 coil. Therefore, each phase resistance of 3-phase set ABC can be measured via the cable 'A+', 'B+', 'C+' and the neutral cable ' B_f ', respectively. However, only the line resistances of the other two 3-phase sets DEF and GHI can be measured via the terminals of each phase as in Fig. 4-20 (b) and (c). The measured resistances are listed in Table 4-4 at 20°C.

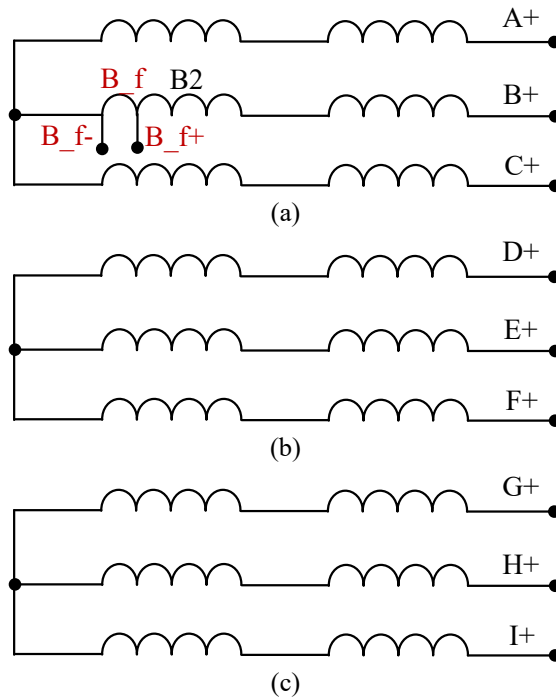


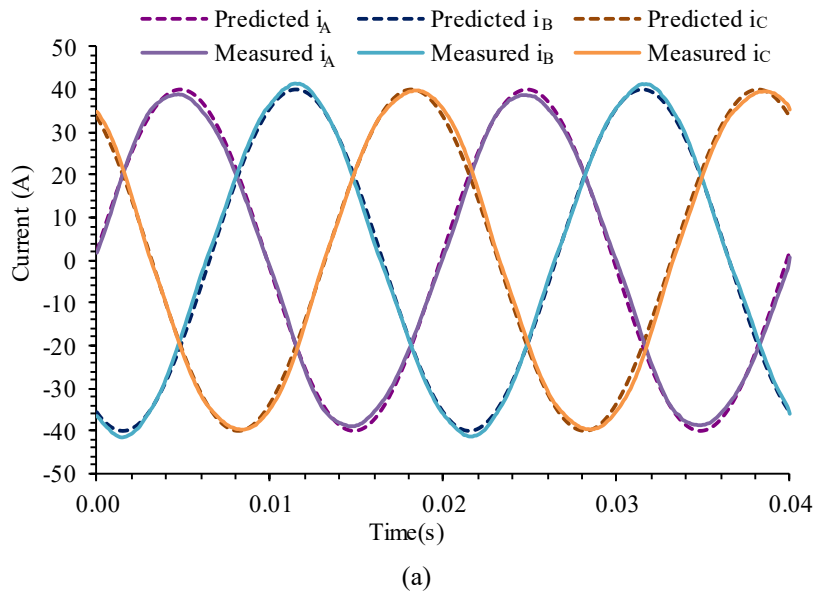
Fig. 4-20. The terminal connections of each 3-phase set. (a) Set ABC. (b) Set DEF. (c) Set GHI.

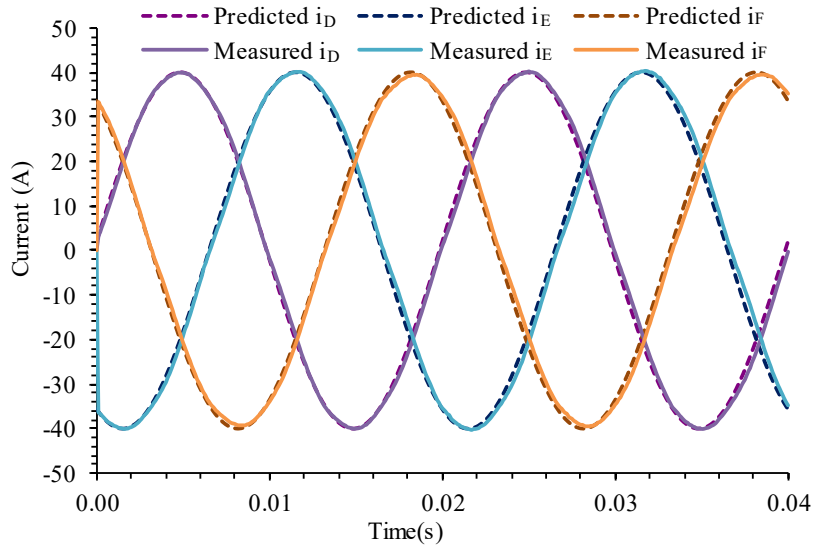
Table 4-4 Measured resistances.

Phase set	Set ABC			Set DEF			Set GHI			
	R_{Bf}	R_A	R_B	R_C	R_{DE}	R_{DF}	R_{EF}	R_{GH}	R_{GI}	R_{HI}
Measured resistance (mΩ)	2.4	20.8	21	20.8	40.6	40.6	40.7	40.7	40.5	40.6

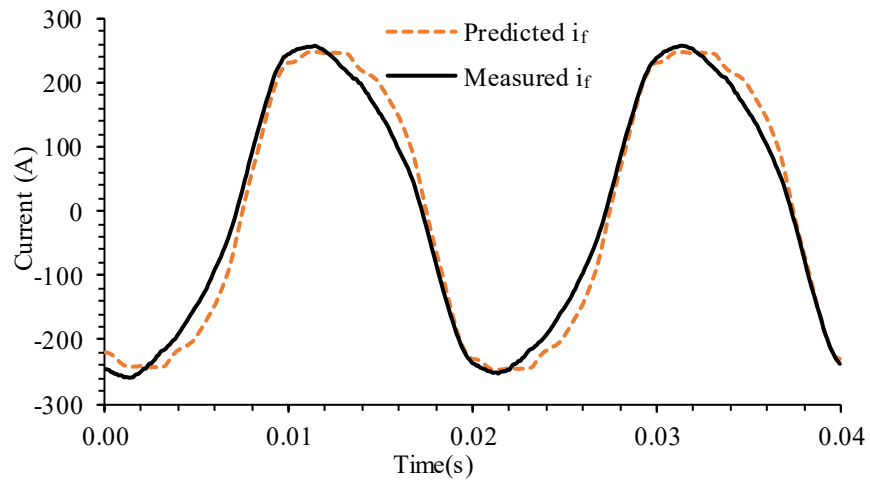
4.6.1.1 Inter-Turn Short Circuit without Terminal Short-Circuit Fault

In order to avoid any damage to the prototype, the one turn SC fault condition is operated at 1000rpm with 40A current excited in the healthy phase for MTPA operation for 0.2s to compare with the predictions by the 2D EM model. Fig. 4-21 (a) and (b) show the comparisons of predicted and measured phase currents in fault set ABC and in healthy set DEF when 40A current is excited in all phases, respectively. The phase currents of healthy set GHI are the same as those of set DEF and are not presented here. It can be observed from Fig. 4-21 (b) that the predicted phase currents of healthy set DEF match quite well with the measured results. However, the measured phase currents of fault set ABC are slightly distorted due to the mutual coupling between the fault turn and healthy turns of the set. This mutual coupling is not captured by the FE model with the ideal current sources shown in Fig. 4-21 (a). This results in the small difference between the predicted and the measured turn fault current waveforms as illustrated in Fig. 4-21 (c). However, the RMS value of the predicted turn fault current only differs from the measured value by 4.4%.





(b)



(c)

Fig. 4-21. Comparison of predicted and measured phase currents and turn fault current under one turn SC at 1000rpm and 40A current. (a) Phase currents in fault set ABC. (b) Phase currents in healthy set DEF. (c) Turn fault current.

The one turn SC fault condition is tested at 1000rpm with variation of load currents from 10A to 80A excited in all phases for 0.2s for MTPA operation. The predicted and measured variations of the RMS turn fault current with the load currents are compared in Fig. 4-22. As can be seen, the predicted and measured RMS fault currents are very close and both increases with load currents.

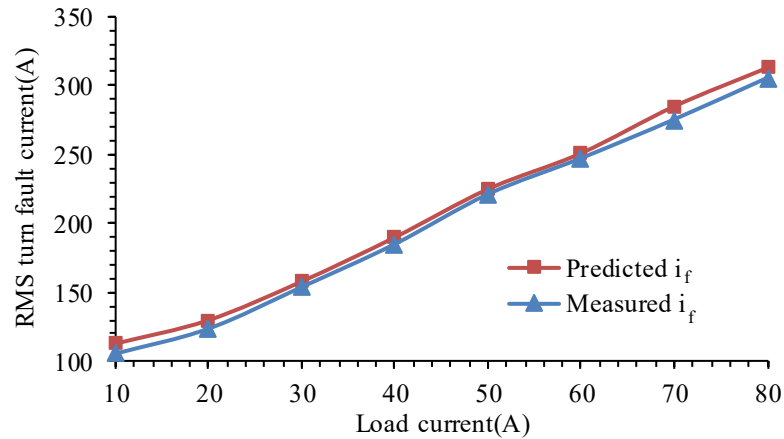


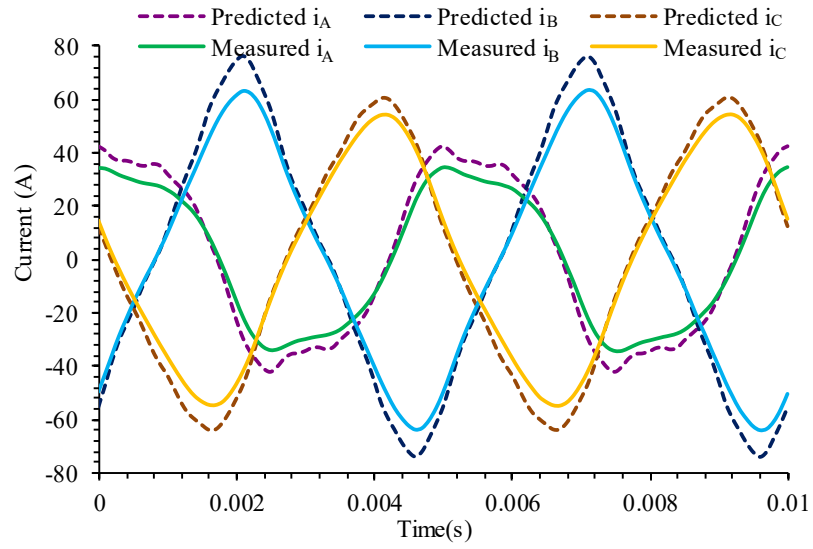
Fig. 4-22. RMS turn fault current with load currents variation.

4.6.1.2 Inter-Turn Short Circuit with Terminal Short-Circuit Fault

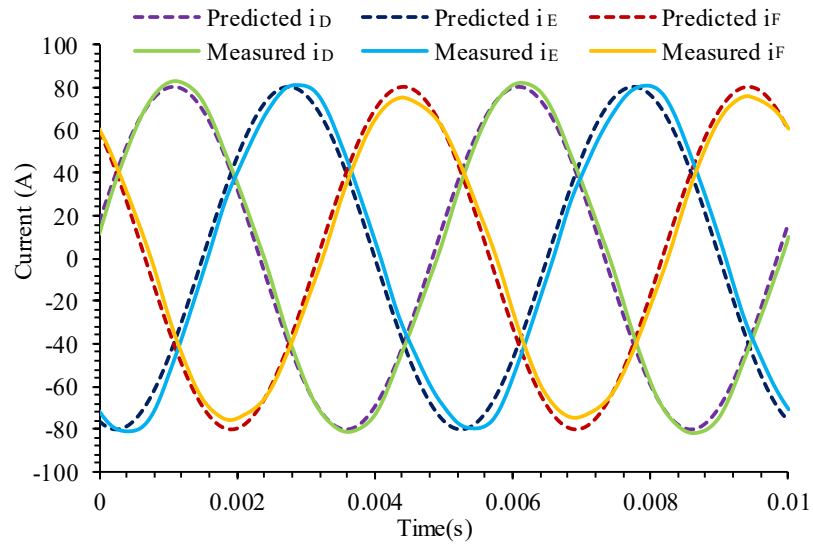
When the mitigation measure of 3-phase terminal SC is applied to the faulted 3-phase set ABC, the turn fault current reduces significantly. Therefore, the prototype can be tested under one turn SC with 3-phase terminal SC when the machine operates at 4000 rpm and is excited with 80A and 120A current in the healthy 3-phase sets for MTPA operation over longer duration.

Firstly, Fig. 4-23 shows the comparisons of predicted and measured current waveforms in the ABC phases, DEF phases and SC turn at 4000rpm when 80A current are excited in the healthy phases. As can be observed, the prediction of phase currents of fault set ABC shown in Fig. 4-23 (a) deviates slightly from the measurement, while the predicted DEF phase currents and turn fault current match quite well with the measured results as shown in Fig. 4-23 (b) and (c), respectively. The difference in the predicted and measured RMS turn fault currents is 9.3% and this is mainly caused by the prediction error of the ABC phase currents. However, because the design measures employed for the fault mitigation, the RMS phase currents in the ABC phases are quite low, being 25.3A, 40.4A and 36.9A, respectively. Consequently, the inaccurate prediction of phase currents of 3-phase set ABC has small effect on the thermal analysis.

Under this operating condition, the RMS phase currents in the other two healthy 3-phase sets are 56.6A, and the fault current in the SC turn after the mitigation action is 2.7 p.u. Consequently, the total heating effect (loss) in the ABC 3-phase set is 2.2 times lower than that of the other two healthy sets.



(a)



(b)

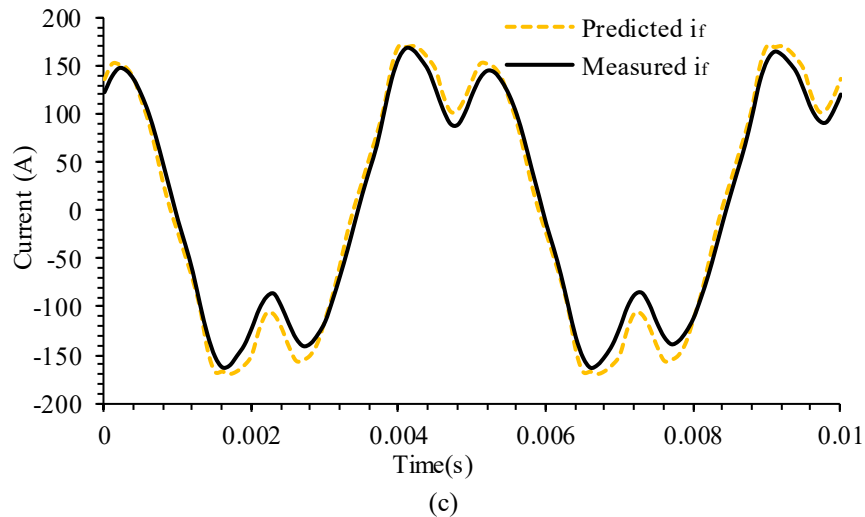
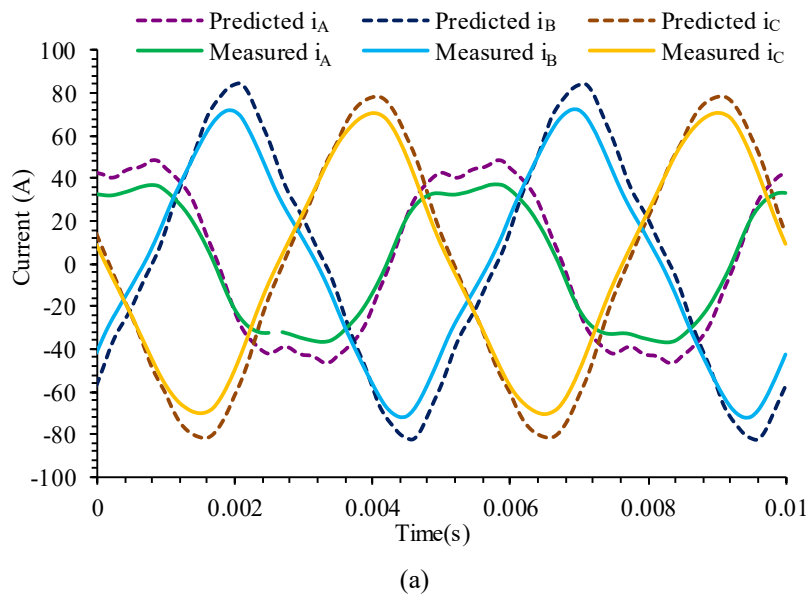


Fig. 4-23. Comparison of predicted and measured phase currents and turn fault current under one turn SC with 3-phase terminal SC at 4000 rpm and 80A current. (a) Phase currents in fault set ABC. (b) Phase currents in healthy set DEF. (c) Turn fault current.

Fig. 4-24 compares the predicted and measured current waveforms in the ABC phases, DEF phases and SC turn at 4000rpm when 120A current are excited in the healthy phases. Similarly, the predicted turn fault current waveform agrees quite well with the measured result and the difference in predicted and measured RMS turn fault is 4.7%. The RMS phase currents in the two healthy 3-phase sets are 84.9A, while the RMS phase currents in the terminal short-circuited ABC set are 28.8A, 45.8A and 47.9A, respectively. Meanwhile, the fault current in the SC turn after the mitigation action is 2.1 p.u. and the total heating effect (loss) in the ABC 3-phase set is 3.5 times lower than that of the other two healthy sets.



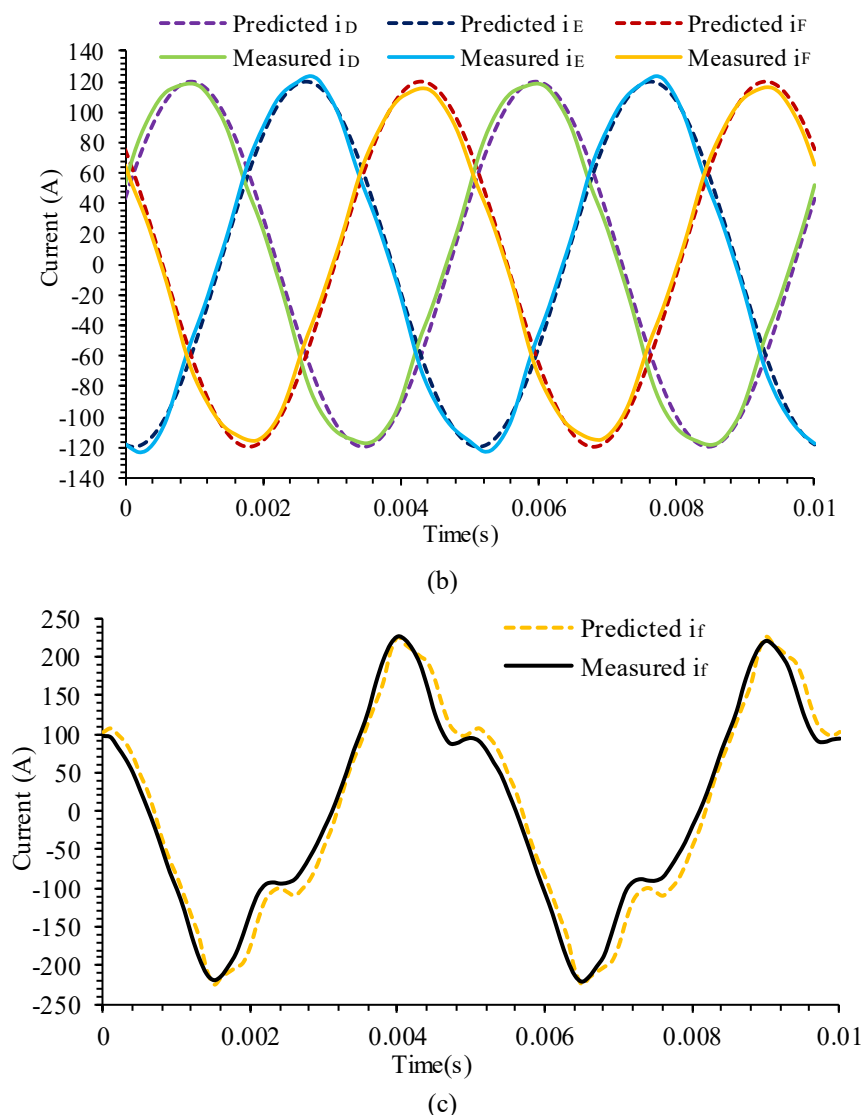


Fig. 4-24. Comparison of predicted and measured phase currents and turn fault current under one turn SC with 3-phase terminal SC at 4000 rpm and 120A current. (a) Phase currents in fault set ABC. (b) Phase currents in healthy set DEF. (c) Turn fault current.

Therefore, it can be concluded that the 2D EM model has good accuracy for predicting currents under various fault conditions, such as one turn SC with or without the mitigation measure of 3-phase terminal SC. Consequently, the copper losses calculated from the 2D EM model are very close to the test results when the effect of temperature is accounted. This, in turn, validates the losses adopted in the thermal models predicted by the 2D EM model.

4.6.2 Comparisons of Measured and 3D Predicted Thermal Performance

The prototype employing the oil cooling system as shown in Fig. 4-19 is further tested for validation of the thermal model. The cooling oil is fed via the inlet and outlet connections as shown in Fig. 4-25 (b) and circulates in the cooling channel shown in Fig. 4-25 (a). The inlet and outlet oil temperatures vary during tests due to the limited capacity of the heat exchanger. These variations are measured by two K-type thermocouples and recorded. The coolant volume flow rate is also recorded. Six temperature sensors are placed in the machine windings, three in the end windings and three in the active windings to measure temperatures in these positions. Moreover, even though the required operation for the designed machine is at high temperature, the thermal test was performed at 20°C ambient temperature for convenience.

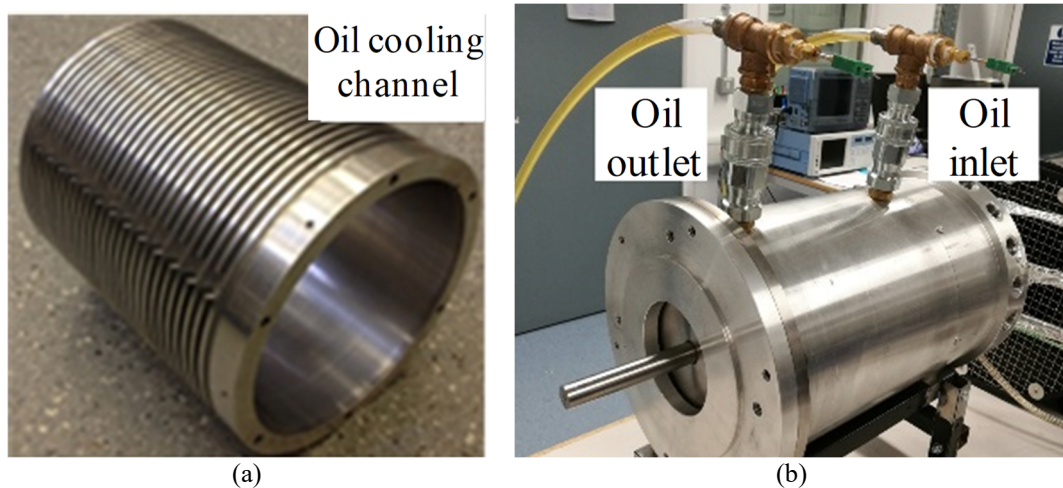


Fig. 4-25. Oil cooling system. (a) Cooling jacket. (b) Assembly.

To represent the experimental condition, it is necessary to model the inlet temperature variations during the tests. Both the LP model in Matlab and the 3D thermal model in JMAG can cope with these practical issues. The inlet, outlet temperatures and the flowrate of cooling oil change during operations could be considered by setting time-dependent R_H and time-dependent thermal convection resistance between the stator cooling channels and the cooling oil in LP and 3D thermal models, respectively, as well as setting the time-dependent ambient temperature boundary in both models. In addition, it can be seen from the winding layout in Fig. 4-1 (a) that the middle part of the slots in a 3-phase winding has more number of overlapped end winding segments than the two sides. To represent the uneven distribution of the copper loss in the end winding region, the copper loss

density in the end winding conductors associated with different slots is set proportional to the number of overlapped end winding segments over the slot. For example, the end winding of slot B4 has one overlapped segment while that of B2 has six. Hence, the copper loss density in the former is 6 times lower than that of the latter. Since in the LP model, the active winding and the end winding are connected to one node as in Fig. 4-8 and Fig. 4-9, the total loss and average temperature of the whole winding per slot is inputted and extracted from this node. Therefore, the 3D thermal model in JMAG is employed to quantify the uneven distribution of the copper loss in the end winding region and compare the temperatures with the six measured temperatures in different regions.

The whole simulation process is divided into a number of steps. In each step, the ambient temperature and the thermal convection resistance of the cooling oil are updated. The temperature distribution is extracted from the result file obtained in the previous step and used to calculate new copper loss as the initial temperature in the current step.

The prototype is first tested under healthy conditions at the base speed of 4000rpm with load current in all phases being set to 80A and 120A for MTPA operation. Since the hotspot temperature under one turn SC can be extremely high, this fault condition is not tested in order to avoid permanent damage of the prototype. However, the fault conditions of one turn SC when the fault mitigation measure (3-phase terminal SC) is applied are tested at the base speed of 4000rpm with load current in healthy phases being set to 80A and 120A. Each thermal test is performed for 2 hours for reaching steady state. The machine temperatures under these four conditions are predicted by the 3D thermal model and the results are compared with the measurements.

4.6.2.1 Healthy Condition at 4000rpm with 80A

The ambient temperature of the thermal test under healthy condition at 4000rpm with 80A for MTPA operation is 20°C, while the inlet and outlet oil temperatures vary from 21°C to 33°C and from 22°C to 39°C, respectively. The flowrate of oil cooling also varies from 4.5 litre/min to 7.5 litre/min because change of viscosity with temperature.

As the temperature distribution should be the same in each 3-phase set under healthy condition, the 1/3 3D thermal model in Fig. 4-11 (a) is adopted in simulation. The resultant temperature distribution of the winding under healthy condition at 4000rpm with

80A is shown in Fig. 4-26, where it is evident that the temperatures in the end winding are higher than those in the active winding. Obvious temperature differences in the end windings associated with each coil are seen in Fig. 4-26 due to the fact that the copper loss assigned to the end-winding segments of each coil is different. The end winding temperature in the inner middle region is 2~15°C higher than the rest. This effect cannot be predicted by Motor-CAD or 3D thermal model assuming symmetry in each slot-tooth region.

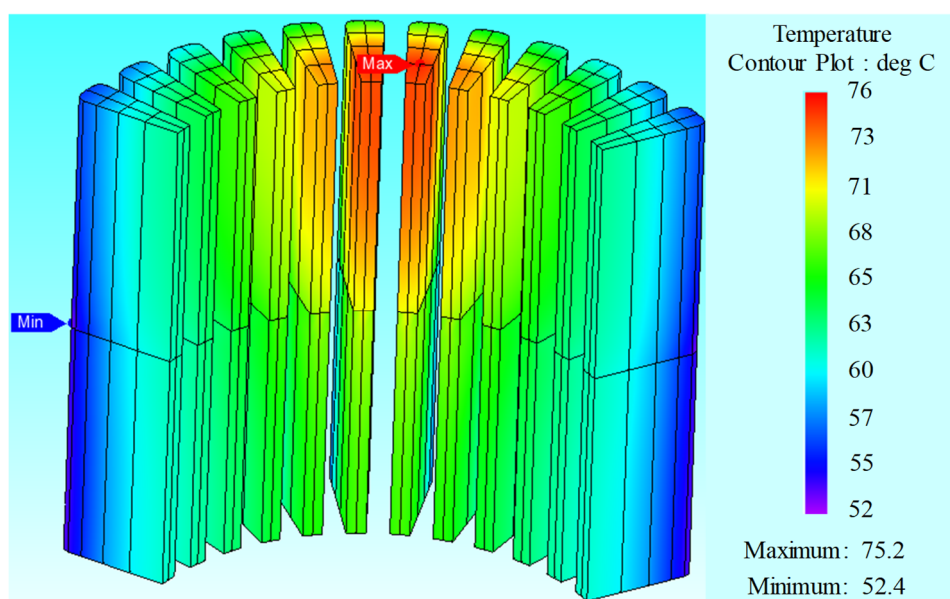


Fig. 4-26. Temperature distribution under healthy condition with 80A.

Among the six temperature sensors, two sensors, denoted as tf_ew and tf_slot , are placed in the end winding and slot region of the faulted turn in coil B2 as the black cuboid as shown in Fig. 4-27. The two sensors, denoted as $b1_slot$ and $e2_slot$ are placed in the middle of slots of coils B1 and E2, respectively. The other two remaining sensors, denoted as $set1_ew$ and $set2_ew$ are placed in the middle region of the end windings of the ABC and DEF 3-phase sets, respectively, as in Fig. 4-27. Additionally, the positions of these sensors are not exact.

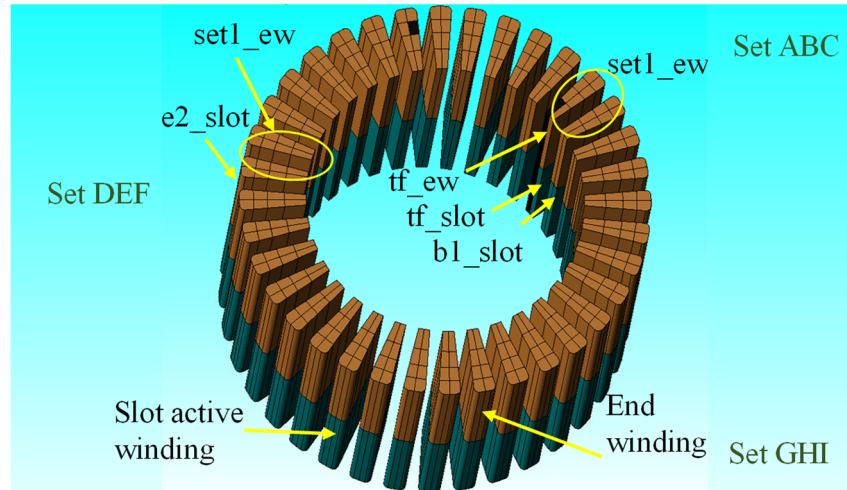


Fig. 4-27. Sensor locations.

Since the exact positions of the thermal sensors are not known, the minimum, average and maximum temperatures of the same region predicted by the 3D thermal model are extracted and compared with the measured results in Table 4-5. Moreover, the values in the last row indicate the difference between the measured and the minimum or the maximum predicted temperatures when the measured temperature is outside the predicted minimum and maximum range.

It can be seen that the measured temperatures in the slot regions by sensors b1_slot, tf_slot and e2_slot are between the minimum and maximum predicted temperatures. The measured temperatures in the end winding regions by sensors set2_ew, set1_ew and tf_ew are higher than the maximum predicted temperatures. The largest difference is 11°C at set2_ew.

Table 4-5 Comparison of measured and predicted temperatures under healthy condition with 80A.

Temperature (°C)	End winding			Active winding		
	set2_ew	set1_ew	tf_ew	b1_slot	tf_slot	e2_slot
Measured	86	80	78	70	69	71
Predicted max	75	75	75	70	72	72
Predicted min	59	59	71	58	67	54
Predicted average	71	71	74	66	71	68
Difference	11	5	3	--	--	--

4.6.2.2 Healthy Condition at 4000rpm with 120A

The ambient temperature of the thermal test under healthy condition at 4000rpm with 120A for MTPA operation is 20°C, while the inlet and outlet oil temperatures vary from 24°C to 44°C and from 25°C to 57°C, respectively. The flowrate of oil cooling also varies from 4.5 litre/min to 7.2 litre/min.

The predicted temperature distribution under healthy condition at 4000rpm with 120A as presented in Fig. 4-28 is similar to Fig. 4-26 but overall temperatures are much higher. The predicted hotspot temperature in the inner middle region of the end winding is 5~30°C higher than the rest. It is clear that this effect cannot be predicted by Motor-CAD or 3D thermal model under same condition but only assuming symmetry in each slot-tooth region as shown in Fig. 4-13 and Fig. 4-14. Moreover, although the average temperatures of different components are close between Fig. 4-28 and Fig. 4-13, the hotspot temperature presented in Fig. 4-28 is around 20°C larger than that presented in Fig. 4-13.

Fig. 4-29 shows the comparisons of transient temperatures between the predictions and measurements. The measured temperature by sensor set2_ew is still higher than the maximum predicted temperature by 3°C. It is seen from Fig. 4-29 and Table 4-5 that the measured temperatures by sensor set2_ew in the end winding region of the DEF 3-phase set are both larger than those by sensor set1_ew in the end winding region of the ABC set. This may be due to the fact that the sensor position in the DEF set is close to the star-neutral connection which introduces extra resistance and loss, and hence higher temperature. The measured temperature by sensor tf_slot is lower than the minimum predicted temperature by 13°C. It is possible that the position of the sensor has been moved toward the tooth where the temperature is lower. This trend is not shown in Table 4-5 because the copper loss density at 80A is less than half at 120A. The measured transient temperatures by sensors set1_ew, tf_ew, b1_slot and e2_slot are all between the minimum and maximum predicted temperatures. It can be concluded that the measured transient and steady-state temperatures agree quite well with the predicted trends and values.

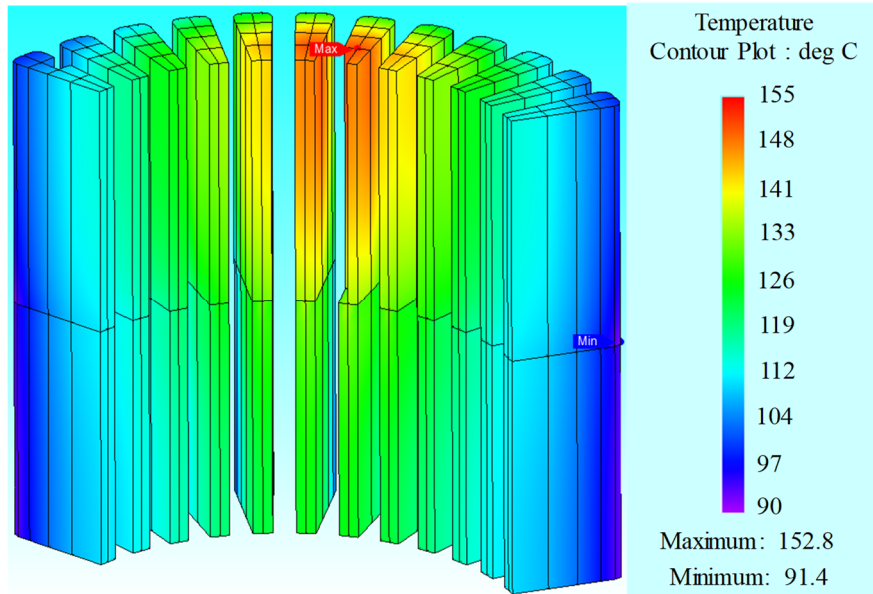
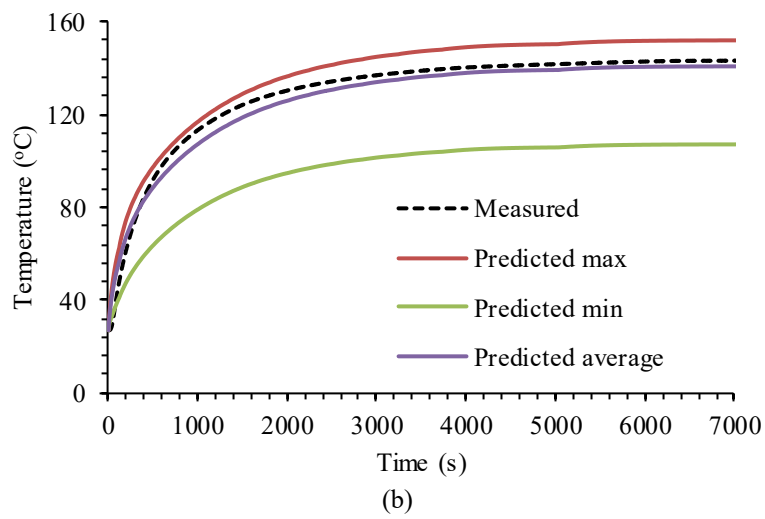
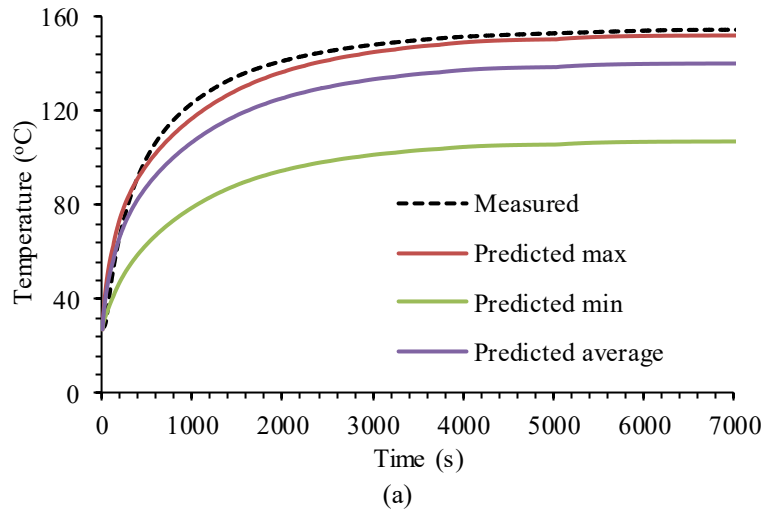
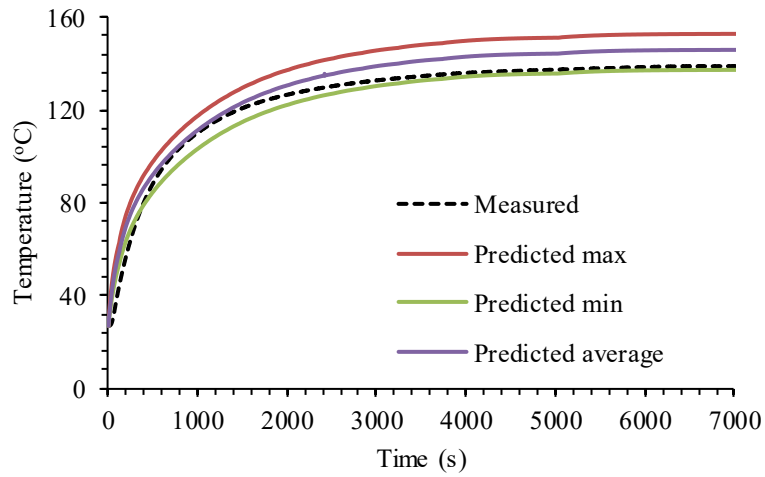
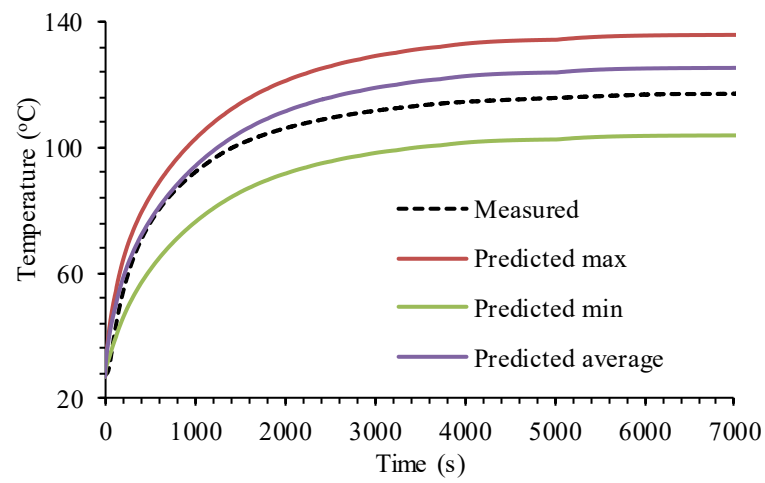


Fig. 4-28. Temperature distribution under healthy condition with 120A.

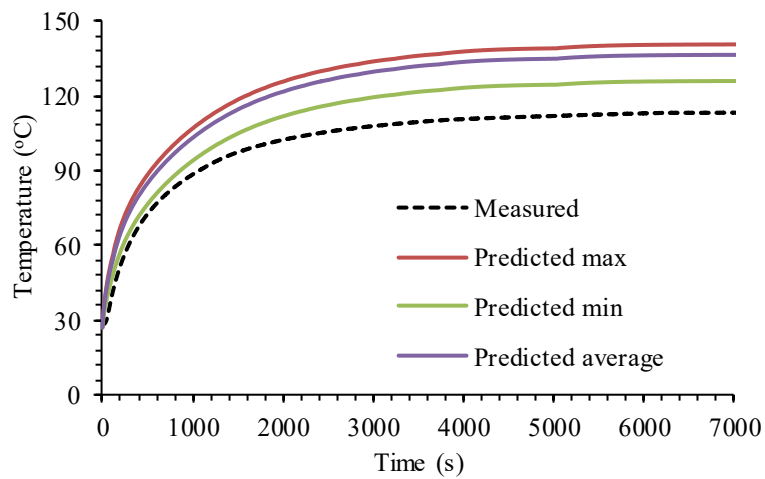




(c)



(d)



(e)

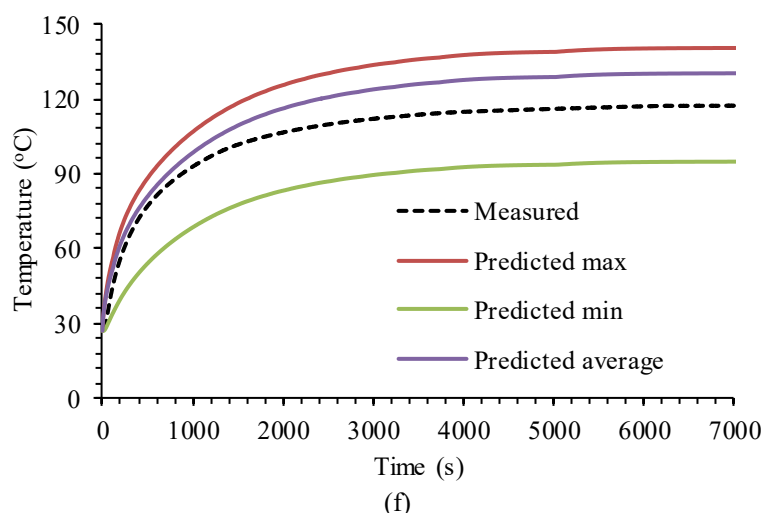


Fig. 4-29. Comparison of predicted and measured transient temperatures of six sensors under healthy condition with 120A. (a) set2_ew. (b) set1_ew. (c) tf_ew. (d) b1_slot. (e) tf_slot. (f) e2_slot.

4.6.2.3 One Turn SC with 3-Phase Terminal SC Fault at 4000rpm with 80A

The prototype has also been tested under one turn SC condition with 3-phase terminal SC applied to ABC phases at 4000rpm when the current in the healthy DEF and GHI phases is controlled to 80A for MTPA operation. The ambient temperature is 20°C, while the inlet and outlet oil temperatures vary from 19°C to 29°C and from 20°C to 35°C, respectively. The flowrate of oil cooling also varies from 4.5 litre/min to 5.7 litre/min.

As observed from Fig. 4-23, the loss distribution is asymmetric in which the total loss in the 3-phase set ABC is 2.2 times lower than that of the other two healthy sets. Therefore, the full 3D thermal model in Fig. 4-11 (b) is adopted for accurate thermal analysis. The predicted temperature distribution presented in Fig. 4-30 shows that the temperature distributions in the two healthy sets are similar or exhibit 3-phase symmetry and their overall temperature is higher than that of the faulty set. The hotspot as shown in Fig. 4-30 is located in the end winding segment of the SC turn due to 2.7 p.u. current in the fault turn.

The comparisons of predicted and measured steady-state temperatures are presented in Table 4-6. It shows that only the measured temperature by sensor set2_ew is larger than the maximum predicted temperature by 5°C. The five other measured temperatures are between the minimum and maximum predicted temperatures.

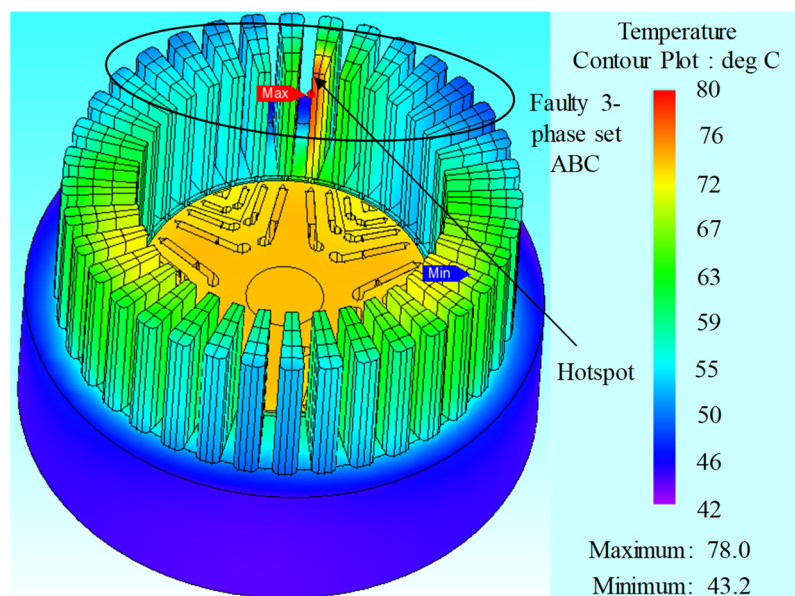


Fig. 4-30. Temperature distribution under fault condition with 80A.

Table 4-6 Comparison of measured and predicted temperatures under fault condition with 80A.

Temperature (°C)	End winding			Active winding		
	set2_ew	set1_ew	tf_ew	b1_slot	tf_slot	e2_slot
Measured	76	63	66	54	62	63
Predicted max	72	66	78	60	69	67
Predicted min	54	49	64	49	61	49
Predicted average	67	57	72	56	68	63
Difference	5	--	--	--	--	--

4.6.2.4 One Turn SC with 3-Phase Terminal SC Fault at 4000rpm with 120A

The prototype has also been tested under one turn SC condition with 3-phase terminal SC applied to ABC phases at 4000rpm when the current in the other two healthy phase sets is controlled to 120A for MTPA operation. The ambient temperature is 20°C, while the inlet and outlet oil temperatures vary from 21°C to 38°C and from 22°C to 49°C, respectively. The flowrate of oil cooling also varies from 4.5 litre/min to 6.6 litre/min.

The predicted temperature distribution is shown in Fig. 4-31. As can be seen, the temperature distributions in the two healthy 3-phase sets are also similar while their overall temperatures are much higher than that of the faulty set. In this case, the hotspot is located in the middle part of the end windings of the healthy 3-phase sets, similar to those seen in Fig. 4-28, because of the much larger copper loss in the healthy phase sets. Table 4-7 compares the steady state temperatures obtained by the predictions and measurements. It is worth noting that although the current in the faulted turn is ~ 2.1 pu as shown in Fig. 4-24, the temperatures in the fault turn measured by sensors tf_ew and

tf_slot are much lower than those in the healthy 3-phase sets measured by sensors set2_ew and e2_slot. This is because the total copper loss in the faulted coil after the mitigation action is much lower than those in the healthy 3-phase sets.

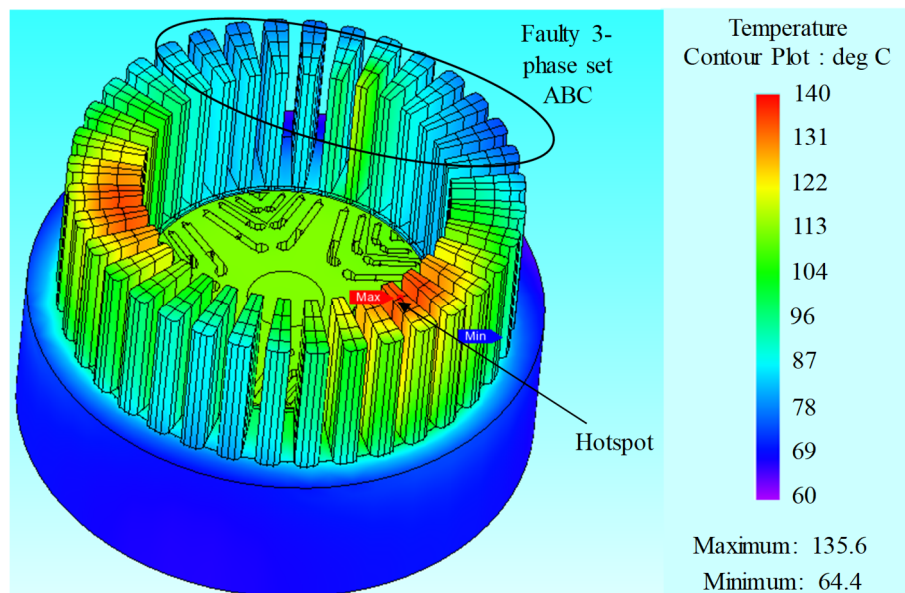


Fig. 4-31. Temperature distribution under fault condition with 120A.

Table 4-7 shows that the measured temperatures by the sensors denoted as set1_ew, tf_ew, b1_slot and e2_slot are between the minimum and maximum predicted temperatures. The measured temperature by sensor set2_ew is larger than the maximum predicted temperature by 8°C, while the measured temperature by sensor tf_slot is 2°C lower than the minimum predicted temperature. These trends are consistent with those observed in the previous sections for the reasons explained. Additionally, Fig. 4-32 (a) and (b) compare the predicted and measured transient temperatures in the fault turn region closed to sensors tf_ew and tf_slot, respectively. As observed, the measured temperatures both agree quite well with the predicted minimum.

Table 4-7 Comparison of measured and predicted temperatures under fault condition with 120A.

Temperature (°C)	End winding			Active winding		
	set2_ew	set1_ew	tf_ew	b1_slot	tf_slot	e2_slot
Measured	143	91	97	75	89	107
Predicted max	135	99	117	91	104	123
Predicted min	92	72	95	73	90	78
Predicted average	124	85	108	83	102	113
Difference	8	--	--	--	-2	--

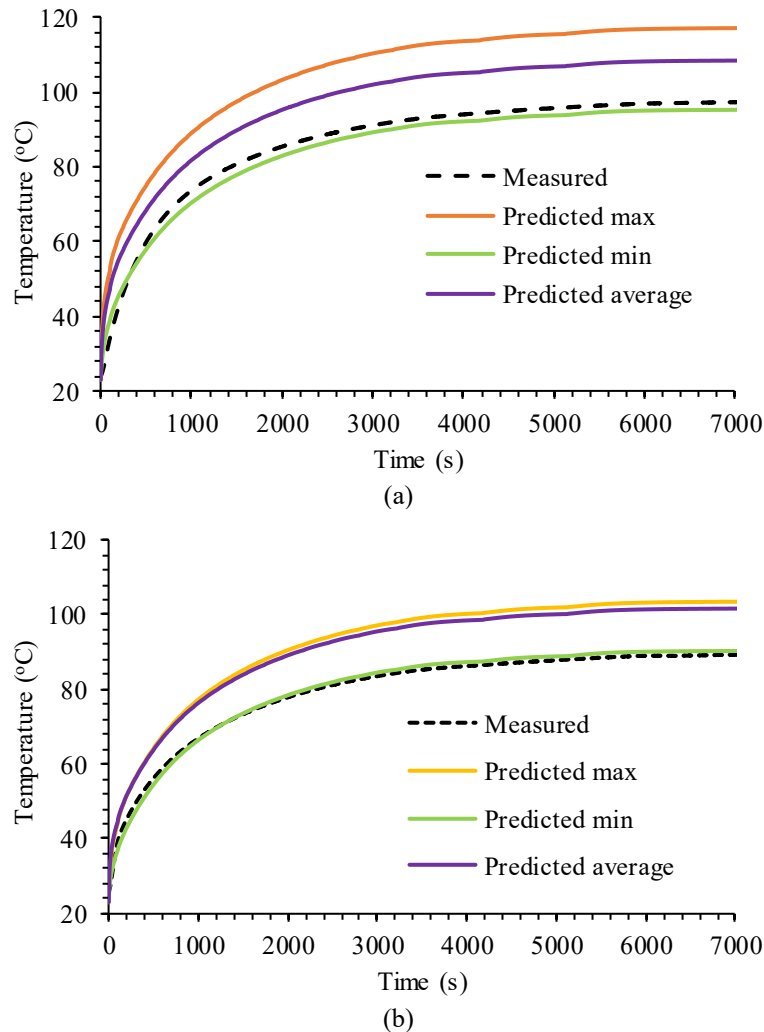


Fig. 4-32. Comparison of predicted and measured transient temperatures in the fault turn region under fault condition with 120A. (a) tf_{ew} . (b) tf_{slot} .

The comparisons of the predictions and measurements under both the healthy and fault conditions demonstrate that the 3D thermal model is quite accurate.

4.7 Thermal Performance of PMASynRM under Rated Operating Condition Based on the 3D Thermal Model

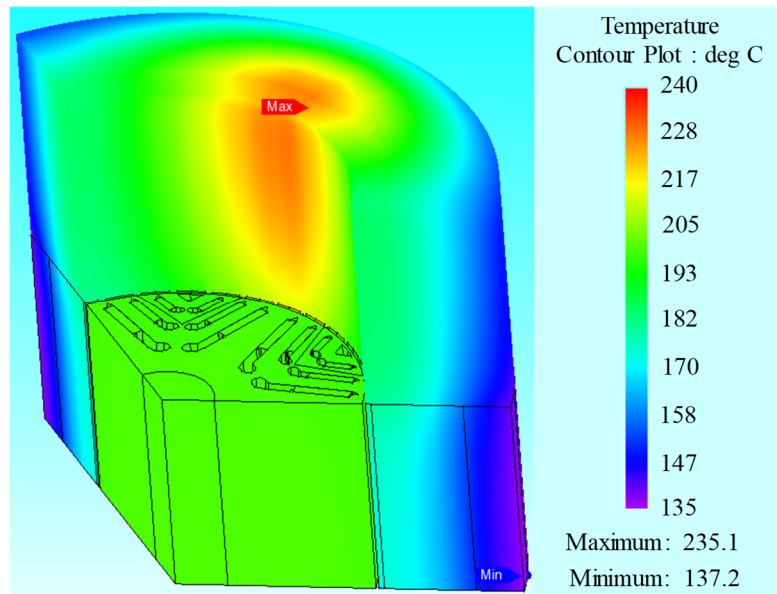
The 3D thermal behaviour should be modelled under the rated operating condition to check its thermal characteristics both under healthy and fault conditions.

4.7.1 Thermal Behaviour under Healthy Condition

The required specification for the prototype is that the ambient temperature is 100°C, while the coolant oil temperature is 110°C at the flowrate 6 litre/min. The eddy current loss in magnets (27.9W) is predicted in 2D EM model at 20°C, while the iron loss (307W)

and copper loss (1300W) are measured at 20°C. Therefore, the eddy current loss in the magnets only accounts for about 2% of the total loss. The hysteresis loss dominating the iron loss (73%) at the operating speed does not vary essentially with the temperature [117]. Moreover, the temperature coefficient of the conductivity of the core material is much lower than the copper. Thus, the iron loss and eddy current loss are considered independent of temperature while the temperature-dependent copper loss is accounted during the simulation.

The 1/3 3D thermal model in Fig. 4-11 (a) is adopted in simulation. The temperature distributions of the machine and the winding under the required healthy operation are presented in Fig. 4-33 (a) and (b), respectively. Moreover, the steady-state temperatures of different components under the required healthy operation are listed in Table 4-8. It is clear that the temperatures of the whole machine are quite high. The average temperature of the winding is 190°C while the hotspot temperature is 235°C which beyond the maximum permissible temperature 220°C.



(a)

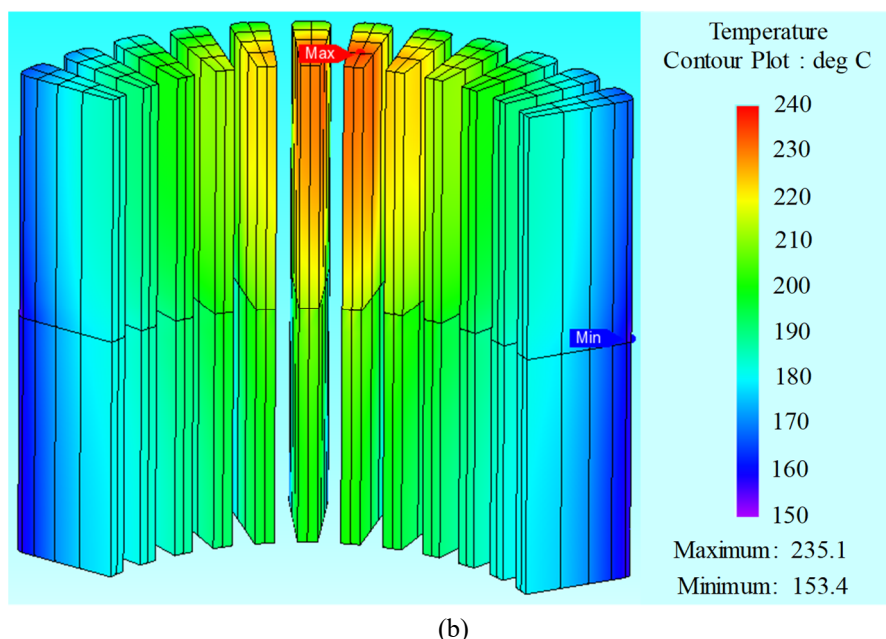


Fig. 4-33. Temperature distribution under required healthy condition. (a) Whole machine. (b) Winding part.

Table 4-8 Temperatures under required healthy condition predicted by 3D model.

Component	Rotor yoke	Magnet	Rotor iron-rib	Stator	Winding	Hotspot
Temperature (°C)	199	199	198	173	190	235

4.7.2 Thermal Behaviour under One Turn SC with Mitigation

When one turn SC occurs, the fault should be detected immediately and the mitigation measure as 3-phase terminal SC should be taken. Therefore, the thermal behaviour under one turn SC with 3-phase terminal SC at 4000rpm with 120A current excited in healthy phases for MTPA operation with 100°C ambient temperature and 110°C coolant oil temperature at the flowrate 6 litre/min is considered.

Firstly, as the temperature of the winding increases significantly from 20°C, the conductivity of the copper wire and the resulted SC fault current will be affected. Therefore, the initial temperature of the winding under fault condition is assumed to be 190°C which is the final steady-state winding temperature under healthy condition as given in Table 4-8. Fig. 4-34 compares the predicted current waveforms in the ABC phases and SC turn at 20°C and 190°C winding temperatures. As observed in Fig. 4-34 (a), the terminal SC phase currents of 3-phase set ABC are the same at the two temperatures because the current is essentially inductance limited, while the SC turn fault current at 190°C is slightly lower than that at 20°C as shown in Fig. 4-34 (b). The RMS value of the SC turn fault current is decreased by 12.4% at the higher temperature

compared to that at 20°C. The reduction is caused by the increase in the turn resistance whose effect on the SC current is not negligible under the one turn SC condition.

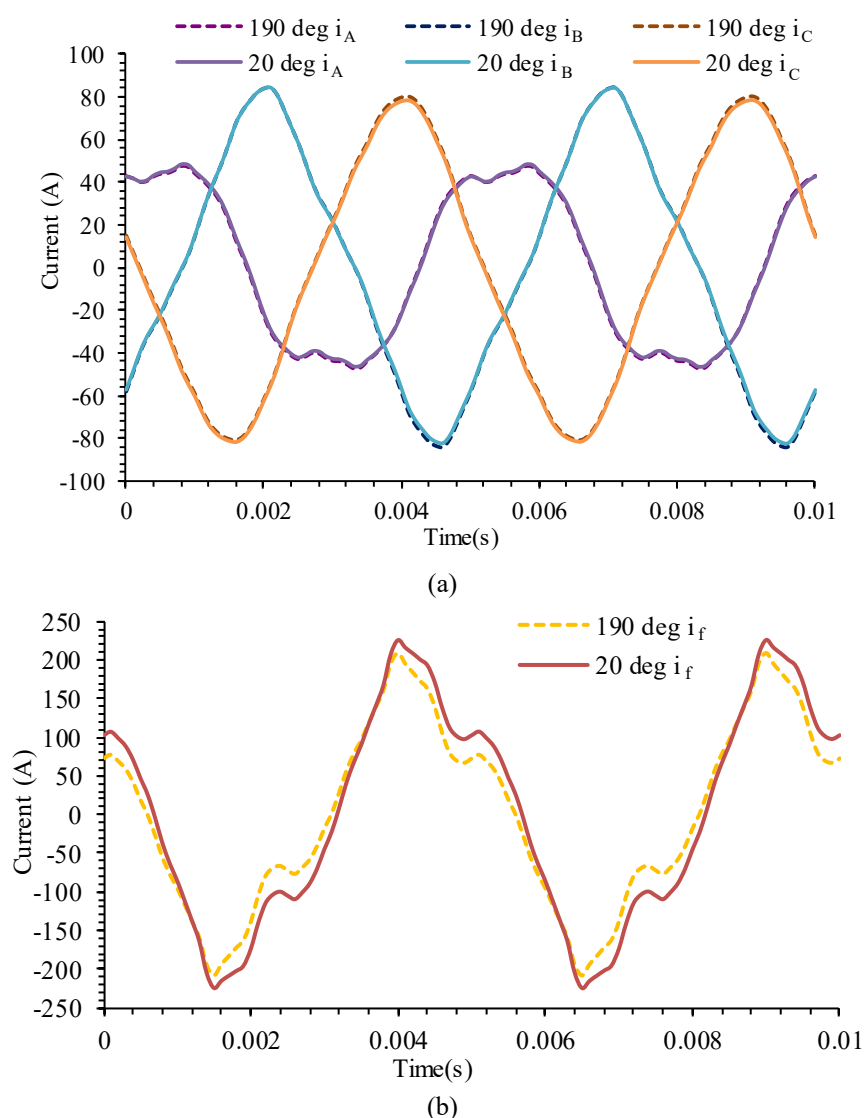


Fig. 4-34. Comparisons of predicted current waveforms between 20°C and 190°C under one turn SC with 3-phase terminal SC at 4000 rpm and 120A current. (a) Phase currents in fault set ABC. (b) Turn fault current in coil B.

The asymmetric loss distribution is represented in the full 3D thermal model shown in Fig. 4-11 (b). The resultant temperature distribution of the machine is presented in Fig. 4-35. As can be seen, the temperature distributions in the two healthy 3-phase sets are similar while their overall temperatures are much higher than that of the faulty set. The hotspot is located in the middle part of the end windings of the healthy 3-phase sets. Compared to Fig. 4-33, the hotspot temperature under the fault condition is 227°C which is lower than that under healthy condition due to the lower loss in the fault 3-phase set.

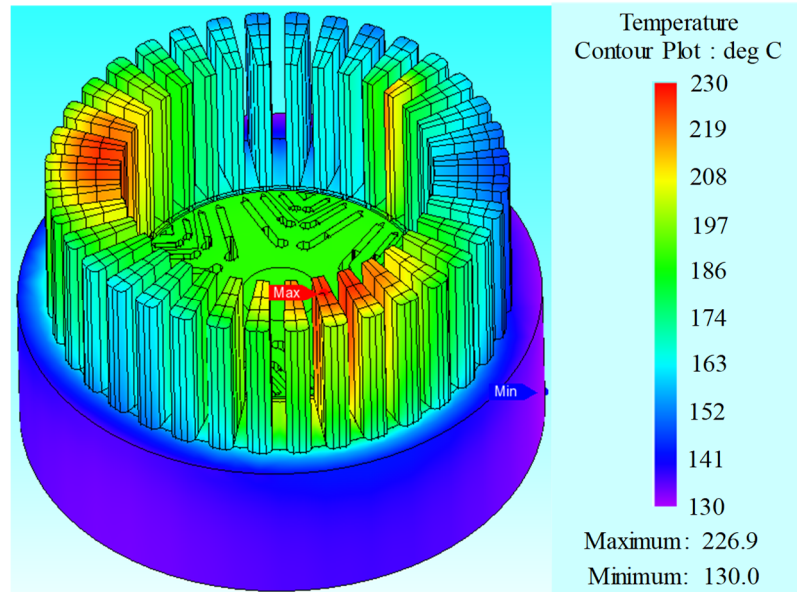


Fig. 4-35. Temperature distribution under fault condition with required operation condition.

4.8 Summary

Transient LP thermal models and a 3D thermal model for thermal analysis under healthy and fault conditions of the triple redundant, 9-phase PMASynRM with spiral cooling jacket system have been established. It has been shown that steady-state temperatures under healthy condition predicted by the LP, 3D thermal models and Motor-CAD are similar. Moreover, both the steady-state and transient temperatures of the machine under SC fault conditions predicted by the LP thermal model agree well with those predicted by the 3D thermal model. The losses predicted by the 2D EM model are compared with measurement, which shows that the predicted losses are sufficiently accurate for being used as inputs in the thermal models. It has also been shown that the predicted machine temperatures by the 3D thermal model under healthy and fault conditions match well with the measurements. Finally, the thermal behaviour of the machine at the rated operation under both healthy and fault conditions are analysed by the 3D model. It is found that the hotspot temperature is slightly over the maximum permissible temperature because of the non-overlapped end winding layout. Therefore, the insulation material should be changed to improve the maximum permissible temperature to be 240°C.

The LP thermal model is easy to build, takes much less time and can predict accurately the average temperatures of different parts and the hotspot temperature of the faulted turn. Both LP and 3D thermal models could deal with practical issues, such as variable copper

loss with the winding temperature, the time-varying coolant temperature and flow rate, etc. However, because of the limited nodes in the LP model, the 3D FE model can provide more detailed temperature distribution with better accuracy and cope with non-uniform end winding layout. The LP model would be more suitable for thermal assessment of the fault tolerant machine in design stages while the 3D model will be more accurate for thermal assessments in real operations. In summary, it can be seen that the thermal model is quite essential to be included in fault analysis for fault tolerance.

Chapter 5 Electromagnetic-Thermal Coupled Simulation for the PMASynRM under Ideal Short-Circuit Fault Conditions

5.1 Introduction

Temperature is one of the key limiting factors for electrical machines in safety critical applications since the insulation life decreases significantly when the winding temperature is beyond a permissible limit [118]. Hence, accurate thermal analysis considering all effects is important at design stage for predicting the temperature distribution and hotspot temperature under healthy as well as fault conditions.

Usually, losses obtained from EM model are simply fed to a LP thermal model or commercial FE tools to obtain the temperature distribution[119] [120]. Copper loss variation with temperature can be accounted under the assumption that the machine current and back emf are independent of temperature. However, this assumption may not be valid for synchronous reluctance machines equipped with permanent magnets as the flux produced by the magnets may strongly depend on temperature. The work described in [94] [121] combines the EM model with a LP thermal model through iterative data exchange for predicting the steady-state average temperature in different parts of a machine when the assumption is no longer true. The technique is computationally efficient, but less accurate. Therefore, FE based EM model combined with a FE based or CFD based thermal model are employed in co-simulations in [103] [122] [123]. However, the two models are not directly connected and the data exchange is manual. While the methods are more accurate, they are time consuming and inefficient.

Very few existing papers have considered the directly coupled EM-thermal simulation based on the FE transient models because of the complexity and different time constants between two physical fields. Moreover, fewer have considered coupled EM-thermal simulations under fault conditions. However, EM-thermal coupled simulation is significantly vital under fault conditions, especially when the current is not known and dependent on the EM behaviour of the machine. Moreover, under some fault conditions,

temperature effects on the winding resistance may have a significant influence on the magnetic field and resultant fault current.

The inter-turn SC within a phase shown in Fig. 5-1 is a typical example.

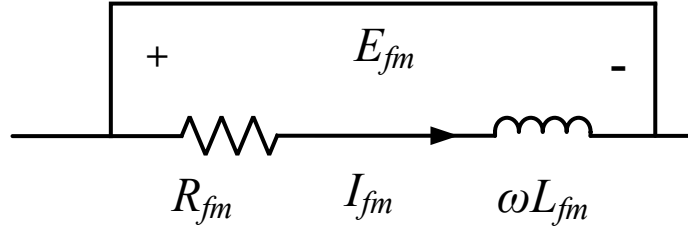


Fig. 5-1. Illustration of inter-turn short circuit condition.

The turn fault current I_{fm} and the copper loss, P_{fm} , of the faulted turns produced by I_{fm} are given in (5-1) and (5-2), respectively:

$$I_{fm} = \frac{E_{fm}}{\sqrt{R_{fm}^2 + (\omega L_{fm})^2}} \quad (5-1)$$

$$P_{fm} = I_{fm}^2 R_{fm} = \left[\frac{E_{fm}}{\sqrt{R_{fm}^2 + (\omega L_{fm})^2}} \right]^2 R_{fm} \quad (5-2)$$

where E_{fm} is the electromotive force of the faulted turns, R_{fm} is the resistance and L_{fm} is the inductance of the faulted turns. In addition, resistance R_{fm} changes linearly with temperature while the reactance ωL_{fm} depends on the operating speed and the square of the number of faulted turns. Therefore, there are three possible cases.

Firstly, the resistance is the dominant component of the impedance ($R_{fm} \gg \omega L_{fm}$) or the resistive and reactive components of a faulted winding may be similar ($R_{fm} \approx \omega L_{fm}$) when a small number of turns are short-circuited or the machine operates at low speed, leading to overestimates of the temperature rise and steady-state temperatures if the temperature effect on resistivity is neglected. When a large number of turns are short-circuited or the machine operates at high speed, the reactance becomes dominant ($R_{fm} \ll \omega L_{fm}$). In this case the resistance increase with temperature has little effect on current while the copper loss increases with temperature. Consequently, the temperature increases faster and reaches the higher value than the prediction without considering the temperature effect. Thus, the EM-thermal coupled simulation is essential to obtain a better insight of the thermal behaviour under these possible cases.

This chapter performs a directly coupled EM-thermal simulation based on 2D transient EM and 3D thermal model of the proposed triple redundant, 9-phase (3x3-phase), PMASynRM with wye-connected winding. A scripting file will be used to exchange data during each step to predict the temperature distribution under various faults at different speeds. The transient temperature results under EM-thermal coupled simulation will be comprehensively compared with those under thermal-only simulation with constant losses. The chapter also discusses the necessity of the EM-thermal coupled simulation against different fault conditions.

Further, as the proposed machine has 17 parallel strands per turn to reduce AC losses. The insulation break down between a few strands of two different turns is possible and realistic. With a few strands short-circuited, the inductances of the SC strands are likely to be similar to that of the complete inter turn SC involving all strands while the resistance of the SC strands is much higher than that of the complete SC. Consequently, the heating effect and temperature rise will be more dramatic. Moreover, since the number of possible SC faults involving a given number of strands and turns are large, this chapter assesses the electromagnetic behaviours on various typical possible SC faults, such as inter-strand SC and intra-strand SC. In addition, due to the large computation time, the EM-thermal coupled simulation is only adopted under inter-strand SC for analysing the most severe fault in respect of thermal behaviour. It gives an insight of the electromagnetic and thermal behaviours under SC faults between strands for the PMASynRM with stranded conductors.

5.2 Electromagnetic-Thermal Coupled Simulation

The EM-thermal coupled simulation will be performed in JMAG by two steps, as shown in Fig. 5-2 [115]. Fig. 5-2 (a) shows the flowchart of step 1 to predict the temperature distribution under healthy condition. As observed, the initial temperature will be assigned to the 2D transient EM and 3D static thermal models at the beginning. Subsequently, the material properties and resistance of the winding in the 2D EM model is updated with predicted temperature distributions by the 3D thermal model in the previous iteration. The calculated losses obtained from the 2D EM model and steady-state temperatures gathered from the thermal model will be exchanged iteratively. When the temperature results satisfy the convergence criterion in which the maximum residual

temperature between the previous and present predictions should be less than 0.1°C , the final temperature distribution under the healthy condition is obtained.

The thermal behaviour under a fault condition is predicted in step 2 according to the flowchart shown in Fig. 5-2 (b). The whole process is divided into a number of appropriate steps. Firstly, the healthy temperature distribution in step 1 will be assigned as the initial temperature to the 2D EM model and the 3D transient thermal model. Subsequently, the temperature-dependent material properties and resistances will be updated in the 2D EM model. The new iron loss, eddy current loss, average copper losses of each turn (fault coil) or each slot (healthy coil) predicted by the 2D EM model are fed to the 3D thermal model that in turn predicts new temperature distribution at the end of the time step. The temperature distribution will be checked for convergence with those predicted in the previous step. If a convergence criterion is not met, the average temperatures of rotor, magnet, stator, each turn of fault phase winding or each healthy phase will be fed to the 2D EM model. The initial temperature of the subsequent 3D thermal model will be updated by the temperature result file from the previous 3D thermal model. The process will repeat until convergence. When the results converge, the transient temperature rise of every step can be extracted. All the coupled simulation processes are controlled by a scripting file.

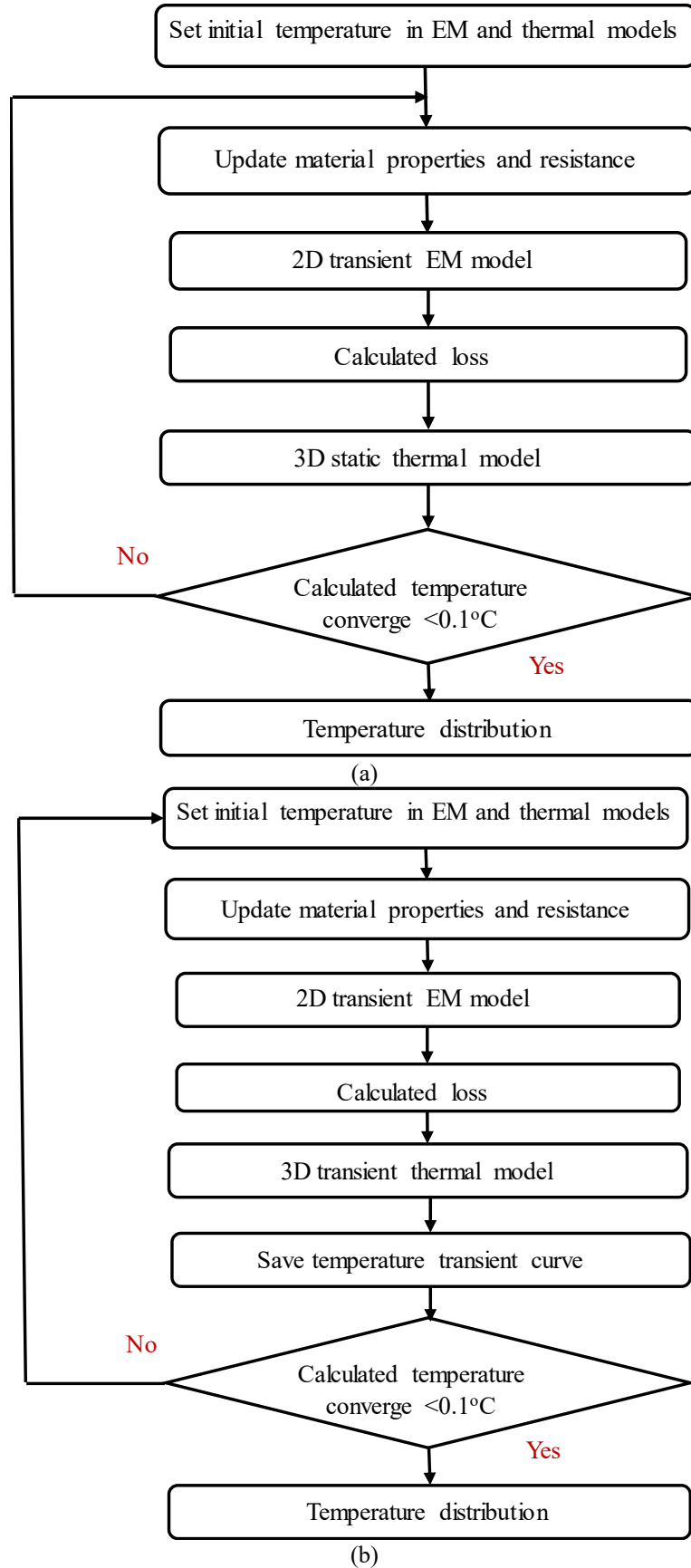


Fig. 5-2. Flowchart of EM-thermal coupled simulation. (a) Step 1: healthy condition. (b) Step 2: fault condition.

The fault tolerant triple redundant, 9-phase (3x3-phase), 36-slot, 6-pole PMASynRM with wye-connected windings is illustrated in Fig. 5-3.

As introduced in Chapter 4, the iron loss and eddy current loss are considered independent of temperature while the temperature-dependent copper loss is accounted during the coupled simulation. The machine employs single layer winding with 2 series connected coils per phase, as shown in Fig. 5-3 and each coil has 8 turns.

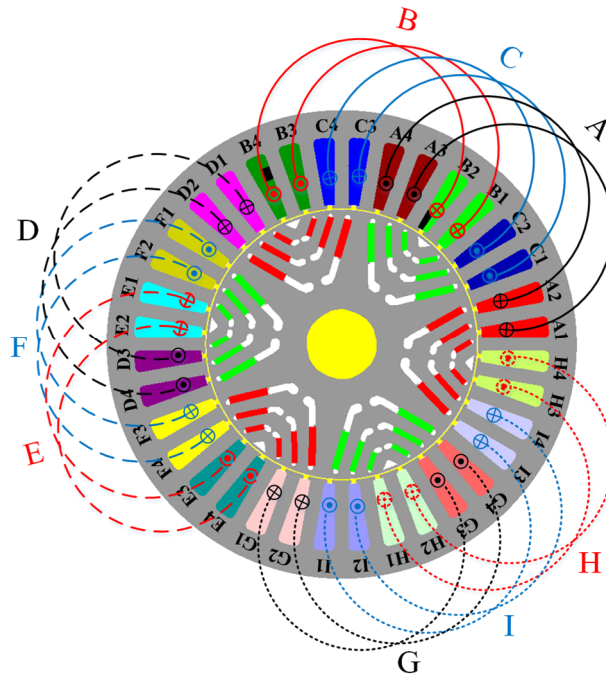


Fig. 5-3. Cross section of a triple redundant, 9-phase PMASynRM.

In addition, as introduced in Chapter 4, the full 3D thermal model is more accurate than the 1/3 model for thermal analysis under fault conditions when the heating effect and temperature distribution in the winding are quite asymmetric. The full 3D thermal model encompassing 36 slots and half of the machine axial length as illustrated in Fig. 5-4 is adopted in JMAG. The model of Fig. 5-4 is the same with that of Fig. 4-11 but with more details indicated. Additionally, measurements on the prototype machine have validated the 2D EM model and the 3D thermal model in Chapter 4.

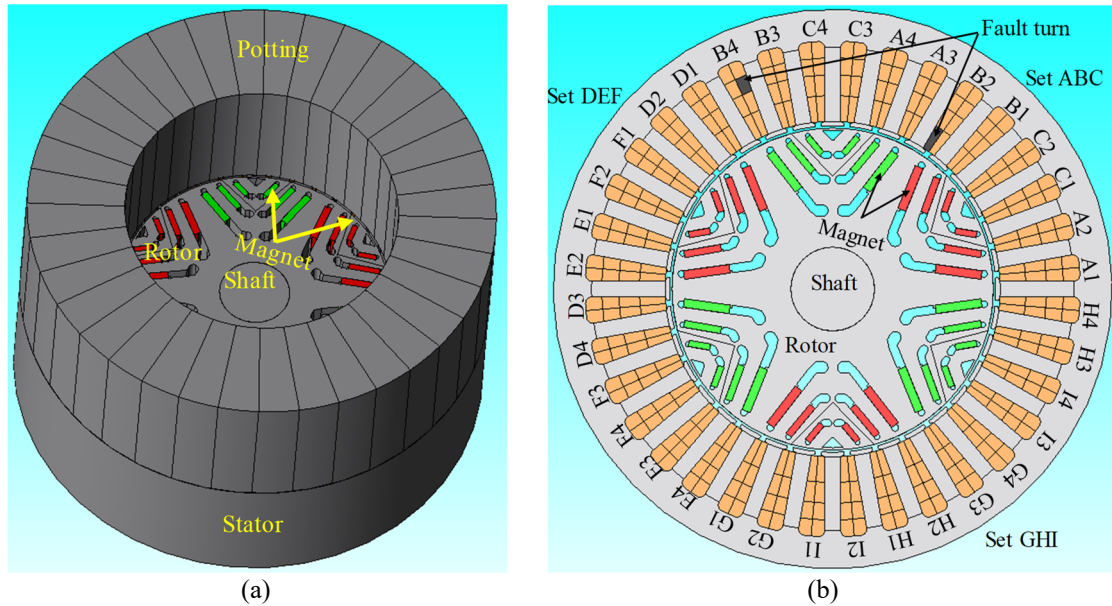


Fig. 5-4. 3D thermal model. (a) Model with potting. (b) Cross section.

5.3 Thermal Behaviour of the PMASynRM under Various Fault Conditions

Five fault conditions considered in this chapter as presented in Table 5-1 are: (1) F1: one turn SC at 500 rpm; (2) F2: one turn SC at 4000 rpm; (3) F3: two turns SC at 4000 rpm; (4) F4: three turns SC at 4000 rpm; (5) F5: one turn SC with 3-phase terminal SC at 4000 rpm. F1 to F4 are considered because inter-turn SC involving a few turns in the SC path will generate excessive fault current and this current is more likely sensible to the winding resistance. Moreover, F5 is considered because it represents the remedial action. In addition, F1 and F2 represent a single turn SC at two different speeds. F3 and F4 are performed to study the influence of number of SC turns on thermal behaviour. As described previously, SC current may be mainly limited by the resistance when a small number of turns are short-circuited or at low speed. However, for this machine at the rated speed of 4000rpm, the SC current is mainly reactance limited with one, two or three SC turns. In contrast, one turn SC at 500 rpm is resistance limited because of low speed. In all five conditions, the currents in healthy phases are set to the rated value with phase angle for MTPA operation. Moreover, the thermal model in all five conditions is under required specification that the ambient temperature is 100°C, while the coolant oil temperature is 110°C at the flowrate 6 litre/min.

Table 5-1. Fault conditions under consideration.

	Fault	Pre-fault operation
F1	One turn SC at 500 rpm	Rated torque
F2	One turn SC at 4000 rpm	Rated torque
F3	Two turns SC at 4000 rpm	Rated torque
F4	Three turns SC at 4000 rpm	Rated torque
F5	One turn SC with 3-phase terminal SC at 4000 rpm	Rated torque

All the faults are assumed to occur in phase B of the 3-phase set ABC. Thus, phase B is divided into the healthy part denoted as Phase_B_healthy and the fault part denoted as SC turn. As the machine has triple 3-phase sets, the mutual coupling between the two healthy 3-phase sets and one faulty 3-phase set will influence the fault current and resultant copper loss. It has been shown in Chapter 2 that when a turn-to-turn SC located in slot B2 and slot B4 which are marked by the two black quadrangles shown in Fig. 5-4 takes place, the SC current and copper loss are the highest.

The coupled simulation under the fault conditions is divided into 48 steps. As temperature increases dramatically at the beginning when the fault occurs and changes much slowly in the late stage, the time step is varied. In the first 30 steps, a time interval of 2s is used, while in the last 18 steps, 40s is used in each step. Thus, the total simulation time is 780s and the computation time is 22h48min in a typical PC. For the purpose comparison, the thermal behaviour under the same fault is also predicted by the thermal model without account of temperature influence on electromagnetic behaviour and the computation time is 37min in a typical PC.

5.3.1 One Turn Short-Circuit at 500rpm

The 3D thermal model as shown in Fig. 5-4 is used to predict the temperature distribution of the machine under healthy condition with the rated current of 120A at 500rpm which will be extracted as the initial temperatures for simulations in fault condition F1. The temperature distribution under healthy condition at 500rpm is presented in Fig. 5-5.

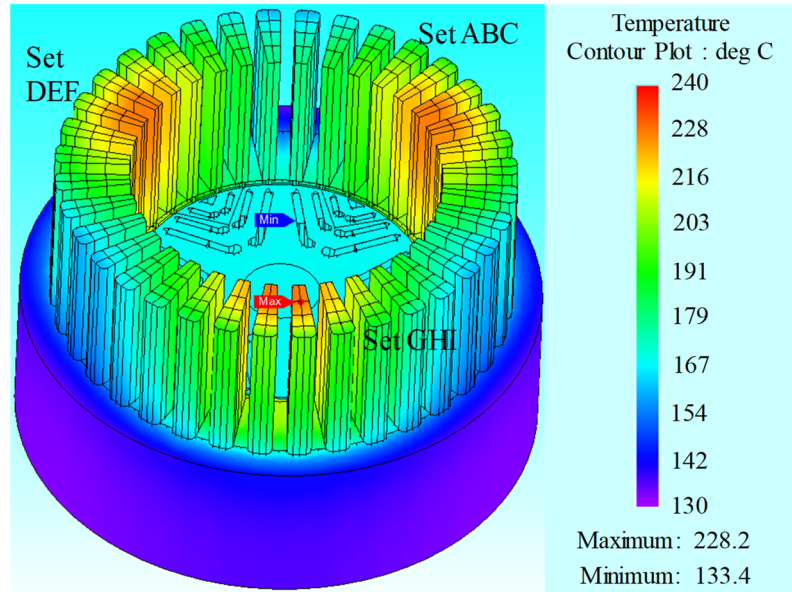


Fig. 5-5. Temperature distribution under healthy condition with the rated current of 120A at 500rpm.

In Fault F1 (one turn SC at 500 rpm), the resistance dominates the fault turn impedance due to low speed. It is validated in Fig. 5-6 that the copper loss in the SC turn reduces with the increase in times and temperature. The transient hotspot temperature rise predicted by the EM-thermal coupled simulation is compared with that predicted by thermal-only simulation in Fig. 5-7. Moreover, Table 5-2 compares the temperature distributions in different parts of the machine at 780s by the two simulation methods.

As observed, the differences between two methods are quite small because the SC current at 500rpm and, hence, the copper loss of the SC turn is relatively small which accounts for smaller than 6% of the total copper loss. With increase in temperature when the fault occurs, the SC current decreases, resulting in lower temperature than that when the influence of temperature on the fault current is neglected. Thus, the EM-thermal coupled simulation improves slightly prediction accuracy under the resistance limited condition at low speed.

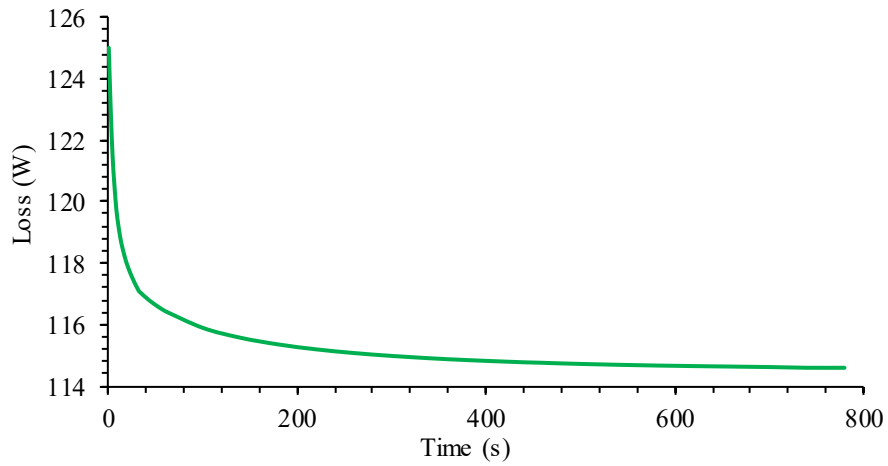


Fig. 5-6. SC turn loss variation with time under one turn SC at 500 rpm.

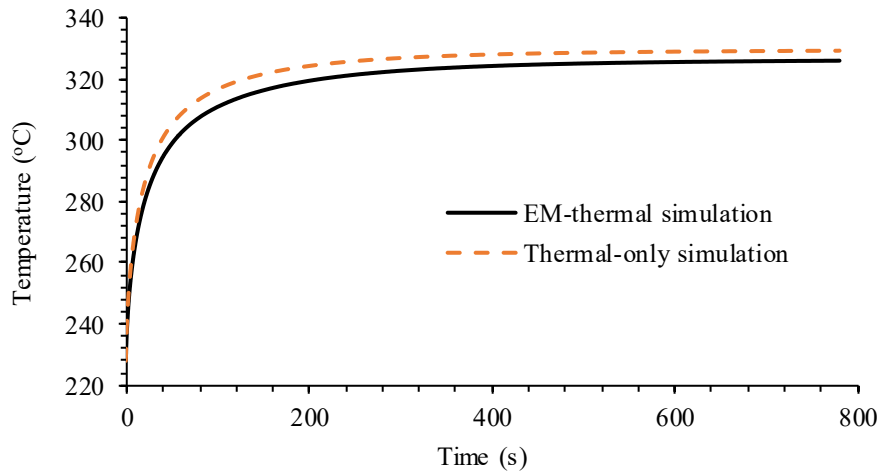


Fig. 5-7. Comparison of hot-spot temperature between two simulations under one turn SC at 500 rpm.

Table 5-2 Comparison of temperatures in different parts at 780s under one turn SC at 500 rpm.

Component temperature	EM-thermal simulation	Thermal-only simulation	Difference
Rotor (°C)	171	171	0
Shaft (°C)	170	170	0
Magnet (°C)	171	171	0
Stator (°C)	158	158	0
Phase D (°C)	188	188	0
Phase E (°C)	186	186	0
Phase F (°C)	186	186	0
Phase G (°C)	186	186	0
Phase H (°C)	186	186	0
Phase I (°C)	186	186	0
Phase A (°C)	193	192	1
Phase C (°C)	190	189	1
Phase B healthy (°C)	200	199	1
SC turn (°C)	227	229	-2
Hotspot (°C)	326	329	-3

5.3.2 One Turn Short-Circuit at 4000rpm

The 3D thermal model shown in Fig. 5-4 is also used to predict the temperature distribution of the machine under healthy condition with the rated current of 120A for MTPA operation at 4000rpm. The resultant temperature distribution, which will be the initial temperatures for simulations in fault conditions F2, F3, F4 and F5, are shown in Fig. 5-8. The temperature distribution in Fig. 5-8 is 3-times repeated of that in Fig. 4-33 with 1/3 3D thermal model.

Table 5-3 compares the steady-state temperatures under healthy condition between 500rpm and 4000rpm. It can be observed from Table 5-3, Fig. 5-5 and Fig. 5-8 that the differences of temperatures of winding, stator and hotspot between 500rpm and 4000rpm are relatively small due to the similar copper loss which accounts for the majority of the total loss. However, the temperatures of the rotor, shaft and magnets at 500rpm are much lower than those at 4000rpm due to the much smaller iron loss and eddy current loss at the lower frequency.

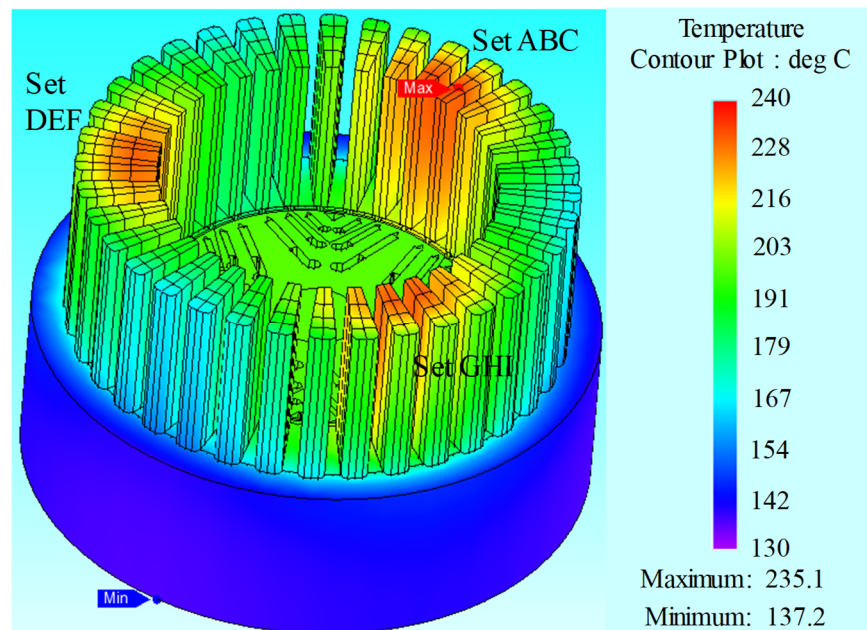
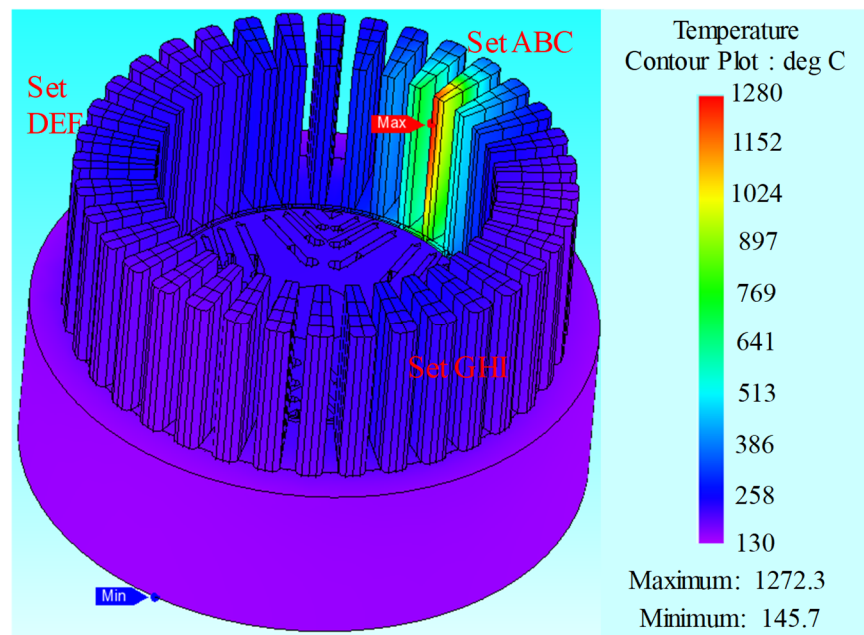


Fig. 5-8. Temperature distribution under healthy condition with the rated current of 120A at 4000rpm.

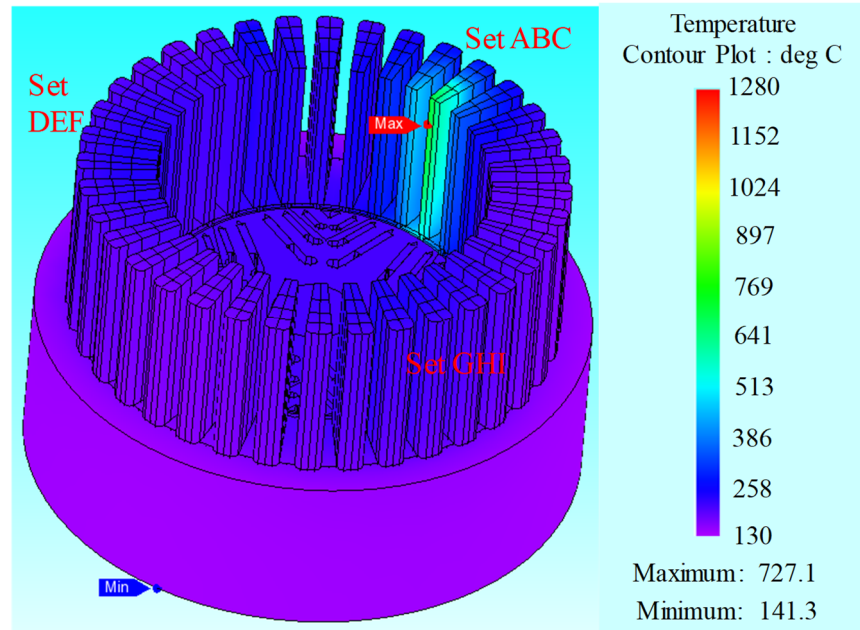
Table 5-3 Comparison of temperatures in different parts under healthy condition at 500 rpm and 4000rpm.

Component temperature	500rpm	4000rpm	Difference
Rotor (°C)	168	198	-30
Shaft (°C)	168	199	-31
Magnet (°C)	168	198	-30
Stator (°C)	154	159	-5
Winding (°C)	183	189	-6
Hotspot (°C)	228	235	-7

Fault F2 is one turn SC at 4000 rpm in which the SC current is extremely high and is largely dependent on the reactance of the short-circuit path. Hence, the resultant loss in the SC turn increases dramatically with both increases in temperature and in the turn resistance. The temperature distributions at 780s under F2 predicted by the two simulation methods are shown in Fig. 5-9 (a) and (b) in the same range of temperature scaling, respectively. As observed from Fig. 5-9, the hotspot is located in the end winding part of the SC turn near the slot opening of slot B2. It is evident that the temperatures of faulted ABC 3-phase set predicted by the EM-thermal coupled simulation are much higher, especially in the regions close to the SC turn than those by the thermal-only simulation.



(a)



(b)

Fig. 5-9. Temperature distribution under F2 at 780s between two simulated methods. (a) EM-thermal coupled simulation. (b) Thermal-only simulation.

Fig. 5-10 illustrates the transient average temperature and loss in the SC turn over the time duration of 780s between the EM-thermal and thermal-only simulations. It is obvious that the resultant loss in the SC turn increases with the increase in temperature in the EM-thermal simulation, while remains steady with the increase in temperature in the thermal-only simulation. In addition, Fig. 5-11 and Table 5-4 compare the transient hotspot temperature over the time duration of 780s, and the temperature distributions in different parts of the machine at 780s, respectively. As observed, the thermal-only simulation underestimates the temperatures in all parts, especially underestimating the temperatures in faulted ABC 3-phase set significantly. Besides, the underestimate of the hotspot temperature becomes larger with increase in time and reaches (545°C) at 780s as shown in Fig. 5-11. The comparison demonstrates the necessity of the EM-thermal coupled simulation under one turn SC at 4000 rpm.

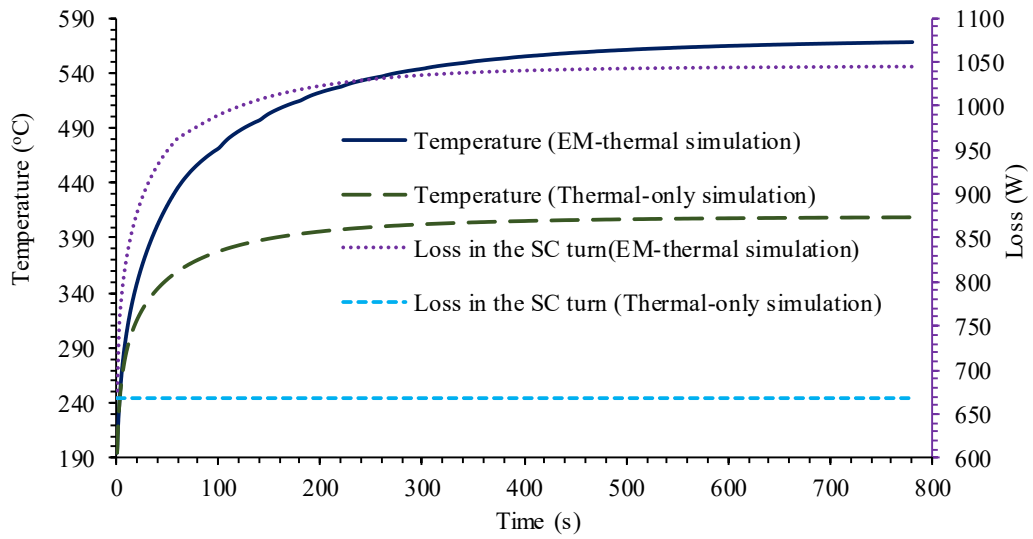


Fig. 5-10. Comparison of the SC turn loss and transient average temperature rises between two simulations under one turn SC at 4000 rpm.

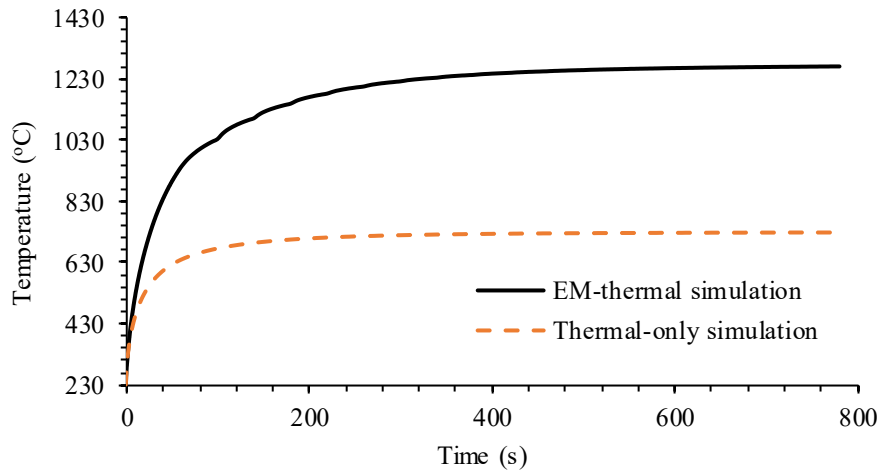


Fig. 5-11. Comparison of the transient hotspot temperature rises between two simulations under one turn SC at 4000 rpm.

Table 5-4 Comparison of temperature values in different parts at 780s under one turn SC at 4000 rpm.

Component temperature	EM-thermal simulation	Thermal-only simulation	Difference
Rotor (°C)	219	209	10
Shaft (°C)	218	209	9
Magnet (°C)	219	209	10
Stator (°C)	185	172	13
Phase D (°C)	213	202	11
Phase E (°C)	203	194	9
Phase F (°C)	204	195	9
Phase G (°C)	202	194	8
Phase H (°C)	203	194	9
Phase I (°C)	202	194	8
Phase A (°C)	274	227	47
Phase C (°C)	243	214	29
Phase B healthy (°C)	343	272	71
SC turn (°C)	569	410	159
Hotspot (°C)	1272	727	545

5.3.3 Two Turns Short-Circuit at 4000rpm

Two turns SC fault at 4000 rpm, denoted as F3, is also simulated. The turn fault current is lower than that under F2 due to increase in inductance of the fault path that is proportional to the square of the number of the SC turns. However, the total copper loss in the faulted two turns under F3 is larger than that in the faulted one turn under F2. This can be confirmed in Fig. 5-12 which compares the total copper loss in the faulted one turn under 1 turn SC and in the faulted two turns under 2 turns SC between two simulated methods over the time duration of 780s. As observed, the SC turn loss under F3 is slightly larger than that under F2 under thermal-only simulation. The SC current is also reactance dominant under F3, and hence the copper loss increases with both increases in temperature and the faulted turn resistances under EM-thermal coupled simulation. The difference of SC turn loss between F3 and F2 becomes larger with time under EM-thermal coupled simulation.

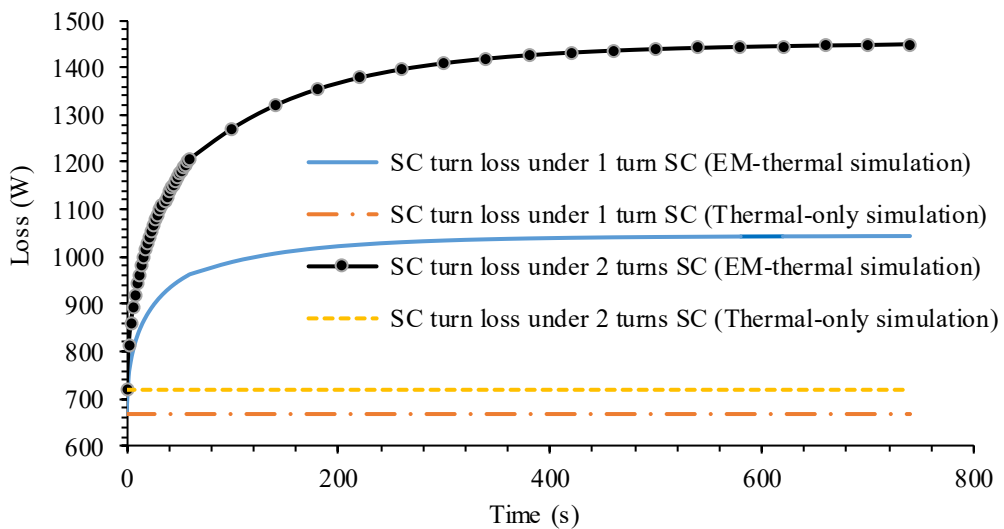


Fig. 5-12. Comparison of the SC turn loss under 1 turn SC and 2 turns SC at 4000 rpm between two simulated methods.

Fig. 5-13 shows the temperature distributions of the prototype at 780s under F3 predicted by the two simulation methods in the same range of temperature scaling, while Table 5-5 compares the temperature distributions in different parts of the machine at 780s. It is obvious that the resultant temperatures predicted by the EM-thermal coupled simulation are also much greater than those by the thermal-only simulation.

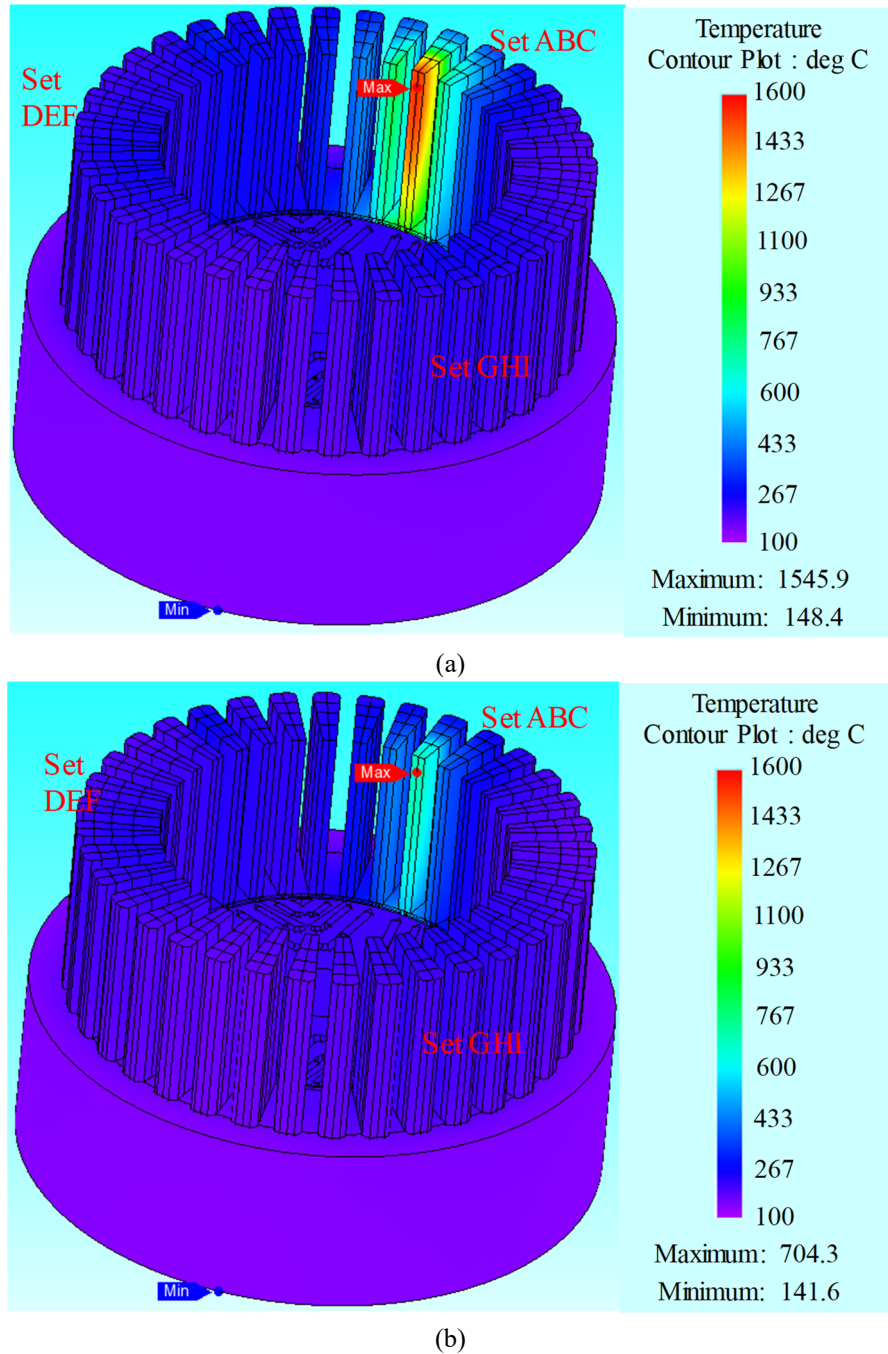


Fig. 5-13. Temperature distribution under F3 at 780s between two simulated methods. (a) EM-thermal coupled simulation. (b) Thermal-only simulation.

Table 5-5 Comparison of temperature values in different parts at 780s under two turns SC at 4000 rpm.

Component temperature	EM-thermal simulation	Thermal-only simulation	Difference
Rotor (°C)	225	209	16
Shaft (°C)	224	210	14
Magnet (°C)	225	210	15
Stator (°C)	193	173	20
Phase D (°C)	221	204	17
Phase E (°C)	207	195	12
Phase F (°C)	208	196	12
Phase G (°C)	206	194	12
Phase H (°C)	207	195	12
Phase I (°C)	206	194	12
Phase A (°C)	297	227	70
Phase C (°C)	262	215	47
Phase B healthy (°C)	384	271	113
SC turn (°C)	672	405	267
Hotspot (°C)	1546	704	842

It is worth noting that under thermal-only simulation, the average temperatures of the machine under two turns SC fault at 4000 rpm are very similar with those under one turn SC fault at 4000 rpm as shown in Table 5-4 and Table 5-5 but with smaller temperatures of SC turn and hotspot. This is because that the difference of the total loss under F3 and F2 is relatively small albeit the region covered by the fault loss under F3 is 2 times larger than that under F2, leading to lower hotspot temperatures under thermal-only simulation. Therefore, it can be concluded that the two turns SC is less severe than one turn SC in this machine. However, it is not true under EM-thermal coupled simulation. Although the region covered by the fault loss under F3 is still 2 times larger than that under F2, as the SC turn loss under F3 is quite higher than that under F2, the temperatures of the machine under two turns SC fault at 4000 rpm are much higher than those under one turn SC fault at 4000 rpm, especially the hotspot temperature. Therefore, the two turns SC is more severe than one turn SC in this machine which demonstrating the necessity of the EM-thermal coupled simulation under two turns SC at 4000 rpm.

5.3.4 Three Turns Short-Circuit at 4000rpm

Three turns SC fault at 4000 rpm, denoted as F4, is also simulated. Fig. 5-14 compares the total copper loss in the faulted one turn under 1 turn SC and in the faulted three turns under 3 turns SC between two simulated methods over the time duration of 780s. It can be seen that the SC turn losses under F4 are smaller than those under F2 both under EM-thermal coupled and thermal-only simulations. Moreover, the region covered by the fault

loss under F4 is 3 times larger than that under F2, leading to lower temperatures compared with that under F2.

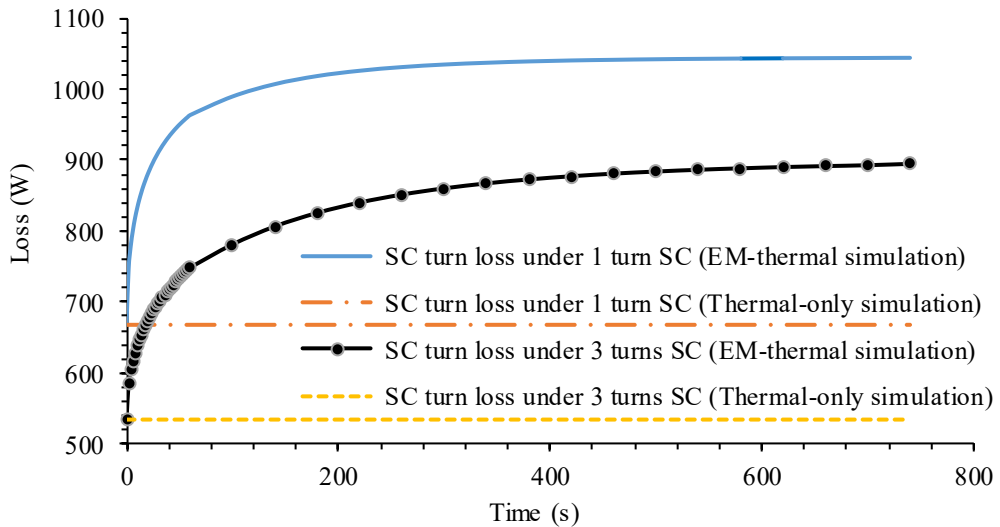


Fig. 5-14. Comparison of the SC turn loss under 1 turn SC and 3 turns SC at 4000 rpm between two simulated methods.

Fig. 5-15 shows the temperature distribution of the prototype at 780s under F4 predicted by the EM-thermal coupled simulation, while Table 5-6 compares the temperature distributions in different parts between two simulation methods of the machine at 780s.

The resultant temperatures predicted by the EM-thermal coupled simulation are still much greater than those by the thermal-only simulation. Moreover, the temperatures of the machine under three turns SC fault at 4000 rpm are much lower than those under one turn SC fault and 2 turns SC fault at 4000 rpm. This means that the two turns SC which is F3 is the most severe fault in this machine in respect of thermal behaviour.

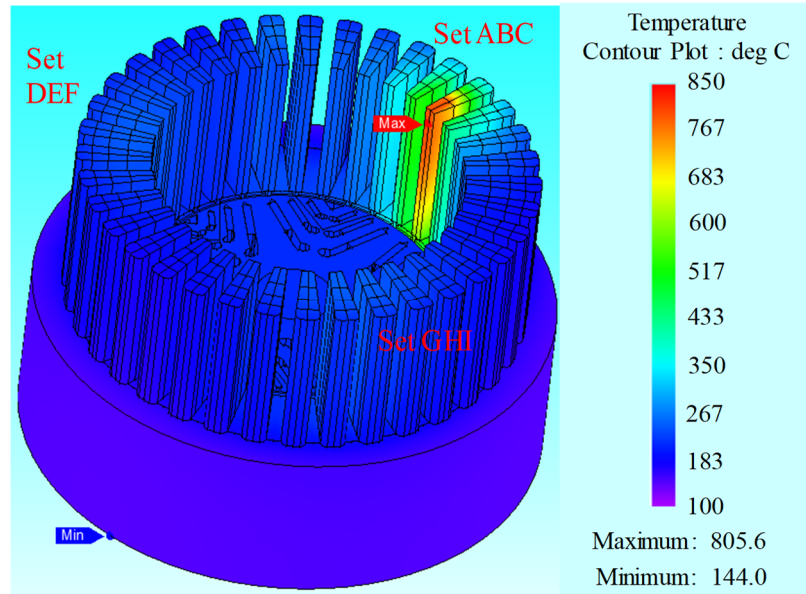


Fig. 5-15. Temperature distribution under F4 at 780s by EM-thermal coupled simulation.

Table 5-6 Comparison of temperature values in different parts at 780s under three turns SC at 4000 rpm.

Component temperature	EM-thermal simulation	Thermal-only simulation	Difference
Rotor (°C)	423	309	114
Shaft (°C)	213	206	7
Magnet (°C)	237	217	20
Stator (°C)	180	169	11
Phase D (°C)	205	196	9
Phase E (°C)	200	193	7
Phase F (°C)	200	193	7
Phase G (°C)	200	193	7
Phase H (°C)	211	203	8
Phase I (°C)	210	203	7
Phase A (°C)	266	224	42
Phase C (°C)	301	250	51
Phase B healthy (°C)	261	220	41
SC turn (°C)	246	216	30
Hotspot (°C)	806	497	309

5.3.5 One Turn Short-Circuit with 3-Phase Terminal SC at 4000rpm

Fault F5 is one turn SC with 3-phase terminal SC at 4000 rpm. The time interval of 40s is used in the first 30 steps and 300s is used in the last 17 steps. The total simulation time is 6300s. Fig. 5-16 and Fig. 5-17 show the current and the copper loss variations of different winding parts of faulted 3-phase set ABC with simulation steps (time). Step zero is healthy condition and fault condition begins from the step 1. It can be observed that when the fault occurs, the currents and losses change rapidly from the healthy values initially and vary slightly during the first a few steps, reaching steady state afterwards.

Fig. 5-17 also compares the copper loss variations of faulted 3-phase set ABC between two simulation methods which are quite close. This indicates that the EM-thermal coupled temperature effect on the resistances, currents and on the losses as well on the steady-state temperatures under F5 is insignificant. The observation is, indeed, confirmed by similar temperature distributions at 6300s predicted by the EM-thermal coupled simulation and by the thermal-only simulation as illustrated in Fig. 5-18 and Fig. 4-35, respectively, as well as in Table 5-7. The differences in different parts between two simulation methods are within 6°C. The hotspot (233°C) located in the middle part of the end windings of the healthy 3-phase sets under EM-thermal coupled simulation is higher than that under thermal-only simulation (226°C) which is still lower than that under healthy condition (235°C).

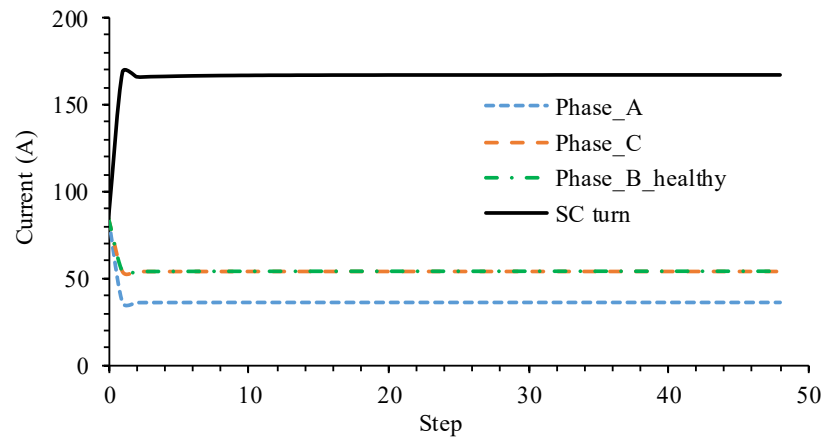


Fig. 5-16. Current variation of faulted 3-phase set ABC with simulation step (time) under F5 under EM-thermal coupled simulation.

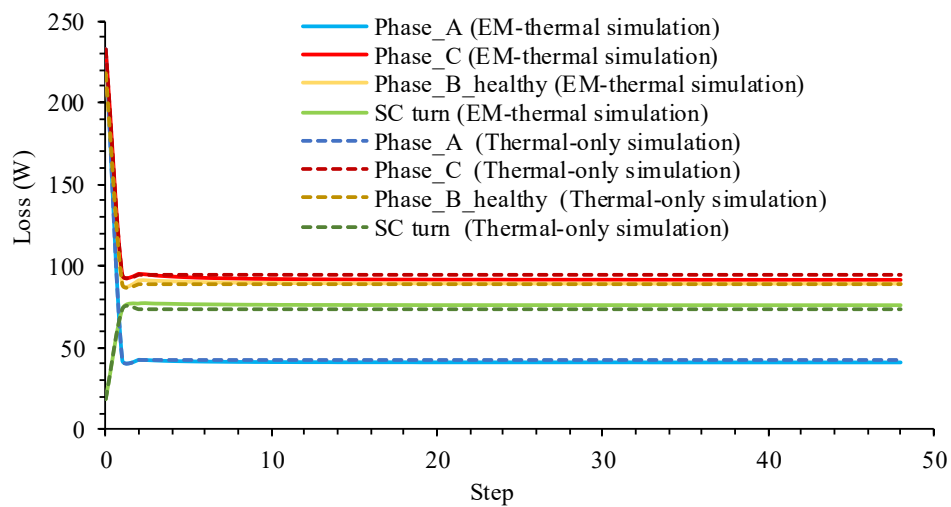


Fig. 5-17. Loss variation of faulted 3-phase set ABC with simulation step (time) under F5 between EM-thermal coupled and thermal-only simulations.

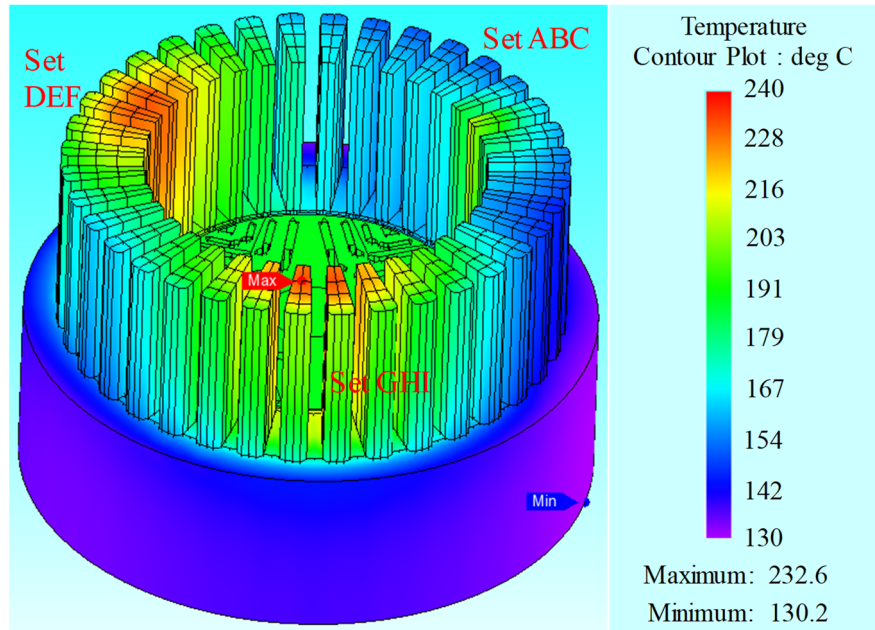


Fig. 5-18. Temperature distribution under F5 at 6300s under EM-thermal coupled simulation.

Table 5-7 Comparison of temperature values in different parts at 6300s under one turn SC with 3-phase terminal SC at 4000 rpm.

Component temperature	EM-thermal simulation	Thermal-only simulation	Difference
Rotor (°C)	189	188	1
Shaft (°C)	190	189	1
Magnet (°C)	189	188	1
Stator (°C)	152	151	1
Phase D (°C)	185	183	2
Phase E (°C)	186	184	2
Phase F (°C)	186	184	2
Phase G (°C)	186	185	1
Phase H (°C)	184	182	2
Phase I (°C)	186	184	2
Phase A (°C)	154	154	0
Phase C (°C)	156	156	0
Phase B healthy (°C)	164	164	0
SC turn (°C)	181	179	2
Hotspot (°C)	233	227	6

Fig. 5-19 shows the transient temperature responses of different winding parts of faulted 3-phase set ABC during the simulation. It shows that the temperatures of phase A, phase C and healthy part of phase B decrease with time while the temperature of the SC turn increases initially due to the increase in the turn loss and decreases afterwards because of the reduction of the copper loss in the other parts of faulted 3-phase set.

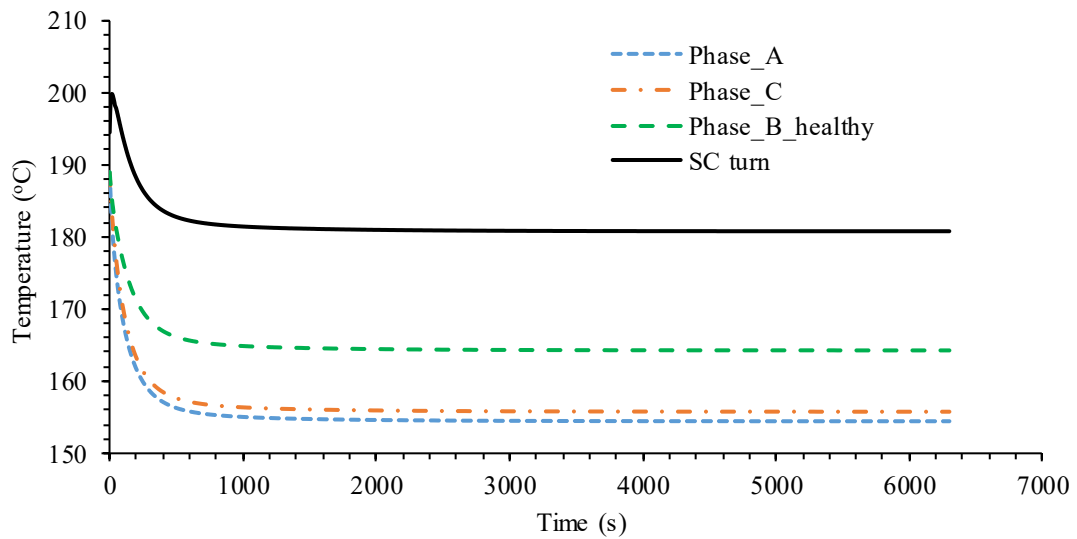


Fig. 5-19. Transient temperature responses. (a) Average temperature of different winding parts. (b) Hotspot.

5.4 Discussion

The results of the study show that under F5 the temperatures predicted by thermal only simulation does not differ significantly from those of EM-thermal coupled simulation. This is because the machine loss in the fault region is under effective control and hence the temperature increase is relatively small. While this demonstrates the effectiveness of the mitigation for the machine under study, the condition cannot be assumed true generally. For example, if a design or mitigation measure is less effective in managing the fault, the fault current may be much high and the thermal only simulation may significantly underestimate the hot spot temperature.

Hence, EM-thermal coupled simulation is necessary for assessing fault behaviour of a machine in design stages when fault current is reactance limited and the resultant heating effect is very significant. The scenario is very much dependent on design and mitigation measures employed. To our knowledge, there is no quantitative rule-of-thumb technique to determine whether thermal-only simulation is adequate without performing EM-thermal coupled simulation first.

For assessing the fault behaviours without mitigation, EM-thermally coupled simulation is necessary. This type of simulation will be useful to evaluate how long the machine can survive for example. Clearly, complete damage to insulation will occur at temperature significantly greater than the thermal index temperature, and the rate of

change of temperature will be significantly underestimated in thermal-only simulation. Moreover, it could give a more accurate study on the influence of number of SC turns on thermal behaviour.

Likewise, when the fault current is resistance limited, the thermal only simulation will overestimate the hot spot temperature. Again, if it is necessary to assess more accurately how long the machine can survive under this fault condition, EM-thermal couple simulation will be necessary.

5.5 EM and Thermal Behaviours for the PMASynRM with Stranded Conductors

Since the proposed machine has 17 parallel strands per turn for reducing AC losses, the possibility and reality of the SC between a few strands of two different turns is quite large. Moreover, with a few strands short-circuited, the flux linkage and inductances of the SC strands are likely to be similar to that of the complete inter turn SC involving all strands, while the resistance of the SC strands is much higher than that of the complete SC. Therefore, the temperature effects during fault transient will be more significant.

Moreover, since the number of possible SC faults involving a given number of strands and turns is significant, the electromagnetic performance of various common possible SC faults, such as inter-strand SC (turn SC between different parallel strands) and intra-strand SC (SC with different number of turns within a strand), have been analysed in this section. Furthermore, all the fault conditions are considered at the rated operation (rated torque at the base speed 4000rpm). In addition, to reduce the large computation time and complexity, EM-thermal coupled simulation is adopted under inter-strand SC to obtain the most severe fault in respect of thermal behaviour.

5.5.1 2D EM Model and 3D Thermal Model

The PMASynRM with 2 series connected coils per phase and each coil having 8 turns with 17 parallel strands is illustrated in Fig. 5-20. The inter-strand and intra-strand SC faults are assumed to occur in coils B2 and B4 close to the slot opening because of the highest SC current and copper loss as a result of the mutual coupling between the two healthy 3-phase sets and the fault 3-phase set. In order to reduce the model complexity and simulation time, each strand in a turn is individually modelled as a rectangle of the

same cross-sectional area for only four coil sides of phase B, B1, B2, B3 and B4. These are idealised representation since in reality the exact location of a turn or a strand is unknown in the mush winding of the prototype machine. Fig. 5-20 illustrates the detail of the modelled B2 and B4 coils with one turn SC involving a single strand marked by the grey rectangles.

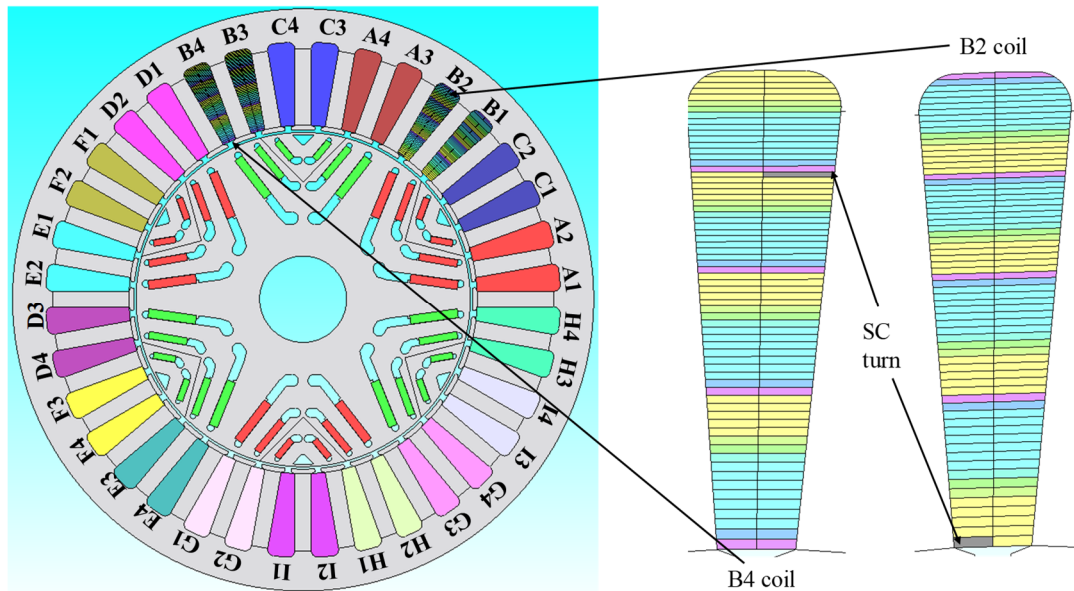


Fig. 5-20. Cross section of a PMASynRM with phase B dividing 17 strands per turn.

The circuit of the PMASynRM EM model is illustrated in Fig. 5-21. Only phase B is modelled with 17 parallel paths, each represents a parallel strand, while the other phases have just one path. In the circuit, the coil sides of phases A, C, D, E, F, G, H, I are denoted as A_P, C_P, D_P, E_P, F_P, G_P, H_P, I_P for positive current, and as A_N, C_N, D_N, E_N, F_N, G_N, H_N, I_N for negative current respectively. Similar notations are used for phase B with parallel strands indicated by B_Si_P/N, where $i = 1, 2, 3, \dots, 17$ denotes the i^{th} strand, and P and N denotes the positive and negative current flows. It should be noted that the predicted ideal phase resistance is adopted in this section which is slightly lower than the measured resistance given in Table 4-4 in Chapter 4 and in sections 5.3 in Chapter 5.

Because of the significant computation time and data storage, the EM-thermal simulation is only performed for inter-strand SC faults to assess the worst fault condition for the general understanding. Moreover, in order to reduce the complexity, the 1/3 3D thermal model with even loss distribution is adopted as shown in Fig. 5-22 where each individual strand of one turn in B2 and B4 coils is individually modelled.

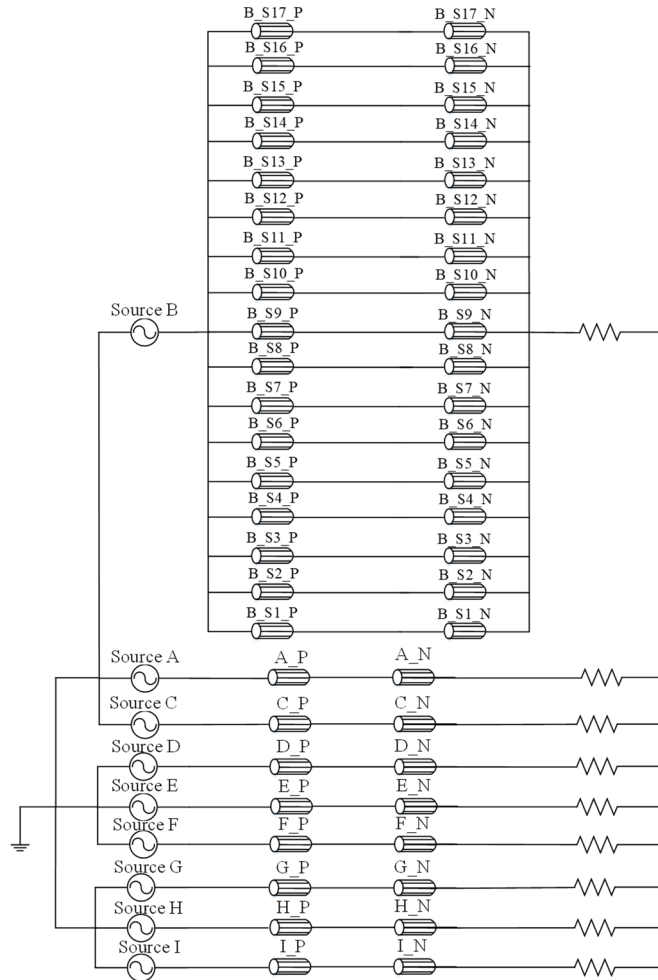


Fig. 5-21. Circuit of a PMASynRM with phase B dividing 17 parallel strands.

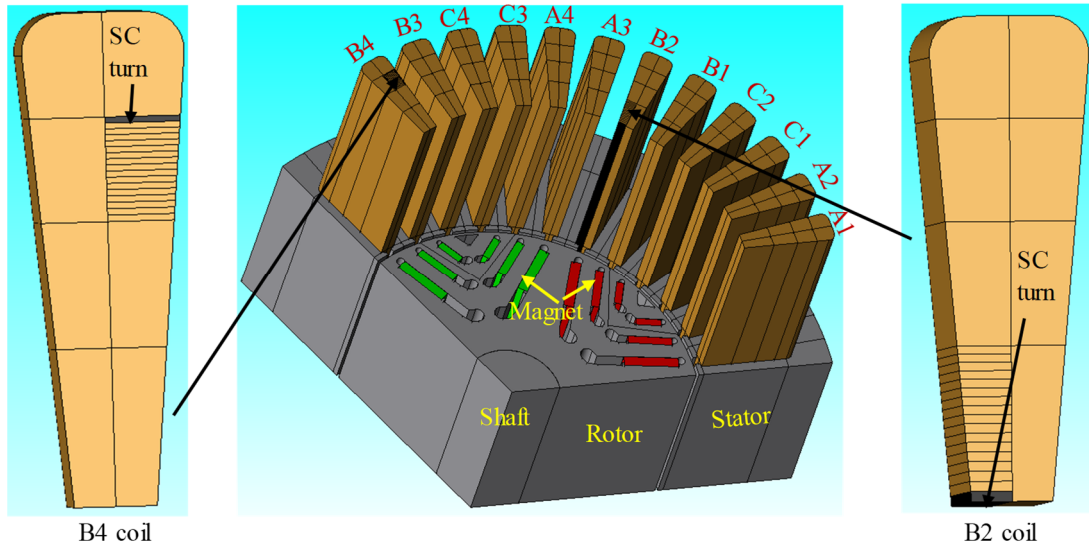


Fig. 5-22. 1/3 3D thermal model with 17 turns individually modelled in B2 and B4 coils.

It should be noted that the EM and thermal behaviours for the motor with stranded coils are simulated under different conditions from those for the motor considering 17

strands as a whole. The simulation results are only compared in this section to assess fault severity.

5.5.2 EM Characteristics for the PMASynRM with Stranded Conductors

The electromagnetic performances under healthy condition and various possible SC faults, such as inter-strand SC and intra-strand SC, have been analysed in this section.

5.5.2.1 Healthy Condition

Under no-load condition, the no-load flux linkage waveforms of the 17 parallel strands of phase B are illustrated in Fig. 5-23. As observed, the no-load flux linkage of each strand represented by S_i , where $i = 1, 2, 3, \dots, 17$, is essentially the same, implying that no significant PM flux leaks to the slots.

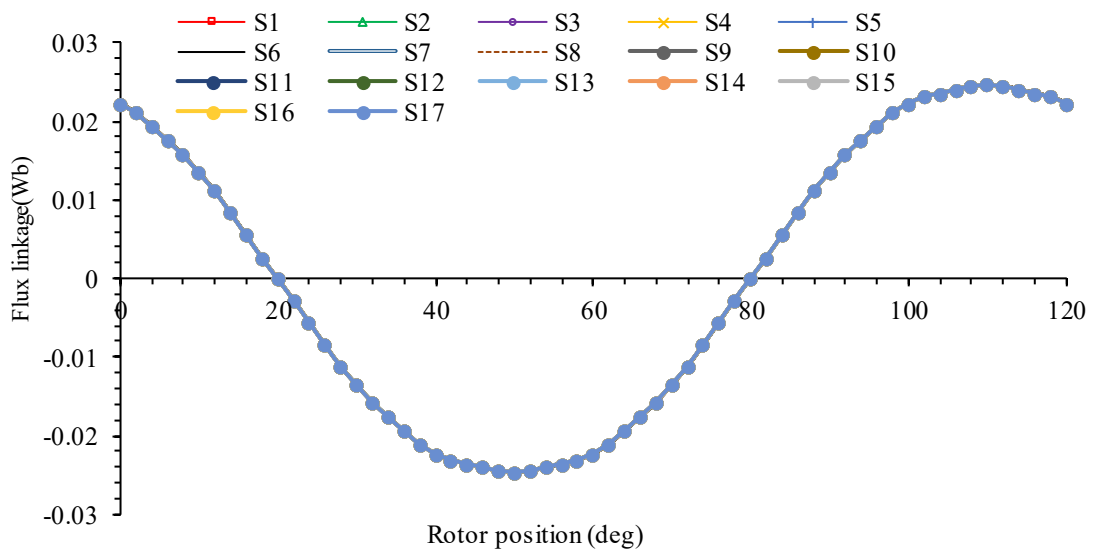


Fig. 5-23. No-load flux linkage waveforms of the 17 parallel strands of phase B.

In the rated operation (rated torque at the base speed 4000rpm), the phase currents are excited with the rated value 120A for MTPA operation. The resultant current waveforms of the 17 parallel strands of phase B are plotted in Fig. 5-24. As observed, the current of each strand differs slightly due to the armature reaction flux leakage in different locations of each strand.

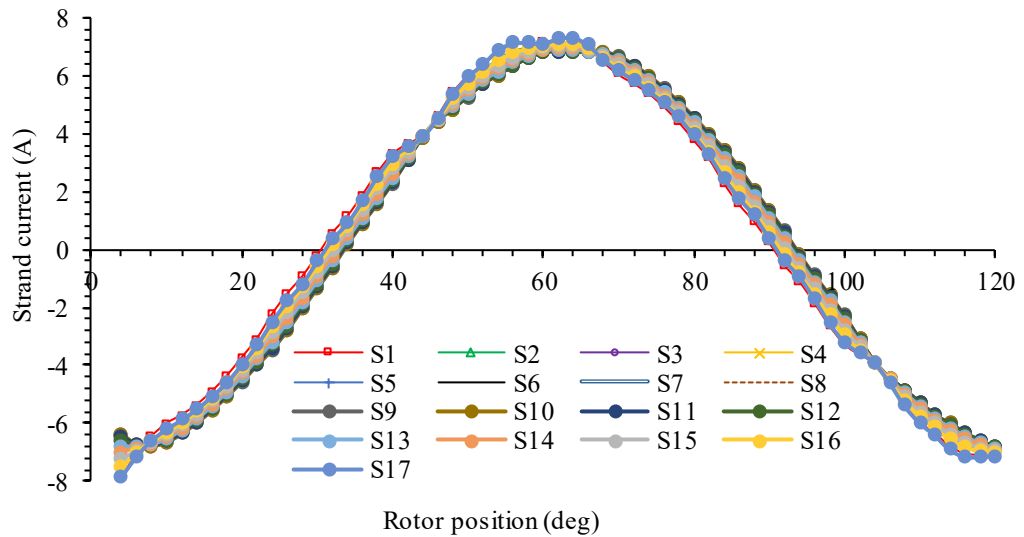


Fig. 5-24. Current waveforms of the 17 parallel strands of phase B at rated operation.

5.5.2.2 Fault Conditions

The SC faults mainly investigated in this section are inter-strand SC and intra-strand SC. The inter-strand SC fault occurs when the insulation between a number of parallel strands across a number of turns breaks down, while the intra-strand SC fault happens when the insulation of the same strand across a different number of turns fails. The electromagnetic performance of the machine under these faults have been analysed and compared in the following section by using the 2D EM model as shown in Fig. 5-20.

5.5.2.2.1 Inter-Strand SC Fault

The inter-strand SC fault may involve in a number of parallel strands varying from one to 17. Fig. 5-25 (a) and (b) illustrate the circuits of phase B for the turn-to-turn SC within one strand and the turn-to-turn SC of 17 parallel strands. As is shown, the healthy and fault strands are divided and indicated by $B_S_i_{h/f_P/N}$ ($i=1, 2, 3, \dots, 17$) where h and f denotes the healthy and fault turns under the fault conditions. The circuits of the other phases are the same as those shown in Fig. 5-21.

For comparison of the worst case with non-stranded coils, the faulted strands are assumed to be short circuited across one turn.

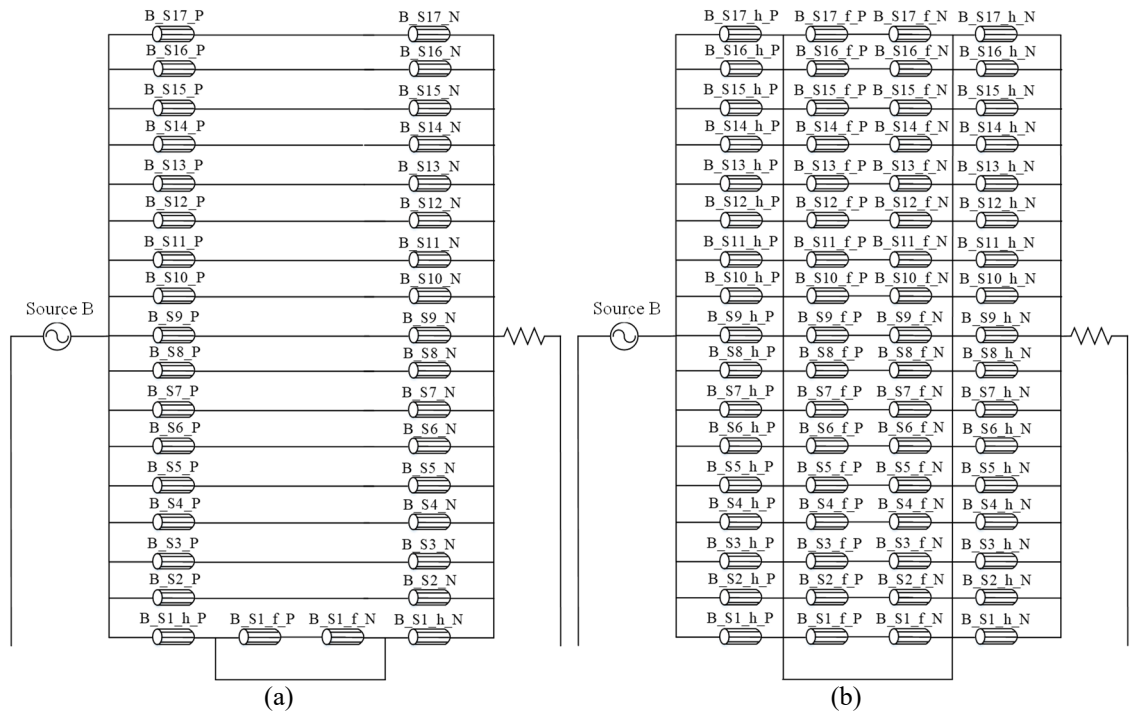


Fig. 5-25. The circuit of phase B with inter strand faults. (a) Turn SC with one strand. (b) Turn SC with 17 parallel strands.

For the windings with non-stranded coils, as previously analysed, the reactance of a single turn at the rated speed denoted as ωL_{fm} is far larger than the resistance denoted as R_{fm} in the SC path shown in Fig. 5-1. However, when considering one turn SC of individual strands, the resistance of one faulted strand R_{fs} is 17 times larger than R_{fm} , while the inductance L_{fs} does not change significantly. Therefore, for each strand, the resistance is larger than the reactance of one turn at the rated speed of this machine.

The illustration of one turn SC occurred in parallel strands is given in Fig. 5-26. I_f is the total turn fault current, I_{strand} is the fault current in each strand, E_{fm} is the emf of the faulted strand, R_{fs} is the resistance and L_{fs} is the inductance of each faulted strand and N_{strand} is the number of faulted parallel strands.

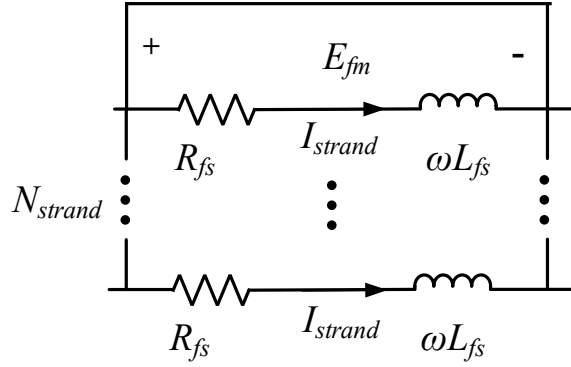


Fig. 5-26. Illustration of turn SC with different number of parallel strands.

I_{fm} and I_{strand} may be estimated in (5-3) and (5-4), respectively, assuming they are not affected by the current in the healthy strands and that the mutual couplings between the parallel strands are ideal:

$$I_{fm} = \frac{E_{fm}}{\sqrt{(R_{fs} / N_{strand})^2 + (\omega L_{fs})^2}} \quad (5-3)$$

$$I_{strand} = \frac{I_{fm}}{N_{strand}} = \frac{E_{fm}}{\sqrt{R_{fs}^2 + (N_{strand} \omega L_{fs})^2}} \quad (5-4)$$

Apparently, with the increase in the number of faulted parallel strands N_{strand} , the total resistance which is inversely proportional to N_{strand} in the SC path decreases, while the reactance and the induced emf in the SC path remains almost the same. Thus the total turn fault current I_f increases with the increase in N_{strand} , while the fault current of each strand I_{strand} decreases with the increase in N_{strand} .

The resultant copper loss in each strand P_{strand} and the total copper loss of all the faulted strands P_{fm} are given in (5-5) and (5-6), respectively:

$$P_{strand} = I_{strand}^2 R_{fs} = \frac{E_{fm}^2 R_{fs}}{R_{fs}^2 + (N_{strand} \omega L_{fs})^2} \quad (5-5)$$

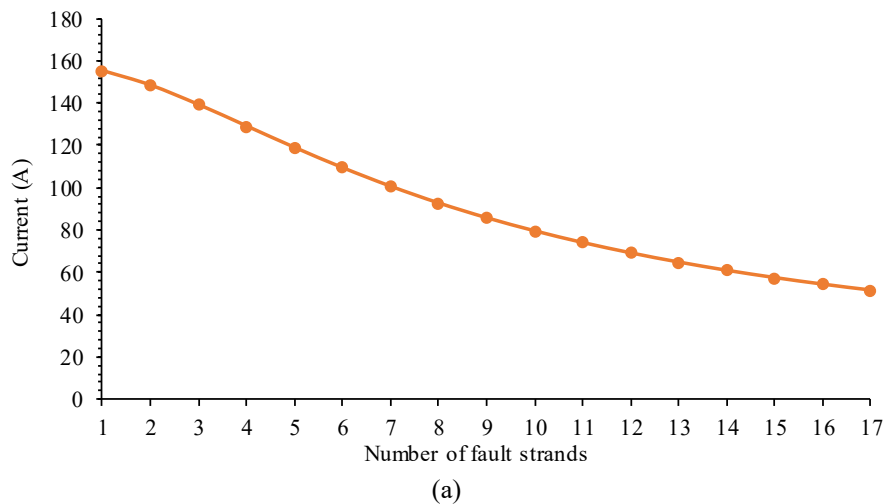
$$P_{fm} = N_{strand} P_{strand} = \frac{N_{strand} E_{fm}^2 R_{fs}}{R_{fs}^2 + (N_{strand} \omega L_{fs})^2} \quad (5-6)$$

It is seen that with the increase in number of faulted parallel strands N_{strand} , the resultant copper loss in each strand P_{strand} decreases. In this machine, as R_{fs} is larger than $\omega_r L_{fs}$ under one turn SC at the rated speed, the total copper loss of all the faulted strands

P_{fm} firstly increases, reaches the peak value and decreases with the number of faulted parallel strands.

The above estimation assumes the current in each strand is the same. However, the current in each strand would be different in FE simulations because the difference in the strand locations and resultant leakage flux.

The trends predicted by the above estimations are validated by 2D FE simulation. The current in each strand is slightly different because the difference in locations and resultant leakage flux. Fig. 5-27 shows the variations of the resultant average RMS fault current in each strand and the losses with the increase in the number of fault parallel strands under one turn SC. As is observed in Fig. 5-27 (a) and (b), with the increase in the number of the faulted parallel strands, the fault current and the resultant copper loss in each strand decrease. The total loss of the SC fault and the loss of phase B increase first, reach their peaks when 6 parallel strands are short-circuited across one turn, and decrease afterward with the increase in the number of faulted parallel strands. This indicates that at 4000rpm the resistance is the dominant component of the impedance in the SC path if the number of short-circuited parallel strands is below 6. It should be noted that because of the ideal current sources for the healthy phases are used in the FE model, the losses of the other phases are the same as those under the healthy condition.



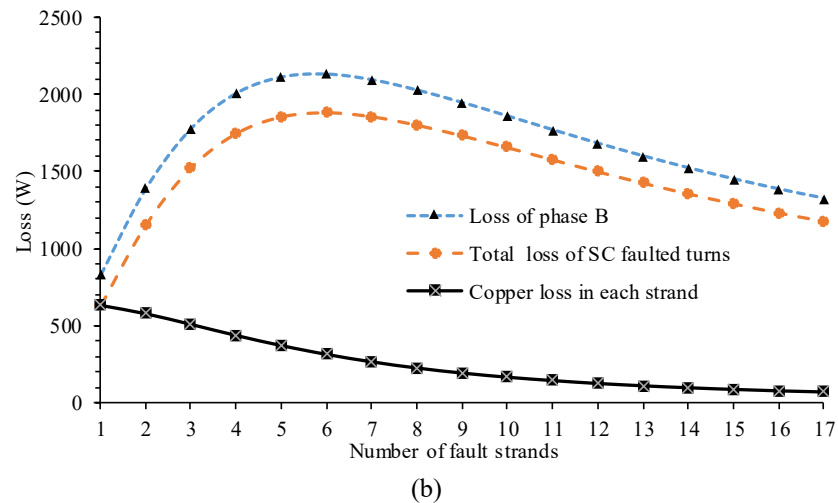


Fig. 5-27. Variations of fault current and loss with number of faulted parallel strands under one turn SC fault. (a) Average RMS fault current in each strand. (b) Losses.

5.5.2.2.2 Intra-Strand SC Fault

The intra-strand SC fault occurs when the insulation of a single strand across a number of turns fails. The number of SC turns may vary from 1 to 16. Fig. 5-28 (a) illustrates the circuit of phase B with an intra-strand fault in which the number of SC turns can vary from 1 to 15 by adjusting the number of turns associated with the conductors B_S1_f_P and B_S1_f_N, and the conductors B_S1_h_P and B_S1_h_N. Fig. 5-28 (b) illustrates the circuit of phase B for the intra-strand SC fault with 16 turns, where the number of turns associated with the conductors B_S1_f_P and B_S1_f_N is 16. The circuits of the other phases are the same as those shown in Fig. 5-21.

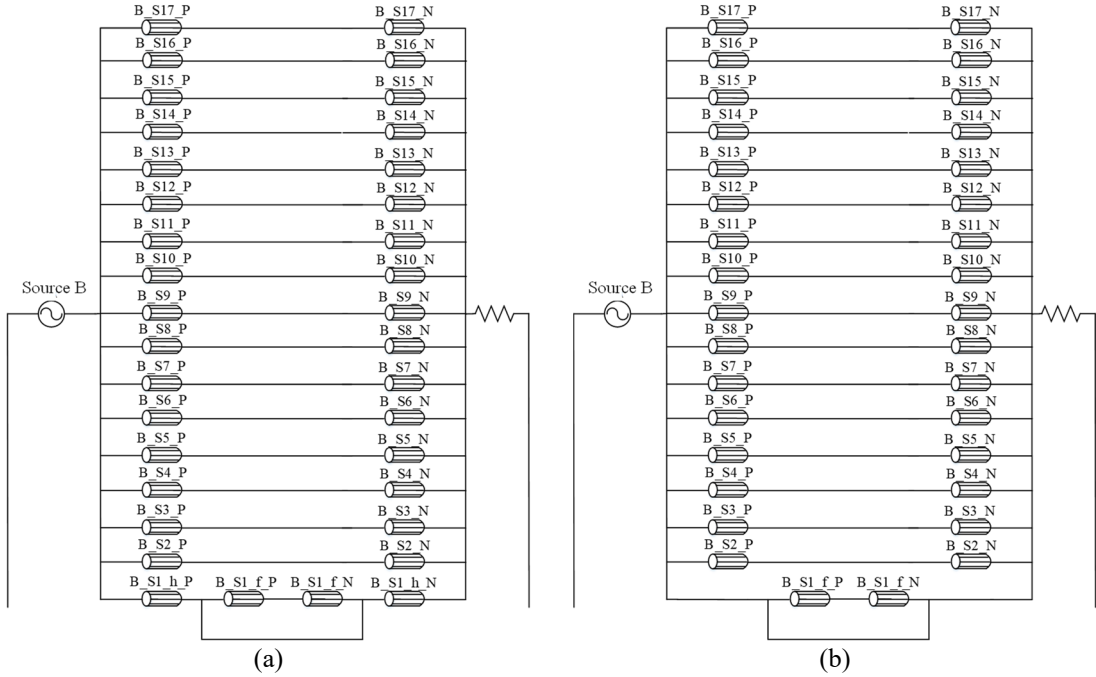


Fig. 5-28. The circuit of phase B with intra-strand SC fault. (a) 1 to 15 SC turns within one strand. (b) 16 SC turns within one strand.

As has been analysed previously, the resistance of one turn in one strand is larger than the reactance of one turn at the rated speed, an intra strand fault with one SC turn may not be the worst case.

Fig. 5-29 shows simplified circuit of the intra-strand fault. N_{turn} is the number of SC turns.

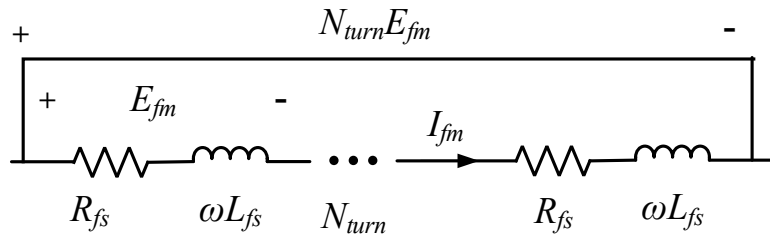


Fig. 5-29. Illustration of different turns SC within one strand.

The turn fault current I_{fm} , the resultant copper loss per SC fault turn P_{turn} and the total copper loss of all the faulted turns P_{fm} are estimated in (5-7), (5-8) and (5-9), respectively:

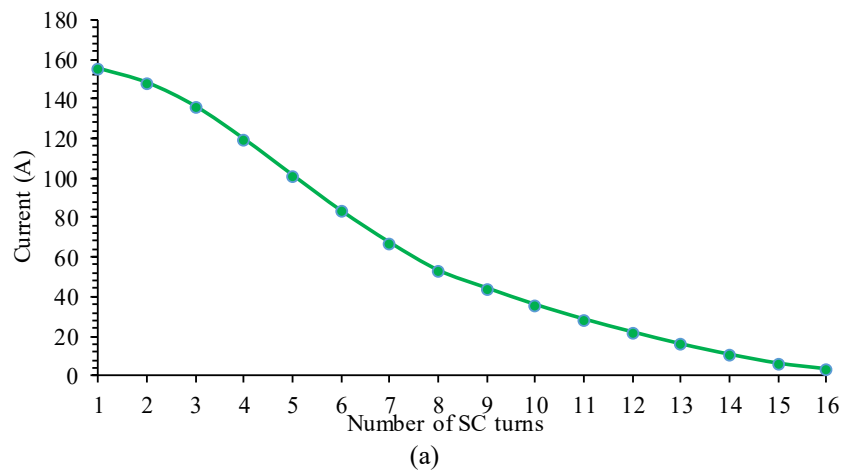
$$I_{fm} = \frac{N_{turn} E_{fm}}{\sqrt{(N_{turn} R_{fs})^2 + (N_{turn}^2 \omega L_{fs})^2}} \quad (5-7)$$

$$P_{turn} = I_{fm}^2 R_{fs} = \frac{E_{fm}^2 R_{fs}}{R_{fs}^2 + (N_{turn} \omega L_{fs})^2} \quad (5-8)$$

$$P_{fm} = N_{turn} P_{turn} = \frac{N_{turn} E_{fm}^2 R_{fs}}{R_{fs}^2 + (N_{turn} \omega L_{fs})^2} \quad (5-9)$$

Apparently, with the increase in number of SC turns N_{turn} , the resistance and the induced emf in the SC path increase linearly with the number of the faulted turns, while the reactance in the SC path increases with the square of the number of the faulted turns. Thus with the increase in N_{turn} , the turn fault current I_{fm} and the resulted copper loss per SC turn P_{turn} decrease, while the total copper loss of all the faulted turns P_{fm} increases initially, reaches the peak value and decreases afterward.

The above predictions are validated by 2D FE simulation in Fig. 5-30 which shows the variations of the resultant RMS fault current and losses with the number of SC turns within one strand. It is seen from Fig. 5-30 (a) and (b) that the SC turn fault current and the resulted copper loss per SC turn decrease with the increase in the number of SC turns. However, the total loss of the faulted turns and the loss of phase B increase first and reach their peaks when 4 turns in one strand is short-circuited. This indicates that at 4000rpm the resistance is dominant in the impedance of the SC path when $N_{turn} < 4$ while the reactance becomes dominant $N_{turn} > 4$ for an SC fault in one strand.



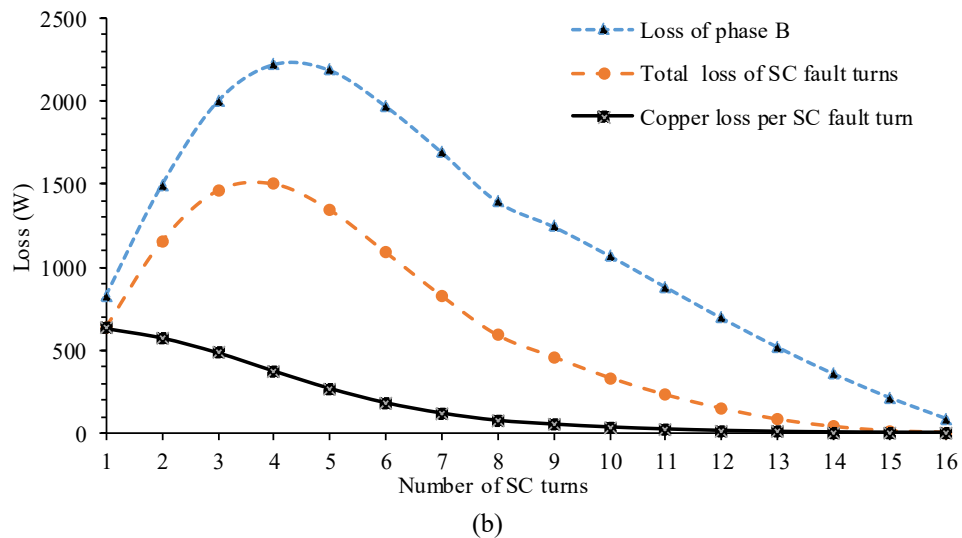


Fig. 5-30. Variations of fault current and losses with the number of SC turns within one strand. (a) Fault current. (b) Losses.

5.5.3 EM-thermal Coupled Simulation under Inter-Strand SC Conditions

However, it is impossible to infer the worst case only by the EM simulations. This is because, for example, under inter-strand fault condition, the one turn SC involving one strand has the largest loss in each strand but the total copper loss under this fault condition is smaller than that under one turn SC with 6 strands. Therefore, the thermal simulation is essential for obtaining the most severe fault in respect of thermal behaviour.

In contrast, as discussed in section 5.4, the thermal-only simulation would overestimate the temperatures under resistance-limited faults while underestimate the temperatures under reactance-limited faults. When the coils with non-stranded conductors is considered, the resistance limited condition appears at low speed (500rpm), and the resultant SC current is relatively small. Consequently, the EM-thermal coupled simulation can only improve accuracy slightly. However, the above analysis shows that the losses with faulted strands at the rated speed are all quite large under both resistance- and reactance-limited conditions as illustrated in Fig. 5-27 and Fig. 5-30. Thus, the EM-thermal simulation should be adopted for analysis of the severity of each fault in respect of thermal behaviour with much higher accuracy.

By way of example, the EM-thermal coupled simulation is employed to assess the thermal behaviour under inter-strand SC faults and to identify the most severe fault condition.

Firstly, as discussed in section 5.5.2.2.1, one turn SC within one strand is a resistance-limited SC fault. The resultant SC current and SC copper loss predicted from the EM-thermal coupled simulation in the faulted strand decrease with increases in temperature and hence in the turn resistance as shown in Fig. 5-31 (a) and (b), respectively. In addition, the reduction of the copper loss in the SC strand is quite large.

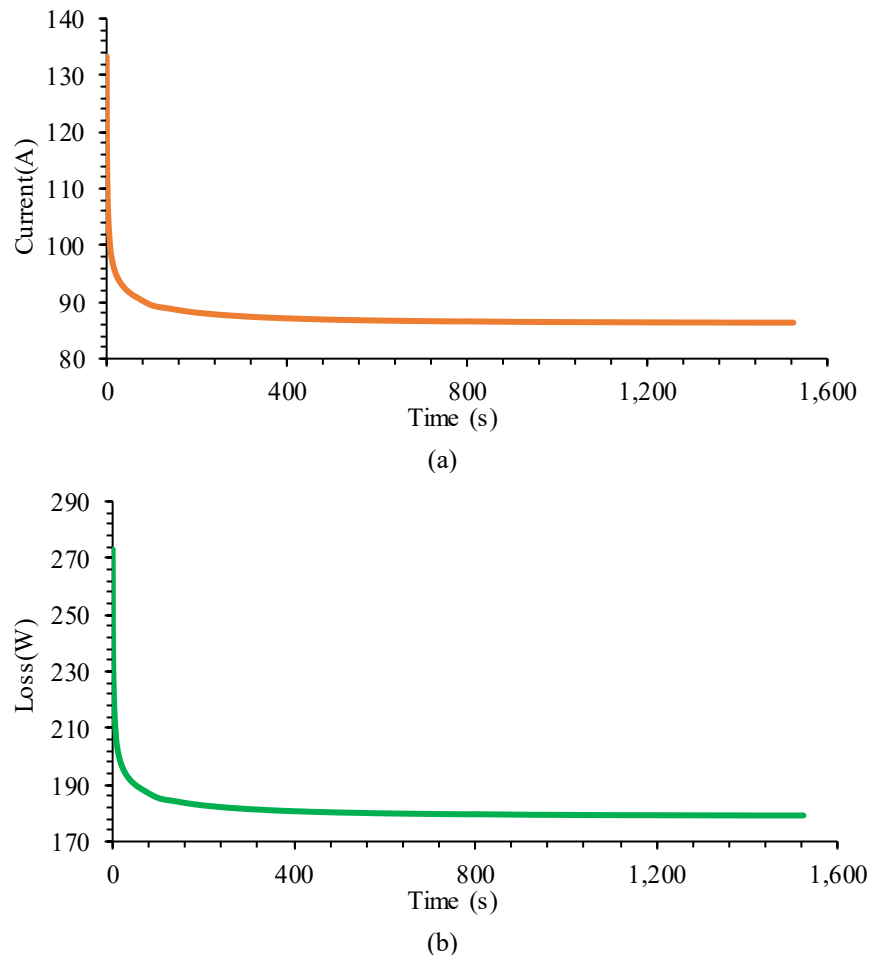
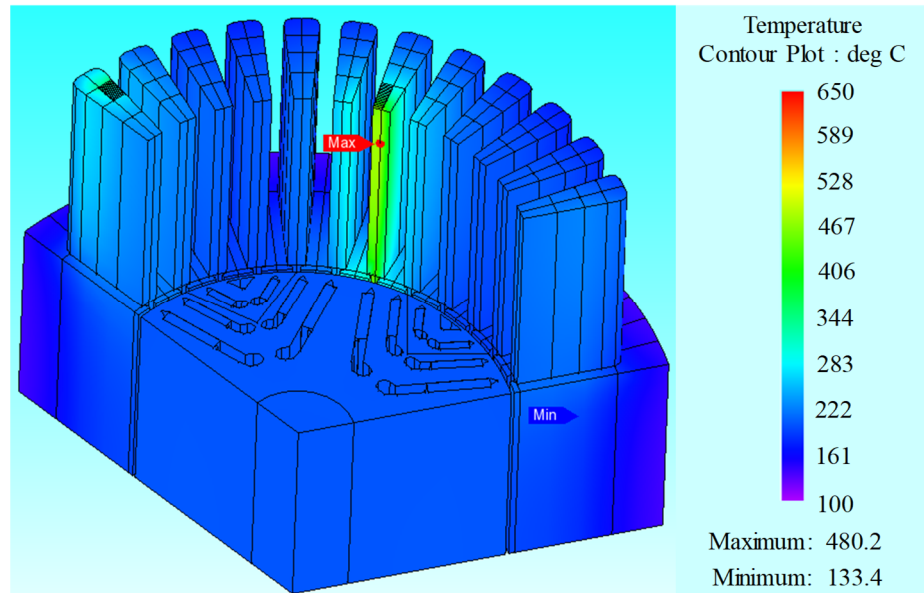


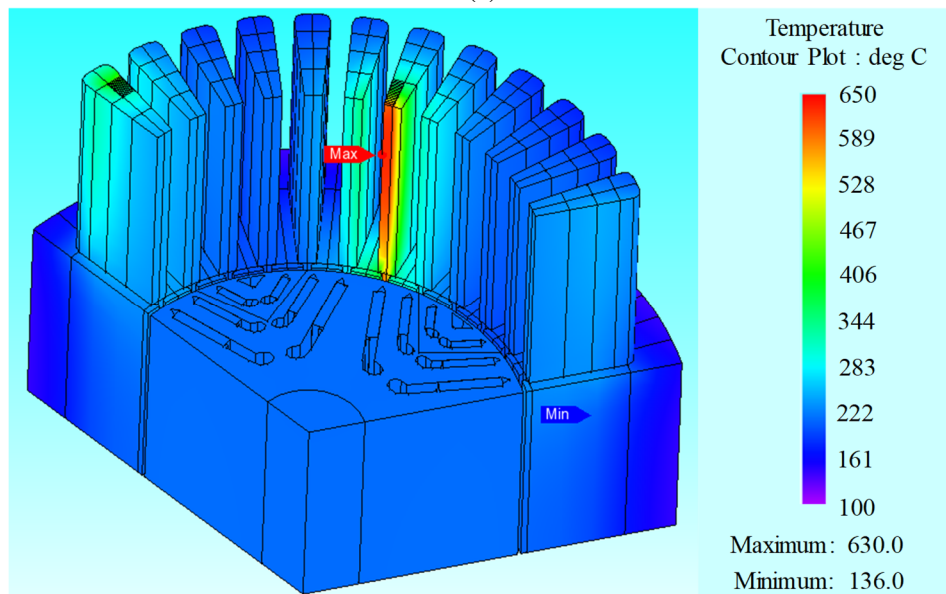
Fig. 5-31. Fault performance with the increase in times under one turn SC within one strand at 4000 rpm. (a) SC current. (b) Copper loss in the SC turn.

The temperature distributions of the motor at 1560s under one turn SC within one strand at the rated speed predicted by the EM-thermal coupled and thermal-only simulations are compared in Fig. 5-32 (a) and (b), respectively, in the same range of temperature scaling. It is evident that the temperatures predicted by the EM-thermal coupled simulation are much lower than those by the thermal-only simulation. The thermal-only simulation overestimates the temperatures in all parts, especially in the hotspot (150°C) at 1560s. Therefore, with increase in temperature when the fault occurs, the SC current decreases, resulting in much lower temperature than that when the

influence of temperature on the fault current is neglected. Thus, it demonstrates that the EM-thermal coupled simulation improves prediction accuracy under the resistance limited condition at the rated speed when the temperature effects on the copper loss of the SC strand is relatively large.



(a)



(b)

Fig. 5-32. Temperature distributions under one turn SC within one strand at rated speed between two simulated methods. (a) EM-thermal coupled simulation. (b) Thermal-only simulation.

The EM-thermal coupled simulation is performed on several fault conditions of inter-strand faults to find the worst case. Based on the losses shown in Fig. 5-27, three cases are considered: (1) one turn SC within one strand with the largest copper loss in the single

strand, (2) one turn SC within 6 strands with the largest total copper loss of the SC fault and (3) one turn SC within 17 strands with all strands short-circuited. The temperature distributions in different parts of the machine at 1560s under these three fault conditions are compared in Table 5-8. It is obvious that due to the large effect of the temperature on the resistance and resultant loss, although one turn SC involving one strand and six strands have the largest loss in the strand and total copper loss, respectively, their SC copper losses in the faulted strands decrease significantly with increases in temperature as a result of the increase in strand resistance. The final temperatures, including hotspot temperatures, are all smaller than those under one turn SC within 17 strands which has both lower loss in each fault strand and total copper loss as shown in Fig. 5-27 but the fault condition is reactance-limited.

Table 5-8 Comparison of temperature values in different parts at 1560s under one turn SC within one, 6 and 17 strands at 4000 rpm.

One turn SC within different parallel strands	One strand	6 strands	17 strands
Rotor (°C)	203	260	308
Shaft (°C)	204	260	307
Magnet (°C)	203	261	308
Stator (°C)	163	208	249
Phase A (°C)	195	261	326
Phase C (°C)	185	232	272
Phase B healthy (°C)	229	394	443
SC turn (°C)	383	706	843
Hotspot (°C)	480	959	1127

Therefore, reactance-limited fault conditions with larger copper loss than one turn SC within 17 strands are assessed. EM-thermal coupled simulations are performed for one turn SC involving 11 strands, 12 strands, 13 strands and 14 strands and their temperature distributions in different parts of the machine at 1560s under these four fault conditions are presented in Table 5-9. It is seen that with the increase in the SC strands, the temperatures of the rotor, shaft, magnet, stator, phase A, phase C and healthy part of phase B increase due to the temperature effects. However, the average temperature of the SC strands and the hotspot temperature under one turn SC within 13 strands are the highest which is the most severe fault under the inter-strand SC fault. The temperature distribution at 1560s under one turn SC within 13 strands is illustrated in Fig. 5-33. It should be noted that the difference in the hot spot temperatures which result from the four fault cases is quite small. In contrast, they all yield excessively high temperature and

hence the damage to the winding insulation will be instant if the fault cannot be detected and mitigated promptly.

Table 5-9 Comparison of temperature values in different parts at 1560s under one turn SC within 11, 12, 13 and 14 strands at 4000 rpm.

One turn SC within different parallel strands	11 strands	12 strands	13 strands	14 strands
Rotor (°C)	297	300	302	304
Shaft (°C)	296	299	301	303
Magnet (°C)	297	300	303	305
Stator (°C)	239	242	244	246
Phase A (°C)	308	313	317	320
Phase C (°C)	263	266	268	270
Phase B healthy (°C)	425	432	437	440
SC turn (°C)	844	850	853	852
Hotspot (°C)	1148	1154	1156	1153

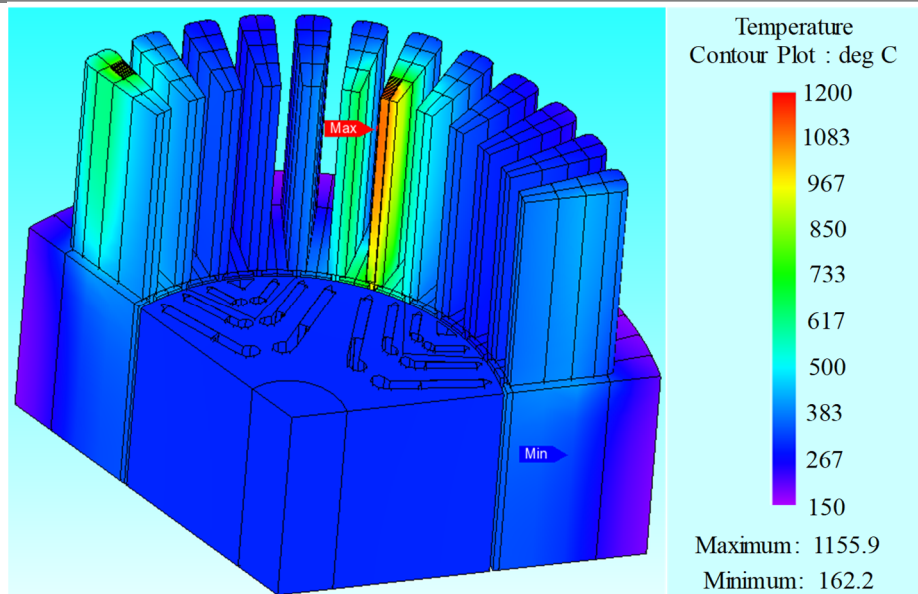


Fig. 5-33. Temperature distribution under one turn SC within 13 strands at 1560s by EM-thermal coupled simulation.

5.6 Summary

This Chapter has performed EM-thermal coupled simulation of a triple redundant, 9-phase PMASynRM with aid of a scripting file. The predicted temperatures by the EM-thermal coupled simulation have been comprehensively compared with those by thermal-only simulation under various faults. It has been shown that at low speed (resistance/reactance limited) or under one turn SC with 3-phase terminal short circuit conditions, the EM-thermal coupled simulation can improve accuracy slightly. However, it is essential to employ the EM-thermal coupled simulation when the fault current is

reactance limited at high speed for the study of the thermal behavior under SC fault conditions.

It has also been shown that two turns SC is more severe thermally than one turn and three turns SC in this machine because of greater loss in the SC turn.

While the temperatures under one turn SC with 3-phase terminal SC predicted by the thermal only and EM-thermal coupled simulations do not differ significantly, this case may not generally be true if the fault current is much greater and the heating effect is more significant, as discussed in section 5.4. In general, it is prudent to perform EM-thermal coupled simulation first to assess if thermal only simulation can be used without significant compromise in accuracy.

Furthermore, this Chapter assesses the electromagnetic behaviour of various possible SC faults when considering each individual strand, such as inter-strand SC and intra-strand SC. It is shown that under inter-strand SC, the resistance is dominant in the impedance of the SC path if the number of short-circuited parallel strands is below 6 while the reactance becomes dominant for the rest. Under intra-strand SC, the resistance is dominant in the impedance of the SC path if the number of short-circuited turns is below 4 while the reactance becomes dominant for the rest. Furthermore, EM-thermal coupled simulations are performed to assess thermal behaviour of one turn SC fault involving in a number of strands. It is shown that the EM-thermal coupled simulation is necessary even if the fault current is resistance limited when the copper loss of the faulted strands is quite large. In addition, the most severe fault is one turn SC within 13 strands among inter-strand SC faults.

In summary, EM-thermal coupled simulations are necessary in fault analysis for fault tolerance due to the accurate prediction of the SC current and temperature distribution in the machine when the SC fault current is influenced by the characteristic of the impedance in the SC path. Moreover, as the same with Chapter 4, the hotspot temperature under one turn SC with a mitigation measure of the 3-phase terminal SC is slightly over the maximum permissible temperature (220°C) because of the non-overlapped end winding layout. Therefore, the insulation material should be changed to improve the maximum permissible temperature to be 240°C to obtain the fault tolerance of the machine.

Chapter 6 Electromagnetic and Thermal Behaviours of the PMASynRM with Insulation Deterioration Fault

6.1 Introduction

Quality of winding insulation is key to the reliability of electrical machines in safety critical applications. However, the winding insulation in electrical machines suffered from combined thermal, electrical, mechanical, and environmental stresses during operation [17]. These stresses result in deterioration of winding insulation and may even lead to short-circuit faults.

Many published papers have studied machine performance under ideal SC fault conditions assuming that the electric resistance of the insulation becomes zero [109] [124] [101]. The work described in [124] investigates the effect of the number of SC turns on SC current and shows that a single-turn SC fault leads to the lowest impedance of the faulty circuit path, resulting in the highest fault current. From this, it can be deduced that a SC fault of one entire phase is less severe. Based on this understanding, most fault detection and mitigation measures reported in literature are tested and validated under the ideal one turn or a few turns SC [109] [101]. In addition, the temperature distribution, especially the hotspot temperature, under one turn SC, when the mitigation measure of 3-phase terminal SC which significantly reduces the turn SC current is applied, has been analysed to ensure fault tolerant ability in terms of thermal behaviour.

However, in reality when the insulation material degrades, the insulation resistance changes in a few orders of magnitude through a complex process, from a few tens/hundreds of Mega ohms in healthy condition to a few hundred ohms before reaching the ideal SC condition (zero resistance). Meanwhile, most papers reviewed in [17] [125] [126] only focus on qualitative evaluations of the thermal ageing behaviour of the insulation for assessing the lifetime of the insulation system. The damage risks of the machine resulting from large current and loss due to aging insulation before reaching the ideal SC condition are seldom considered. Lack of this knowledge may lead to

inappropriate requirements and specifications for fault detection methods and mitigation measures as well as for assessment of fault tolerant machine drive systems as a whole.

As known, the electric machine is not yet sufficiently fault tolerant without the fault detection and mitigation. The fault detection must respond quickly and accurately for application of appropriate mitigation measure to prevent fault propagation before causing damage to the whole system. Therefore, it is essential to have the understanding of the characteristics during insulation deterioration process for achieving a reliable fault detection and mitigation measure as well as high fault tolerant machine.

This chapter will analyse the electromagnetic and thermal behaviours under insulation deterioration leading to SC faults of a triple redundant 9-phase PMASynRM. In addition, it will quantify the range of the cut-through resistance, which is defined as the minimum resistance before irreversible damage of insulation due to heating would take place, for all possible faulty insulation volumes by 3D thermal modelling under turn-to-turn insulation deterioration leading to SC faults. Further, the insulation resistance thresholds for fault detection and mitigation to prevent the catastrophic failure have been given. In addition, an example with particular insulation volume has been analysed with a 3D thermal model to show the aging process when the electrical resistance decreasing with increase in temperature. Tests are performed to validate the predicted EM behaviour under turn-to-turn insulation deterioration leading to SC faults.

6.2 EM Behaviour under Insulation Deterioration Leading to SC Faults

The EM behaviour under insulation deterioration leading to one turn, two turns, three turns and one phase SC faults are comprehensively analysed for the triple redundant, 9-phase PMASynRM to give a better insight of the fault behaviours. A number of definitions are made to aid the analysis.

6.2.1 Electromagnetic Behaviour

As previously analysed and demonstrated, the triple 9-phase PMASynRM drive as shown in Fig. 5-3 can sustain and tolerate a single turn SC fault in the leading or trailing coils of a 3-phase winding when a terminal SC through 3-phase inverter is applied on the faulted 3-phase set as the fault mitigation measure. In addition, because when the SC turn

is located in the trailing coil of phase B in slots B2 and B4, the resultant SC current and copper loss are the largest, without loss of generality, all insulation faults considered in this chapter are assumed in phase B and thus the terminal SC will be applied to 3-phase set ABC.

The cut-through temperature, at which complete and irreversible damage to insulation will take place, of the polyester enamelled wire used in this prototype, is 320°C. At this temperature, the insulating film on the wire deforms almost instantly and sufficiently so that very low resistant electrical contact between turns will take place [127]. Thus, we can assume that after reaching the cut-through temperature, the electrical insulation resistance decreases to zero very quickly and irreversibly.

When turn-to-turn insulation deteriorates, the electrical resistance of the insulation reduces. Consequently under the influence of turn-to-turn voltage, significant current may flow through the insulation. Without loss of generality, the EM behaviours when insulation associated with one turn, two turns, three turns and one phase deteriorates in the PMASynRM can be comprehensively analysed. Fig. 6-1 illustrates the electric circuit of the finite element model of the machine used in the analysis. The insulation deterioration is represented by an insulation resistance denoted by R_{in} across the associated number of turns considered. All analyses are performed at the rated condition of 4000rpm with 120A current in the healthy phases for MTPA operation. To represent a gradual process of the insulation degradation in the analyses, the insulation resistance R_{in} that forms the fault current path is varied from a quite large value (1000Ω) representing significant deterioration to a very small value (0.01mΩ) close to ideal SC.

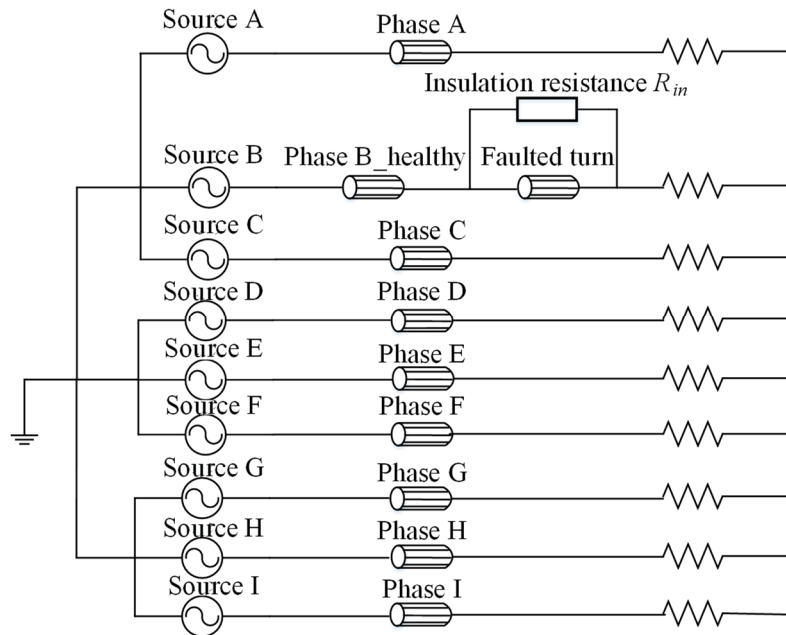
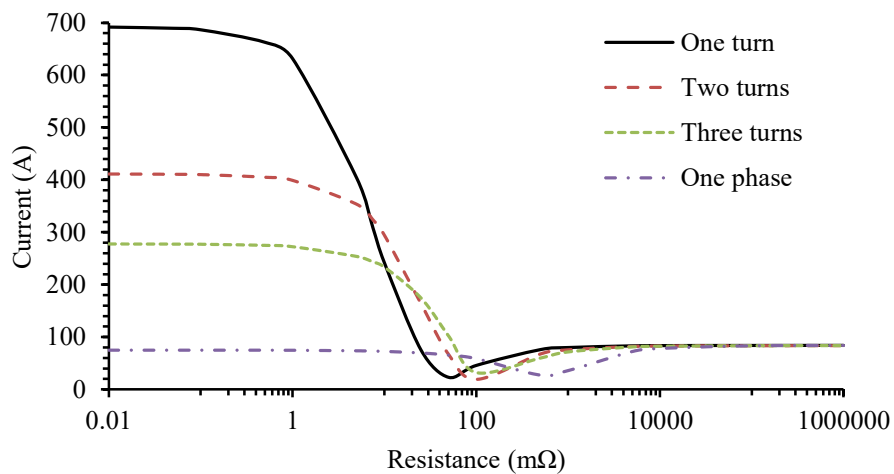
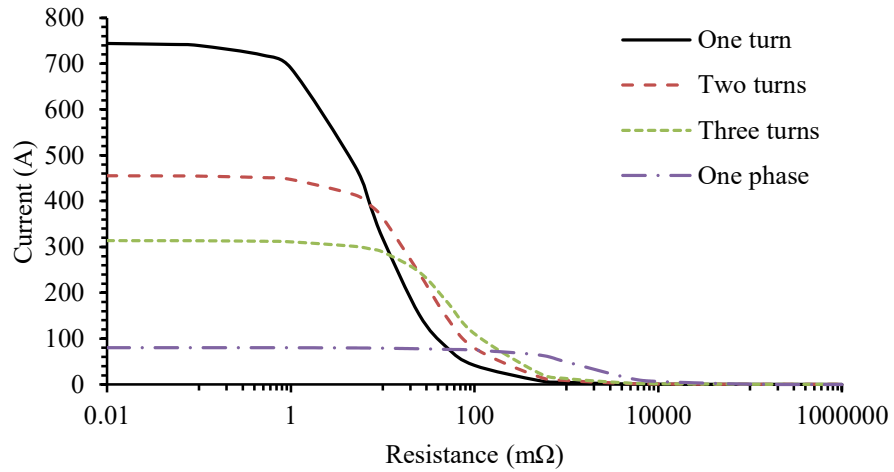


Fig. 6-1. The electric circuit under insulation deterioration leading to one turn, two turns, three turns SC.

It can be seen from Fig. 6-2 (a) and (b) that the variations of the RMS currents in the faulted turns and insulation resistance are similar under insulation deterioration leading to SC fault. All the RMS currents reach peak when the resistance is $0.01\text{m}\Omega$ and the peak current decreases with the number of faulted turns. However, for a given number of faulted turns, the current incurred in the faulted turns reaches a minimum lower than that in the healthy operation for a specific value of the insulation resistance as shown in Fig. 6-2 (a). This is because at such a specific condition, more current is diverted into the insulation resistance branch and, consequently, the current in the faulted turns is lower than that in the healthy operation.



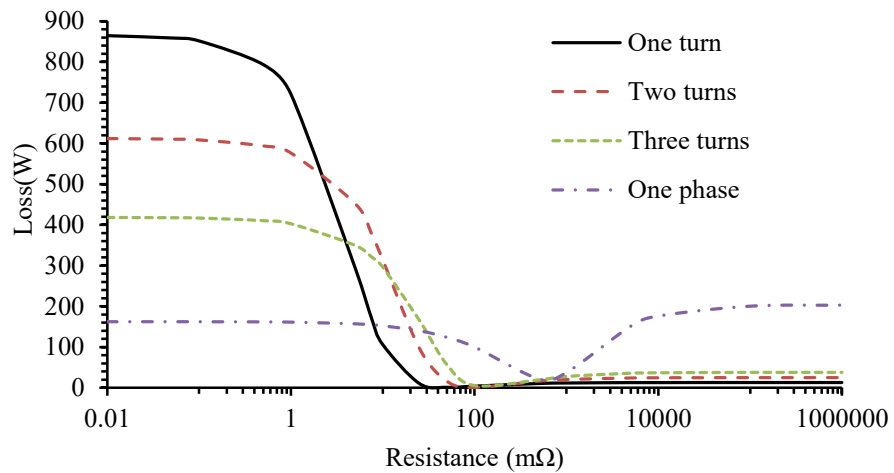
(a)



(b)

Fig. 6-2. RMS currents under insulation deterioration leading to one turn, two turns, three turns and one phase SC. (a) RMS currents in the faulted turn. (b) RMS currents in the insulation resistance.

The variations of the losses in the faulted turns and in insulation resistance are significantly different when the insulation resistance varies from 0.01mΩ to 1000Ω as observed in Fig. 6-3 (a) and (b), respectively.



(a)

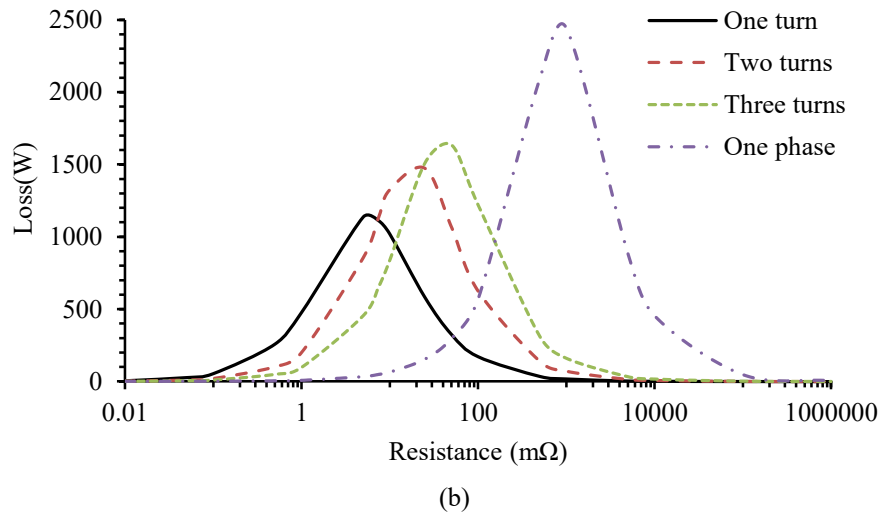


Fig. 6-3. Losses under insulation deterioration leading to one turn, two turns, three turns and one phase SC. (a) Losses in the faulted turn. (b) Losses in the insulation resistance.

As observed from Fig. 6-3 (a), all the copper losses in the faulted turns reach peak when the insulation resistance is the lowest $0.01\text{m}\Omega$ close to ideal short circuit. The peak loss decreases with the number of faulted turns. These results support the conclusion in [124] that under ideal SC faults, one turn SC is the most severe fault while one phase SC is thermally sustainable for this machine because the copper loss under ideal one phase SC is even lower than that under the rated healthy condition. Moreover, when the current in the faulted turns reaches a minimum, the loss in the faulted turns also reaches a minimum lower than that in the healthy operation for a specific value of the insulation resistance.

In contrast, as can be seen from Fig. 6-3 (b), the losses in the insulation resistance exhibit a very different characteristic. The losses are negligible when the resistance is either very large 1000Ω , representing the early stage of insulation degradation or very small $0.01\text{m}\Omega$, close an ideal SC. When the resistance reduces from 1000Ω , the loss associated with a given number of faulted turns increases dramatically and reaches a peak which is much larger than the copper loss in ideal SC. It is also evident that the peak loss increases with the number of faulted turns and hence the fault across one phase winding gives rise to the largest peak loss. This is because the resistance at which the peak occurs increases with the number of SC turns. However, since the probability of turn-to-turn SC fault is much larger than the other fault conditions, turn-to-turn insulation deterioration leading to SC faults is studied in this chapter to assess the fault behaviours.

Since the peak loss in the insulation resistance occurs before an ideal SC, fault detection and mitigation measures have to be applied when the resistance is sufficiently large to avoid the temperature in the fault region reaches the cut-through temperature when irreversible damage or even catastrophic failure may occur.

6.2.2 Critical Electrical Insulation Resistance

During the insulation degradation process the actual insulation resistance is not known. However, from the foregoing analysis two critical electrical insulation resistances are defined. Fig. 6-4 and Fig. 6-5 illustrate the loss variations in the faulted turn and in the insulation resistance with insulation resistance under one turn fault, respectively. As shown in Fig. 6-5, the insulation resistance that yields the peak loss for a given number of faulted turns is defined as the peak loss resistance denoted by R_{pmax} . For one turn fault this value is $5\text{m}\Omega$. The second critical resistance defined is the cut-through resistance R_{ct} which results in the temperature in the insulation reaches the cut-through temperature due to the loss P_{ct} incurred in it. This loss is defined as cut-through loss. From Fig. 6-5, for a given cut-through loss there are two corresponding electrical resistances and the larger one is the cut-through resistance as indicated.

The cut-through resistance R_{ct} is dependent on weakened insulation volume and the number of turns associated the weak insulation. For each condition, the fault detection and mitigation action should ideally be applied before the insulation deteriorates to reach the cut-through resistance, otherwise the electrical insulation resistance will decrease in an avalanche manner to reach the peak loss resistance, leading to complete failure. This process will be studied in section 6.5.

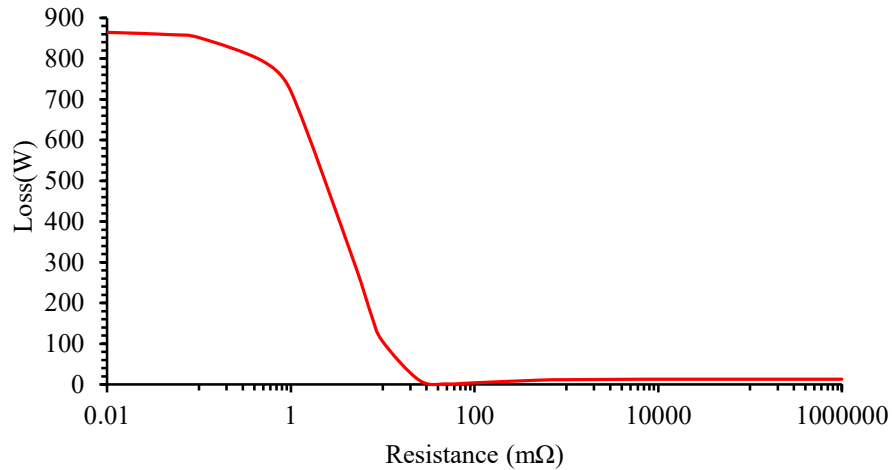


Fig. 6-4. Loss variation in the faulted turn with insulation resistance under turn-to-turn insulation deterioration leading to SC fault.

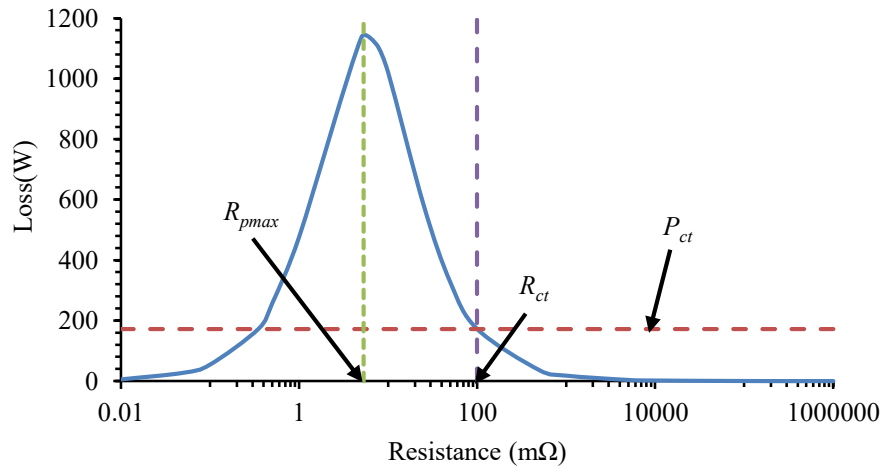


Fig. 6-5. Loss variation in the insulation resistance with insulation resistance under turn-to-turn insulation deterioration leading to SC fault.

6.3 Thermal Model and Cut Through Resistances

From previous analysis, if all the information of the region where insulation has significantly been deteriorated is known, a 3D thermal model representing the insulation and machine operating condition can be built to assess the resultant thermal behaviour. The loss in the faulty region can be varied and the value that results in the hotspot temperature of 320°C can be identified as the cut-through loss. The corresponding cut-through resistance can be obtained according to Fig. 6-5 in the case of single turn SC.

However, the difficulty of this approach is that the location, shape and volume of the deteriorated insulation are often unknown. Parametric study together with appropriate assumptions are made to overcome this difficulty.

6.3.1 3D Thermal Model

A 3D thermal model has been built in JMAG to help determine the cut-through resistance. All the thermal parameters, including conductivity, convective coefficients, contact thermal parameters, capacity, losses and temperature boundary are set based on those described in Chapter 4.

The one third model of the machine containing 12 slots with full axial length is shown in Fig. 6-6 with different components indicated. Fig. 6-7 illustrates the red region where insulation has been significantly degraded with three dimensional parameters, the length a , the thickness b and the height c . It is located close to the slot opening and at the top of B2 coil end winding part because it is the region with the hottest temperature. The shape of insulation is assumed to be cuboid. The conductivity and capacity of the insulation region are obtained from the insulation material, while the thermal parameters of windings are obtained by calculating the equivalent conductivity and capacity which consist of copper and insulation as described in Chapter 4.

While the volume of the degraded insulation is difficult to measure in test or predict by theory, the boundaries of the three dimensional parameters can be defined. The minimum value of the three dimensions of the insulation volume is all set to 0.1mm according to the standard of the copper wire diameter based on IEC 60317-0-1. The upper-bound of c is the half length of a turn, 224mm. If we assume each turn occupies the same volume, the upper-bound of a is 8.3mm while the maximum value for b is 2mm, equal to the slot width minus integer multiple of the wire diameter.

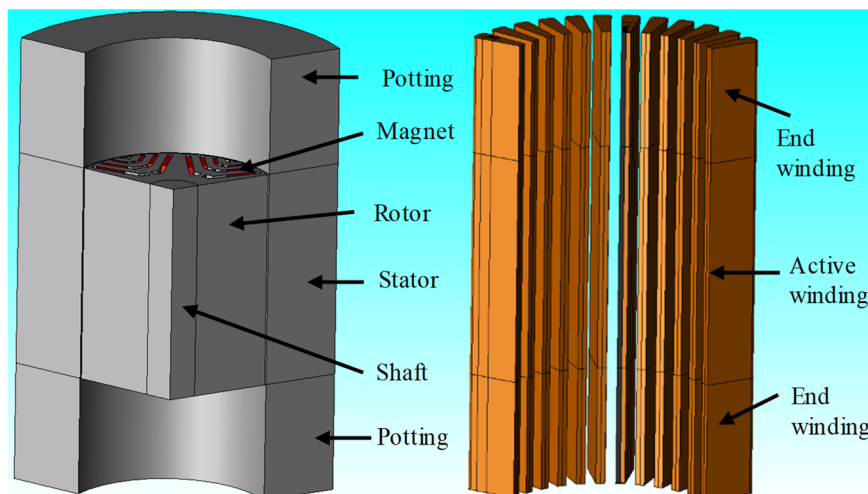


Fig. 6-6. One third model with whole axial length.

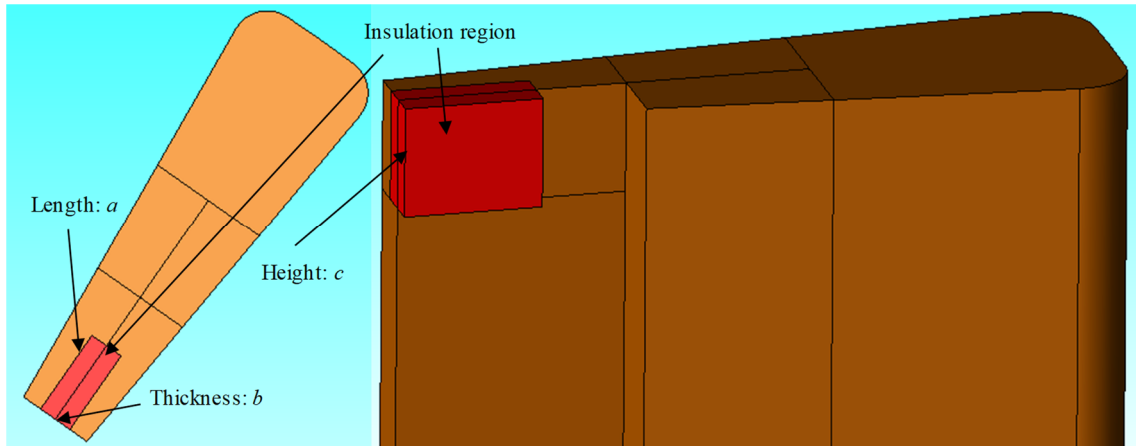


Fig. 6-7. Insulation region located in one slot with three dimensions.

6.3.2 Boundary of Cut-Through Resistance

As there are infinite possible combinations of degraded insulation volumes, two insulation volumes which result in the smallest and the largest cut-through resistance will be analysed. Thus, the cut-through resistances of all other insulation volumes are between the two extremes.

It is likely that insulation deterioration begins in a very tiny volume. Hence Case 1 with $a=b=c=0.1\text{mm}$ is the smallest volume under consideration. It can be shown that the cut-through loss associated with Case 1 is the smallest in all other possible volumes of the dimensional combinations due to the highest heat flux density for a given loss. The cut-through loss can be determined by varying the loss in this volume under the rated operating condition, and evaluating the resultant temperature. For example, from the temperature distribution obtained from 3D thermal model as shown in Fig. 6-8, the average and the hotspot temperatures of the insulation region are 271°C and 320°C which reaches the cut-through temperature. Therefore, the loss in the insulation resistance under this condition is found to be the cut-through loss of Case 1 which is 1.4W (P_{ctl_s}).

Then, according to Fig. 6-5, the corresponding cut-through resistance is the largest which is 13Ω (R_{ctl_l}). In addition, the insulation material resistivity can be obtained as:

$$\rho_{ct} = \frac{R_{ct} * a * c}{b} \quad (6-1)$$

Therefore, the insulation material resistivity of Case 1 is the smallest which is defined as ρ_{ctl_s} ($1.9 \times 10^{-6} \Omega \cdot \text{m}$). It is 100 times higher than the copper resistivity ($1.72 \times 10^{-8} \Omega \cdot \text{m}$).

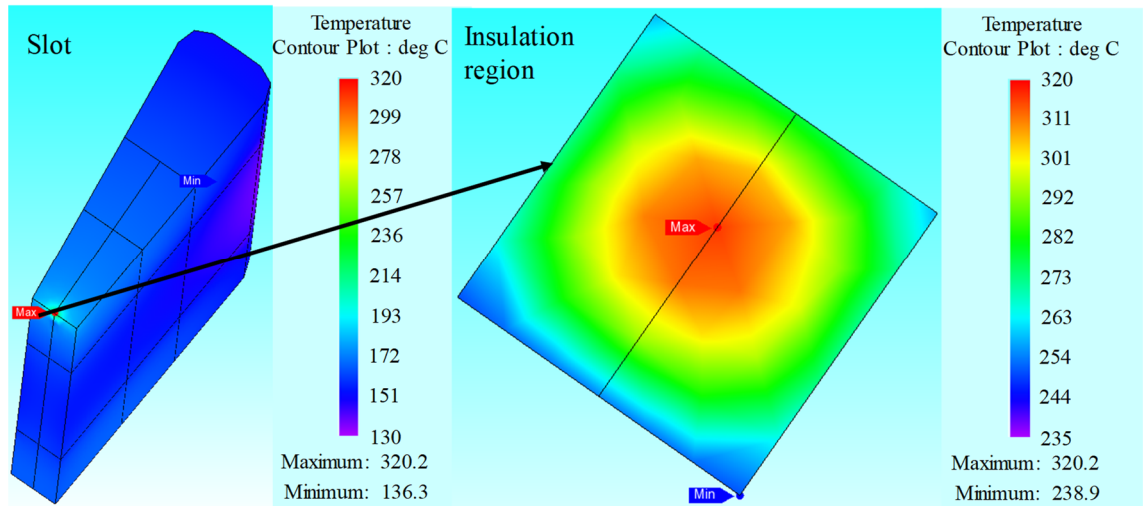


Fig. 6-8. Temperature distributions of slot and insulation region in Case 1.

Conversely, the largest insulation volume ($a=8.3\text{mm}$, $b=2\text{mm}$, $c=224\text{mm}$) has also been investigated. However, as the heat is mainly transferred from b direction, when the insulation volume is sufficiently large, the thickness b instead of heat density is the most critical parameter that determines the resultant temperature. From Table 6-1, it can be seen that for a given loss, the most optimistic case for the lowest hotspot temperature is that the thickness b is minimum and the other two parameters are at their maximum values.

Table 6-1 Temperatures with different thicknesses.

Thickness b (mm)	0.1	0.5	1	2
Hotspot temperature ($^{\circ}\text{C}$)	327	349	375	427
Average temperature($^{\circ}\text{C}$)	300	311	322	339

Thus, Case 2 ($a=8.3\text{mm}$, $b=0.1\text{mm}$, $c=224\text{mm}$) can accommodate the largest cut-through loss P_{ct2_l} (144W) in which the resulted average temperature and the hotspot temperature of the insulation is 300°C and 328°C , respectively, as shown in Fig. 6-9. This leads to the smallest cut-through resistance R_{ct2_s} (0.12Ω) and the largest insulation material resistivity ρ_{ct2_l} ($2.28 \times 10^{-3}\Omega \cdot \text{m}$) which is $1e5$ times higher than the copper resistivity. The cut-through resistances of all other insulation volumes will be between 13Ω and 0.12Ω . Case 1 is the worst case which is quite likely in reality while Case 2 is the most optimistic case.

It should be noted that the same process can be used to determine the maximum and minimum cut-through resistances for any given number of turns associated with the degraded insulation volumes.

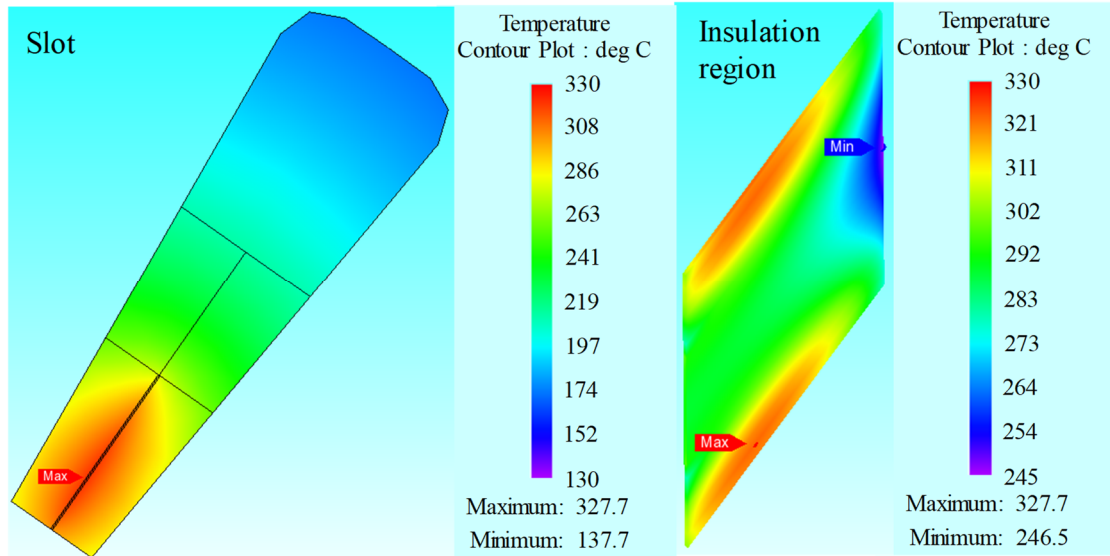


Fig. 6-9. Temperature distributions of slot and insulation region in Case 2.

6.4 Fault Detection Threshold

Since the fault current and resultant heating effect are critically dependent on the insulation resistance, it is important to establish some threshold values for the resistance so that a detection scheme should be able to detect the fault and a mitigation measure is taken to prevent further deterioration.

For the fault detection scheme, the 2nd harmonic in IAP and IRP produced by an SC fault can be chosen as turn fault indicators since the increase of the 2nd harmonic in IAP and IRP as a result of the fault is comparatively higher than the 2nd harmonic voltage or current [101]. In real operations, it is likely that the motor has small inherent unbalance due to manufacturing tolerance and disparities in converter characteristics, the 2nd IAP and IRP may exist in healthy conditions. The effectiveness of this fault detection needs therefore assessed against the test results and it is possible to employ calibration and online learning to improve detection sensitivity and accuracy [128].

The current and loss variations when the insulation resistance is equal to 0, the maximum loss point, R_{pmax} , and the maximum and minimum cut-through resistances before and after the mitigation measure (3-phase terminal SC through inverter) are presented in Table 6-2 and Table 6-3, respectively. R_{ct_l} , which is the maximum cut-through resistance, is also the minimum threshold of the turn-to-turn insulation resistance that a detection scheme should respond and a mitigation action applies.

Table 6-2 Currents and losses before the mitigation measure of 3-phase terminal SC.

Insulation resistance (Ω)	RMS current in faulted turn (A)	RMS current in insulation resistance (A)	Loss in faulted turn (W)	Loss in insulation resistance (W)
0	697	756	837	0
0.005 (R_{pmax})	403	477	280	1136
0.12 (R_{ct2_s})	52	35	5	144
13 (R_{ct1_l})	83	0.33	12	1.4

Table 6-3 Currents and losses after the mitigation measure of 3-phase terminal SC.

Insulation resistance (Ω)	RMS current in faulted turn (A)	RMS current in insulation resistance (A)	Loss in faulted turn (W)	Loss in insulation resistance (W)
0	271	212	126	0
0.005 (R_{pmax})	152	96	40	46
0.12 (R_{ct2_s})	74	6	9	5
13 (R_{ct1_l})	71	0.06	9	0.05

It can be seen from Table 6-2 and Table 6-3 that the currents and losses under all the cases reduce significantly after the mitigation measure. The most significant loss reduction is seen when the insulation resistance equals to the peak loss resistance, R_{pmax} . The temperature distributions, when the fault is detected at three typical stages of insulation degradation and the mitigation action is subsequently taken, are further analysed.

6.4.1 Fault Detected and Mitigated when $R_{in} \geq R_{ct_l}$

If the insulation degradation fault can be detected and the mitigation measure is applied before the insulation resistance is reduced to R_{ct_l} (13Ω), the temperature in all possible insulation volumes will not reach the cut-through temperature and will be significantly lower after the mitigation action. The temperature distributions under one turn SC with insulation resistance of 13Ω when the mitigation action is applied and under the ideal one turn SC with the same mitigation action are shown in Fig. 6-10 and Fig. 6-11, respectively, with the same range of temperature scaling. In addition, the steady-state temperatures of various components under these two fault conditions are also compared in Table 6-4.

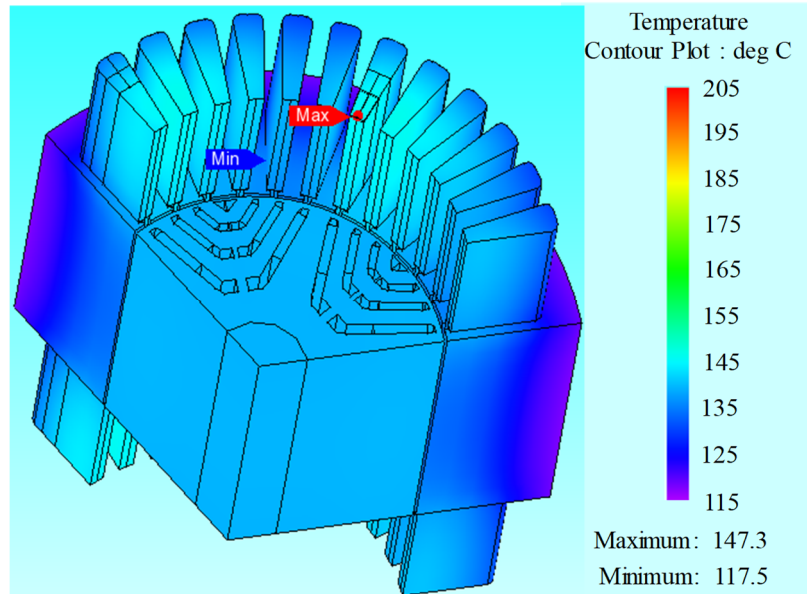


Fig. 6-10. Temperature distribution when insulation resistance is 13Ω and mitigation action is applied.

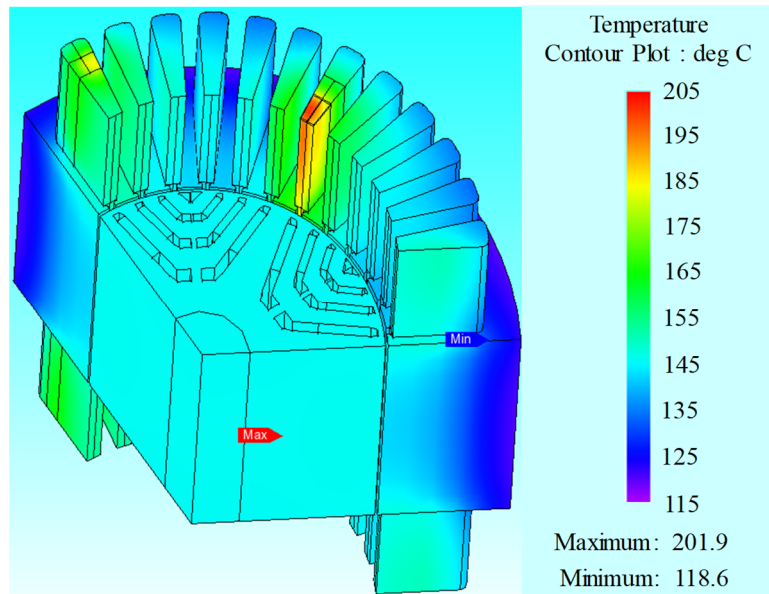


Fig. 6-11. Temperature distribution when insulation resistance is 0Ω and mitigation action is applied.

Table 6-4 Temperature distributions under fault conditions with two insulation resistances.

Temperature (°C)	Rotor	Stator	Phase A	Phase C	Phase B healthy	Faulted turn	Insulation	Hotspot
0 Ω	146	130	140	140	151	182	194	201
13 Ω	140	126	133	137	139	141	147	147
Difference	6	4	7	3	12	41	47	54

As observed, the average temperatures of the faulted turn and insulation as well as the hotspot temperature under one turn SC with insulation resistance of 13Ω after the mitigation measure are 41°C, 47°C and 54°C lower than those under the ideal one turn SC, respectively.

6.4.2 Fault Detected and Mitigated when $R_{ct_l} > R_{in} \geq R_{ct2_s}$

If the insulation resistance is lower than the maximum cut-through resistance R_{ct_l} , whether the fault insulation region will reach the cut-through temperature will depend on its volume. If the fault is detected and the mitigation measure is taken, it is likely that further deterioration can be managed because the fault current is significantly reduced. If the insulation resistance is reduced close to the minimum cut-through resistance R_{ct2_s} (0.12Ω) and no mitigation action is taken, the maximum temperature of all possible insulation volumes will reach the cut-through temperature. Consequently, the rate of reduction of the insulation resistance will accelerate, passing R_{pmax} and finally approaching zero if no mitigation is taken. However, if a mitigation action is taken before the insulation resistance reaches R_{pmax} , the resultant loss will be less than 46W as shown in Table 6-3. Since this loss is much smaller and so is the heating effect, the mitigation action may reduce the rate of reduction or prevent further reduction of the insulation resistance, depending on the actual volume of the faulty region. In the worst case, the final steady-state temperature distribution when the mitigation action is applied but the insulation resistance is still reduced close to the ideal SC is the same as that shown in Fig. 6-11. Because the machine under study is designed to cope with this condition, the mitigation action is still effective in preventing a catastrophic failure and sustaining continued operation under the fault condition.

6.4.3 Fault Detected and Mitigated when $R_{in} \approx R_{pmax}$

When the insulation resistance approaches R_{pmax} , the resultant loss increases dramatically to more than 1000W. Thus, even if the fault is detected and the mitigation action is taken, it is unlikely that further reduction in the insulation resistance can be stopped. However, the mitigation action is still effective in reducing the fault current when R_{in} becomes 0, and consequently facilitates fault tolerant operation.

6.5 Transient Ageing Process with Insulation Deterioration Fault

The foregoing analysis assumes a constant value of resistance for the insulation material in the faulted region. In reality, the insulation material resistivity will decrease with increase in temperature before the insulation resistance reaches the peak loss

resistance and the process is irreversible. Thus, from Fig. 6-5, the decrease in the insulation resistance will further increase the loss and consequently the temperature. The process might trigger an avalanche effect.

The quantitative relationship between the insulation electrical resistance and the temperature is not available and may differ with different insulation material and manufacturing processes. Thus, this chapter studies an example of Case 3 in which the faulty insulation volume is assumed for $a=1\text{mm}$, $b=0.1\text{mm}$, $c=1\text{mm}$ and assumes that the insulation resistivity halves for a 10°C increase in temperature based on IEEE Std 43-2000 [129] to provide an insight of the transient process of insulation aging.

Electromagnetic-thermally coupled simulations introduced in Chapter 5 are performed and the results show that when the initial insulation resistances are greater than 100Ω for the assumed faulty volume the resultant fault current is very small (0.03A), and no avalanche effect is seen, i.e., insulation resistance (resistivity) reaches a constant value in steady state and the hotspot temperature is below the cut-through temperature.

However, when the initial insulation resistance is 100Ω or smaller, avalanche effect will be triggered. The simulation process with initial insulation resistance of 100Ω is divided to 16 iterations, and the simulation time step is varied. In addition, the losses in the faulted turn and in the insulation resistance are updated in each iteration based on the results of the EM simulation in Fig. 6-4 and Fig. 6-5. The parameters of each iteration, such as the insulation resistance, the simulation time, the current and loss in the insulation resistance, the average and hotspot temperatures of the insulation, are presented in Table 6-5. Besides, the variations of insulation resistance and hotspot temperature with time are presented in Fig. 6-12 and Fig. 6-13, respectively.

As can be seen, when $t < 90\text{s}$, the insulation resistance decreases gradually but is still larger than 20Ω . Thus, the current and loss in the insulation resistance as well as the average and hotspot temperatures in the faulty insulation increase gradually with time but the hotspot temperature is below 220°C at 90s . After this point, the temperature quickly increases. Therefore, the insulation resistance decreases dramatically to quite small value due to the avalanche effect. The hotspot temperature exceeds 320°C in just 0.1144s .

Table 6-5 Characteristics during the transient ageing process of Case 3.

Step	Insulation resistance (Ω)	Time (s)	Current in insulation (A)	Loss in insulation (W)	Average/ Hotspot temperature ($^{\circ}\text{C}$)
1	infinite	--	0	0	169/169
2	100	10	0.04	0.2	175/178
3	65.52	10	0.07	0.29	178/181
4	53.22	10	0.08	0.36	180/185
5	46.01	10	0.09	0.41	182/187
6	40.33	10	0.11	0.47	184/189
7	35.36	10	0.12	0.54	186/193
8	30.35	10	0.14	0.62	189/196
9	25.35	10	0.17	0.75	193/202
10	19.21	10	0.23	0.98	200/212
11	11.66	0.1	0.37	1.59	210/228
12	5.91	0.01	0.73	3.12	220/249
13	2.88	0.003	1.48	6.32	231/272
14	1.34	0.001	3.16	13.4	243/297
15	0.58	0.0003	7.26	30.6	254/318
16	0.27	0.0001	15.49	64.8	262/334

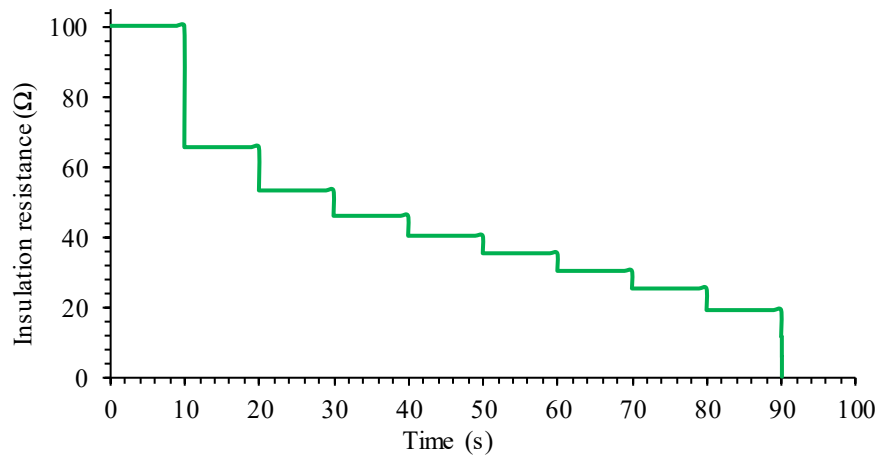


Fig. 6-12. Variation of insulation resistance with time.

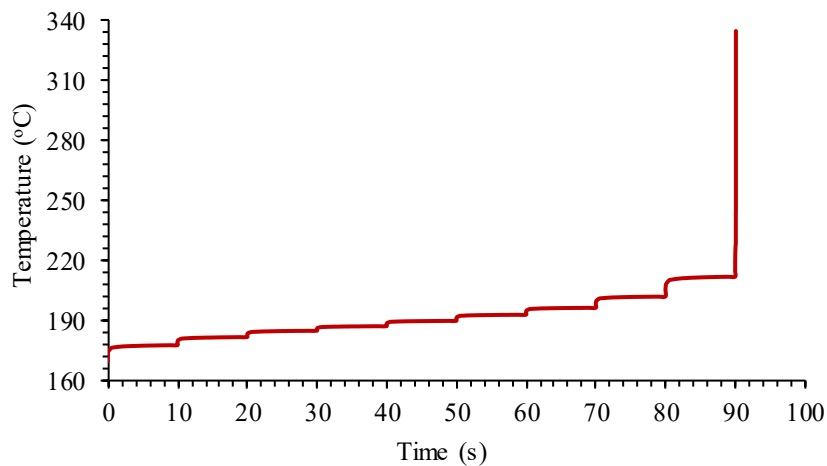


Fig. 6-13. Variation of hotspot temperature in faulty insulation with time.

If the insulation volume, the number of turns involved or the relationship between the insulation electrical resistance and the temperature are different from the example, the rate of insulation resistance reduction and the point of triggering the avalanche will be different but a similar trend would be seen before the insulation resistance drops down to zero. It follows that even if the insulation resistance is relatively large and the resultant loss is relatively small, a rapid deterioration may result from the fact that insulation resistance decreases with increase in temperature.

6.6 Comparisons between Measured and 2D Predicted EM Performance with Different Insulation Resistances

The variation of fault current with insulation resistance across one turn is measured on the prototype machine in order to validate the electromagnetic prediction of the fault current and resultant losses. The prototype PMASynRM is mounted on the test rig employing the oil cooling system presented in Chapter 4 section 4.6 for the validation. As the insulation volume and the material characteristics are hardly controllable in a test, it is not possible to experimentally validate the thermal behaviour of the transient ageing process of the prototype. However, the EM behaviours under turn-to-turn insulation deterioration leading to SC fault with different insulation resistances shown in Fig. 6-4 and Fig. 6-5 are tested and validated. This validation is quite important as all the studies in this chapter are based on this.

One single turn is brought out from the winding by the cables. The fault emulation cables are connected to extra resistor representing the state of insulation degradation via a high current relay shown in Fig. 6-14 and Fig. 6-15 to control the fault.

Two types of resistors are used for emulation of insulation resistance. The TGHG series precision current sense resistors [130] are used in Fig. 6-14 with the values of 1m Ω , 2m Ω , 5m Ω , 10m Ω , 25m Ω , and 0.1 Ω . The copper bars with negligible resistance connect the resistor to the cable and relay. The HS aluminium housed resistors [131] are used in Fig. 6-15 with the values of 1 Ω and 100 Ω . As the resistance in this case is relatively large, cables with 2.3m Ω are adopted for connection. All the resistors are measured to obtain the real resistances. The total resistance of the terminal cables and relay for the fault

emulation is $1.4\text{m}\Omega$. Thus single turn SC with the insulation resistance lower than $1.4\text{m}\Omega$ cannot be tested and validated.

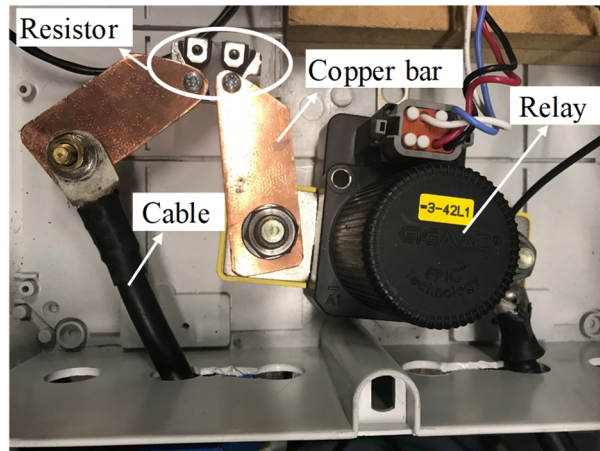


Fig. 6-14. Relay and precision current sense resistors.

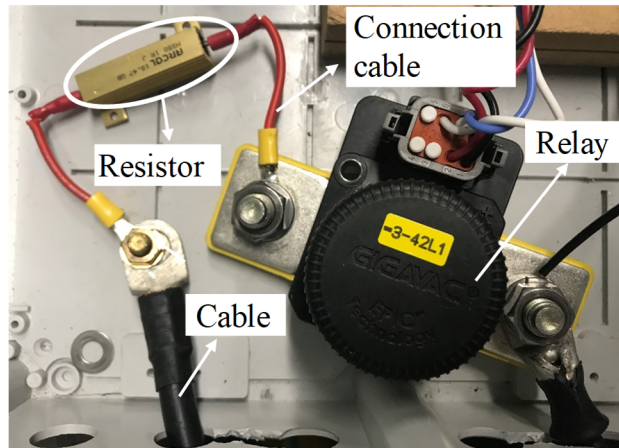


Fig. 6-15. Relay and aluminum housed resistors.

In order to avoid damage to the prototype, the tests are operated at 2000rpm and 1000rpm with 40A current excited in the healthy phases for MTPA operation. The results will be scaled to and compared with the prediction shown in Fig. 6-4 and Fig. 6-5. Each test will be operated for 0.2s.

6.6.1 Insulation Deterioration at 2000rpm with 40A Current

EM behaviours of the prototype machine under emulated turn-to-turn insulation deterioration leading to SC fault with varying insulation resistances at 2000rpm with 40A current excited in all the phases have been analysed.

Firstly, Fig. 6-16 (a), (b), and (c) compare the predicted and measured currents in the faulted turn, in the insulation resistance and in the phases of the fault set when the single turn is short-circuited with the minimum resistance ($1.4\text{m}\Omega$), respectively.

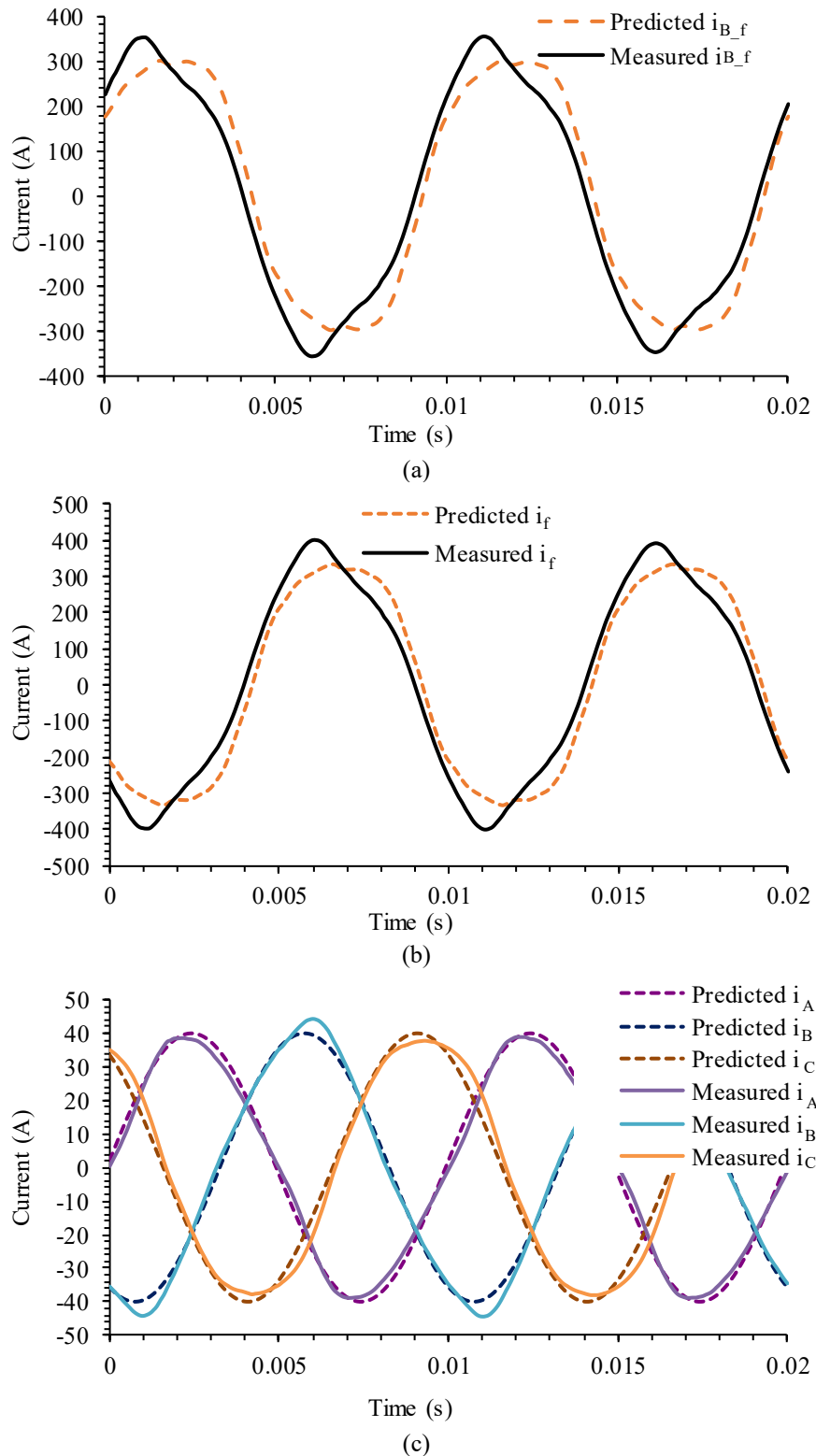


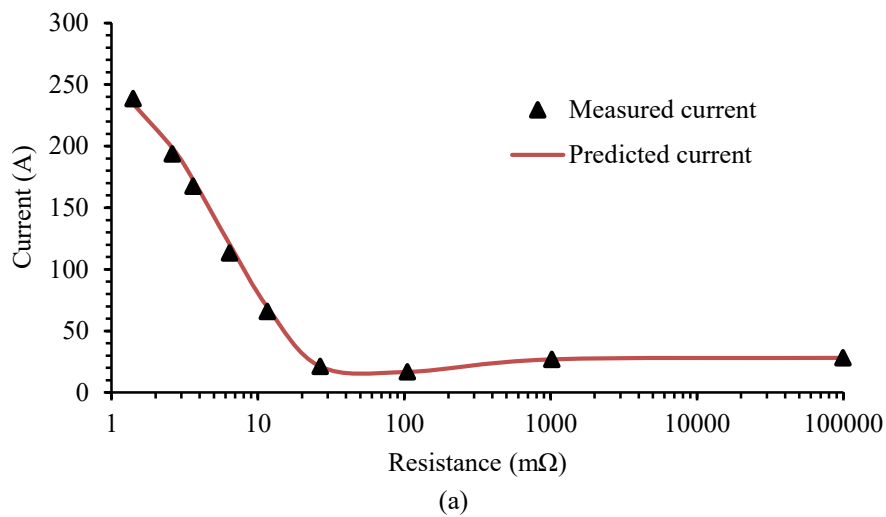
Fig. 6-16. Comparison of predicted and measured currents at 2000rpm with 40A without extra resistor. (a) Currents in the faulted turn. (b) Currents in the insulation resistance. (c) Phase currents in fault set.

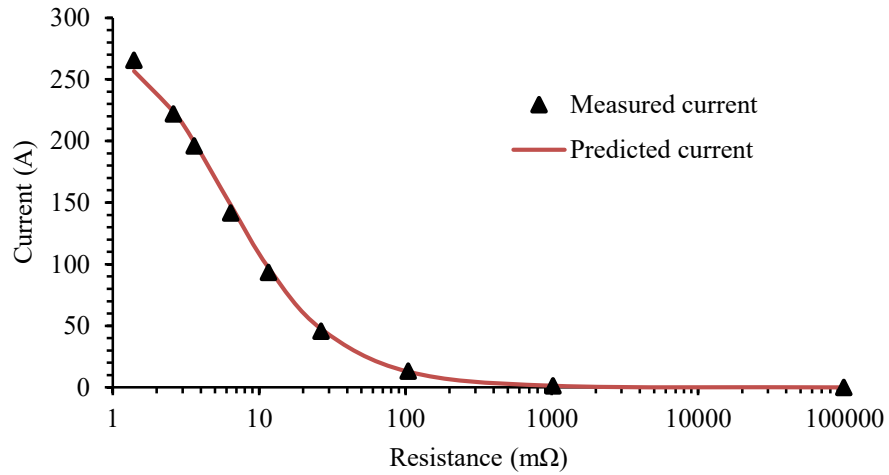
As the ideal current sources are adopted in the FE model, all the phase currents are ideally sinusoidal. The measured phase currents in the two healthy 3-phase sets are also quite close to sinusoidal, while the measured phase currents in the fault set are slightly

distorted. This distortion is not captured by the FE model and results in the small deviations between the predicted and the measured current waveforms in Fig. 6-16 (a) and (b). However, the RMS values of the predicted currents in the faulted turn and in the insulation resistance, which are important for thermal analysis, only differ from the measured values by 2.5% and 4.0%, respectively.

The resistance across the emulated fault turn is varied, and the measured RMS currents in the faulted turn and in the insulation resistance with the insulation resistances have been obtained and compared with the predicted currents in Fig. 6-17. As observed, the measured and predicted currents agree quite well and the maximum differences of the RMS currents in the faulted turn and in the insulation resistance when the emulated insulation resistance varies from 1.4mΩ to 100Ω are 6.3% and 4.7%, respectively.

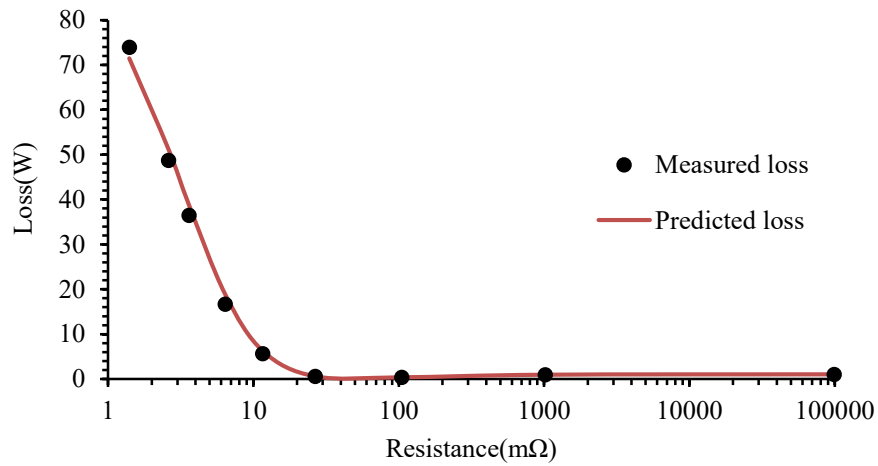
The comparison of the predicted and measured loss variations in the faulted turn and in the insulation resistance are illustrated in Fig. 6-18 (a) and (b), respectively. It is evident that the measured losses match well with the predicted losses. The maximum differences of the losses in the faulted turn and in the insulation resistance are 13.1% and 9.4%, respectively.



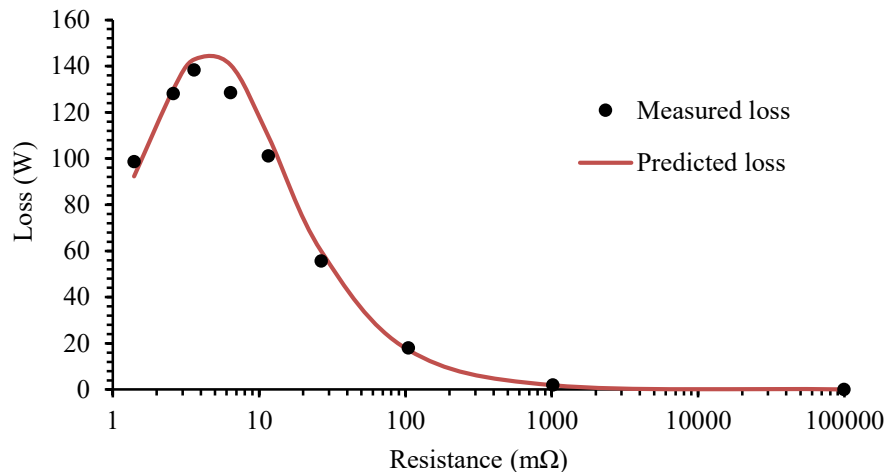


(b)

Fig. 6-17. Comparison of predicted and measured RMS currents under insulation deterioration at 2000rpm with 40A. (a) RMS currents in the faulted turn. (b) RMS currents in the insulation resistance.



(a)



(b)

Fig. 6-18. Comparison of predicted and measured losses under insulation deterioration at 2000rpm with 40A. (a) Losses in the faulted turn. (b) Losses in the insulation resistance.

6.6.2 Insulation Deterioration at 1000rpm with 40A Current

The test was repeated at 1000rpm with 40A current excited in all the phases. From Fig. 6-19, the maximum differences between the predicted and measured RMS currents in the faulted turn and in the insulation resistance when the emulated insulation resistance varies from $1.4\text{m}\Omega$ to 100Ω are 15.2% and 8.6%, respectively. Therefore, the maximum differences between the predicted and measured losses in the faulted turn and in the insulation resistance shown in Fig. 6-20 are relatively large, being 28.0% and 16.4%, respectively. They occur when the insulation resistance is below $5\text{m}\Omega$, and unquantified parasitic resistance of the cable and connectors has more significant effect on the measurement accuracy. However, the waveforms of the predicted and measured losses in the faulted turn and in the insulation resistance have the similar trends.

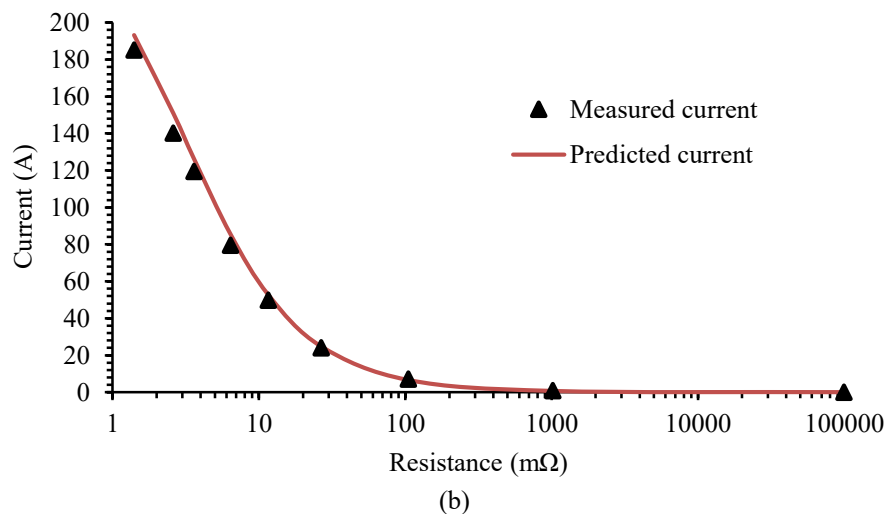
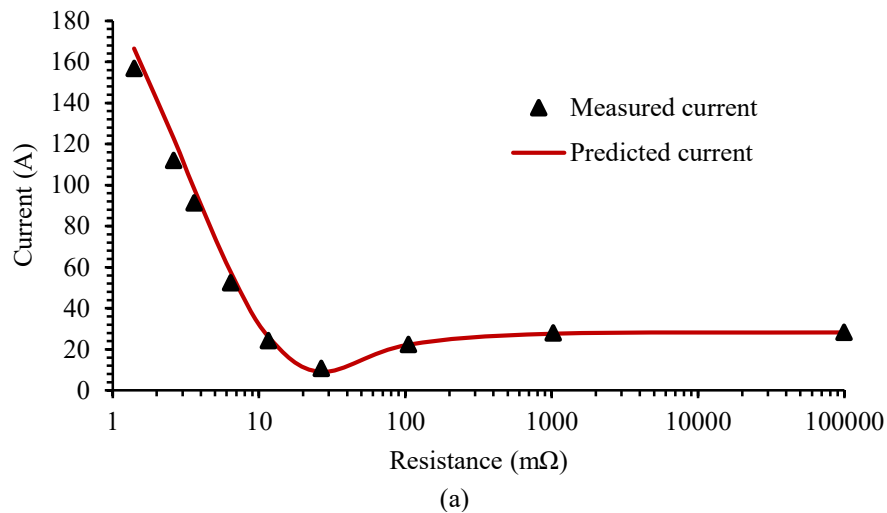


Fig. 6-19. Comparison of predicted and measured RMS currents under insulation deterioration at 1000rpm with 40A. (a) RMS currents in the faulted turn. (b) RMS currents in the insulation resistance.

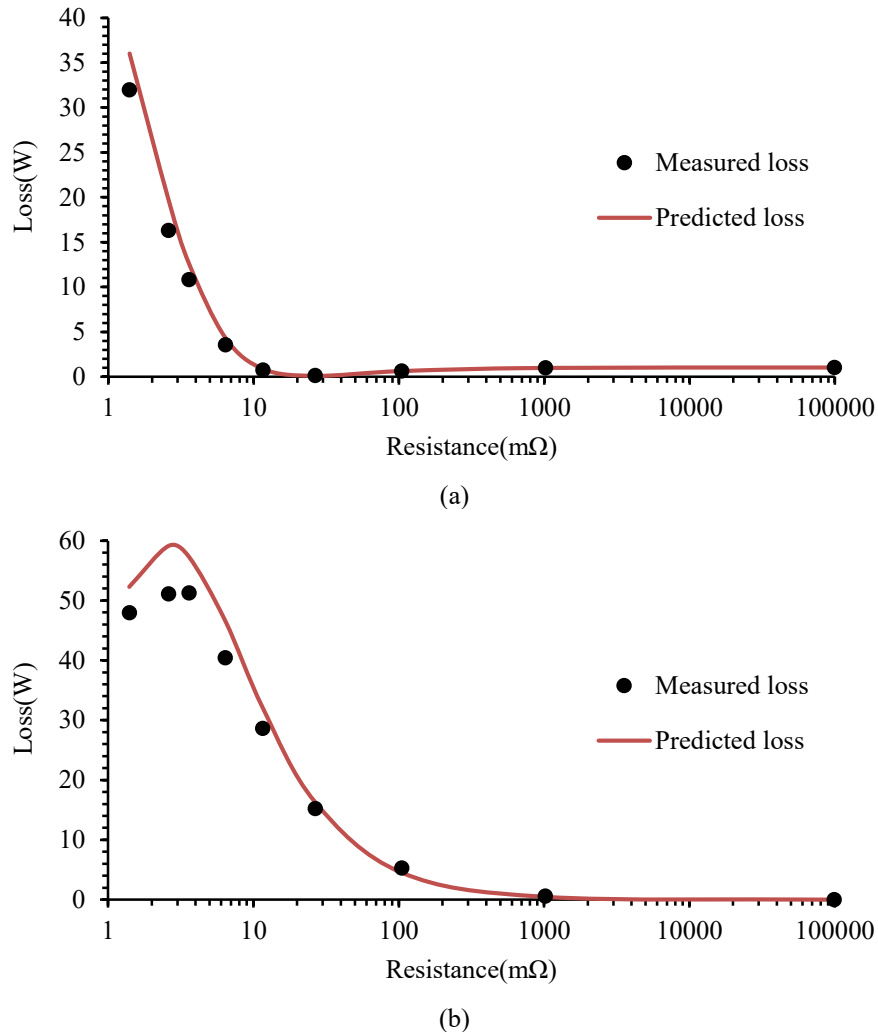


Fig. 6-20. Comparison of predicted and measured losses under insulation deterioration at 1000rpm with 40A. (a) Losses in the faulted turn. (b) Losses in the insulation resistance.

Therefore, the reasonably matched results validate that the FE model could predict the EM behaviours under insulation deterioration leading to SC fault. Since a similar thermal model with Fig. 6-6 in this chapter is also validated in Chapter 4, these validations support the findings of the FE simulation in this chapter.

6.7 Summary

This chapter has assessed the EM and thermal behaviour of the triple-redundant PMASynRM under insulation deterioration leading to SC faults. It has been shown that the loss in the faulty insulation region increases with reduction of insulation resistance before reaching a peak. This behaviour would dramatically increase the temperature in the faulty region and accelerate the insulation deterioration, triggering an avalanche effect when the insulation material resistivity decreases with the increase in temperature. To

prevent this process, fault detection needs to be effective when the insulation resistance is greater than a threshold and a mitigation action is taken. Finally, the tests on a prototype machine drive have validated the predicted EM behaviour under turn-to-turn insulation deterioration leading to SC faults.

This chapter shows that the machine is fault tolerant with mitigation measure. Furthermore, the EM and thermal behaviour of the machine under insulation deterioration leading to SC faults should be evaluated for assessing the fault tolerance of the machine and obtaining more accurate threshold of fault detection. Moreover, the fault can be better managed if an insulation break-down can be detected at early stage before an avalanche effect is triggered which means the sensitive and robust fault detection would improve the fault tolerance. Moreover, the fault is detectable by the 2nd harmonic in IAP and IRP produced by an SC fault and mitigatable by the 3-phase terminal short-circuit of the faulty set. However, the magnitudes of the 2nd harmonic at early stage of an insulation break-down are relatively small which increases the difficulty of the accurate detection. In addition, it is likely that the machine has small 2nd IAP and IRP under healthy conditions in real world due to manufacturing tolerance and disparities in converter characteristics. The effectiveness of this fault detection needs therefore assessed against the test results and it is possible to employ calibration and online learning to improve detection sensitivity and accuracy.

Chapter 7 Case Study: Electromagnetic and Thermal Behaviours of a 2.5 MW Permanent Magnet Generator

7.1 Introduction

A 2.5 MW permanent magnet generator operating at +/- 1.5kV DC has been designed for E-Fan-X demonstrator. The generator employs 18-slot 12-pole surface-mounted PM machine topology and contains two 3-phase channels, each being controlled by an independent standard 3-phase converter, as shown in Fig. 7-1. Concentrated coils are wound on each tooth and each phase consists of 3 coils in parallel to form wye connection. In order to enhance power density and reduce the harmonics in the back emf and torque ripple, Halbach magnetisation with optimal 3 magnet segments per pole is utilised. The generator is cooled by oil flow through stator back iron and slots as well as by forced air flow in the cooling channels in the rotor hub. The main specification of the generator is summarised and given in Table 7-1.

The electrical power generator employs IT grounding system, which implies that the neutrals of the two 3-phase windings are floating and the generator housing (stator iron), rotor shaft/gas turbine and converters heatsinks, etc., are not connected to the common reference (“ground”) of the DC power source. The IT grounding system is advantageous in that any single point to housing short-circuit failure will not have a significant consequence and lead to loss of availability.

This chapter analyses potential electric failure modes resulting from insulation breakdown and quantifies their severity and consequences by employing simulation techniques described in the previous chapters. 2D non-linear, transient finite element analysis has been employed to predict EM behaviours and currents of the generator in various fault conditions, and 3D FE analysis is performed to assess the thermal impact of a number of typical fault scenarios. The impacts of worst case faults are assessed and the limitation on existing measures for fault mitigation is highlighted. Recommendations are made for future work.

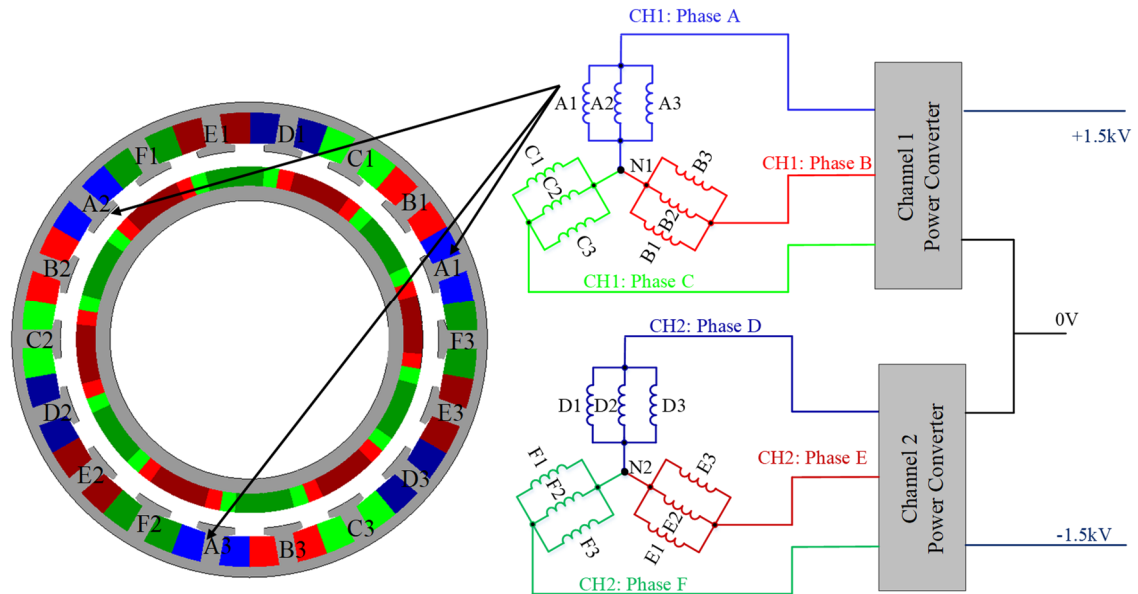


Fig. 7-1. Cross section and winding connection of a 2.5 MW PM Generator.

Table 7-1 Specification of a 2.5 MW PM generation.

Quantity	Value
Operation modes	Generating only
Output power	2.56 MW
DC Bus voltage	± 1.5 kV
Number of 3-phase channels	2
Efficiency target	$> 98\%$
Nominal machine operating speed	15,000 rpm (fixed)
Rate phase current (RMS/Peak)	815/1125.6 A
Rated torque (Average/Peak)	1574.1/1618.5 Nm

7.2 Critical Electrical Failure Modes

Among various electrical failure modes of the PM generator, short circuit failures resulting from insulation degradation and breakdown are the most critical since they will give rise to excessive fault current and rapid temperature rise in the fault region, and lead to catastrophic consequences.

Fig. 7-2 shows the coil distribution in the 18-slot of the generator and zoomed view of the coil layout. Each coil contains 8 turns arranged in the 2x4 layout. Rectangle litz wire of appropriate strands and size is used for the coil to minimise winding AC loss. For notational convenience, each turn of the coil is numbered as shown. This name convention will be used throughout the chapter unless otherwise stated. The copper strands within the litz wire are insulated by polyester/poly-amideimide coating with the cut through temperature 340°C. Each turn is separated from other by 0.05mm adhesive Kapton film. The adhesive Kapton film has no melting point and can function at 220°C to 240°C for

continuous service, and intermittent at 400°C. An insulation layer is wrapped around each row of 4 turns and the whole coil is covered and protected by another insulation layer before it is inserted in slots. Slot liner and insulation with appropriate thickness are used to isolate the coils from the stator lamination and other neighbouring coils.

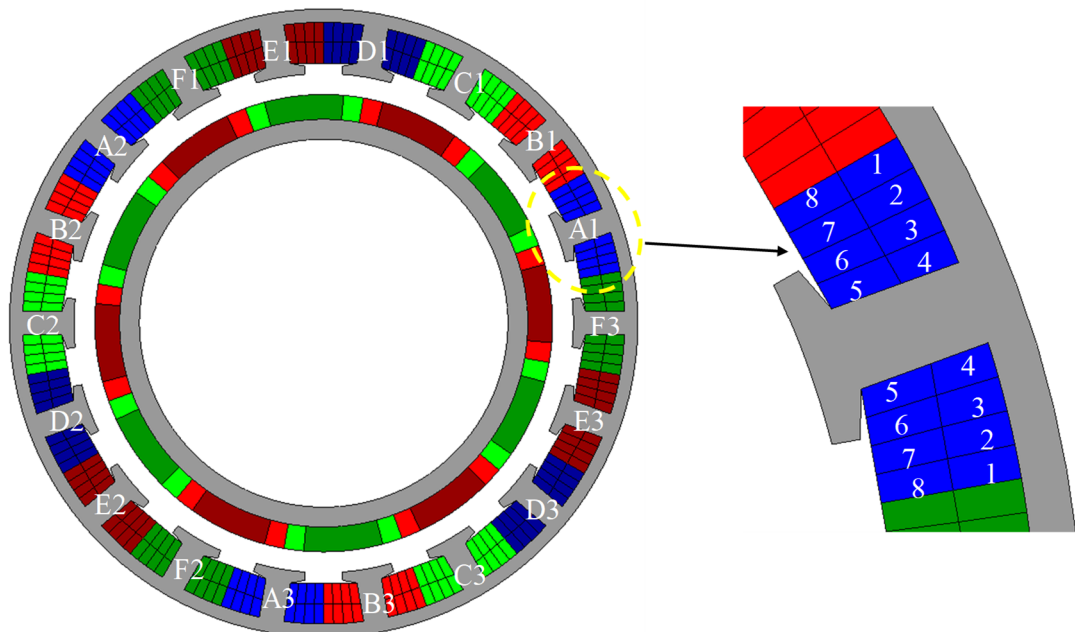


Fig. 7-2. Coil distribution and zoomed view of coil layout.

There are potentially 5 SC failure modes as a result of insulation break down.

1. Insulation failure **within litz wire bundle**: less likely because low voltage stress between strands and the effect is an increase in AC loss, which is considered to be benign, and hence not analysed in the chapter.
2. Insulation failure **between turns within a coil**: most likely because the turn-to-turn insulation is very thin, and uneven voltage distribution in a coil with fast switching inverter. It leads to extremely large current, and has catastrophic effect if not dealt with immediately.
3. Insulation failure **between two phases in the same 3-phase channel**: very likely because of high voltage stress (line-to-line) between two phases co-located in the same slot. The effect and consequence are similar to failure mode 2.
4. Insulation failure **between two phases in two separate 3-phase channels**: also very likely because of high voltage stress (line-to-line voltage plus 750V DC offset) and co-location of two phases of two separate channels in the same slots, e.g. coil A1 and coil F3, etc., as shown in Fig. 7-2. The fault is a very challenging

problem because it will lead to enormous SC current and hence catastrophic effect. However, the SC path is formed via converter and DC-link. If the faulted phases are isolated from the converters, the fault can be managed. Since the behaviour of a phase-to-phase SC fault between two 3-phase channels is dependent on converter operation and co-simulation of the FE model with the converters and control which requires prohibitively long simulation time, it is not analysed in the study.

5. Insulation failure **between phase and stator iron (housing)**: since the star neutral and housing is not grounded, the effect is benign. However this fault should be detected to avoid a catastrophic secondary failure.

Detailed analysis will be made for failure modes 2 and 3.

7.3 Turn-to-Turn Short Circuit

Theoretically, turn-to-turn insulation failure can take place in any coil and any phase, and the number of turns being short-circuit can vary in this generator from 1 (single turn) to 8 (all turns in a coil). In the latter case, the fault effectively causes terminal SC of the whole phase because the other two coils of the phase are in parallel with the faulted coil. It is well known that the severity of the fault or SC current is dependent on the number of turns being short-circuited, the location of the faulty coil in relation to other phases, and the position of the faulted turns in a slot. In order to identify the worst case, FE simulations are performed on a number of typical fault scenarios.

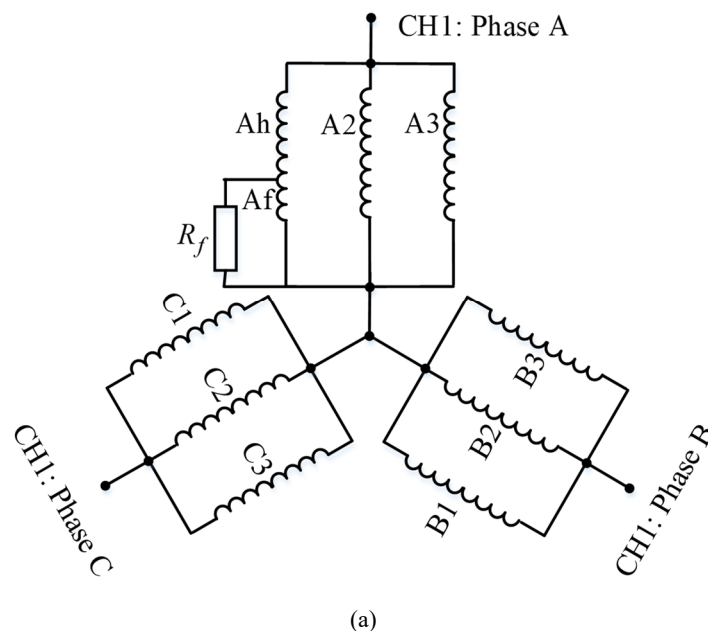
A FE model of the generator has been built in Flux2D with all the design parameters and material properties set. Due to asymmetry caused by a fault, full 2D geometry of the generator has to be included in the FE model. Simulations at the rated operation in healthy condition are performed. The generator performances predicted by the model agree with those given in Table 7-1 and the differences are within 1~3%. This may be caused by the fact that the mesh size of the FE model with full geometry is not as refined as the model which exploits periodicity with $1/6^{\text{th}}$ of the geometry.

With the validated model, FE simulations for various turn-to-turn fault cases are carried out. In each case, the generator is assumed to operate at the rated condition under current source excitation which represents ideal closed-loop current control by the

converters, and the short circuit is ideal with zero contact/external resistance in the SC path. The magnet temperature and winding temperature are assumed to be 200°C and 220°C, respectively, in all simulations unless otherwise stated. Non-ideal SC with varying contact resistance will be assessed subsequently.

7.3.1 Influence of Number of Short-Circuited Turns

Without loss of generality, a turn-to-turn SC fault is assumed to occur in coil A1 shown in Fig. 7-3 (a) where Af and Ah represent the short-circuited part and the remaining healthy part of the coil, respectively. The contact/external resistance R_f is assumed to zero for ideal SC. Fig. 7-3 (b), (c), and (d) show the fault scenarios with one, three and five SC turns, respectively. In each case, an SC fault consists of equal number of conductors in the upper and bottom rows of the 2x4 coil layout which are marked by yellow rectangles. In reality, the conductors in an SC fault may be in the same row, and hence the SC scenarios shown in Fig. 7-3 represent average effect. The fault currents and resulting torque waveforms with one, three and five SC turns are compared in Fig. 7-4, while the RMS currents, losses associated with the SC, and average torques are compared in Table 7-2.



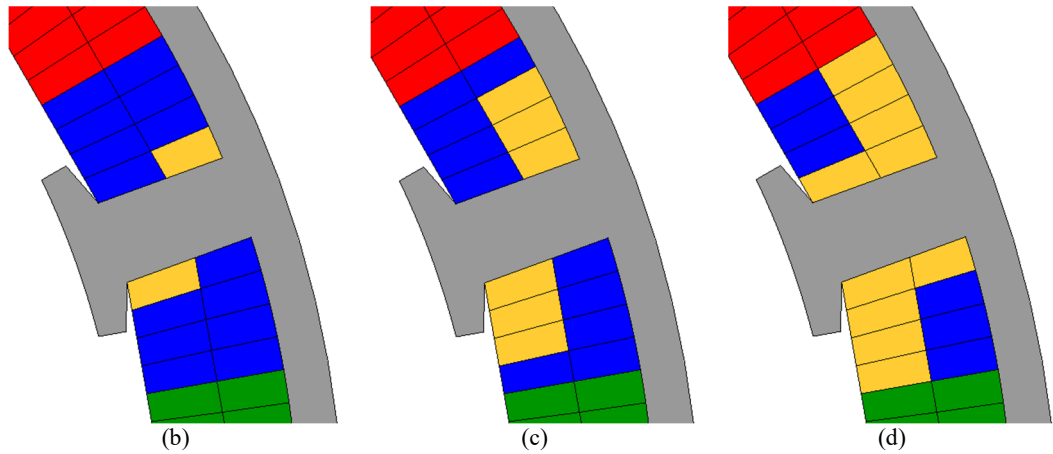
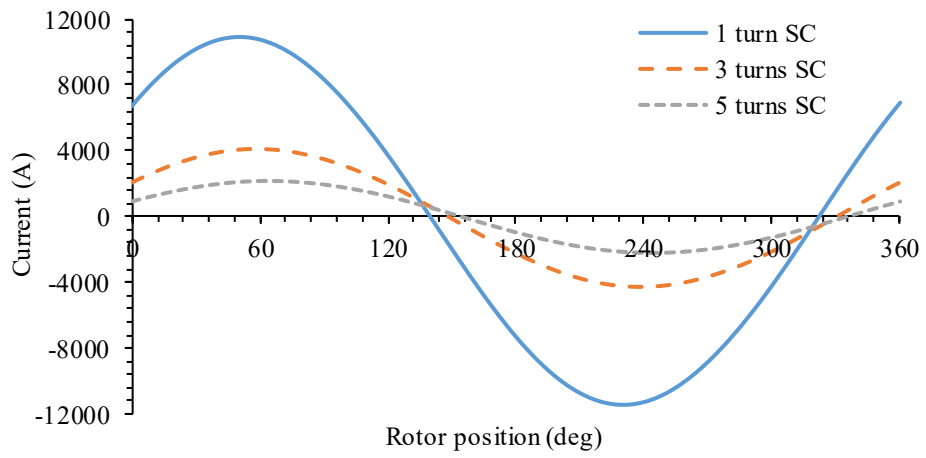
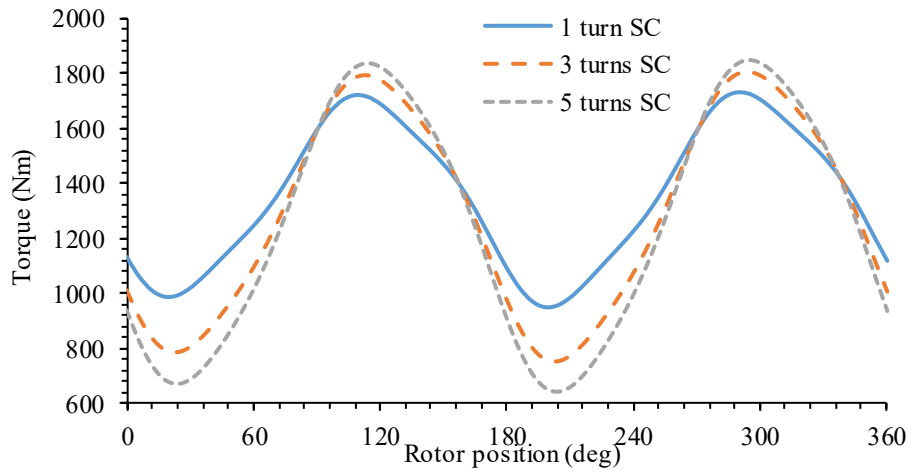


Fig. 7-3. Short-circuited turns (in yellow) in coil A1. (a) SC in coil A1. (b) One turn SC. (c) Three turns SC. (d) Five turns SC.



(a)



(b)

Fig. 7-4. Comparison of SC currents and torques under one, three and five SC turns. (a) SC turn fault current. (b) Torque.

Table 7-2 Comparison of fault behaviours under one, three and five SC turns.

SC turns	1 turn	3 turns	5 turns
Fault Current (rmsA)	7870	2939.8	1530.8
Fault current normalised to rated (p.u.)	29	10.8	5.6
Loss in SC turns (kW)	76	32	14
Current in healthy turns (rmsA)	983	1241	1385
Current in healthy coils A2/A3 (rmsA)	298	437	510
Total loss (kW)	92	51	32
Torque (Nm)	1349	1288	1255

As can be seen, one turn SC gives rise to the largest fault current, being 29 times greater than the rated. The resultant heating effect in the SC turn will be more than 800 times greater, leading to rapid increase in temperature. As the number of SC turns increases, the SC current reduces significantly. In contrast, the current in the healthy turns of the coil increases with the number of SC turns. An SC fault in one coil will also affect the other two healthy coils because they are connected in parallel to the faulty coil. Indeed, the influence is more pronounced when the number of SC turns is greater, but the level is much less significant compared to the current in the faulted turns. The faults also cause a large torque pulsation, and its magnitude increases with the number of SC turns albeit the influence on the average torque is less significant.

The faults will also affect the operation of other phases due to mutual coupling, manifesting in the voltage distortions under ideal current control. These effects are far less significant than the SC fault currents and hence not presented and discussed further.

7.3.2 Influence of Short-Circuited Turn Fault in Different Phases

Because the phase windings in a 3-phase channel are not symmetrically positioned in the stator, e.g., phase B is between phases A and C, which are adjacent to phase F and phase D of channel 2, respectively, the influence of SC turn fault in difference phases as shown in Fig. 7-5 is investigated. Fig. 7-6 compares the SC currents and torques when one turn SC in the outmost slot position takes place in phases A, B and C. The corresponding RMS currents, losses and average torques are listed in Table 7-3. It is evident from Fig. 7-6 and Table 7-3 that the fault occurring in difference phases only affects the phase shifts of the fault current and resultant torque. The magnitudes of the fault current and torque, and the heating effect are not affected.

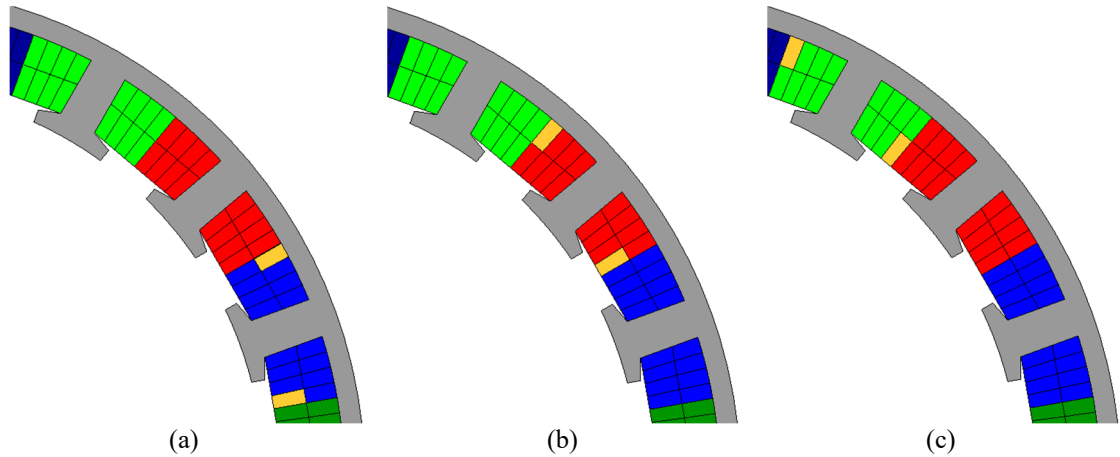


Fig. 7-5. One turn SC (in yellow) in different phases. (a) Phase A. (b) Phase B. (c) Phase C.

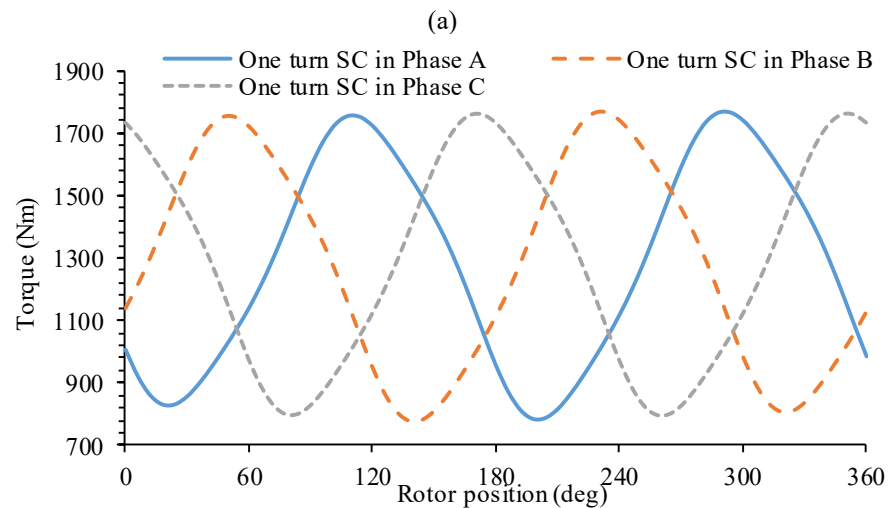
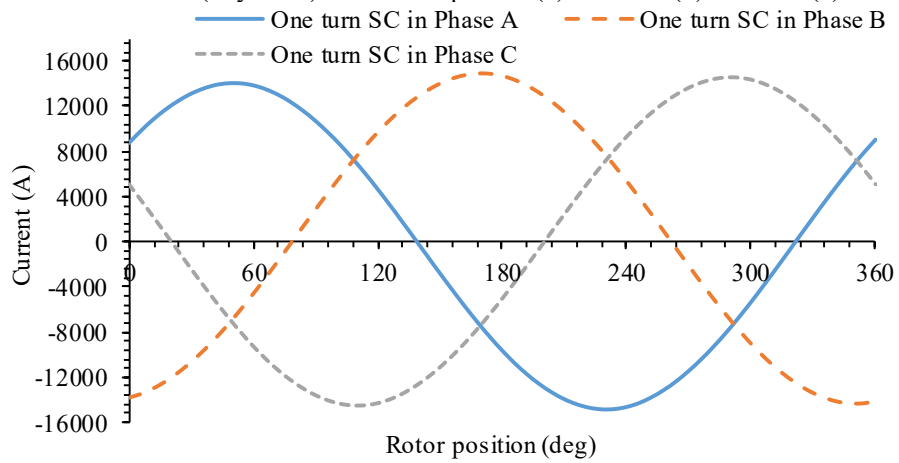


Fig. 7-6. Comparison of fault currents and torques when one turn SC occurs in different phases. (a) SC turn fault current. (b) Torque.

Table 7-3 Comparison of fault behaviours when one turn SC occurs in different phases.

One turn SC in different phases	Phase A	Phase B	Phase C
RMS fault current (A)	10208	10273	10625
SC turns loss (kW)	128	129	129
Total loss (kW)	145	147	147
Torque (Nm)	1278	1277	1290

Fig. 7-7 compares the phase voltage waveforms in the rated load, no load and one turn SC condition in phase A1 coil. The RMS phase voltage is 604V under the rated load, 510V under no load, and 214V under the fault condition. The significant reduction is caused by the SC current which produces the flux in the opposite direction of the PM flux as seen in Fig. 7-8. Consequently, from Fig. 7-8, the currents in two healthy coils A2 and A3 also produce the flux in the opposite direction of the PM flux as a result of the phase voltage reduction. Because of the parallel connection of coils A2 and A3 with the faulty coil A1 and current source which represents ideal closed loop current control, the current in the remaining healthy turns of the faulty coil A1 is significantly increased.

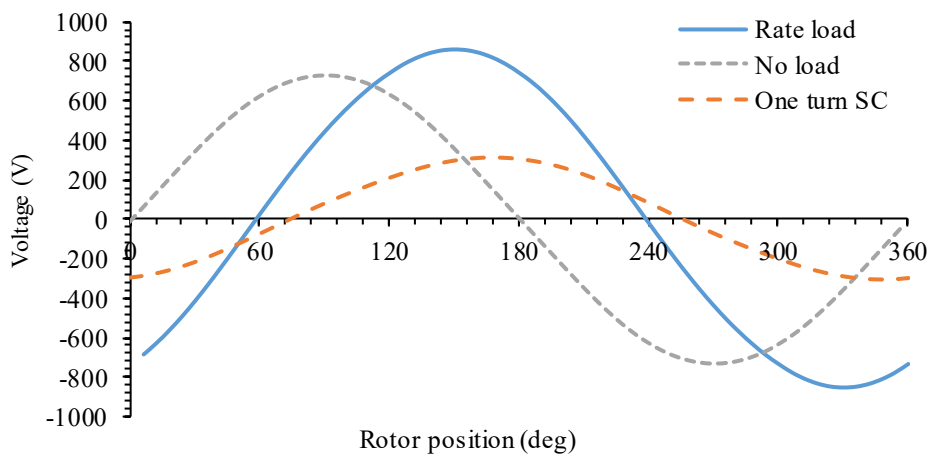


Fig. 7-7. Comparison of phase voltage of coil A under rated load, no load and one turn SC in phase A1.

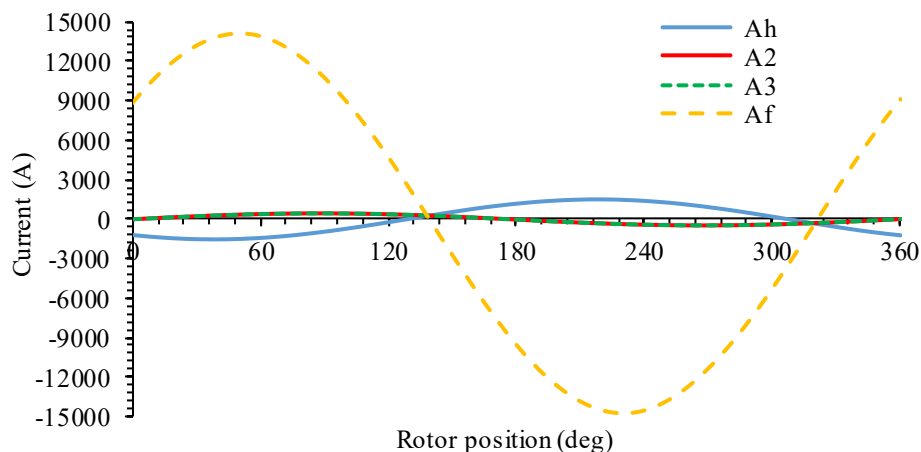


Fig. 7-8. Comparison of currents of Ah, A2, A3, and Af under one turn SC in phase A1 coil.

7.3.3 Influence of Short-Circuited Turn Fault Position in Slots

Since SC fault current is governed by the flux linkage of the faulted turns, the position of the fault in a slot will also influence the slot leakage flux and, consequently, the fault

current. The fault behaviours when one turn SC occurs at three different positions in coil A1 slots shown in Fig. 7-9 are compared in Fig. 7-10. The SC turn is located in the outmost position but in the different rows in position 1 (between the 1st and the 8th turns), in the same upper row in position 2 (between the two 1st turns) and in the same bottom row in position 3 (between the two 8th turns). It is seen that the turn fault current when the SC turn located in the two different rows is between those generated when the SC turn located in the same row. Moreover, the SC turn located in the position 3 (between the two 8th turns) in the same row close to the slot opening with more slot leakage flux will lead to the larger turn fault current and torque ripple.

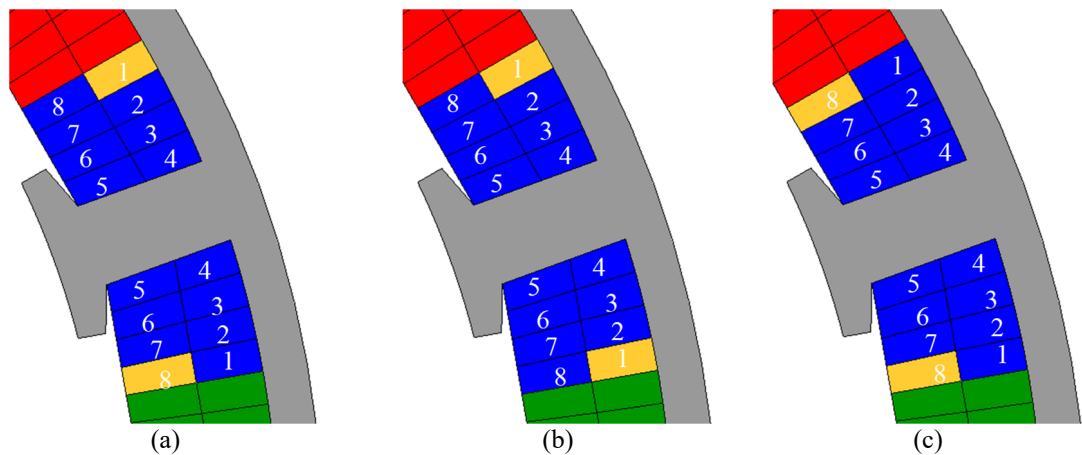
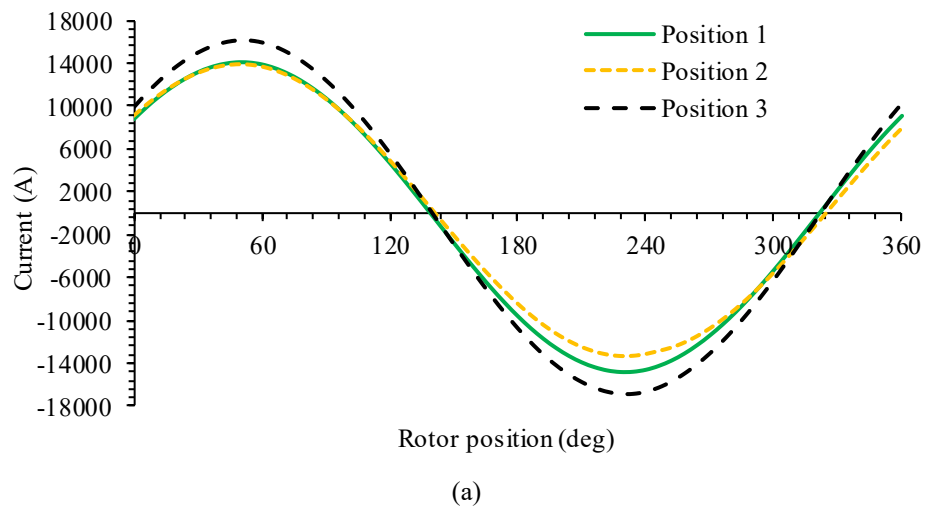
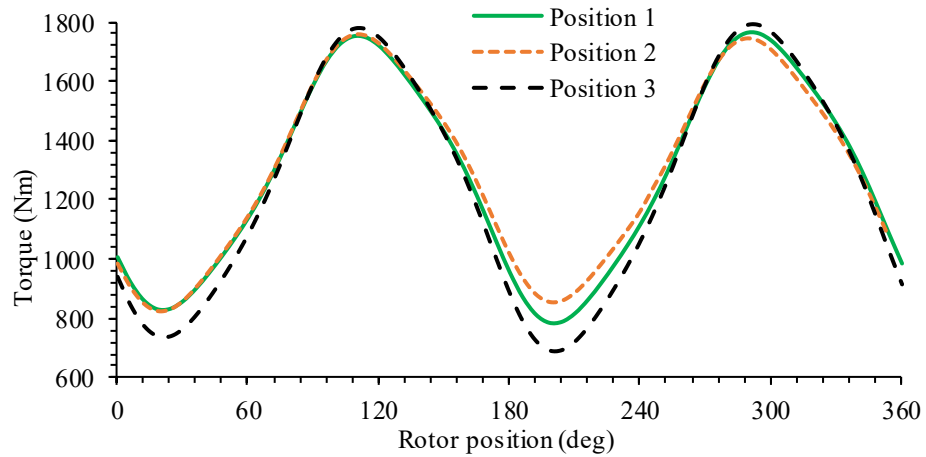


Fig. 7-9. One turn SC (in yellow) at three different positions in coil A1 slots. (a) Position 1. (b) Position 2. (c) Position 3.





(b)

Fig. 7-10. Comparison of SC currents and torques when one turn SC occurs at three positions in coil A1 slots. (a) SC turn fault current. (b) Torque.

Therefore, the fault behaviours when one turn SC occurs at eight different positions (between the same numbered two turns from 1 to 8) in coil A1 slots and the RMS currents, the associated losses, as well as the torques are compared in Table 7-4.

It is seen that the SC turn located in turn 7 as shown in Fig. 7-11 (a), with large slot leakage flux will lead to the largest turn fault current of 45 p.u. and the resulting heating effect is 178% greater than that in turn 4 shown in Fig. 7-11 (b) which yields the lowest turn fault current. The difference in the reduction in average torque of the eight fault positions is relatively small.

It follows that the worst case turn-to-turn short circuit is a single turn SC which occurs close to the slot opening where the leakage flux is relatively large.

Table 7-4 Comparison of fault behaviours when one turn SC occurs at eight positions in coil A1 slots.

SC turn number	Turn 1	Turn 2	Turn 3	Turn 4	Turn 5	Turn 6	Turn 7	Turn 8
RMS fault current (A)	9657	10042	9288	7323	8740	10980	12078	11613
RMS fault current normalised to rated (p.u.)	36	37	34	27	32	40	45	43
Loss in SC turn (kW)	114	123	106	66	94	148	179	165
Total loss (kW)	132	143	125	82	111	168	199	184
Torque (Nm)	1293	1273	1297	1364	1341	1341	1341	1246

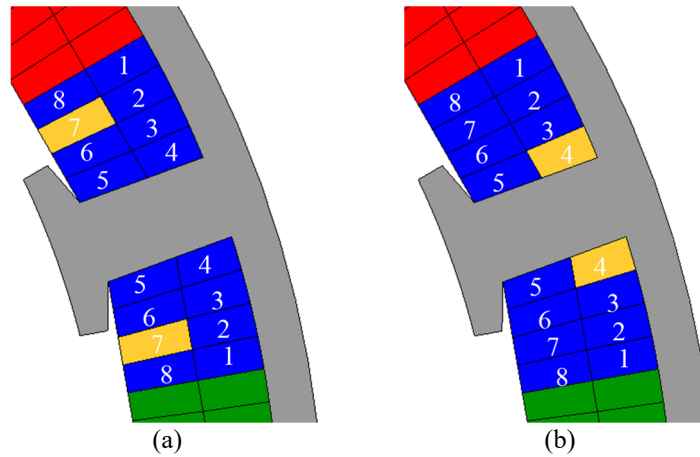


Fig. 7-11. One turn SC (in yellow) at two different positions in coil A1 slots. (a) Turn 7. (b) Turn 4.

7.4 Phase-to-Phase Short Circuit within One 3-Phase Channel

From the coil layout definition shown in Fig. 7-2, it is most likely that a phase-to-phase (or inter-phase) SC takes place when the insulation between two neighbouring coils which belong to two different phases but share the same slot breaks down. Hence there are two possible phase-to-phase SCs: SC between the two 1st turns and the two 8th turns of the two adjacent coils. Without loss of generality, it is assumed that the 8th turn will be connected to the phase terminal while the 1st turn to neutral, as shown in Fig. 7-12. Hence, the two possible SC scenarios are shown in Fig. 7-13 and Fig. 7-14, respectively.

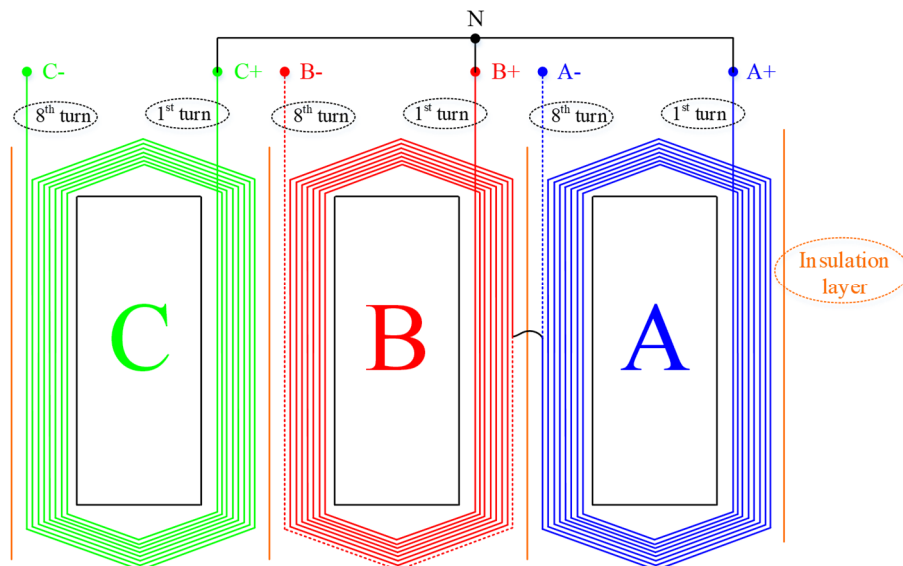


Fig. 7-12. Phase winding connection.

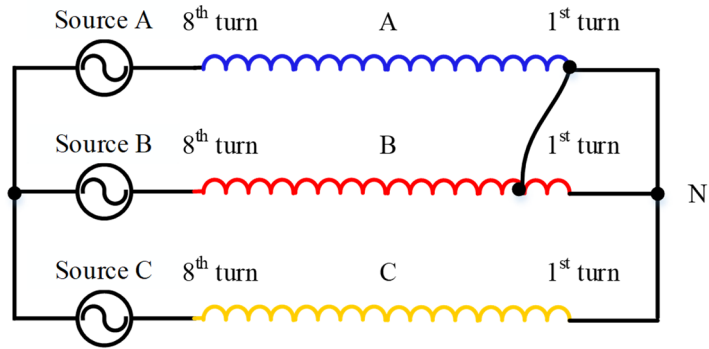


Fig. 7-13. Circuit illustration of inter-phase fault between two 1st turns.

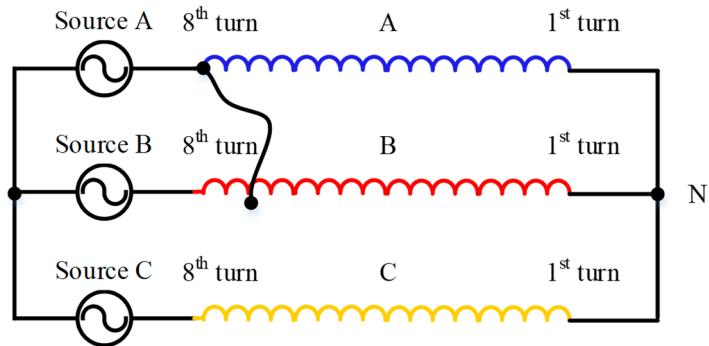


Fig. 7-14. Circuit illustration of inter-phase fault between two 8th turns.

As can be seen, the inter-phase fault shown in Fig. 7-14 is essentially a two phase terminal SC and the resultant fault current is similar to the single phase terminal SC, and is much lower than that of turn-to-turn SC, as analysed in section 7.3.

The inter-phase fault shown in Fig. 7-13 is similar to single turn SC as illustrated in Fig. 7-15. The resultant fault currents and torques are compared in Fig. 7-16, where Af and Bf represent the SC part of the coil A and B, respectively. As will be seen, the fault current magnitudes and resultant torques of the two fault scenarios are very similar albeit the differences in phase shifts of the SC currents are evident.

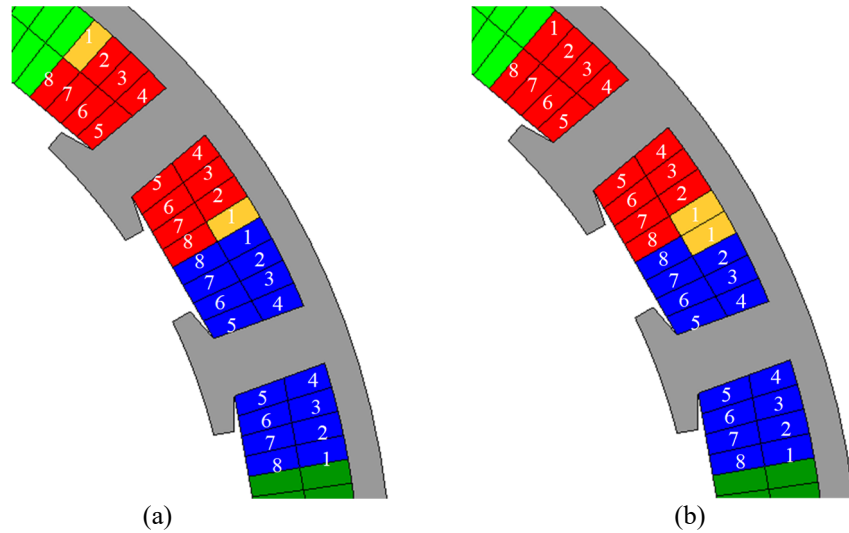


Fig. 7-15. Illustration of turn-to-turn and phase-to-phase SC in the 1st turns. (a) One turn SC in phase B in the 1st turns. (b) Inter phase SC in phases A and B between two 1st turns.

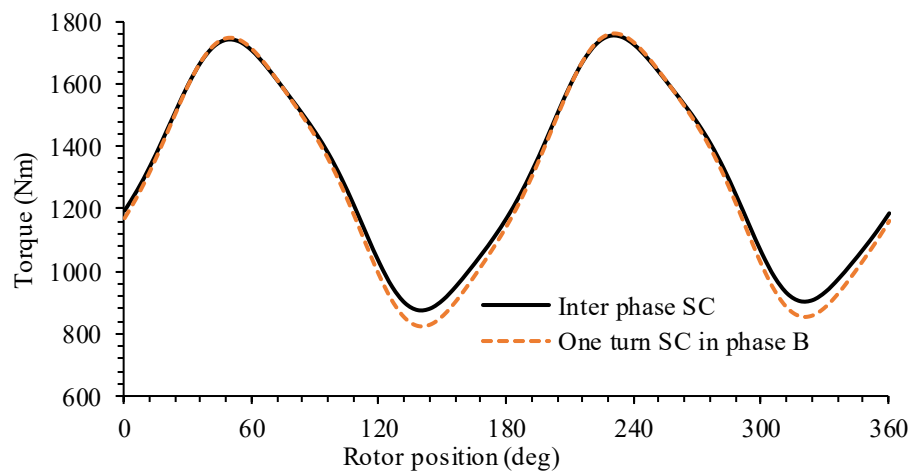
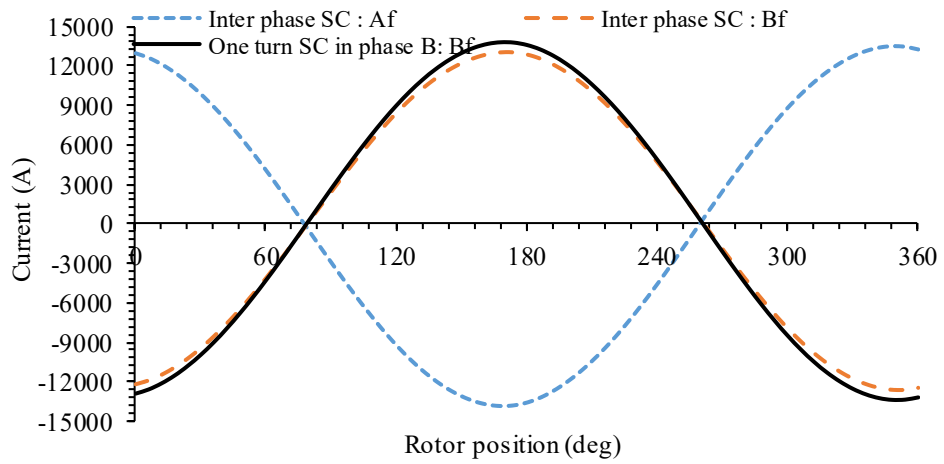


Fig. 7-16. Comparison of fault currents and torques under one turn SC in phase B and inter-phase SC. (a) SC turn fault current. (b) Torque.

The above analysis shows that the worst case inter-phase SC is similar to single turn SC in a coil which is the worst case of all possible SCs within one 3-phase channel.

It is important to point out that fault signature, i.e., any changes reflected in phase voltages and currents as a result of an SC fault, is not necessarily proportional to fault severity. For a turn-to-turn SC, the fault current and hence its severity is the largest when a single turn is short-circuit while its fault signature is the least noticeable in the phase voltage and current. For a phase-to-phase SC, its severity is less than a single turn SC, but the fault will give rise to a much great unbalance in the phase voltages and currents, and hence is much easy to detect. A phase-to-phase SC usually triggers converter overcurrent protection.

7.5 Measures to Reduce Short-Circuit Current

To identify possible mitigation measures for the worst SC fault, the effect of two actions are also simulated.

7.5.1 Terminal Short-Circuit

Upon detection of an SC fault, terminal short-circuit may be applied to reduce the turn-to-turn fault current. This measure is effective when the terminal SC current in healthy condition is close to one p.u., so that the remedial action is thermally sustainable. Terminal SC is applied to all phases in channel one when a single turn SC which occurs in coil A1 in the worst position turn 7 as in Fig. 7-11 (a) has been detected and the results before and after the terminal SC are compared in Table 7-5.

As can be seen, after the terminal SC, the fault current in the SC turn has been reduced significantly from 45 p.u. to 13 p.u. However, the currents in the healthy phases are increased to ~ 2.0 p.u. While the loss in the SC turn (heating effect) has reduced by 11 times compared to the SC fault without terminal SC, the losses in the faulted turn and in the healthy coils with the terminal SC are far too high to avoid catastrophic consequence. The average torque is reduced to 46% of the healthy operation after the application of terminal SC.

Table 7-5 Comparison of fault behaviours of one turn SC before and after application terminal SC in phase A.

Condition	1 turn SC	1 turn SC with terminal SC
Fault current (rmsA)	12078	3385
Fault current (p.u.)	45	13
Loss in SC turns (kW)	179	14
Current in healthy turns (rmsA)	1222	202
Currents in coils A2/A3 (rmsA)	389	550
Currents in coils B1/B2/ B3 (rmsA)	275/270/270	415/417/417
Currents in coils C1/C2/ C3 (rmsA)	271/272/272	461/462/462
Total loss(kW)	199	33
Torque (Nm)	1341	724

7.5.2 Switch-off Engine (Generator Speed Reduced to 10% Rated Speed)

Since terminal SC is unable to manage an SC fault, an alternative measure is to switch-off engine upon detection of an SC fault. This would mean loss of all generator power but due to wind-mill effect, the generator would still rotate at about 10% rated speed. The fault behaviours when one turn SC occurs in coil A1 in turn 7 as shown in Fig. 7-11 (a) at 10% rated speed with all other phases being deactivated are also simulated and the results are compared to the fault at the rated speed in Table 7-6. It can be seen that the SC turn current at 10% rated speed reduces to about 40% compared with the value at the rated speed. In addition, currents in the healthy turns of coil A1 and in the healthy coils A2 and A3 are 393 rmsA, and 197 rmsA respectively. Clearly, this level of the fault current is not sustainable.

The forgoing analysis shows that existing measures, other than mechanical disconnection of the generator from the engine, are not able to manage the worst case turn fault in a sustainable manner.

Table 7-6 Comparison of fault behaviours of one turn SC in phase A under rated speed and one turn SC in phase A with all other phases being deactivated under 10% rated speed.

Condition	1 turn SC under rated speed	1 turn SC with all other phases deactivated under 10% rated speed
Fault current (rmsA)	12078	5072
Fault current (p.u.)	45	17
Loss in SC turns (kW)	179	27
Current in healthy turns (rmsA)	1222	393
Currents in coils A2/A3 (rmsA)	389	197
Total loss(kW)	199	28
Torque (Nm)	1341	-183

7.6 Influence of SC Contact Resistance on Fault Current

The foregoing study assumes that the contact insulation resistance, R_f , which forms a SC path in Fig. 7-3 (a), is zero. This is unlikely in real operation. It is more likely that this resistance decreases as the insulation degrades and reaches a very low value when the insulation breaks down. To investigate this effect, simulations with one turn SC in coil A1 in turn 7 as shown in Fig. 7-11 (a) with non-zero contact resistance are performed. The value of this resistance is set to 0, 1, 10, 100, 1000, 10000 and 100000 times of one turn resistance ($1.22\text{m}\Omega$ at 220°C) and they are denoted by R0, R1, R10, R100, R1000, R10000 and R100000, respectively. The fault behaviours with one turn SC in coil A1 when the contact resistance is varied are simulated, and the resultant SC currents and losses are given in Table 7-7 together with those in healthy condition when the contact resistance is infinite.

Table 7-7 Comparison of SC currents and associated losses under healthy and one turn SC with variable contact resistances.

	R0	R1	R10	R100	R1000	R10000	R100000	Healthy
$R_f (\Omega)$	0	1.22E-03	0.0122	0.1224	1.224	12.24	122.4	infinity
Current in SC turn (rmsA)	12078	11189	4382	323	223	267	271	272
Current in R_f (rmsA)	13282	12359	5041	595	60	6	0.6	0
Current in SC turn (p.u.)	45	41	16	1.2	0.8	1.0	1.0	1.0
Loss in SC turn (W)	178561	153249	23505	128	61	87	90	90
Loss in R_f (W)	0	186349	310066	43256	4422	444	49	0

As can be seen, the fault current in the SC turn decreases as the contact resistance increases. When the contact resistance reaches 122.4Ω (100000 times one turn resistance), the fault current is less than 1.0 rmsA, essentially benign. It should, however, be noted that as the contact resistance increases, the loss incurred in it increases initially, and reaches extremely high value of 310kW when the contact resistance is 10 times the one turn resistance. This is because at this point, the fault current is still very large and the current in the contact resistance is even larger than the current in the faulted turn. Consequently, the loss in the contact resistance is more than 10 times greater than that in the faulted turn. As the contact resistance continues to increase, its loss starts to decrease.

The phenomenon may have a serious consequence if a fault occurs in real time operation. As we can expect, the contact resistance reduces as the insulation degrades. When the contact resistance is greater than 100Ω , the fault current is very small and net effect would be benign. Consequently it would be very difficult to detect this fault from voltage and current measurements. As the contact resistance decreases, the loss incurred in it increases and reaches 444W when the contact resistance is about 100000 times one turn resistance (12.2Ω). The current in the SC turn is, however, very close to the healthy value, being even slightly lower. The 444W loss in the contact resistance may give rise to a local high temperature hotspot, and accelerate the insulation degradation while fault detection under this condition by any conventional means is still very difficult. If the contact resistance decreases further, the loss incurred in it will increase to a level that the temperature increase will be dramatic. Consequently, when the contact resistance is decreased to a threshold value, an avalanche effect may take place until local hotspot temperature reaches above the maximum working temperature (400°C). At this point, the contact resistance would decrease to zero very quickly and irreversibly which may reach the peak loss at R10, leading to complete failure.

It can also be seen that when the contact resistance increases from R0 to R1, the fault current is reduced only by 8.9%. This implies that the dominant factor which governs the SC current is inductance, or the SC turn fault current is inductance limited. Under this condition, the losses incurred in the faulted turn and in the contact resistance will increase further when their temperatures increase under the fault condition.

The previous analysis shows that it is essential to detect the fault at early stage when the contact resistance is sufficiently large. For this purpose, the 2nd harmonic in IAP and IRP produced by an SC fault are evaluated as turn fault indicators. Fig. 7-17 and Fig. 7-18 show the 2nd harmonic variations of IAP and IRP with variable contact resistances, respectively, where p_{12} and p_{22} denote the 2nd IAP harmonics in channel 1 and channel 2, respectively, while q_{12} and q_{22} denote the 2nd IPR harmonics in channels 1 and 2, respectively. Table 7-8 presents the corresponding numerical values and the ratios of the harmonics between the faulty and healthy channels together with those under healthy condition. Theoretically, if the two channels are perfect balanced, the 2nd harmonics should be zero. Hence residual harmonics are caused by numerical simulation errors.

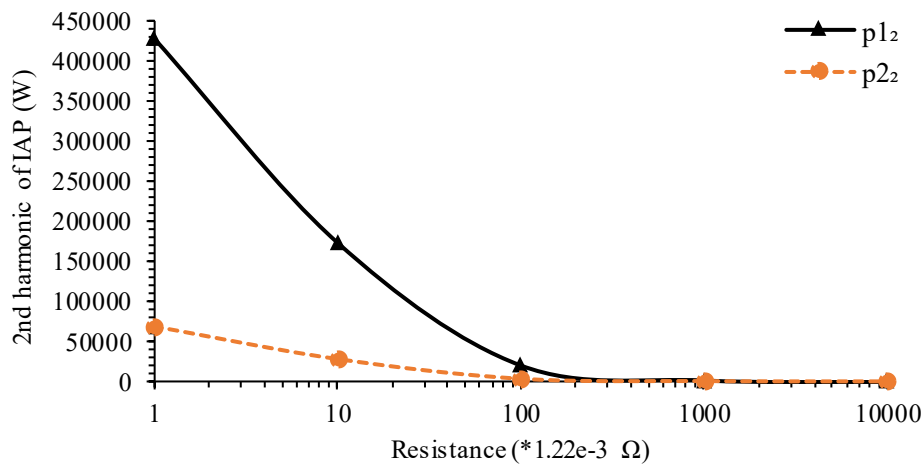


Fig. 7-17. Variation of 2nd IAP harmonic with variable contact resistances.

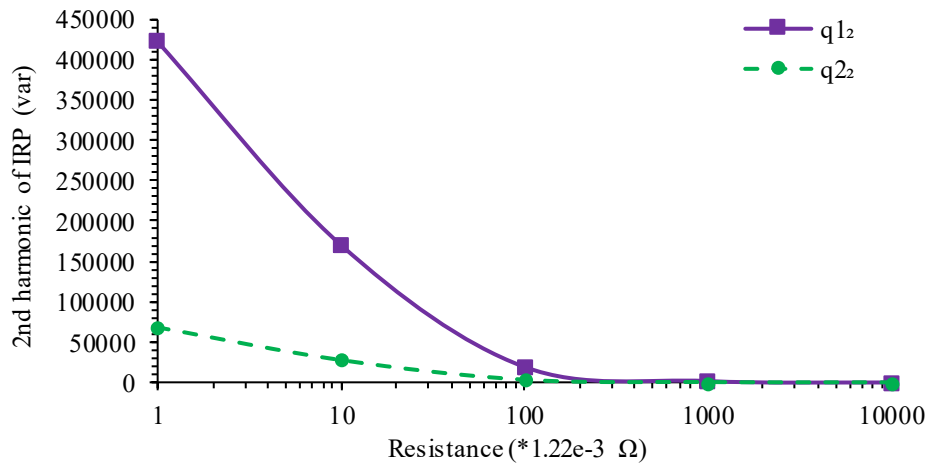


Fig. 7-18. Variation of 2nd IRP harmonic with variable contact resistances.

Table 7-8 Variations of 2nd IAP and IRP harmonics with variable contact resistances under one turn SC in coil A1.

	Healthy	R0	R1	R10	R100	R1000	R10000	R100000
p1 ₂ (W)	3	461460	427564	173781	20849	2123	213	23
p2 ₂ (W)	2	74584	69533	28312	3316	333	32	2
p1 ₂ / p2 ₂	2	6	6	6	6	6	7	12
q1 ₂ (var)	2	454632	422327	171000	19888	2017	202	22
q2 ₂ (var)	1	73829	68412	27803	3330	337	33	3
q1 ₂ / q2 ₂	2	6	6	6	6	6	6	8

Under the SC fault conditions, the 2nd IAP and IRP harmonics increase dramatically in the fault 3-phase channel when the contact resistance is relatively small. Because the mutual coupling between the two 3-phase channels, the fault in channel 1 also gives rise to the 2nd IAP and IRP harmonics in channel 2 although their magnitudes in channel 2 are much small. As the contact resistance increases, the fault current decreases, and the IAP and IRP harmonics also decrease in both channels. However the ratios between the two channels only change slightly between 6 and 7 when the contact resistance varies from

R0 to R10000. The ratios may be a good indicator that allows detection of an SC turn fault at an early stage. It should be noted that when the contact resistance is R100000 or greater, the fault signature is very small, and the larger ratios shown in Table 7-8 may be caused by numerical errors. In real operations, it is likely that the generator has small inherent unbalance due to manufacturing tolerance and disparities in converter characteristics, the 2nd IAP and IRP may exist in healthy conditions. The effectiveness of this fault detection needs therefore assessed against the test results and it is possible to employ calibration and online learning to improve detection sensitivity and accuracy [128].

The analysis in section 7.5.2 shows that if the turn-to-turn insulation is completely break down with zero contact resistance, switching-off the engine which reduces the generator speed to 10% of the rated due to windmill effect is unable to reduce the fault current to a sustainable level. In earlier stage of the insulation break down, however, the contact resistance will not be zero. Hence, the fault behaviours at 10% rate speed with variable contact resistance are simulated. The fault currents and associated losses under the worst case one turn SC in the turn 7, as shown in Fig. 7-11 (a), at 10% rated speed when all other phases are deactivated with the contact resistance varying from R0 to R100000 are given in Table 7-9. It can be observed that with the contact resistance at R100000, R10000 and R1000, the fault currents and resultant losses are insignificant. However, if the contact resistance is reduced to below R10, the losses in the faulted region are excessive and likely to cause further damage to insulation. If the fault can be detected in early stage when the contact resistance is above R100, it may be contained by switching off the engine immediately.

Table 7-9 Fault currents and losses under one turn SC at 10% rated speed when all other phases are deactivated with variable contact resistances.

	Contact resistance (Ω)						
	R0	R1	R10	R100	R1000	R10000	R100000
	0	0.001224	0.01224	0.1224	1.224	12.24	122.4
Current (rmsA)							
In healthy turn	393.0	203.5	36.7	4.0	0.4	0.0	0.0
In healthy coils A1/A2	196.5	101.7	18.4	2.0	0.2	0.0	0.0
In faulted turn	4678.9	2422.4	437.0	47.3	0.5	0.5	0.0
In contact resistance	5071.7	2625.8	473.7	51.3	4.8	0.5	0.1
Fault current (p.u.)	17.2	8.9	1.6	0.2	0.0	0.0	0.0
Loss (W)							
In healthy turns	1037.9	278.2	9.1	0.1	0.0	0.0	0.0
In healthy coils	296.5	79.5	2.6	0.0	0.0	0.0	0.0
In faulted turn	26795.5	7182.5	233.7	2.7	0.0	0.0	0.0
In contact resistance	0.0	8439.3	2746.0	322.2	32.8	3.3	0.3
Total	28426.7	16059.1	2993.9	325.1	32.8	3.3	0.3
Torque (Nm)	-183.3	-103.7	-19.4	-2.1	-0.2	0.0	0.0

7.7 Thermal Impact of Short Circuit Fault

It has been shown in sections 7.3 and 7.5 that in the worst case, i.e., a single turn short circuit fault close to slot opening region, will produce the loss in the faulted turn 1000 times greater than that of healthy operation. With present of nonzero contact resistance, the fault current is much smaller, but the loss in the contact resistance becomes very large. In both cases, it is important to understand how quickly the temperature will rise to a level that will cause permanent damage. Extensive thermal analyses of a number of representative fault conditions will be assessed in this section.

7.7.1 3D Thermal Model

Fig. 7-19 shows the 3D model containing one thirty-sixth (half slot) of the generator in which various components and cooling channels are also illustrated. The generator is cooled by oil flow in the stator through the cooling channels in the stator back iron and those in the slots as well as by the air flow in the rotor air channels. A peek sleeve is attached to the stator bore to prevent the cooling oil from leaking into the airgap. The relevant parameters and thermal properties are listed in Table 7-10.

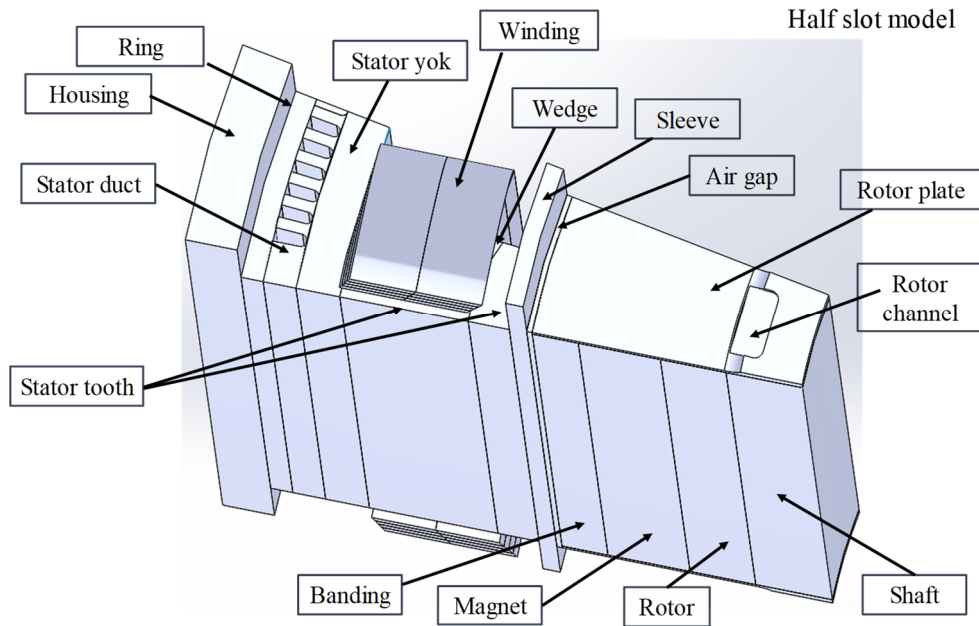
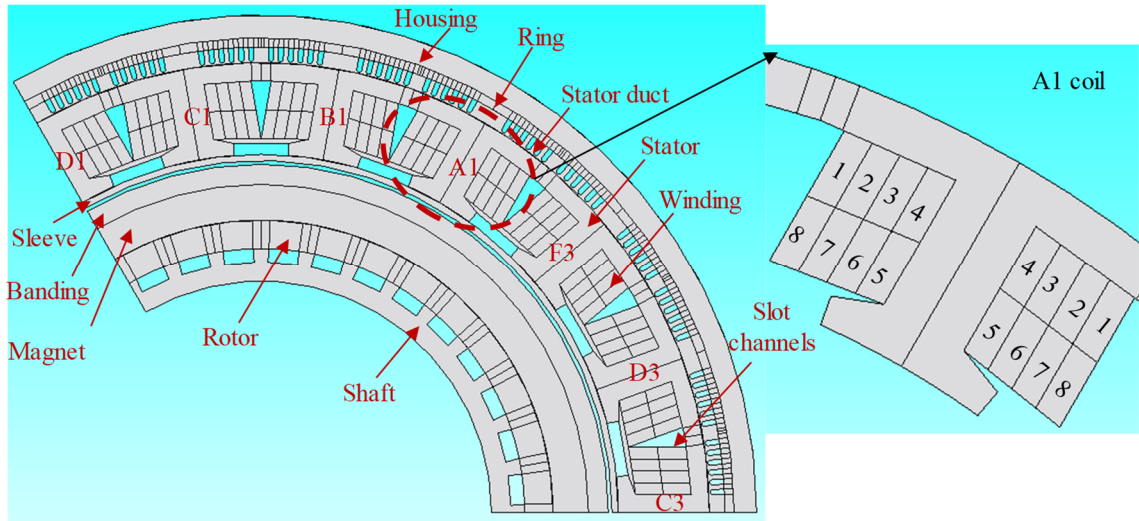


Fig. 7-19. 3D 1/36 (half slot) model.

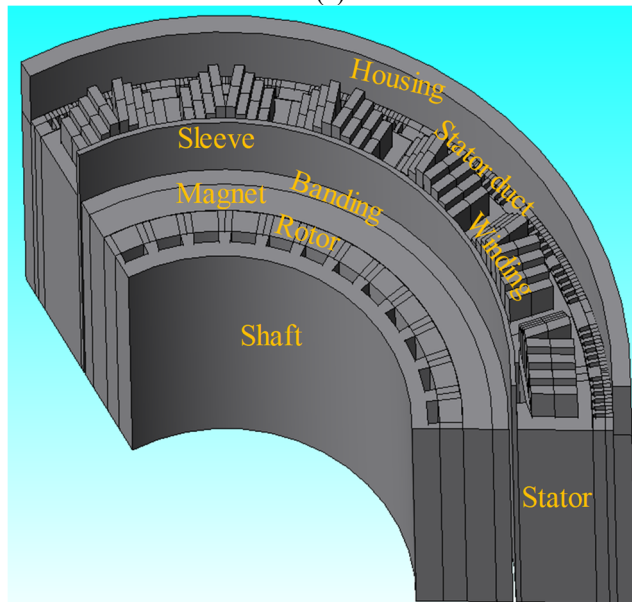
Table 7-10 Parameters and thermal properties.

End winding length	37.7 mm
Thermal conductivity of stator sleeve and rotor banding	0.3 W/m/K
Thermal conductivities of slot liners, resin and impregnation	0.2 W/m/K.
Stator cooling oil	Midel transformer oil
Cooling oil inlet temperature and flowrate	70°C and 3.0652 kg/s
Inlet temperature and the flowrate of air flow through rotor air channels	40°C and 0.3915 kg/s
Inlet temperature and the flowrate of the air flowing through airgap	40°C and 0.0435 kg/s
Ambient temperature	40°C

In healthy operation, the temperature distribution in each slot of the generator is identical and hence the half slot model is sufficient to simulate the thermal behaviour. In a fault condition, however, this symmetry no longer exists, and a full 3D geometry will be needed to model the thermal behaviour. This would increase the computation time dramatically. Given that the heating effect of fault current will be local, one third of the generator consisting of 6 slots and 1/2 axial length will be modelled with the faulted coil in the middle (coil A1), as shown in Fig. 7-20.



(a)



(b)

Fig. 7-20. 3D thermal model of generator in JMAG. (a) Radial cross section of 3D thermal model. (b) 3D thermal model.

Since specialised tools for motor thermal analysis, such as Motor-CAD, cannot model asymmetric thermal behaviour in fault conditions, JMAG which supports co-simulation of electromagnetic and thermal fields in electrical machines introduced in Chapter 5 is used for the thermal analysis. To reduce complexity of the model, the end winding is simplified in the 3D thermal model with straight segments of the same equivalent length as those in the prototype machine as shown in Fig. 7-20.

The effect of litz wire winding comprising copper conductors and insulations are modelled as conductors with anisotropic thermal conductivity using the Hashin and Shtrickman approximation [132] [133]. The radial/circumferential equivalent thermal

conductivity and equivalent specific heat capacity of the litz wire are calculated by equations (4-10) to (4-13) in Chapter 4.

The generator thermal behaviour at the rated operation in healthy condition with the losses distribution given in Table 7-11 is predicted by both JMAG and Motor-CAD.

Table 7-11 Losses under rated healthy condition.

Copper loss (kW)	Stator iron loss (kW)	Rotor iron loss (kW)	Magnet eddy current loss (kW)	Windage loss (kW)
10.54	11.2	1.3	2.7	1.8

Fig. 7-21 and Fig. 7-22 show the steady state temperature distributions of the generator and windings predicted by JMAG, respectively, when the generator operates at the rated healthy condition. It is seen that the temperature in the middle of each coil is the highest, and reaches 235°C. The average temperature of the end winding region is lower than that of the active winding region. This is because the total end winding region is immersed in the cooling oil, while the active winding region is cooled by the cooling oil flowing through the slot channels. Table 7-12 compares JMAG and Motor-CAD predicted steady state temperatures in various parts of the generator. It is evident that the predicted steady-state temperatures by the two modelling tools agree quite well. For example, the hotspot temperature predicted by Motor-CAD is 4°C lower than that predicted by JMAG. This is because Motor-CAD uses lumped parameter model which may not be able to predict hotspot temperature precisely. The difference, however, is less than 2%.

The comparisons of transient temperature rises in different components of the generator predicted by JMAG and Motor-CAD under healthy condition are shown in Fig. 7-23. Again, good agreements between the two predictions are seen. The good agreements by the two modelling tools provide the confidence that the established JMAG model is capable of predicting the generator thermal behaviour.

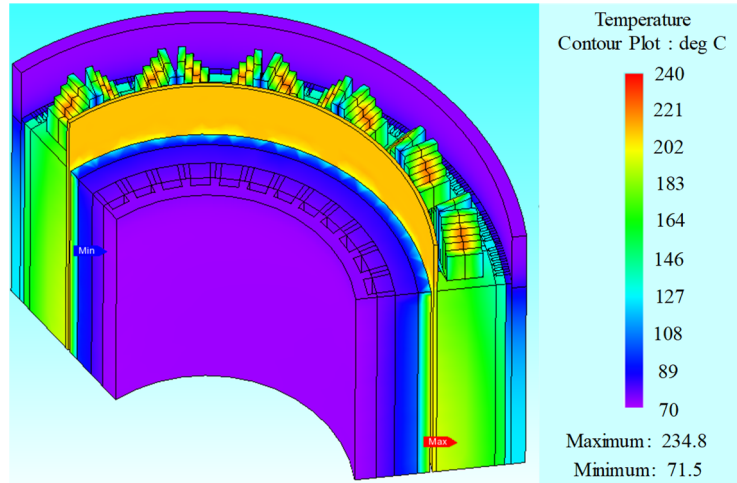


Fig. 7-21. Steady state temperature distribution of the generator predicted by JMAG under healthy condition.

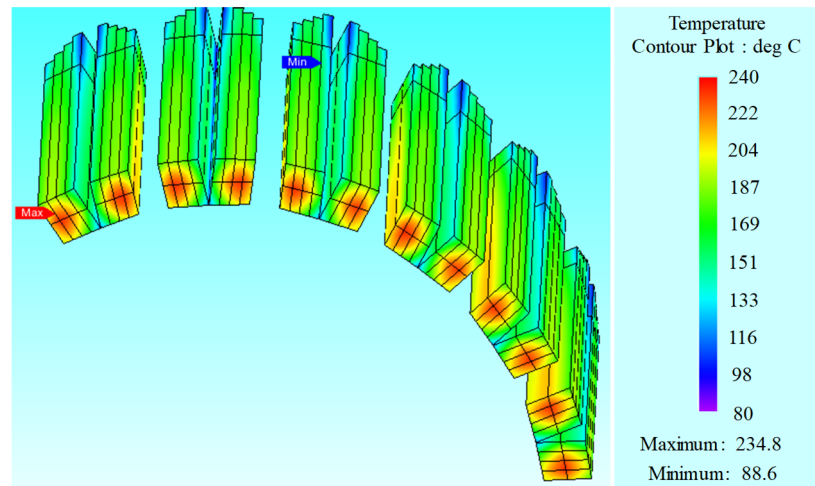


Fig. 7-22. Temperature distribution of windings predicted by JMA under healthy condition.

Table 7-12 Comparisons of JMAG and Motor-CAD predicted temperatures in healthy condition.

Temperature (°C)	Motor-CAD	JMAG	Difference
Rotor channels air	52	53	1
Stator duct oil	71	73	2
Slot gap oil	73	74	1
Slot opening oil	76	74	-2
Shaft	72	73	1
Rotor	83	80	-3
Magnet	95	91	-4
Airgap	200	202	2
Housing	121	114	-7
Stator core	151	155	4
Winding Average	192	194	2
End Winding Average	180	182	2
Hotspot	231	235	4

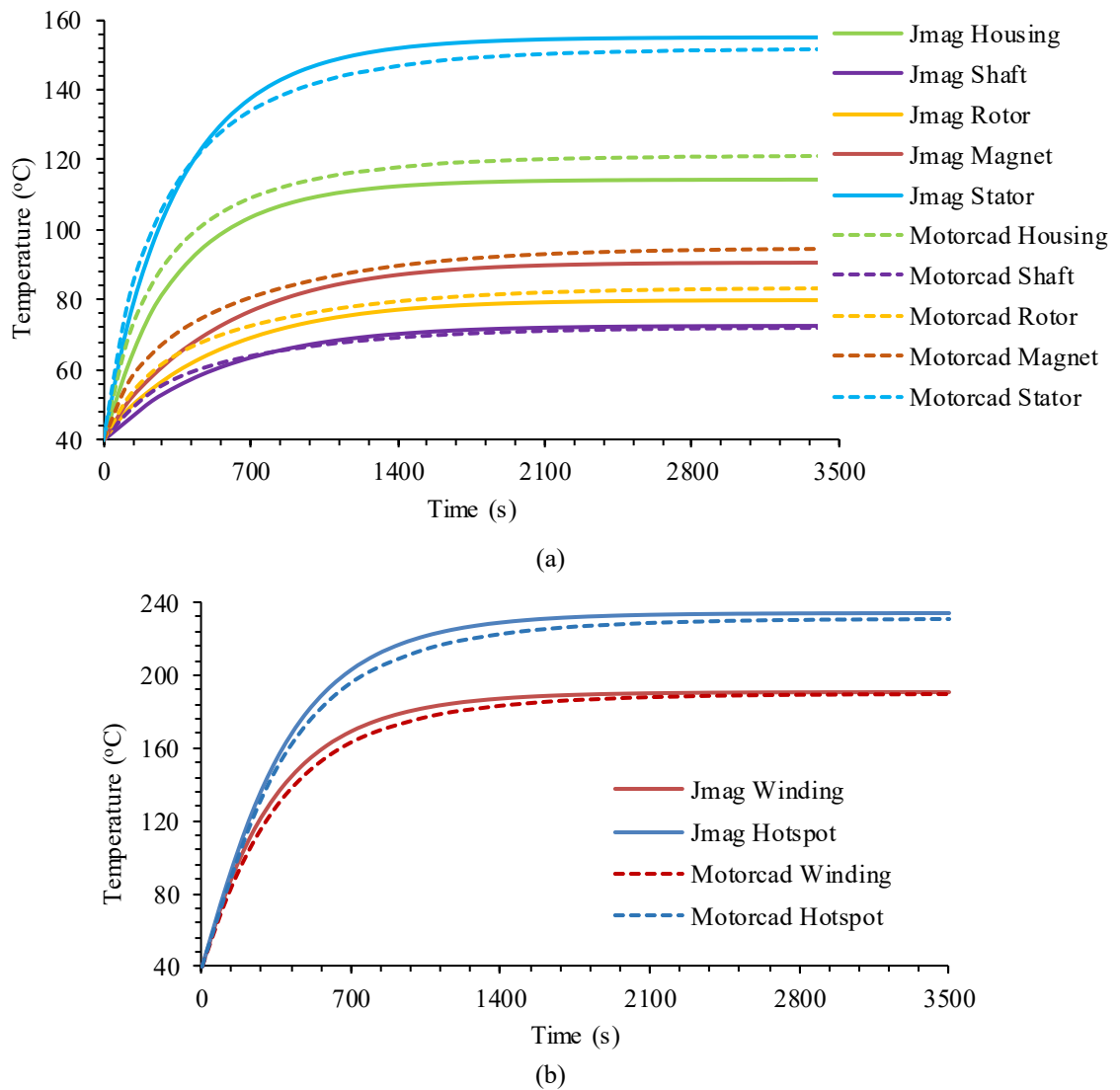


Fig. 7-23. Comparisons of transient temperature rises between Motor-CAD and JMAG. (a) Housing, shaft, rotor, magnet and stator. (b) Winding and hotspot.

7.7.2 Thermal Behaviours in Short-Circuit Fault Conditions

With the established 3D model, the thermal impact of SC faults will be investigated. Since a single turn SC fault is the worst case, the study will focus on a few typical scenarios associated with a single turn SC fault. In each case, simulations will be performed for the rated operation in healthy condition until the thermal steady-state is reached. A SC turn fault will be injected and subsequent transient temperature behaviour will be simulated. The time instant when a fault is injected is defined as $t = 0$ for the transient simulations described in this section.

7.7.2.1 One Turn SC Fault with Zero Contact Resistance

A single turn fault is assumed in coil A1 and as has been shown in section 7.3, a single turn SC in turn 7 will lead to the most severe fault scenario. Before the fault is injected, the temperature distribution in each turn in healthy in steady-state is given in Table 7-13. The 1st and 8th turns have the lowest temperatures because the cooling oil flows through the slot channels, while the other six turns have relatively similar temperatures. Subsequently, the resulting thermal impact when a single turn SC occurs in turn 7 with zero contact resistance will be investigated. Fig. 7-24 shows the cross sectional view of the thermal model with turn 7 being short-circuited as marked by the two black quadrangles.

Table 7-13 Temperature distribution of coil A1 under healthy condition.

Turn number	Turn 8	Turn 7	Turn 6	Turn 5	Turn 4	Turn 3	Turn 2	Turn 1
Average Temperature (°C)	160	196	213	208	197	209	199	168
Max Temperature (°C)	208	230	235	234	234	234	230	208

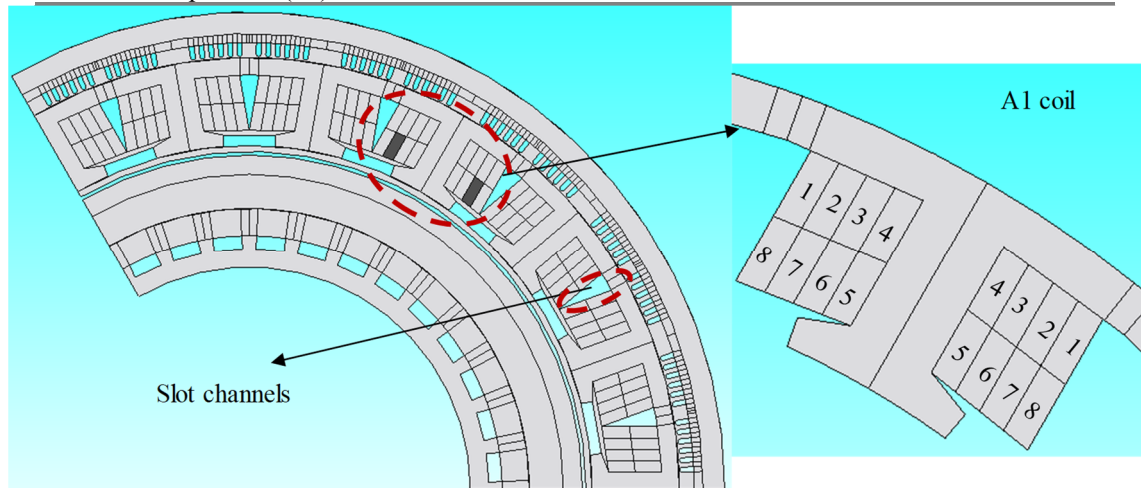


Fig. 7-24. Cross section of thermal model with turn 7 SC.

As has been shown in section 7.6, the fault current of the generator with one turn SC is inductance limited, so the influence of the variation of temperature on the resistance in the SC path of the turn fault current is negligible. Hence, electromagnetic-thermal coupled simulation is not necessary. However, the increase in temperature will further increase the turn losses. To assess the effect of loss increase with temperature, simulations are performed both with constant loss and with loss variation with temperature.

Fig. 7-25 shows the temperature distributions in the generator and in the SC turn 7 at 0.19s when loss increase with temperature is neglected while Fig. 7-26 shows the

temperature distributions at the same time instant, but the loss increase with temperature is accounted. It can be seen that the hotspots are located in the middle of active winding region in both cases. It is also seen that the hotspot temperature 550°C, when the loss increase with temperature is account, is larger than that with constant loss (485°C) at 0.19s.

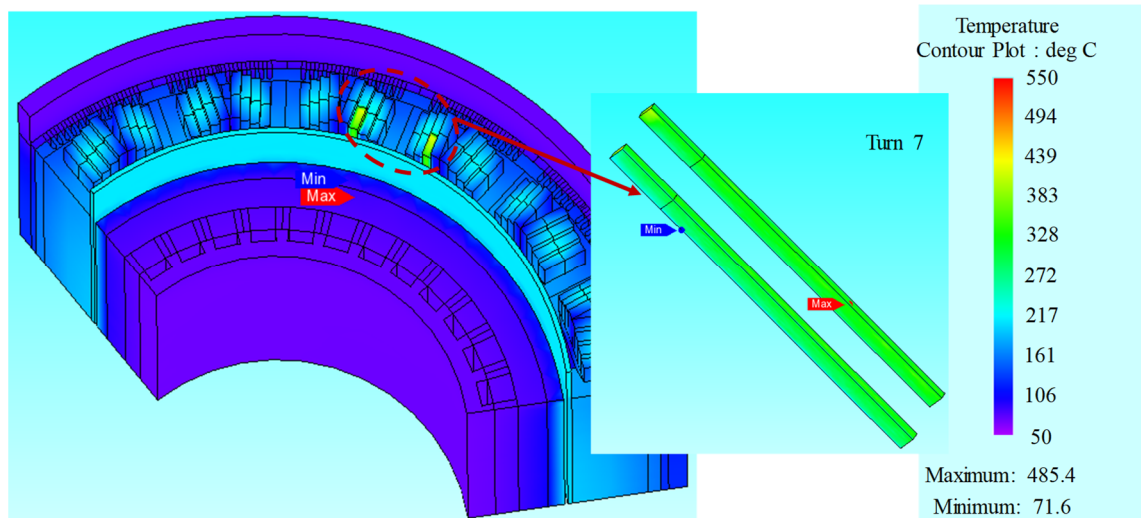


Fig. 7-25. Temperature distributions at 0.19s under turn 7 SC with constant loss in generator and SC turn.

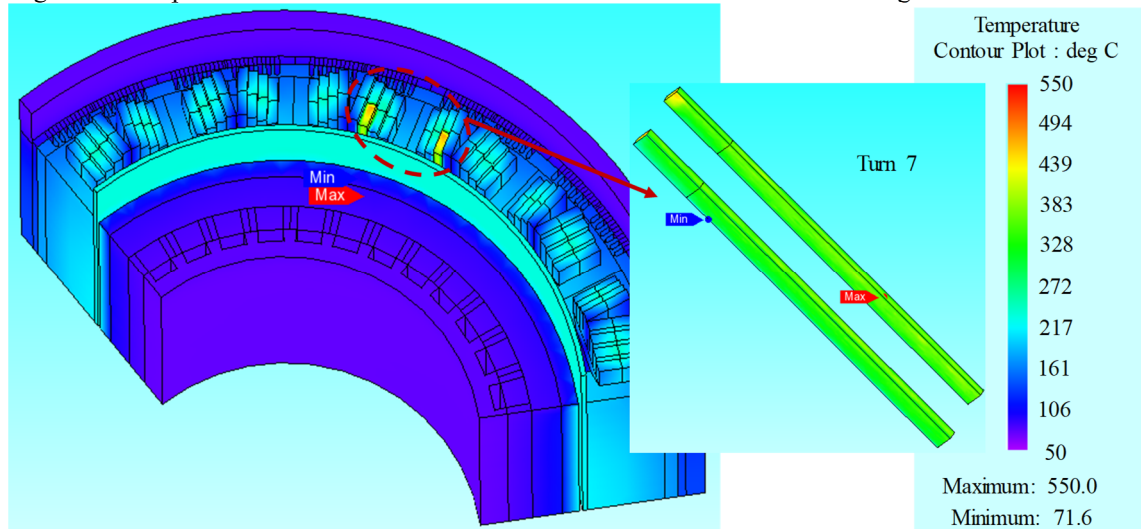


Fig. 7-26. Temperature distributions at 0.19s under turn 7 SC when loss increase with temperature is accounted in generator and SC turn.

Because the simulated time duration is 0.19s which is quite short, the average temperatures of different components which are not close to the faulted turn, including the shaft, magnets, housing, rotor, stator core, and healthy coils are not much different from their values in the healthy condition during the transient process regardless whether the loss increase with temperature is neglected or accounted as shown in Table 7-14. However, the temperatures in the faulted coil A1 increase very quickly as shown in Table

7-15 and Table 7-16 for the cases without and with account of the loss increase with temperature. It is evident that when the loss increase with temperature is accounted, the temperature rise in the fault coil is much faster, especially the hotspot temperature, the rate of increase is 25% greater.

Table 7-14 Average temperatures in healthy regions during transient of turn 7 SC both with constant and variable loss.

Time	Temperatures in healthy regions (°C)						
	Shaft	Magnet	Housing	Rotor	Stator	Active winding	End winding
0.00s	73	91	114	80	155	194	182
0.19s	73	91	114	80	155	194	182

Table 7-15 Temperatures in faulted coil A1 under turn 7 SC with constant loss.

	Temperatures in fault coil A1 (°C)				
	Healthy turns, active	Faulted turn, active	Healthy turns, end winding	Faulted turn, end winding	Hotspot
At 0.00s	193	196	182	187	235
At 0.19s	202	378	187	362	485
Temperature rise	9	182	5	175	250
Rate of increase (°C/s)	47	958	26	921	1316

Table 7-16 Temperatures in faulted coil A1 under turn 7 SC with variable loss.

	Temperatures in fault coil A1 (°C)				
	Healthy turns, active	Faulted turn, active	Healthy turns, end winding	Faulted turn, end winding	Hotspot
At 0.00s	193	196	182	187	235
At 0.19s	205	421	188	398	550
Temperature rise	12	225	6	211	315
Rate of increase (°C/s)	63	1184	32	1111	1658

Fig. 7-27 compares transient temperature rises of the active winding, end winding and hotspot of the faulted turn with constant and variable loss. It can be seen that when time is less than 0.1s, the difference between the two is insignificant. With increase in time, the temperature increase is much faster when the temperature effect on the losses is accounted. For the insulation class used in the generator design, it is assumed that irreversible damage to insulation will occur at 400°C. From the simulation results shown in Fig. 7-27, the insulation of the faulted turn will be completely damaged at 0.2s, and with the rate of increase in temperature, it can be estimated that the hotspot temperature will reach the copper melting point of 1085°C in less than 0.5s.

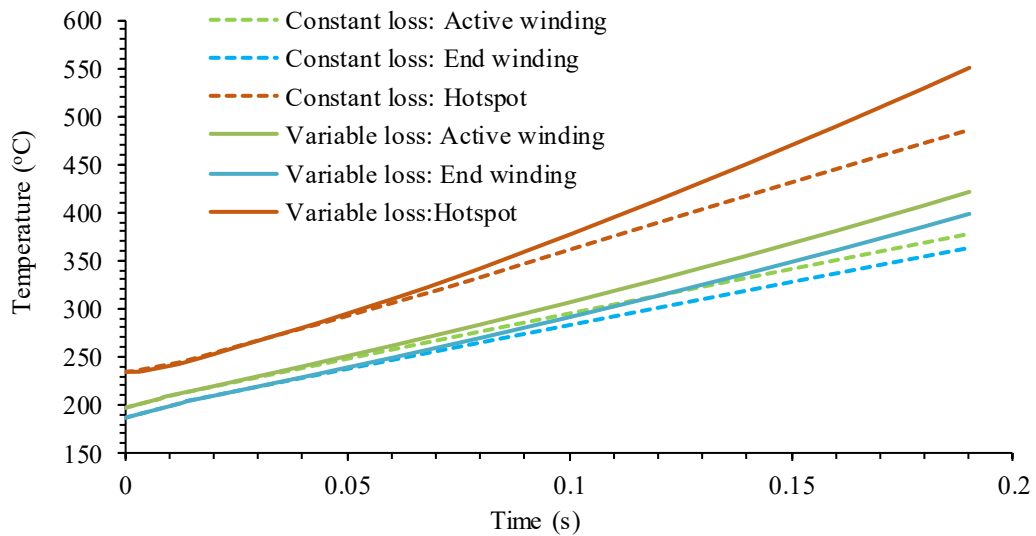


Fig. 7-27. Comparisons of transient temperature rises of the active winding, end winding and hotspot of the faulted turn with constant and variable loss.

7.7.2.2 One Turn SC with Variable Contact Resistance

It is unlikely that an insulation break down will lead immediately to a short circuit with zero contact resistance. The fault currents and associated losses when turn 7 is short-circuited with various contact resistances are given in Table 7-7. Hence thermal simulations with nonzero contact resistance are performed for two cases: $R_f = R10$ (0.0122 Ω) which has the peak loss in the insulation, and $R_f = R100000$ (122.4 Ω) in which the contact resistance is quite large resulting in very small fault current which is quite difficult to detect. In both cases, the region that forms the contact resistance is assumed to be 10mm*10mm in width and depth, and 1.00mm in thickness, and the loss that incurs in the contact resistance will be assigned in this region. In real operation, it is very difficult to know the size of the fault region, but it is likely that any fault starts in a relatively small region and spreads quickly into a large region when the temperature rises quickly and becomes excessive in a short period. Thus, the simulations performed serve the purpose of understanding the phenomenon, rather than for predicting actual temperature distribution.

The fault region is assumed to be located at the axial centre of the active winding between turn 7 and turn 6 as presented in Fig. 7-28. It can be seen that with $R_f = R10$, the fault current which flows in the contact resistance reaches 5041 (rmsA) and the resultant loss is 310kW. It is very likely that the temperature in the contact region will reach 400°C almost instantly and lead to the complete SC failure as well as reach the copper melting point.

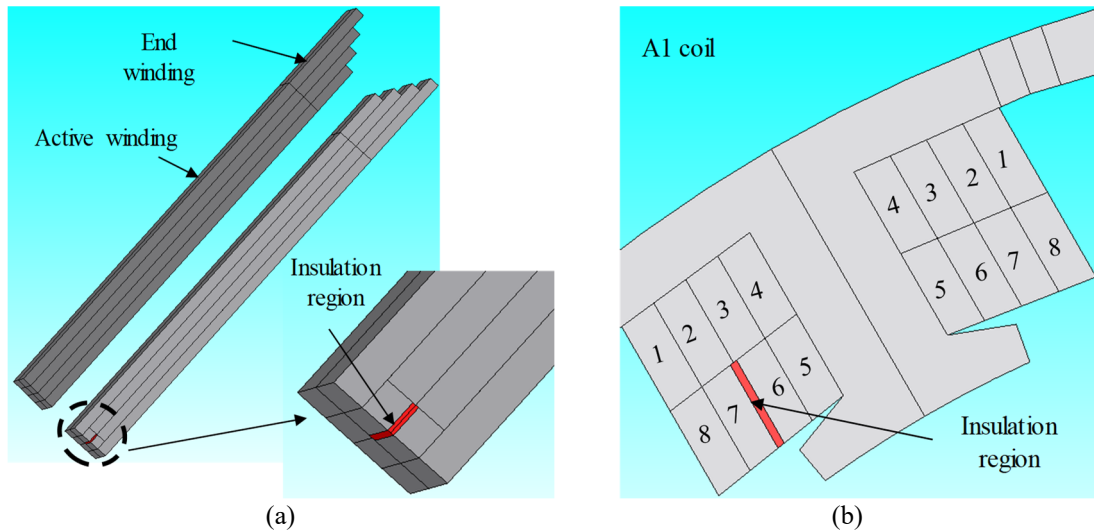


Fig. 7-28. Insulation region located at the axial centre of the active winding between turn 7 and turn 6. (a) Axial cross section. (b) Radial cross section.

Since the expected temperature rise will be extremely quick when a single turn SC takes place in turn 7 with $R_f = R_{10}$, the simulation step is set to $10 \mu s$ and the total simulation time is 0.5ms. Because of very short time duration, the temperatures at 0.5ms in other parts of the generator excepted for the faulted coil do not change from their initial values. The temperature rises of the fault coil and in the contact resistance are given in Table 7-17 while Fig. 7-29 shows the average and hotspot temperature rises in the contact resistance with time. It can be seen that the thermal shock is essentially in the contact region with the rate of temperature increase more than 1.5 million degrees per second. The hotspot temperature reaches $400^\circ C$ around 0.1 ms, almost instantly. Then the contact resistance becomes zero and leads to the complete SC failure whose thermal impact has been analysed in section 7.7.2.1.

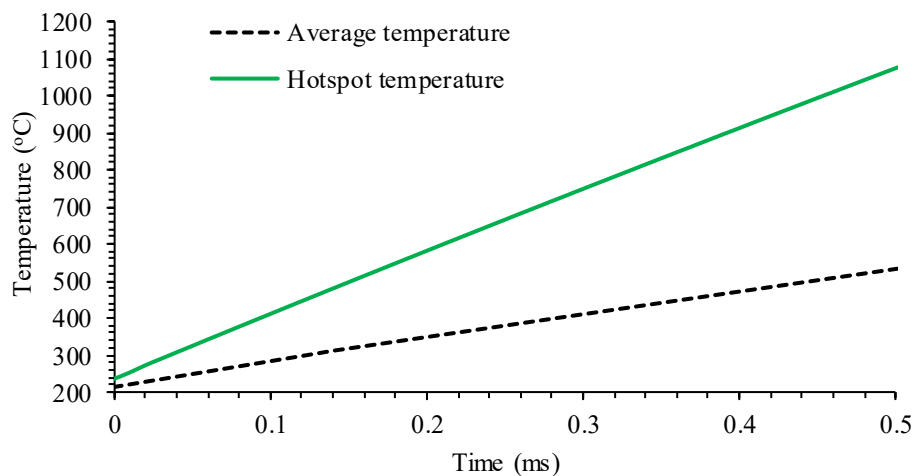


Fig. 7-29. Average temperature and hotspot temperature rises in contact resistance with time. Table 7-17 Temperatures at 0.5ms when one turn SC takes place in turn 7 with $R_f=R_{10}$.

	Temperature (°C)				
	Healthy turns	Faulted coil A1		Contact resistance	
		Turn 7, active	Turn 6, active	Average	Hotspot
At 0.0ms	193	196	213	211	235
At 0.5ms	201	214	232	537	1088
Temp. rise (°C)	8	18	19	326	853
Rate of increase (°C /s)	17488	39187	42564	724910	1895112

When the contact resistance is much large at R100000, the current in the faulted turn is almost the same with the rated although a quite small portion of current, 0.63 rmsA, is diverted to the contact resistance. This current however incurs 49W loss in the contact resistance. Fig. 7-30 shows the steady state temperature distribution in the contact resistance. As can be seen, the hotspot is also located in the contact resistance region because very high loss density. Similar to the previous case, there are virtually no temperature increases in other regions of the generator, except for the windings with few degrees difference (3°C) and faulted coil. Table 7-18 shows the temperatures and temperature rises in the faulted coil A1 and in the contact resistance. It should be noted that even with a relatively small fault current, the hotspot temperature still reaches 400°C at 172s and leads to the complete SC failure

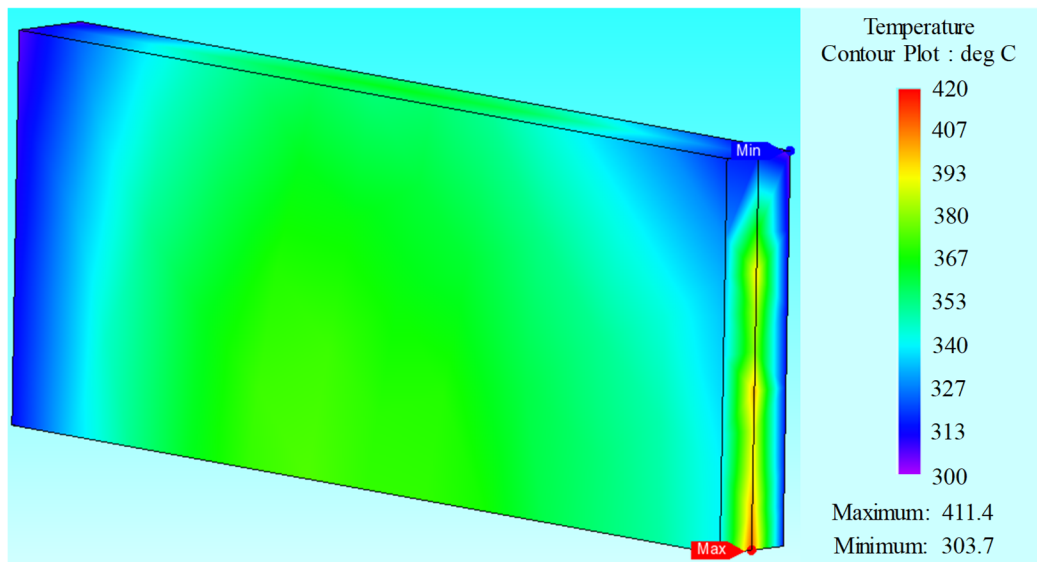


Fig. 7-30. Temperature distribution in the contact resistance (insulation) when one turn SC takes place in turn 7 with $R_f=R100000$.

Table 7-18 Temperatures when one turn SC takes place in turn 7 with $R_c=R100000$.

	Temperature (°C)				
	Healthy turns	Faulted coil A1		Contact resistance	
		Turn 7, active	Turn 6, active	Average	Hotspot
At 0.00s	193	196	213	211	235
Steady state	214	242	261	353	411
Temp. rise	21	46	48	142	176

The above simulations reiterate a potentially vicious cycle with avalanche effect when the insulation breaks down. When the contact resistance as a result of insulation break down is reduced to below $R100000$, the loss incurred in the contact resistance will lead to an increase in the local hotspot temperature rapidly, reaching 400°C . Consequently the contact resistance eventually becomes zero and the winding temperature may reach the copper melting point very quickly.

Because of a very rapid increase in temperature in the fault region, the temperature in the other parts of the generator does not change over the simulation period of interest. It is therefore possible to model the faulted coil only by setting appropriate boundary conditions. This would significantly reduce simulation time.

7.8 Summary

This chapter investigates the EM behaviours and currents of the generator in various fault conditions, such as the insulation failure between turns within a coil and between two phases in the same 3-phase channel by 2D FE analysis. Firstly, the contact/external resistance is assumed to zero for ideal SC. It is found that the worst case of insulation failures between turns within a coil is a single turn SC at turn 7 close to the slot opening where the leakage flux is relatively large. Meanwhile, the worst case insulation failure between two phases in the same 3-phase channel is similar to single turn SC in a coil. Therefore, it can be concluded that a single turn SC at turn 7 is the worst case of all possible SCs within one 3-phase channel. Moreover, it is also found that existing fault measures, namely 3-phase terminal SC or switching-off engine (at a windmill speed of 10% rated with all other phases being deactivated), other than mechanical disconnection of the generator from the engine, are not able to manage the worst case turn fault in a sustainable manner. The fault behaviours with one turn SC at turn 7 in coil A1 when the non-zero contact resistance is varied are also simulated. It is found that when the contact resistance is decreased to a threshold value, an avalanche effect may take place until local

hotspot temperature reaches above the maximum working temperature (400°C). Subsequently the contact resistance would decrease very quickly and irreversibly. When it reaches at R10, the loss incurred is at the maximum, leading to complete failure. Therefore, it is essential to detect the fault at early stage when the contact resistance is sufficiently large. It has been shown that if the fault can be detected in early stage when the contact resistance is above R100, the fault may be contained by switching off the engine immediately.

The 3D FE analysis is performed to assess the thermal impact, especially how quickly the temperature will rise to a level that will cause permanent damage, of a number of typical fault scenarios. For a single turn SC at turn 7 with zero contact resistance, the insulation of the faulted turn will be completely damaged at 0.2s, and based on the rate of increase in temperature, it can be estimated that the hotspot temperature will reach the copper melting point of 1085°C in less than 0.5s. The simulations with nonzero contact resistance are performed at R10 which has the peak loss in the insulation, and at R100000 which has very small fault current. It can be concluded that when the contact resistance as a result of insulation break down is reduced to below R100000, the loss incurred in the contact resistance will lead to increase in the local hotspot temperature rapidly, reaching 400°C. Consequently the contact resistance eventually becomes zero and the winding may reach the copper melting point very quickly.

It has shown that there is no effective means to manage a worst case short circuit fault in the PM generator other than mechanical disconnection of the generator from the engine. While potential fault mitigation measures should be more comprehensively identified and analysed, the studies have shown that with known existing fault mitigation techniques, the fault can only be managed if an insulation break down can be detected at very early stage before an avalanche effect is triggered. This, indeed, raises further challenge on the sensitivity and robustness of fault detection techniques. Further research in this direction is necessary regardless of what mitigation measure would be taken.

The earlier approaches developed for the PMASynRM, including electromagnetic models, thermal models and EM-thermal coupled simulations, are all applicable for the larger PM generator under critical fault conditions with and without mitigation measure. The post-fault EM and thermal performances show that the machine has no fault tolerance.

If some forms of fault tolerance are required, it would be worthwhile to investigate more suitable machine technology and topology for which critical SC faults can be better managed, for example, by design of machine with one p.u. inductance. Of course, a delicate trade-off for power/torque density, efficiency, thermal management and fault-tolerance will be inevitable.

Chapter 8 Conclusions and Future Work

8.1 Summary

The electrification of air transport, such as AEA and MEA, has gained a worldwide interest recently. Therefore, the electric drive for such safety critical application has been extensively researched in order to reduce weight, cost and maintenance, while improve power density, efficiency, availability and fault tolerant capability. Particularly, the electric drive should be capable of continuing operating in a satisfactory manner or at least being extremely unlikely to cause catastrophic damage under various faults both on the machine and drive sides.

In addition to the fundamental requirements for a fault tolerant machine, the specific requirements of the machine in the thesis is high performance, high fault tolerance, good demagnetisation withstand ability and thermal robustness. Therefore, a great deal of potential fault tolerant machine topologies are reviewed and then a triple redundant, 9-phase (3x3-phase) PMASynRM with segregated wye-connected winding is proposed as a promising solution but needing extensive design and fault tolerant study. In order to achieve that, the current state-of-the-art techniques of fault modelling, demagnetisation analysis and thermal analysis techniques are reviewed.

The triple redundant, 9-phase PMASynRM with segregated wye-connected windings controlled by independent three 3-phase inverters for enhancing physical, thermal and electrical isolations is studied in Chapter 2 in detail. PMASynRM has comparable performance with conventional PM machines in terms of efficiency and torque density, while it has excellent fault tolerant capability under many common faults. Among common faults, inter-turn short-circuit fault is particularly critical due to large circulating current which is usually mitigated by application of terminal SC. However, the zero sequence flux linkage due to mutual magnetic coupling between different 3-phase sets cannot be nullified since there is no path for the zero sequence current for the wye-connected winding which might result in significant fault current. Therefore, a new triple redundant, 9-phase PMASynRM with segregated delta-connected windings with the same topology, the same fundamental MMF, the line currents and the slot fill factor as those of PMASynRM with the wye-connected windings is proposed in this Chapter. The

equivalent inter-turn fault models of delta- and wye-connected windings are established to assess the effect of the zero sequence current on the inter-turn fault current with the aid of FE analysis. It follows that the zero sequence current in the delta-connected winding helps lower the turn flux linkage and hence will further reduce the fault current in the fault turns. Subsequently, the characteristics of the delta- and wye-connected PMASynRMs under healthy and various fault conditions, including OC, inter-turn SC and terminal SC, are evaluated and compared via FE simulation. It has been shown that the delta-connected PMASynRM has better fault tolerance compared with the wye-connected PMASynRM because it has much higher average torque and smaller torque ripple under one-phase open-circuit fault, as well as has significantly lower turn fault current and lower hotspot temperature under one turn short-circuit with application of three phase terminal short-circuit.

As a permanent magnet machine is vulnerable to demagnetisation which will weaken its output performance, the risk of partial irreversible demagnetisation of the triple redundant PMASynRM with the wye-connected winding under various critical faults has been comprehensively assessed in Chapter 3. Firstly, the flux density in the direction of magnetisation is decomposed in each magnet element for accurately assessing demagnetisation. Then, the employed continuous demagnetisation model is introduced in this Chapter. It uses the BH curve and recoil line of the magnets to determine the remanence of magnets in each element in each step, records the minimum flux density during the fault transient, as well as evaluates post-demagnetisation performance, such as the demagnetisation distribution, and the reduction in back-emf and output torque. The critical fault conditions with respect to demagnetisation, such as short-circuit and voltage reversal faults at peak torque and base speed, are comprehensively assessed. It can be seen that terminal and inter-turn short-circuit faults will not produce any degree of partial irreversible demagnetisation. Moreover, although all the voltage-reversal faults result in significant partial irreversible demagnetisation, the reduction in output torque is modest due to advanced design features employed for the permanent magnet rotor. Moreover, the asymmetric demagnetisation will not lead to the additional harmonics in the output torque. Finally, from the comparisons of transient responses of the wye- and delta-connected winding under critical fault condition, it can be concluded that the machines with both windings have very strong demagnetisation withstand capability.

Furthermore, as the insulation failure largely influenced by the winding temperature is one of the dominant failure modes within the machine, accurately predicting temperature distribution and hotspot temperature of the wye-connected PMA SynRM with the spiral cooling jacket under various conditions is vital and investigated in Chapter 4. Firstly, a simple transient LP model which could predict symmetric temperature distributions under healthy condition and a more complex transient LP model which could predict asymmetric temperature distributions under fault conditions are established. Afterwards, a 3D thermal model for numerical simulation by finite element analysis is also built. Both the two established thermal models have similar predictions to those obtained from the Motor-CAD under healthy condition, and they also have well-matched steady-state and transient temperature predictions under SC fault conditions. The LP thermal model is faster and computationally more efficient for predicting accurately the average temperatures of different parts and the hotspot temperature of the faulted turn. Both two models could deal with practical issues, such as variable copper loss with the winding temperature, the time-varying coolant temperature and flow rate, etc. However, because of the limited nodes in the LP model, the 3D FE model can provide more detailed temperature distribution with better accuracy and cope with non-uniform end winding layout. To validate the predictions, a prototype of the PMA SynRM has been built and tested. The losses predicted by the 2D EM model are compared with measurement, which shows that the predicted losses are sufficiently accurate for being used as inputs in the thermal models. It has also been shown that the predicted machine temperatures by the 3D thermal model under healthy and fault conditions match well with the measurements. Finally, the thermal behaviour of the machine at the required operation under both healthy and fault conditions are analysed by the 3D model. It is found that the hotspot temperature is slightly over the maximum permissible temperature. It has been concluded that the LP model would be more suitable for thermal assessment of the fault tolerant machine in design stages while the 3D model will be more accurate for thermal assessments in real operations.

As under some fault conditions, temperature effects on the winding resistance has a significant influence on resultant fault current and magnetic field, a directly coupled EM-thermal simulation based on 2D transient EM and 3D thermal model with aid of a scripting file is established in Chapter 5. The EM-thermal coupled simulation and the

thermal-only simulation with constant losses are performed on the proposed triple redundant, 9-phase PMASynRM with wye-connected winding under five fault conditions at different speeds for comparison. It has been shown that at low speed (resistance/reactance limited) or under one turn SC with 3-phase terminal short circuit conditions, the EM-thermal coupled simulation can improve accuracy slightly. However, it is essential to employ the EM-thermal coupled simulation when the fault current is reactance limited at high speed for the study of the thermal behaviour under SC fault conditions. Furthermore, this Chapter also assesses the EM behaviour of various possible SC faults when considering each individual strand, such as inter-strand SC and intra-strand SC, and thermal behaviour of one turn SC fault involving in a number of strands by EM-thermal coupled simulations. It is shown that the EM-thermal coupled simulation is necessary even if the fault current is resistance limited when the copper loss of the faulted strands is quite large. Moreover, the EM-thermal coupled simulation gives a more accurate means to study the influence of number of SC turns on thermal behaviour. It has been shown that two turns SC is more severe thermally than one turn and three turns SC in this machine instead of the prediction by the thermal-only simulation that one turn SC is the most thermally severe fault. It also shows that among inter-strand SC faults, the most severe fault is one turn SC within 13 strands.

All the short-circuit fault conditions considered in the foregoing chapters are based on ideal short-circuit fault conditions assuming that the electrical resistance of the insulation becomes zero. However, this assumption may not be true in reality. Therefore, the damage risks of the PMASynRM under insulation deterioration process when the insulation resistance changes from a few hundreds of Mega ohms in healthy condition to zero resistance in ideal SC condition, are assessed in the Chapter 6. Based on the electromagnetic behaviour assessment which is validated by test results, it has been shown that the loss in the faulty insulation region increases with reduction of the insulation resistance before reaching a peak and finally becomes zero in an ideal SC. This behaviour would dramatically increase the temperature in the faulty region and may exasperate the failure. Moreover, from the example with particular insulation volume when the electrical resistance decreases with increase in temperature, it has been found that an avalanche effect may be triggered that accelerates the insulation deterioration. To prevent this process, the range of the cut-through resistance, which is defined as the

minimum insulation resistance before irreversible damage of insulation due to heating would take place, for all possible faulty insulation volumes are quantified by 3D thermal modelling under turn-to-turn insulation deterioration leading to SC faults for obtaining the insulation resistance thresholds. It can be concluded that fault detection needs to be effective when the insulation resistance is greater than a threshold and a mitigation action is subsequently taken.

At last, the simulation techniques described in the previous chapters are employed to analyse potential electric failure modes resulting from insulation breakdown and their severity and consequences of a 2.5 MW, two 3-phase permanent magnet generator operating at +/- 1.5kV DC for E-Fan-X demonstrator in Chapter 7. The EM behaviours of the generator in various fault conditions are analysed by 2D FE analysis to identify the worst case of all possible SCs within one 3-phase channel when the contact/external resistance is assumed to zero. It is also found that existing fault mitigation measures, namely 3-phase terminal SC or switching-off engine, other than mechanical disconnection of the generator from the engine, are not able to manage the worst case turn fault in a sustainable manner. Moreover, the analysis of the worst case when the non-zero contact resistance is varied shows that the fault can only be managed if an insulation breakdown can be detected at very early stage before an avalanche effect is triggered. Afterwards, the thermal impact of a number of typical fault scenarios is assessed by the 3D FE analysis and it is concluded that the temperature will rise to a level that will cause permanent damage very quickly. Therefore, recommendations are made in this chapter that it would be worthwhile to investigate more suitable machine technology and topology for which critical SC faults can be better managed if some forms of fault tolerance are required and hence mechanical disconnection is not desirable.

In summary, it can be concluded that the electromagnetic analysis, thermal analysis and demagnetisation analysis are essential for assessing the fault tolerance of the machine by evaluating the capability of the machine to operate continuously under principal fault conditions with satisfactory performance which are set as bench marks in Chapter 1. In addition, these analyses are also useful to determine sensitive fault detection methods and effective fault mitigation for managing critical faults.

The EM analysis is adopted to assess the torque and torque ripple under principal faults. The continuous demagnetisation assessment is accurate to analyse the post-fault performance under the worst fault condition. The LP model could give a quick prediction of the temperature distribution at design stage. The EM-thermal coupled simulation is not only accurately predicting the SC current and temperature distribution when the SC fault current is influenced by the impedance in the SC path, but also assessing the behaviour under insulation deterioration leading to SC faults and obtaining more accurate threshold of fault detection.

Therefore, after all above analyses, the PMASynRM has acceptable post-fault torque and torque ripple under all critical faults according to the ‘bench marks’ of fault tolerance. After changing the insulation material to improve the maximum permissible temperature to be 240°C, the hotspot temperatures of the PMASynRM under critical SC fault with mitigation measure are smaller than the maximum permissible temperature. This PMASynRM is fault tolerance.

Additionally, it also shows that sensitive and robust fault detection which could detect an insulation break down at early stage before an avalanche effect is triggered is important and would improve the fault tolerance. However, as the unbalance at early stage of an insulation break-down are relatively small which increases the difficulty of the accurate detection. The possible fault detection to detect the 2nd harmonic IAP and IRP is proposed, but not deeply analysed. Moreover, the LP thermal model with limited nodes cannot give a detailed temperature distribution compared to the 3D model.

8.2 Future Work

Some possible future work is recommended:

1. More sensitive and robust fault detection technique. The investigation in the thesis shows that the fault can only be managed if an insulation break down can be detected when insulation resistance is greater than a threshold before an avalanche effect is triggered. Therefore, further research on improving the sensitivity and robustness of fault detection techniques is necessary.
2. Development of more comprehensive 3D lumped parameter thermal model. As the active winding and the end winding are connected to one node in the transient

LP model introduced in this thesis, it cannot quantify the uneven distribution of the copper loss in the end winding region. Therefore, a more accurate 3D LP thermal model that represents temperature distributions in the active winding and the end winding with more nodes should be further investigated.

3. Electromagnetic and thermal analysis for the PMASynRM with strands conductors. As introduced in Chapter 5, the proposed machine has 17 parallel strands per turn and an insulation breakdown between a few strands of two different turns is possible and realistic. It is obvious that the number of possible SC faults involving a given number of strands and turns are large. Chapter 5 only investigates the EM performance under inter-strand SC and intra-strand SC at the rated torque/ base speed as well as the thermal performance under inter-strand SC because of the large computation time and data storage to give a general insight. Therefore, comprehensive investigation on the EM and thermal behaviours on more various fault conditions under different operating conditions are essential. The worst fault with SC strands and its severity compared with the complete inter turn SC fault should be fully analysed.

REFERENCES

- [1] A. Boglietti, A. Cavagnino, A. Tenconi, and S. Vaschetto, "The safety critical electric machines and drives in the more electric aircraft: A survey," *IECON Proc. (Industrial Electron. Conf.)*, pp. 2587–2594, 2009.
- [2] W. Cao, B. C. Mecrow, G. J. Atkinson, J. W. Bennett, and D. J. Atkinson, "Overview of electric motor technologies used for more electric aircraft (MEA)," *IEEE Trans. Ind. Electron.*, vol. 59, no. 9, pp. 3523–3531, 2012.
- [3] B. Sarlioglu and C. T. Morris, "More Electric Aircraft: Review, Challenges, and Opportunities for Commercial Transport Aircraft," *IEEE Trans. Transp. Electrification*, vol. 1, no. 1, pp. 54–64, 2015.
- [4] A. C. Hoffman *et al.*, "Advanced Secondary Power System for Transport Aircraft," *NASA Tech. Pap.*, 1985.
- [5] A. G. Jack, B. C. Mecrow, and J. A. Haylock, "A Comparative Study of Permanent Magnet and Switched Reluctance Motors for," *Ind. Appl. IEEE Trans.*, vol. 32, no. 4, pp. 889–895, 1996.
- [6] B. C. Mecrow, D. J. Atkinson, A. G. Jack, S. Green, J. A. Haylock, and J. Coles, "The need for fault tolerance in an aeroengine electric fuel control system," *IEE Colloquium (Digest)*, no. 180, pp. 55–59, 1999.
- [7] A. H. Bonnett and G. C. Soukup, "Cause and Analysis of Stator and Rotor Failures in Three-Phase Squirrel-Cage Induction Motors," *IEEE Trans. Ind. Appl.*, vol. 28, no. 4, pp. 921–937, 1992.
- [8] P. O. Donnell, C. Heising, C. Singh, and S. J. Wells, "Report of Large Motor Reliability Survey of Industrial and Commercial Installations: Part I," *IEEE Trans. Ind. Appl.*, vol. IA-21, no. 4, pp. 853–864, 1985.
- [9] O. V. Thorsen and M. Dalva, "A Survey of Faults on Induction Motors in Offshore Oil Industry, Petrochemical Industry, Gas Terminals, and Oil Refineries," *IEEE Trans. Ind. Appl.*, vol. 31, no. 5, pp. 1186–1196, 1995.
- [10] S. Yang, A. Bryant, P. Mawby, D. Xiang, L. Ran, and P. Tavner, "An industry-based survey of reliability in power electronic converters," *IEEE Trans. Ind. Appl.*, vol. 47, no. 3, pp. 1441–1451, 2011.
- [11] B. Lu and S. K. Sharma, "A literature review of IGBT fault diagnostic and protection methods for power inverters," *IEEE Trans. Ind. Appl.*, vol. 45, no. 5, pp. 1770–1777, 2009.
- [12] R. V. White, "Fault tolerance in distributed power systems," *IV IEEE Int. Power Electron. Congr. Tech. Proceedings. CIEP 95*, pp. 121–128, 1995.
- [13] G. Choi and T. M. Jahns, "Interior permanent magnet synchronous machine rotor demagnetization characteristics under fault conditions," *2013 IEEE Energy Convers. Congr. Expo. ECCE 2013*, pp. 2500–2507, 2013.

- [14] B. A. Welchko, T. M. Jahns, and S. Hiti, "IPM synchronous machine drive response to a single-phase open circuit fault," *IEEE Trans. Power Electron.*, vol. 17, no. 5, pp. 764–771, 2002.
- [15] V. I. Patel, J. Wang, and S. S. Nair, "Demagnetization Assessment of Fractional-Slot and Distributed Wound 6-Phase Permanent Magnet Machines," *IEEE Trans. Magn.*, vol. 51, no. 6, pp. 1–11, 2015.
- [16] S. S. Nair, V. I. Patel, and J. Wang, "Post-Demagnetization Performance Assessment for Interior Permanent Magnet AC Machines," *IEEE Trans. Magn.*, vol. 52, no. 4, pp. 1–10, 2016.
- [17] M. Farahani, E. Gockenbach, H. Borsi, K. Schäfer, and M. Kaufhold, "Behavior of machine insulation systems subjected to accelerated thermal aging test," *IEEE Trans. Dielectr. Electr. Insul.*, vol. 17, no. 5, pp. 1364–1372, 2010.
- [18] C. M. Stephens, "Fault detection and management system for fault tolerant switched reluctance motor drives," *IEEE Trans. Ind. Appl.*, vol. 27, no. 6, pp. 1098–1102, 1991.
- [19] N. Bianchi, S. Bolognani, and M. D. Pr e, "Design of a fault-tolerant IPM motor for electric power steering," *IEEE Trans. Veh. Technol.*, vol. 55, no. 4, pp. 1102–1111, 2006.
- [20] B. Vaseghi, N. Takorabet, J. P. Caron, B. Nahid-Mobarakeh, F. Meibody-Tabar, and G. Humbert, "Study of different architectures of fault-tolerant actuator using a two-channel pm motor," *IEEE Trans. Ind. Appl.*, vol. 47, no. 1, pp. 47–54, 2011.
- [21] M. Beltr o, D. R. Corr ea, S. Member, C. B. Jacobina, and S. Member, "An induction motor drive system with improved fault tolerance," *IEEE Trans. Ind. Appl.*, vol. 37, no. 3, pp. 873–879, 2001.
- [22] A. Sayed-Ahmed and N. A. O. Demerdash, "Fault-tolerant operation of delta-connected scalar- and vector-controlled AC motor drives," *IEEE Trans. Power Electron.*, vol. 27, no. 6, pp. 3041–3049, 2012.
- [23] N. Bianchi, S. Bolognani, M. Dai Pr e, and E. Fornasiero, "Post-fault operations of five-phase motor using a full-bridge inverter," *PESC Rec. - IEEE Annu. Power Electron. Spec. Conf.*, pp. 2528–2534, 2008.
- [24] E. Levi, "Multiphase electric machines for variable-speed applications," *IEEE Trans. Ind. Electron.*, vol. 55, no. 5, pp. 1893–1909, 2008.
- [25] L. Parsa and H. A. Toliyat, "Fault-tolerant interior-permanent-magnet machines for hybrid electric vehicle applications," *IEEE Trans. Veh. Technol.*, vol. 56, no. 4, pp. 1546–1552, 2007.
- [26] P. B. Machines, K. Atallah, J. Wang, and D. Howe, "Torque-ripple minimization in modular permanent-magnet brushless machines," *IEEE Trans. Ind. Appl.*, vol. 39, no. 6, pp. 1689–1695, 2003.
- [27] M. J. Duran, I. Gonzalez Prieto, M. Bermudez, F. Barrero, H. Guzman, and M. R. Arahal, "Optimal fault-tolerant control of six-phase induction motor drives with parallel converters," *IEEE Trans. Ind. Electron.*, vol. 63, no. 1, pp. 629–640, 2016.

- [28] M. Barcaro, N. Bianchi, and F. Magnussen, "Configurations of fractional-slot IPM motors with dual three-phase winding," *2009 IEEE Int. Electr. Mach. Drives Conf. IEMDC '09*, pp. 936–942, 2009.
- [29] M. Barcaro, N. Bianchi, and F. Magnussen, "Analysis and tests of a dual three-phase 12-slot 10-pole permanent-magnet motor," *IEEE Trans. Ind. Appl.*, vol. 46, no. 6, pp. 2355–2362, 2010.
- [30] B. Wang, J. Wang, B. Sen, A. Griffio, Z. Sun, and E. Chong, "A Fault-Tolerant Machine Drive Based on Permanent Magnet-Assisted Synchronous Reluctance Machine," *IEEE Trans. Ind. Appl.*, vol. 54, no. 2, pp. 1349–1359, 2018.
- [31] S. Gopalakrishnan, A. M. Omekanda, and B. Lequesne, "Classification and remediation of electrical faults in the switched reluctance drive," *IEEE Trans. Ind. Appl.*, vol. 42, no. 2, pp. 479–486, 2006.
- [32] C. M. Spargo, B. C. Mecrow, J. D. Widmer, and C. Morton, "Application of Fractional-Slot Concentrated Windings to Synchronous Reluctance Motors," *IEEE Trans. Ind. Appl.*, vol. 51, no. 2, pp. 1446–1455, 2015.
- [33] C. M. Spargo, B. C. Mecrow, and J. D. Widmer, "A Seminumerical Finite-Element Postprocessing Torque Ripple Analysis Technique for Synchronous Electric Machines Utilizing the Air-Gap Maxwell Stress Tensor," *IEEE Trans. Magn.*, vol. 50, no. 5, pp. 1–9, 2014.
- [34] C. M. Spargo, B. C. Mecrow, J. D. Widmer, and C. Morton, "Application of Fractional-Slot Concentrated Windings to Synchronous Reluctance Motors," *IEEE Trans. Ind. Appl.*, vol. 51, no. 2, pp. 1446–1455, 2015.
- [35] J. Wang, K. Atallah, Z. Q. Zhu, and D. Howe, "Modular three-phase permanent-magnet brushless machines for in-wheel applications," *IEEE Trans. Veh. Technol.*, vol. 57, no. 5, pp. 2714–2720, 2008.
- [36] D. Ishak, Z. Q. Zhu, and D. Howe, "Comparison of PM brushless motors, having either all teeth or alternate teeth wound," *IEEE Trans. Energy Convers.*, vol. 21, no. 1, pp. 95–103, 2006.
- [37] A. Mitcham, G. Antonopoulos, and J. Cullen, "Favourable slot and pole number combinations for fault-tolerant PM machines," *IEE Proceedings-Electric Power Appl.*, vol. 151, no. 5, pp. 1271–1282, 2005.
- [38] D. Ishak, Z. Q. Zhu, and D. Howe, "Permanent magnet brushless machines with unequal tooth widths and similar slot and pole numbers," *Conference Rec. 2004 IEEE Ind. Appl. Conf. 2004. 39th IAS Annu. Meet.*, pp. 1055–1061, 2004.
- [39] G. J. Atkinson, B. C. Mecrow, A. G. Jack, D. J. Atkinson, P. Sangha, and M. Benarous, "The analysis of losses in high-power fault-tolerant machines for aerospace applications," *IEEE Trans. Ind. Appl.*, vol. 42, no. 5, pp. 1162–1170, 2006.
- [40] B. Wang, J. Wang, A. Griffio, and B. Sen, "A general modeling technique for a triple redundant 3×3 -Phase PMA SynRM," *IEEE Trans. Ind. Electron.*, vol. 65, no. 11, pp. 9068–9078, 2018.

- [41] B. Sen, J. Wang, and P. Lazari, "A High-Fidelity Computationally Efficient Transient Model of Interior Permanent-Magnet Machine with Stator Turn Fault," *IEEE Trans. Ind. Electron.*, vol. 63, no. 2, pp. 773–783, 2016.
- [42] D. C. Patel and M. C. Chandorkar, "Modeling and analysis of stator interturn fault location effects on induction machines," *IEEE Trans. Ind. Electron.*, vol. 61, no. 9, pp. 4552–4564, 2014.
- [43] A. Gandhi, T. Corrigan, and L. Parsa, "Recent advances in modelling and online detection of stator interturn faults in electrical motors," *IEEE Trans. Ind. Electron.*, vol. 58, no. 5, pp. 1564–1575, 2011.
- [44] S. M. A. Cruz and A. J. M. Cardoso, "Multiple reference frames theory: A new method for the diagnosis of stator faults in three-phase induction motors," *IEEE Trans. Energy Convers.*, vol. 20, no. 3, pp. 611–619, 2005.
- [45] C. H. D. Angelo, G. R. Bossio, S. J. Giaccone, M. I. Valla, J. A. Solsona, and G. O. García, "On-line model-based stator-fault detection and identification in induction motors," *IEEE Trans. Ind. Electron.*, vol. 56, no. 11, pp. 4671–4680, 2009.
- [46] R. M. Tallam, T. G. Habetler, and R. G. Harley, "Transient model for induction machines with stator winding turn faults," *IEEE Trans. Ind. Appl.*, vol. 38, no. 3, pp. 632–637, 2002.
- [47] S. M. A. Cruz and A. J. M. Cardoso, "Diagnosis of stator inter-turn short circuits in DTC induction motor drives," *IEEE Trans. Ind. Appl.*, vol. 40, no. 5, pp. 1349–1360, 2004.
- [48] H. A. Toliyat and T. A. Lipo, "Transient analysis of cage induction machines under stator, rotor bar and end ring faults," *IEEE Trans. Energy Convers.*, vol. 10, no. 2, pp. 241–247, 1995.
- [49] X. Luo, Y. Liao, H. A. Toliyat, A. El-Antably, and T. A. Lipo, "Multiple coupled circuit modeling of induction machines," *IEEE Trans. Ind. Appl.*, vol. 31, no. 2, pp. 311–318, 1995.
- [50] G. Bossio, C. D. Angelo, J. Solsona, G. García, and M. I. Valla, "2-D model of the induction machine: An extension of the modified winding function approach," *IEEE Trans. Energy Convers.*, vol. 19, no. 1, pp. 144–150, 2004.
- [51] G. M. Joksimovic and J. Penman, "The detection of inter-turn short circuits in the stator windings of operating motors," *IEEE Trans. Ind. Electron.*, vol. 47, no. 5, pp. 1078–1084, 2000.
- [52] X. Tu, L. A. Dessaint, M. El Kahel, and A. O. Barry, "A new model of synchronous machine internal faults based on winding distribution," *IEEE Trans. Ind. Electron.*, vol. 53, no. 6, pp. 1818–1827, 2006.
- [53] J. Hang, J. Zhang, M. Cheng, and J. Huang, "Online Interturn Fault Diagnosis of Permanent Magnet Synchronous Machine Using Zero-Sequence Components," *IEEE Trans. Power Electron.*, vol. 30, no. 12, pp. 6731–6741, 2015.

- [54] B. Sen, J. Wang, and P. Lazari, "A detailed transient model of Interior Permanent Magnet motor accounting for saturation under stator turn fault," *2013 IEEE Energy Convers. Congr. Expo. ECCE 2013*, pp. 3548–3555, 2013.
- [55] B. Sen and J. Wang, "Analytical modelling of stator turn fault in surface mounted permanent magnet machines," *2013 IEEE Energy Convers. Congr. Expo. ECCE 2013*, pp. 4445–4452, 2013.
- [56] J. C. Urresty, J. R. Riba, and L. Romeral, "Influence of the stator windings configuration in the currents and zero-sequence voltage harmonics in permanent magnet synchronous motors with demagnetization faults," *IEEE Trans. Magn.*, vol. 49, no. 8, pp. 4885–4893, 2013.
- [57] J. Faiz and H. Nejadi-Koti, "Demagnetization Fault Indexes in Permanent Magnet Synchronous Motors-An Overview," *IEEE Trans. Magn.*, vol. 52, no. 4, pp. 1–11, 2016.
- [58] G. Choi and T. M. Jahns, "Demagnetization Characteristics of Permanent Magnet Synchronous Machines," *IECON 2014 - 40th Annu. Conf. IEEE Ind. Electron. Soc.*, pp. 469–475, 2014.
- [59] G. Choi and T. M. Jahns, "Post-demagnetization characteristics of permanent magnet synchronous machines," *2015 IEEE Energy Convers. Congr. Expo. ECCE 2015*, pp. 1781–1788, 2015.
- [60] A. Sarikhani and O. A. Mohammed, "Demagnetization control for reliable flux weakening control in PM synchronous machine," *IEEE Trans. Energy Convers.*, vol. 27, no. 4, pp. 1046–1055, 2012.
- [61] J. A. Farooq, A. Djerdir, and A. Miraoui, "Analytical modeling approach to detect magnet defects in permanent-magnet brushless motors," *IEEE Trans. Magn.*, vol. 44, no. 12, pp. 4599–4604, 2008.
- [62] J. Wang, W. Wang, K. Atallah, and D. Howe, "Demagnetization Assessment for Three-Phase Tubular Brushless," *IEEE Trans. Magn.*, vol. 44, no. 9, pp. 2195–2203, 2008.
- [63] K. C. Kim, K. Kim, H. J. Kim, and J. Lee, "Demagnetization analysis of permanent magnets according to rotor types of interior permanent magnet synchronous motor," *IEEE Trans. Magn.*, vol. 45, no. 6, pp. 2799–2802, 2009.
- [64] S. Morimoto, S. Ooi, Y. Inoue, and M. Sanada, "Experimental evaluation of a rare-earth-free PMASynRM with ferrite magnets for automotive applications," *IEEE Trans. Ind. Electron.*, vol. 61, no. 10, pp. 5749–5756, 2014.
- [65] M. Kimiabeigi, J. D. Widmer, N. J. Baker, R. Martin, B. C. Mecrow, and A. Michaelides, "Three-Dimensional Modelling of Demagnetization and Utilization of Poorer Magnet Materials for EV/HEV Applications," *IEEE Trans. Energy Convers.*, vol. 31, no. 3, pp. 981–992, 2016.
- [66] G. Zhao, L. Tian, Q. Shen, and R. Tang, "Demagnetization analysis of permanent magnet synchronous machines under short circuit fault," *Asia-Pacific Power Energy Eng. Conf. APPEEC*, pp. 1–4, 2010.

- [67] J. D. McFarland and T. M. Jahns, "Investigation of the rotor demagnetization characteristics of interior PM synchronous machines during fault conditions," *IEEE Trans. Ind. Appl.*, vol. 50, no. 4, pp. 2768–2775, 2014.
- [68] V. I. Patel, J. Wang, and S. S. Nair, "Demagnetization Assessment of Fractional-Slot and Distributed Wound 6-Phase Permanent Magnet Machines," *IEEE Trans. Magn.*, vol. 51, no. 6, pp. 1–11, 2015.
- [69] S. Ruoho, E. Dlala, and A. Arkkio, "Comparison of demagnetization models for finite-element analysis of permanent-magnet synchronous machines," *IEEE Trans. Magn.*, vol. 43, no. 11, pp. 3964–3968, 2007.
- [70] G. Choi and T. M. Jahns, "Interior permanent magnet synchronous machine rotor demagnetization characteristics under fault conditions," *2013 IEEE Energy Convers. Congr. Expo. ECCE 2013*, pp. 2500–2507, 2013.
- [71] G. H. Kang, J. Hur, H. Nam, J. P. Hong, and G. T. Kim, "Analysis of irreversible magnet demagnetization in line-start motors based on the finite-element method," *IEEE Trans. Magn.*, vol. 39, no. 3 I, pp. 1488–1491, 2003.
- [72] Y. Zhilichev, "Analysis of permanent magnet demagnetization accounting for minor B–H curves," *IEEE Trans. Magn.*, vol. 44, no. 11, pp. 4285–4288, 2008.
- [73] P. Zhou, D. Lin, Y. Xiao, N. Lambert, and M. A. Rahman, "Temperature-dependent demagnetization model of permanent magnets for finite element analysis," *IEEE Trans. Magn.*, vol. 48, no. 2, pp. 1031–1034, 2012.
- [74] S. S. Nair, V. I. Patel, and J. Wang, "Post-Demagnetization Performance Assessment for Interior Permanent Magnet AC Machines," *IEEE Trans. Magn.*, vol. 52, no. 4, pp. 1–10, 2016.
- [75] S. Nategh, *Thermal analysis and management of high-performance electrical machines*. KTH Royal Institute of Technology, 2013.
- [76] A. Boglietti, A. Cavagnino, D. Staton, M. Shanel, M. Mueller, and C. Mejuto, "Evolution and modern approaches for thermal analysis of electrical machines," *IEEE Trans. Ind. Electron.*, vol. 56, no. 3, pp. 871–882, 2009.
- [77] R. L. Kotnik, "Equivalent thermal circuit for nonventilated motors," *Electr. Eng.*, vol. 74, no. 3, pp. 1604–1609, 1955.
- [78] P. H. Mellor, D. Roberts, and D. R. Turner, "Lumped parameter thermal model for electrical machines of TEFC design," *IEE Proc. B Electr. Power Appl.*, vol. 138, no. 5, pp. 205–218, 1991.
- [79] M. S. Rajagopal, "Transient thermal analysis of induction motors," *IEEE Trans. Energy Convers.*, vol. 13, no. 1, pp. 62–69, 1998.
- [80] A. Boglietti, A. Cavagnino, M. Lazzari, and M. Pastorelli, "A Simplified Thermal Model for Variable-Speed Self-Cooled Industrial Induction Motor," *IEEE Trans. Ind. Appl.*, vol. 39, no. 4, pp. 945–952, 2003.

- [81] F. Presentation, "Thermal analysis of a high-speed generator," *38th IAS Annu. Meet. Conf. Rec. Ind. Appl. Conf. 2003.*, pp. 547–554, 2003.
- [82] A. M. El-Refaie, N. C. Harris, T. M. Jahns, and K. M. Rahman, "Thermal analysis of multibarrier interior PM synchronous machine using lumped parameter model," *IEEE Trans. Energy Convers.*, vol. 19, no. 2, pp. 303–309, 2004.
- [83] H. Li and Y. Shen, "Thermal analysis of the permanent-magnet spherical motor," *IEEE Trans. Energy Convers.*, vol. 30, no. 3, pp. 991–998, 2015.
- [84] M. Galea, C. Gerada, T. Raminosa, and P. Wheeler, "A thermal improvement technique for the phase windings of electrical machines," *IEEE Trans. Ind. Appl.*, vol. 48, no. 1, pp. 79–87, 2012.
- [85] A. Boglietti, A. Cavagnino, and D. Staton, "Determination of critical parameters in electrical machine thermal models," *IEEE Trans. Ind. Appl.*, vol. 44, no. 4, pp. 1150–1159, 2008.
- [86] A. Boglietti and A. Cavagnino, "Analysis of the endwinding cooling effects in TEFC induction motors," *IEEE Trans. Ind. Appl.*, vol. 43, no. 5, pp. 1214–1222, 2007.
- [87] A. Boglietti, A. Cavagnino, D. A. Staton, M. Popescu, C. Cossar, and M. I. McGilp, "End space heat transfer coefficient determination for different induction motor enclosure types," *IEEE Trans. Ind. Appl.*, vol. 45, no. 3, pp. 929–937, 2009.
- [88] D. Staton, A. Boglietti, and A. Cavagnino, "Solving the more difficult aspects of electric motor thermal analysis," *IEEE Trans. Energy Convers.*, vol. 20, no. 3, pp. 620–628, 2005.
- [89] Y. K. Chin, and D. A. Staton, "Transient thermal analysis using both lumped-circuit approach and finite element method of a permanent magnet traction motor," *2004 IEEE Africon. 7th Africon Conf. Africa*, pp. 1027–1036, 2004.
- [90] D. A. Staton and A. Cavagnino, "Convection heat transfer and flow calculations suitable for electric machines thermal models," *IEEE Trans. Ind. Electron.*, vol. 55, no. 10, pp. 3509–3516, 2008.
- [91] J. Wang, F. Wang, and X. Kong, "Losses and thermal analysis of high speed PM machine," *2008 Jt. Int. Conf. Power Syst. Technol. IEEE Power India Conf.*, pp. 1–5, 2008.
- [92] C. Mejuto, M. Mueller, M. Shanel, A. Mebarki, and D. Staton, "Thermal modelling investigation of heat paths due to iron losses in synchronous machines," *4th IET Int. Conf. Power Electron. Mach. Drives (PEMD 2008)*, pp. 225–229, 2008.
- [93] Y. Huai, R. V. N. Melnik, and P. B. Thogersen, "Computational analysis of temperature rise phenomena in electric induction motors," *Appl. Therm. Eng.*, vol. 23, no. 7, pp. 779–795, 2003.
- [94] D. Joo, J. H. Cho, K. Woo, B. T. Kim, and D. K. Kim, "Electromagnetic field and thermal linked analysis of interior permanent-magnet synchronous motor for agricultural electric vehicle," *IEEE Trans. Magn.*, vol. 47, no. 10, pp. 4242–4245, 2011.

- [95] S. J. Pickering, D. Lampard, and M. Shanel, "Modelling ventilation and cooling of the rotors of salient pole machines," *IEMDC 2001 - IEEE Int. Electr. Mach. Drives Conf.*, pp. 806–808, 2001.
- [96] D. Lampard, S. J. Pickering, and J. Mugglestone, "The use of computational fluid dynamics to model the air flow in the end region of a TEFC induction motor," *IEE Colloquium on Modelling the Performance of Electrical Machines*. pp. 2/1-2/5, 1997.
- [97] S. H. Moon, J. H. Yun, W. G. Kim, and J. P. Kim, "Thermal-flow analysis and cooling performance enhancement of a totally enclosed fan-cooled motor," *2013 Int. Conf. Electr. Mach. Syst.*, pp. 2028–2030, 2013.
- [98] D. A. Howey, A. S. Holmes, and K. R. Pullen, "Measurement and CFD prediction of heat transfer in air-cooled disc-type electrical machines," *IEEE Trans. Ind. Appl.*, vol. 47, no. 4, pp. 1716–1723, 2011.
- [99] C. Kral, A. Haumer, M. Haigis, H. Lang, and H. Kapeller, "Comparison of a CFD analysis and a thermal equivalent circuit model of a TEFC induction machine with measurements," *IEEE Trans. Energy Convers.*, vol. 24, no. 4, pp. 809–818, 2009.
- [100] J. Zhu, N. Ertugrul, and W. L. Soong, "Detection and remediation of switch faults on a fault tolerant permanent magnet motor drive with redundancy," *ICIEA 2007 2007 Second IEEE Conf. Ind. Electron. Appl.*, pp. 96–101, 2007.
- [101] Bo Wang, J. Wang, A. Griffo, and B. Sen, "Stator Turn Fault Detection by Second Harmonic in Instantaneous Power for a Triple-Redundant Fault-Tolerant PM Drive," *IEEE Trans. Ind. Electron.*, vol. 65, no. 9, pp. 7279–7289, Sept. 2018.
- [102] P. Arumugam, C. Gerada, T. Hamiti, C. Hill, and S. Bozhko, "A review on turn-turn short circuit fault management," *2015 Int. Conf. Electr. Syst. Aircraft, Railw. Sh. Propuls. Road Veh.*, pp. 1–5, 2015.
- [103] J. Wang, W. Wang, K. Atallah, and D. Howe, "Design of a linear permanent magnet motor for active vehicle suspension," *2009 IEEE Int. Electr. Mach. Drives Conf. IEMDC '09*, pp. 585–591, 2009.
- [104] J. Nerg, M. Rilla, and J. Pyrhönen, "Thermal analysis of radial-flux electrical machines with a high power density," *IEEE Trans. Ind. Electron.*, vol. 55, no. 10, pp. 3543–3554, 2008.
- [105] A. Boglietti, E. Carpaneto, M. Cossale, and S. Vaschetto, "Stator-Winding Thermal Models for Short-Time Thermal Transients: Definition and Validation," *IEEE Trans. Ind. Electron.*, vol. 63, no. 5, pp. 2713–2721, 2016.
- [106] P. Zhang, Y. Du, T. G. Habetler, and B. Lu, "Magnetic effects of DC signal injection on induction motors for thermal evaluation of stator windings," *IEEE Trans. Ind. Electron.*, vol. 58, no. 5, pp. 1479–1489, 2011.
- [107] W. Jiang and T. M. Jahns, "Coupled Electromagnetic-Thermal Analysis of Electric Machines Including Transient Operation Based on Finite-Element Techniques," *IEEE Trans. Ind. Appl.*, vol. 51, no. 2, pp. 1880–1889, 2015.

- [108] Motor-CAD. [Online]. Available: www.motor-design.com.
- [109] A. Sarikhani and O. A. Mohammed, "Inter-turn fault detection in PM synchronous machines by physics-based back electromotive force estimation," *IEEE Trans. Ind. Electron.*, vol. 60, no. 8, pp. 3472–3484, 2013.
- [110] M. Manana, A. Arroyo, A. Ortiz, C. J. Renedo, S. Perez, and F. Delgado, "Field winding fault diagnosis in DC motors during manufacturing using thermal monitoring," *Appl. Therm. Eng.*, vol. 31, no. 5, pp. 978–983, 2011.
- [111] G. J. Li, J. Ojeda, E. Hoang, and M. Gabsi, "Thermal-electromagnetic analysis of a fault-tolerant dual-star flux-switching permanent magnet motor for critical applications," *IET Electr. Power Appl.*, vol. 5, no. 6, pp. 503–513, 2011.
- [112] Z. Hashin and S. Shtrikman, "A Variational approach to the theory of the effective magnetic permeability of multiphase materials," *J. Appl. Phys.*, vol. 33, no. 10, pp. 3125–3131, 1962.
- [113] N. Simpson, R. Wrobel, and P. H. Mellor, "Estimation of equivalent thermal parameters of impregnated electrical windings," *IEEE Trans. Ind. Appl.*, vol. 49, no. 6, pp. 2505–2515, 2013.
- [114] L. Idoughi, X. Mininger, and F. Bouillault, et al. "Thermal model with winding homogenization and FIT discretization for stator slot," *IEEE Trans. Magn.*, vol. 47, no. 12, pp. 4822–4826, 2011.
- [115] JMAG. [Online]. Available: www.jmag-international.com.
- [116] D. P. Kulkarni, G. Rupertus, and E. Chen, "Experimental investigation of contact resistance for water cooled jacket for electric motors and generators," *IEEE Trans. Energy Convers.*, vol. 27, no. 1, pp. 204–210, 2012.
- [117] S. Xue, W. Q. Chu, Z. Q. Zhu, J. Peng, S. Guo, and J. Feng, "Iron loss calculation considering temperature influence in non-oriented steel laminations," *IET Sci. Meas. Technol.*, vol. 10, no. 8, pp. 846–854, 2016.
- [118] X. Zhu, Z. Xiang, L. Quan, W. Wu and Y. Du, "Multimode optimization design methodology for a flux-controllable stator permanent magnet memory motor considering driving cycles," *IEEE Trans. Ind. Electron.*, vol. 65, no. 7, pp. 5353–5366, 2018.
- [119] M. Popescu, DG. Dorrell, L. Alberti, N. Bianchi, et al., "Thermal analysis of duplex three-phase induction motor under fault operating conditions," *IEEE Trans. Ind. Appl.*, vol. 49, no. 4, pp. 1523–1530, 2013.
- [120] Q. Lu, X. Zhang, Y. Chen, X. Huang, et al., "Modeling and Investigation of Thermal Characteristics of a Water-Cooled Permanent-Magnet Linear Motor," *IEEE Trans. Ind. Appl.*, vol. 51, no. 3, pp. 2086–2096, 2015.
- [121] S. Ruoho, J. Kolehmainen, J. Ikaheimo, and A. Arkkio, "Interdependence of Demagnetization, Loading, and Temperature Rise in a Permanent-Magnet Synchronous Motor," *IEEE Trans. Magn.*, vol. 46, no. 3, pp. 949–953, 2010.

- [122] X. Sun, M. Cheng, S. Zhu, and J. Zhang, "Coupled Electromagnetic-Thermal-Mechanical Analysis for Accurate Prediction of Dual-Mechanical-Port Machine Performance," *IEEE Trans. Ind. Appl.*, vol. 48, no. 6, pp. 2240-2248, 2012.
- [123] X. Zhang, W. Li, B. Kou, J. Cao, H. Cao, C. Gerada, et al., "Electrothermal Combined Optimization on Notch in Air-Cooled High-Speed Permanent-Magnet Generator," *IEEE Trans. Magn.*, vol. 51, no. 1, pp. 1-10, 2015.
- [124] Z. Sun, J. Wang, D. Howe, and G. Jewell, "Analytical prediction of the short-circuit current in fault-tolerant permanent-magnet machines," *IEEE Trans. Ind. Electron.*, vol. 55, no. 12, pp. 4210-4217, 2008.
- [125] C. Shaver, M. Rumbaugh, and S. Cain, "Accelerated thermal life testing for random-wound, polyimide wrapped medium voltage machines," *2014 IEEE Electr. Insul. Conf.*, pp. 353-358, 2014.
- [126] F. Kielmann and M. Kaufhold, "Evaluation analysis of thermal ageing in insulation systems of electrical machines - A historical review," *IEEE Trans. Dielectr. Electr. Insul.*, vol. 17, no. 5, pp. 1373-1377, 2010.
- [127] PAR UK Ltd, "POLYESTER C200 ROUND + HEAT SEALED PET FILM," datasheet.
- [128] R. Hu, J. Wang, B. Sen, A. R. Mills, E. Chong and Z. Sun, "PWM Ripple Currents Based Turn Fault Detection for Multiphase Permanent Magnet Machines," *IEEE Trans. Ind. Appl.*, vol. 53, no. 3, pp. 2740-2751, 2017.
- [129] IEEE Std 43-2000: "IEEE Recommended Practice for Testing Insulation Resistance of Rotating Machinery," 2000.
- [130] Ohmite Mfg Co, "TGHG Series Precision Current Sense Resistors," datasheet.
- [131] Arcol UK Ltd, "HS Aluminium Housed Resistors," datasheet.
- [132] R. Wrobel, S. Ayat, and J. L. Baker, "Analytical methods for estimating equivalent thermal conductivity in impregnated electrical windings formed using Litz wire," *2017 IEEE Int. Electr. Mach. Drives Conf. IEMDC 2017*, pp. 1-8, 2017.
- [133] S. Ayat, R. Wrobel, J. Goss, and D. Drury, "Estimation of equivalent thermal conductivity for impregnated electrical windings formed from profiled rectangular conductors," *8th IET Int. Conf. Power Electron. Mach. Drives (PEMD 2016)*, pp. 1-6, 2016.

TABLE OF FIGURES

Fig. 1-1. PMSM voltage-source drive schematic[13]	3
Fig. 1-2. Schematic of two redundant motor actuators.	9
Fig. 1-3. 3-phase motor-drive system configurations. (a) Middle point of the DC link. (b) Converter fourth leg. [21]	10
Fig. 1-4. Delta-connected three-phase stator winding with one phase open-circuit fault. [22].....	10
Fig. 1-5. Five-phase half-bridge converters of a five-phase fault tolerant machine. [23].....	11
Fig. 1-6. Schematic of a double-wye PM motor architecture [20]	12
Fig. 1-7. Schematic of the dual three-phase motor drive [29]	12
Fig. 1-8. Schematic of the triple three-phase motor winding layout. [30].....	13
Fig. 1-9. Switched reluctance motor. (a) Cross section. (b) Three-phase asymmetric half bridge converter.	14
Fig. 1-10. FSCW synchronous reluctance motor. (a) Cross section. (b) Three-phase voltage source inverter. [34]	14
Fig. 1-11. The PM machine with 12 slots and 10 poles. (a) Stator with coils on adjacent teeth. (b) Stator with coils on alternate teeth. [38].....	15
Fig. 1-12. Alternative design for 12-slot 10-pole machine with alternate teeth wound on wider teeth. [38]	15
Fig. 1-13. The equivalent circuit of 3-phase delta connected machine windings with turn fault on single phase.....	18
Fig. 1-14. The equivalent circuit of 3-phase wye connected machine windings with turn fault on single phase.....	18
Fig. 2-1. PMASynRM with segregated triple wye-connected 3-phase windings.....	36
Fig. 2-2. PMASynRM with segregated triple delta-connected 3-phase windings.....	38
Fig. 2-3. Schematic of the delta-connected PMASynRM with turn fault in single phase.....	39
Fig. 2-4. Schematic circuit simulated for PMASynRM with wye-connected winding configuration when set ABC is in terminal SC.....	42
Fig. 2-5. Phase flux linkages of wye-connected 3-phase set ABC with terminal SC without neutral line.	43
Fig. 2-6. Schematic circuit simulated for PMASynRM with wye-connected winding with neutral line when set ABC is in terminal SC.	43
Fig. 2-7. Schematic circuit simulated for PMASynRM with delta-connected set ABC in terminal SC and other two healthy wye-connected sets.....	44
Fig. 2-8. Phase flux linkages of 3-phase set ABC with terminal SC with neutral line.....	45
Fig. 2-9. Comparison of turn flux linkages with or without neutral line.	45

Fig. 2-10. Comparison of no-load line-to-line back emf between delta- and wye-connected machines. (a) Back emf. (b) Harmonic.....	46
Fig. 2-11. Comparison of phase currents between delta- and wye-connected machines at rated operation.	47
Fig. 2-12. Zero sequence current of delta-connected machine at rated operation.	47
Fig. 2-13. Comparison of torques between delta- and wye-connected PMASynRMs at rated torque and base speed. (a) Torque. (b) Harmonic.	48
Fig. 2-14. Schematic of one phase winding OC in delta connected winding.	50
Fig. 2-15. Phasor diagram of currents in one-phase open-circuit fault for a balanced operation.....	50
Fig. 2-16. Line and phase currents of the fault set ABC under Delta_S2. (a) Line currents between healthy condition and Delta_S2. (b) Phase currents under Delta_S2.	52
Fig. 2-17. Comparison of torque waveforms between wye-connected machine and Delta_S1 and Delta_S2 under F1.....	53
Fig. 2-18. One 3-phase open-circuit fault at rated torque and base speed of delta-connected machine. (a) Inverter OC (Delta_C1). (b) Winding OC (Delta_C2).	54
Fig. 2-19. Phase currents of 3-phase set ABC under one 3-phase open-circuit fault in Delta_C1.....	54
Fig. 2-20. Phase currents of 3-phase set DEF in Delta_C1 and Delta_C2 under F2.	55
Fig. 2-21. Comparison of output torques between wye-connected PMASynRM and Delta_C1 and Delta_C2 under F2.....	56
Fig. 2-22. Comparison of phase currents of set ABC of delta-connected machine under healthy condition and F3.....	57
Fig. 2-23. Comparison of turn fault currents between delta- and wye-connected machines under F3.	57
Fig. 2-24. Comparison of output torques between delta- and wye-connected PMASynRMs under F3.	57
Fig. 2-25. Cross section of SC turn in B2 coil of PMASynRM.....	59
Fig. 2-26. Variations of turn fault current in coils with amplitude and gamma angle of currents in healthy sets (a) A1. (b) A2. (c) B1. (d) B2. (e) C1. (f) C2.....	59
Fig. 2-27. Comparison of phase currents of set ABC of wye-connected machine under healthy condition and F4.....	60
Fig. 2-28. Comparison of phase currents of set ABC of delta-connected machine under healthy condition and F4.....	61
Fig. 2-29. Comparison of turn fault currents in the fault turn between wye- and delta-connected machines under F4.....	62
Fig. 2-30. Comparison of output torques between wye- and delta-connected machines under F4.	62
Fig. 3-1. Cross-section of 9-phase, 36-slot, 6-pole PMASynRM. (a) Winding layout. (b) Magnet layout.	68
Fig. 3-2. Decomposition of flux density of M1N1_1 and M1N2_1	69
Fig. 3-3. Demagnetisation characteristics of VACOMAX 225 HR	70

Fig. 3-4. Flow chart of continuous demagnetisation analysis.....	70
Fig. 3-5. Demagnetisation BH curve with virgin curve at 300° C explaining partial demagnetisation.	71
Fig. 3-6. Characteristics under 3-phase short-circuit condition. (a) Transient phase currents of phase A, B, C. (b) D-q axis current trajectory.	73
Fig. 3-7. Transient currents of phase B and fault turn during fault transient process under F4.	74
Fig. 3-8. Transient phase currents and current trajectories in the d-q axis plane under various voltage-reversal conditions. (a) Transient phase currents of phase A, B, C under F5. (b) D-q axis current trajectory under F5. (c) Transient phase currents of phase A, B, C under F6. (d) D-q axis current trajectory under F6. (e) Transient phase currents of phase A, B, C under F7. (f) D-q axis current trajectory under F7.	78
Fig. 3-9. Comparison of the back emfs before and after faults. (a) F5. (b) F6. (c) F7.	79
Fig. 3-10. Comparison of the output torques before and after faults F5, F6, F7.	79
Fig. 3-11. Corresponding position of all the magnets of the machine with partial demagnetised area.....	82
Fig. 3-12. Partial demagnetised area and no-load flux density waveform after F5 (a) Demagnetised area. (b) Post-fault no-load flux density.	82
Fig. 3-13. Partial demagnetised area and no-load flux density waveform after F6 (a) Demagnetised area. (b) Post-fault no-load flux density.	83
Fig. 3-14. Partial demagnetised area and no-load flux density waveform after F7 (a) Demagnetised area. (b) Post-fault no-load flux density.	84
Fig. 3-15. Pre-fault no-load flux density.....	85
Fig. 3-16. Space harmonic distribution of airgap flux density before and after 3-phase voltage-reversal fault.	85
Fig. 3-17. Comparison of the pre-fault and post-fault back emf of phase A generated by pole-pair M1N and M2P.	86
Fig. 3-18. Space harmonic distribution of back emf before and after 3-phase voltage-reversal fault.....	86
Fig. 3-19. Torque harmonic distribution before and after 3-phase voltage-reversal fault.....	86
Fig. 4-1. Cross section of a triple redundant, 9-phase PMASynRM. (a) Winding Layout. (b) Named slots and short-circuit turn.	92
Fig. 4-2. Illustration of the spiral cooling jacket system of machine.....	92
Fig. 4-3. The schematic of 1/6 rotor part.	93
Fig. 4-4. LP thermal model of the rotor part.	94
Fig. 4-5. The schematic of a half slot and tooth.....	95
Fig. 4-6. LP thermal model of the stator part.....	95
Fig. 4-7. LP thermal model of the whole motor.....	98
Fig. 4-8. LP thermal model of the healthy slot and tooth.	102
Fig. 4-9. LP thermal model of the fault slot and tooth with inter-turn SC.	102

Fig. 4-10. LP thermal model of the stator part.....	104
Fig. 4-11. 3D thermal model. (a) 1/3 model. (b) Whole model.....	106
Fig. 4-12. Schematic diagram of heat equivalent circuit of this motor.....	106
Fig. 4-13. Temperature distribution of 3D thermal model under healthy condition.	108
Fig. 4-14. Temperature distribution of Motor-CAD under healthy condition.....	109
Fig. 4-15. Transient average temperatures between LP model, 3D model and Motor-CAD under healthy condition. (a) Magnet. (b) Winding.	110
Fig. 4-16. Transient temperatures between LP and 3D models under one turn SC fault. (a). Average temperatures. (b). Hotspot temperatures.	112
Fig. 4-17. Transient temperatures between LP and 3D models under one turn SC fault with 3-phase terminal SC applied for fault mitigation. (a). Average temperatures. (b). Hotspot temperatures.....	112
Fig. 4-18. The prototype on the test rig with oil cooling system.	114
Fig. 4-19. Motor winding leads and relay for turn fault. (a) Leads. (b) Relay.	115
Fig. 4-20. The terminal connections of each 3-phase set. (a) Set ABC. (b) Set DEF. (c) Set GHI.....	115
Fig. 4-21. Comparison of predicted and measured phase currents and turn fault current under one turn SC at 1000rpm and 40A current. (a) Phase currents in fault set ABC. (b) Phase currents in healthy set DEF. (c) Turn fault current.	117
Fig. 4-22. RMS turn fault current with load currents variation.	118
Fig. 4-23. Comparison of predicted and measured phase currents and turn fault current under one turn SC with 3-phase terminal SC at 4000 rpm and 80A current. (a) Phase currents in fault set ABC. (b) Phase currents in healthy set DEF. (c) Turn fault current.....	120
Fig. 4-24. Comparison of predicted and measured phase currents and turn fault current under one turn SC with 3-phase terminal SC at 4000 rpm and 120A current. (a) Phase currents in fault set ABC. (b) Phase currents in healthy set DEF. (c) Turn fault current.....	121
Fig. 4-25. Oil cooling system. (a) Cooling jacket. (b) Assembly.	122
Fig. 4-26. Temperature distribution under healthy condition with 80A.	124
Fig. 4-27. Sensor locations.....	125
Fig. 4-28. Temperature distribution under healthy condition with 120A.	127
Fig. 4-29. Comparison of predicted and measured transient temperatures of six sensors under healthy condition with 120A. (a) set2_ew. (b) set1_ew. (c) tf_ew. (d) b1_slot. (e) tf_slot. (f) e2_slot.....	129
Fig. 4-30. Temperature distribution under fault condition with 80A.	130
Fig. 4-31. Temperature distribution under fault condition with 120A.	131
Fig. 4-32. Comparison of predicted and measured transient temperatures in the fault turn region under fault condition with 120A. (a) tf_ew. (b) tf_slot.....	132
Fig. 4-33. Temperature distribution under required healthy condition. (a) Whole machine. (b) Winding part.	134

Fig. 4-34. Comparisons of predicted current waveforms between 20°C and 190°C under one turn SC with 3-phase terminal SC at 4000 rpm and 120A current. (a) Phase currents in fault set ABC. (b) Turn fault current in coil B.....	135
Fig. 4-35. Temperature distribution under fault condition with required operation condition.....	136
Fig. 5-1. Illustration of inter-turn short circuit condition.....	139
Fig. 5-2. Flowchart of EM-thermal coupled simulation. (a) Step 1: healthy condition. (b) Step 2: fault condition.....	142
Fig. 5-3. Cross section of a triple redundant, 9-phase PMASynRM.	143
Fig. 5-4. 3D thermal model. (a) Model with potting. (b) Cross section.	144
Fig. 5-5. Temperature distribution under healthy condition with the rated current of 120A at 500rpm...	146
Fig. 5-6. SC turn loss variation with time under one turn SC at 500 rpm.	147
Fig. 5-7. Comparison of hotspot temperature between two simulations under one turn SC at 500 rpm...	147
Fig. 5-8. Temperature distribution under healthy condition with the rated current of 120A at 4000rpm.	148
Fig. 5-9. Temperature distribution under F2 at 780s between two simulated methods. (a) EM-thermal coupled simulation. (b) Thermal-only simulation.....	150
Fig. 5-10. Comparison of the SC turn loss and transient average temperature rises between two simulations under one turn SC at 4000 rpm.	151
Fig. 5-11. Comparison of the transient hotspot temperature rises between two simulations under one turn SC at 4000 rpm.....	151
Fig. 5-12. Comparison of the SC turn loss under 1 turn SC and 2 turns SC at 4000 rpm between two simulated methods.....	152
Fig. 5-13. Temperature distribution under F3 at 780s between two simulated methods. (a) EM-thermal coupled simulation. (b) Thermal-only simulation.....	153
Fig. 5-14. Comparison of the SC turn loss under 1 turn SC and 3 turns SC at 4000 rpm between two simulated methods.....	155
Fig. 5-15. Temperature distribution under F4 at 780s by EM-thermal coupled simulation.....	156
Fig. 5-16. Current variation of faulted 3-phase set ABC with simulation step (time) under F5 under EM-thermal coupled simulation.	157
Fig. 5-17. Loss variation of faulted 3-phase set ABC with simulation step (time) under F5 between EM-thermal coupled and thermal-only simulations.	157
Fig. 5-18. Temperature distribution under F5 at 6300s under EM-thermal coupled simulation.....	158
Fig. 5-19. Transient temperature responses. (a) Average temperature of different winding parts. (b) Hotspot.	159
Fig. 5-20. Cross section of a PMASynRM with phase B dividing 17 strands per turn.....	161
Fig. 5-21. Circuit of a PMASynRM with phase B dividing 17 parallel strands.	162
Fig. 5-22. 1/3 3D thermal model with 17 turns individually modelled in B2 and B4 coils.	162

Fig. 5-23. No-load flux linkage waveforms of the 17 parallel strands of phase B.	163
Fig. 5-24. Current waveforms of the 17 parallel strands of phase B at rated operation.	164
Fig. 5-25. The circuit of phase B with inter strand faults. (a) Turn SC with one strand. (b) Turn SC with 17 parallel strands.....	165
Fig. 5-26. Illustration of turn SC with different number of parallel strands.....	166
Fig. 5-27. Variations of fault current and loss with number of faulted parallel strands under one turn SC fault. (a) Average RMS fault current in each strand. (b) Losses.	168
Fig. 5-28. The circuit of phase B with intra-strand SC fault. (a) 1 to 15 SC turns within one strand. (b) 16 SC turns within one strand.	169
Fig. 5-29. Illustration of different turns SC within one strand.....	169
Fig. 5-30. Variations of fault current and losses with the number of SC turns within one strand. (a) Fault current. (b) Losses.	171
Fig. 5-31. Fault performance with the increase in times under one turn SC within one strand at 4000 rpm. (a) SC current. (b) Copper loss in the SC turn.	172
Fig. 5-32. Temperature distributions under one turn SC within one strand at rated speed between two simulated methods. (a) EM-thermal coupled simulation. (b) Thermal-only simulation.	173
Fig. 5-33. Temperature distribution under one turn SC within 13 strands at 1560s by EM-thermal coupled simulation.	175
Fig. 6-1. The electric circuit under insulation deterioration leading to one turn, two turns, three turns ...	180
Fig. 6-2. RMS currents under insulation deterioration leading to one turn, two turns, three turns and one phase SC. (a) RMS currents in the faulted turn. (b) RMS currents in the insulation resistance.	181
Fig. 6-3. Losses under insulation deterioration leading to one turn, two turns, three turns and one phase SC. (a) Losses in the faulted turn. (b) Losses in the insulation resistance.....	182
Fig. 6-4. Loss variation in the faulted turn with insulation resistance under turn-to-turn insulation deterioration leading to SC fault.	184
Fig. 6-5. Loss variation in the insulation resistance with insulation resistance under turn-to-turn insulation deterioration leading to SC fault.	184
Fig. 6-6. One third model with whole axial length.	185
Fig. 6-7. Insulation region located in one slot with three dimensions.	186
Fig. 6-8. Temperature distributions of slot and insulation region in Case 1.....	187
Fig. 6-9. Temperature distributions of slot and insulation region in Case 2.....	188
Fig. 6-10. Temperature distribution when insulation resistance is 13 Ω and mitigation action is applied.	190
Fig. 6-11. Temperature distribution when insulation resistance is 0 Ω and mitigation action is applied. .	190
Fig. 6-12. Variation of insulation resistance with time.....	193
Fig. 6-13. Variation of hotspot temperature in faulty insulation with time.	193

Fig. 6-14. Relay and precision current sense resistors.....	195
Fig. 6-15. Relay and aluminum housed resistors.	195
Fig. 6-16. Comparison of predicted and measured currents at 2000rpm with 40A without extra resistor. (a) Currents in the faulted turn. (b) Currents in the insulation resistance. (c) Phase currents in fault set.....	196
Fig. 6-17. Comparison of predicted and measured RMS currents under insulation deterioration at 2000rpm with 40A. (a) RMS currents in the faulted turn. (b) RMS currents in the insulation resistance.....	198
Fig. 6-18. Comparison of predicted and measured losses under insulation deterioration at 2000rpm with 40A. (a) Losses in the faulted turn. (b) Losses in the insulation resistance.....	198
Fig. 6-19. Comparison of predicted and measured RMS currents under insulation deterioration at 1000rpm with 40A. (a) RMS currents in the faulted turn. (b) RMS currents in the insulation resistance.....	199
Fig. 6-20. Comparison of predicted and measured losses under insulation deterioration at 1000rpm with 40A. (a) Losses in the faulted turn. (b) Losses in the insulation resistance.....	200
Fig. 7-1. Cross section and winding connection of a 2.5 MW PM Generator.....	203
Fig. 7-2. Coil distribution and zoomed view of coil layout.	204
Fig. 7-3. Short-circuited turns (in yellow) in coil A1. (a) SC in coil A1. (b) One turn SC. (c) Three turns SC.	207
Fig. 7-4. Comparison of SC currents and torques under one, three and five SC turns. (a) SC turn fault current. (b) Torque.....	207
Fig. 7-5. One turn SC (in yellow) in different phases. (a) Phase A. (b) Phase B. (c) Phase C.....	209
Fig. 7-6. Comparison of fault currents and torques when one turn SC occurs in different phases. (a) SC turn fault current. (b) Torque.....	209
Fig. 7-7. Comparison of phase voltage of coil A under rated load, no load and one turn SC in phase A1.	210
Fig. 7-8. Comparison of currents of Ah, A2, A3, and Af under one turn SC in phase A1 coil.....	210
Fig. 7-9. One turn SC (in yellow) at three different positions in coil A1 slots. (a) Position 1. (b) Position 2. (c) Position 3.	211
Fig. 7-10. Comparison of SC currents and torques when one turn SC occurs at three positions in coil A1 slots. (a) SC turn fault current. (b) Torque.....	212
Fig. 7-11. One turn SC (in yellow) at two different positions in coil A1 slots. (a) Turn 7. (b) Turn 4.....	213
Fig. 7-12. Phase winding connection.	213
Fig. 7-13. Circuit illustration of inter-phase fault between two 1 st turns.....	214
Fig. 7-14. Circuit illustration of inter-phase fault between two 8 th turns.....	214
Fig. 7-15. Illustration of turn-to-turn and phase-to-phase SC in the 1 st turns. (a) One turn SC in phase B in the 1 st turns. (b) Inter phase SC in phases A and B between two 1 st turns.	215
Fig. 7-16. Comparison of fault currents and torques under one turn SC in phase B and inter-phase SC. (a) SC turn fault current. (b) Torque.....	215

Fig. 7-17. Variation of 2nd IAP harmonic with variable contact resistances.	220
Fig. 7-18. Variation of 2 nd IRP harmonic with variable contact resistances.	220
Fig. 7-19. 3D 1/36 (half slot) model.	223
Fig. 7-20. 3D thermal model of generator in JMAG. (a) Radial cross section of 3D thermal model. (b) 3D thermal model.	224
Fig. 7-21. Steady state temperature distribution of the generator predicted by JMAG under healthy condition.	226
Fig. 7-22. Temperature distribution of windings predicted by JMA under healthy condition.	226
Fig. 7-23. Comparisons of transient temperature rises between Motor-CAD and JMAG. (a) Housing, shaft, rotor, magnet and stator. (b) Winding and hotspot.	227
Fig. 7-24. Cross section of thermal model with turn 7 SC.	228
Fig. 7-25. Temperature distributions at 0.19s under turn 7 SC with constant loss in generator and SC turn.	229
Fig. 7-26. Temperature distributions at 0.19s under turn 7 SC when loss increase with temperature is accounted in generator and SC turn.	229
Fig. 7-27. Comparisons of transient temperature rises of the active winding, end winding and hotspot of the faulted turn with constant and variable loss.	231
Fig. 7-28. Insulation region located at the axial centre of the active winding between turn 7 and turn 6. (a) Axial cross section. (b) Radial cross section.	232
Fig. 7-29. Average temperature and hotspot temperature rises in contact resistance with time.	232
Fig. 7-30. Temperature distribution in the contact resistance (insulation) when one turn SC takes place in turn 7 with $R_f=R100000$	233
Fig. A-1. Transient LP thermal model under healthy condition.	266
Fig. A-2. Transient LP thermal model under fault condition.	267
Fig. A-3. Transient LP thermal model under fault condition of 3-phase set ABC.	268
Fig. A-4. Transient LP thermal model under fault condition of healthy slot.	269
Fig. A-5. Transient LP thermal model under fault condition of fault slot B2.	269
Fig. A-6. Transient LP thermal model under fault condition of fault slot B4.	270

LIST OF TABLES

Table 2-1. Design specifications of the machine	37
Table 2-2. Comparison of performances between delta- and wye-connected PMASynRMs at rated torque and base speed.....	49
Table 2-3. Comparison of performances between delta- and wye-connected PMASynRMs at peak torque at base speed.....	49
Table 2-4. Fault Conditions under Consideration.....	49
Table 2-5. Comparison of performances under F1	53
Table 2-6. Comparison of performances under F2	56
Table 2-7. Comparison of performances under F3	58
Table 2-8. Comparison of performances under F4	62
Table 2-9. Comparison of temperatures under F4 predicted by LP model between wye- and delta-connected machines.....	62
Table 2-10. Comparison of performances under fault conditions between wye- and delta-connected machines.....	63
Table 3-1. Fault conditions under consideration.....	72
Table 3-2 Comparison of currents and post demagnetisation performances under Faults F1 to F4.	74
Table 3-3 Comparison of the lowest flux density along the magnetising direction of all magnets during fault transient.	75
Table 3-4 Comparison of transient currents and post demagnetisation performances under Faults F5 to F7.	80
Table 4-1 Comparison of temperatures under healthy condition predicted by LP model, 3D model and Motor-CAD.	109
Table 4-2 Comparison of temperatures under one turn SC fault predicted by LP and 3D models.	110
Table 4-3 Comparison of temperatures under one turn SC fault with 3-phase terminal SC for fault mitigation predicted by LP and 3D models.....	111
Table 4-4 Measured resistances.	116
Table 4-5 Comparison of measured and predicted temperatures under healthy condition with 80A.	125
Table 4-6 Comparison of measured and predicted temperatures under fault condition with 80A.....	130
Table 4-7 Comparison of measured and predicted temperatures under fault condition with 120A.....	131
Table 4-8 Temperatures under required healthy condition predicted by 3D model.....	134
Table 5-1. Fault conditions under consideration.....	145
Table 5-2 Comparison of temperatures in different parts at 780s under one turn SC at 500 rpm.....	147

Table 5-3 Comparison of temperatures in different parts under healthy condition at 500 rpm and 4000rpm.	149
Table 5-4 Comparison of temperature values in different parts at 780s under one turn SC at 4000 rpm.	151
Table 5-5 Comparison of temperature values in different parts at 780s under two turns SC at 4000 rpm.	154
Table 5-6 Comparison of temperature values in different parts at 780s under three turns SC at 4000 rpm.	156
Table 5-7 Comparison of temperature values in different parts at 6300s under one turn SC with 3-phase terminal SC at 4000 rpm.	158
Table 5-8 Comparison of temperature values in different parts at 1560s under one turn SC within one, 6 and 17 strands at 4000 rpm.	174
Table 5-9 Comparison of temperature values in different parts at 1560s under one turn SC within 11, 12, 13 and 14 strands at 4000 rpm.	175
Table 6-1 Temperatures with different thicknesses.	187
Table 6-2 Currents and losses before the mitigation measure of 3-phase terminal SC.	189
Table 6-3 Currents and losses after the mitigation measure of 3-phase terminal SC.	189
Table 6-4 Temperature distributions under fault conditions with two insulation resistances.	190
Table 6-5 Characteristics during the transient ageing process of Case 3.	193
Table 7-1 Specification of a 2.5 MW PM generation.	203
Table 7-2 Comparison of fault behaviours under one, three and five SC turns.	208
Table 7-3 Comparison of fault behaviours when one turn SC occurs in different phases.	209
Table 7-4 Comparison of fault behaviours when one turn SC occurs at eight positions in coil A1 slots.	212
Table 7-5 Comparison of fault behaviours of one turn SC before and after application terminal SC in phase A.	217
Table 7-6 Comparison of fault behaviours of one turn SC in phase A under rated speed and one turn SC in phase A with all other phases being deactivated under 10% rated speed.	217
Table 7-7 Comparison of SC currents and associated losses under healthy and one turn SC with variable contact resistances.	218
Table 7-8 Variations of 2 nd IAP and IRP harmonics with variable contact resistances under one turn SC in coil A1.	220
Table 7-9 Fault currents and losses under one turn SC at 10% rated speed when all other phases are deactivated with variable contact resistances.	222
Table 7-10 Parameters and thermal properties.	223
Table 7-11 Losses under rated healthy condition.	225
Table 7-12 Comparisons of JMAG and Motor-CAD predicted temperatures in healthy condition.	226

Table 7-13 Temperature distribution of coil A1 under healthy condition.	228
Table 7-14 Average temperatures in healthy regions during transient of turn 7 SC both with constant and variable loss.	230
Table 7-15 Temperatures in faulted coil A1 under turn 7 SC with constant loss.	230
Table 7-16 Temperatures in faulted coil A1 under turn 7 SC with variable loss.	230
Table 7-17 Temperatures at 0.5ms when one turn SC takes place in turn 7 with $R_f=R10$	232
Table 7-18 Temperatures when one turn SC takes place in turn 7 with $R_f=R100000$	234

Appendix A Lumped Parameter Thermal Model in Matlab

The transient LP thermal models proposed in Chapter 4 are built under healthy and fault conditions in Matlab for fast prediction of thermal behaviour of the machine.

Fig. A-1 is the transient LP thermal model under healthy condition. Fig. A-2 is the whole system of the transient LP thermal model under fault condition, while Fig. A-3 to Fig. A-6 are subsystems of the transient LP thermal model under fault condition. Fig. A-3 presents the thermal model of 3-phase set ABC which is the same with thermal models of 3-phase sets DEF and GHI. Moreover, Fig. A-4 illustrates the thermal model of all healthy slots, while Fig. A-5 and Fig. A-6 show the thermal models of slots B2 and B4 containing inter-turn fault, respectively.

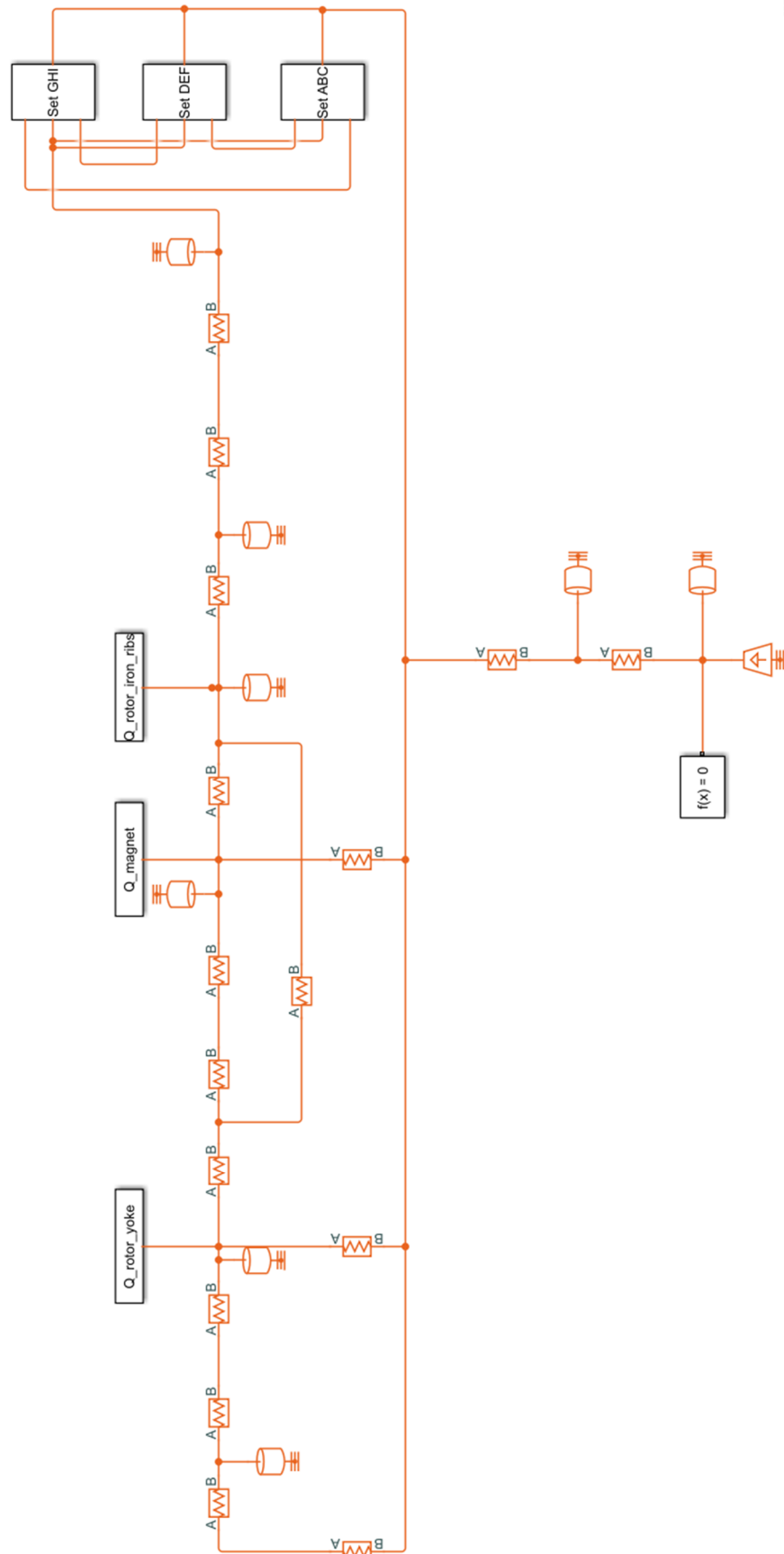


Fig. A-2. Transient LP thermal model under fault condition.

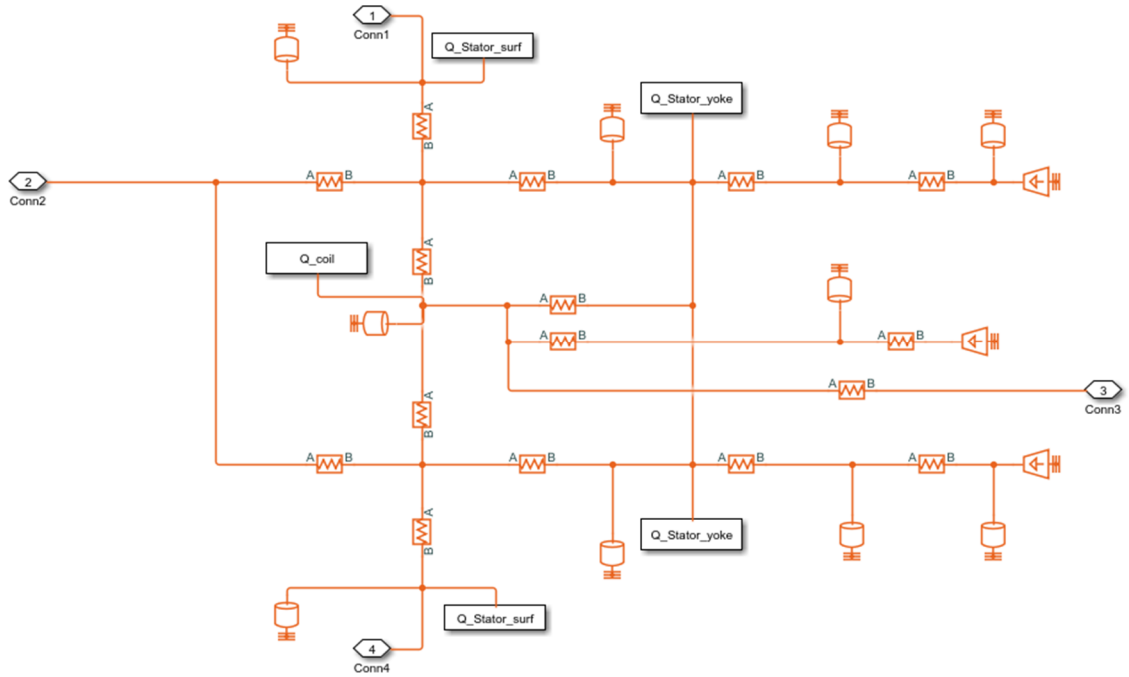


Fig. A-4. Transient LP thermal model under fault condition of healthy slot.

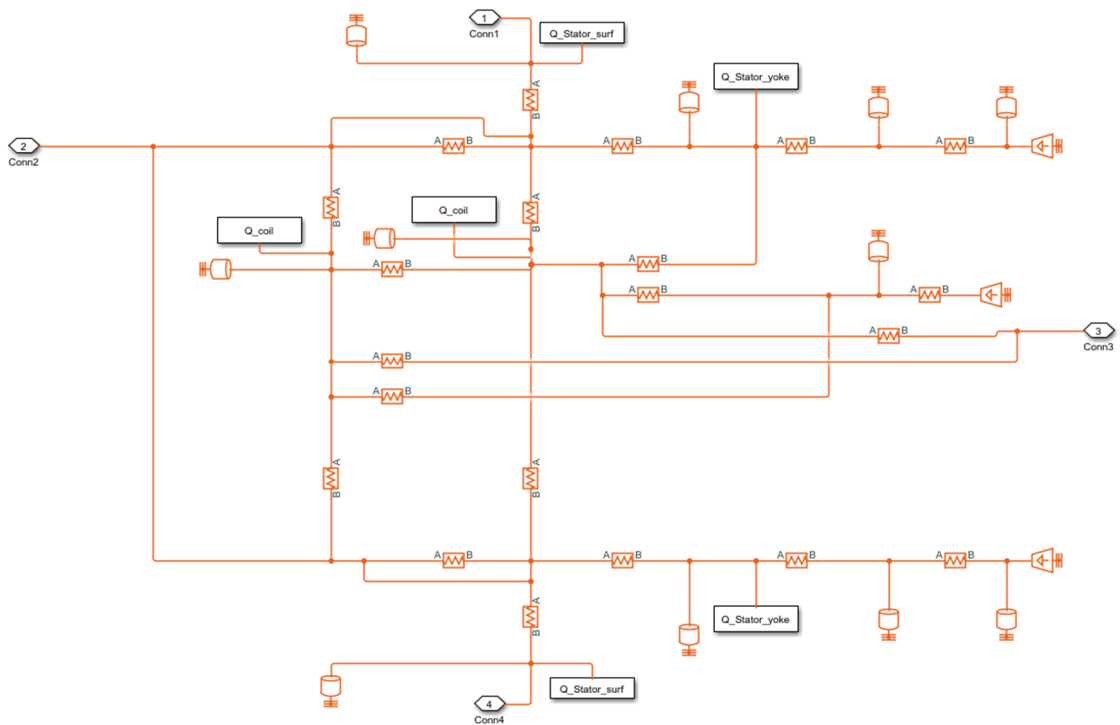


Fig. A-5. Transient LP thermal model under fault condition of fault slot B2.

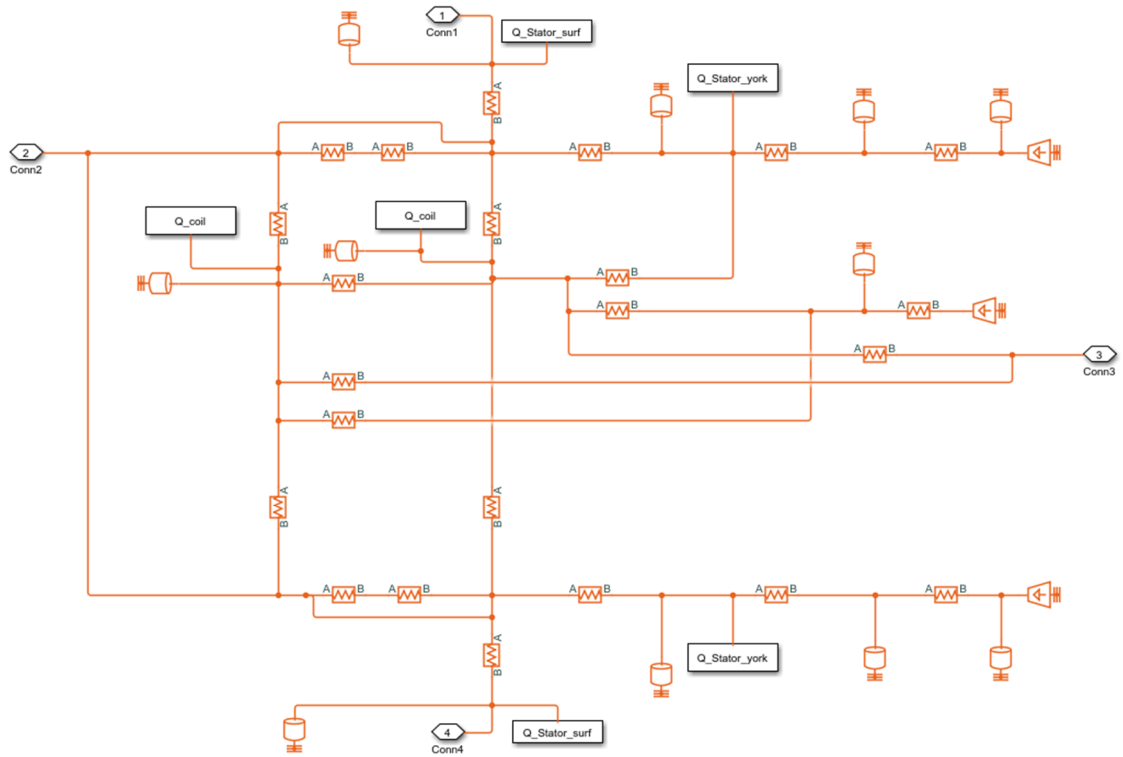


Fig. A-6. Transient LP thermal model under fault condition of fault slot B4.

Appendix B EM-Thermal Coupled Simulation Code

The python script is used in EM-thermal coupled simulation for automatically exchanging data between 2D EM and 3D thermal models in JMAG

```
***** Script to for EM-thermal coupled simulation in 2D EM and 3D thermal models in JMAG *****
```

```
app = designer.GetApplication()
***** Define heat source amount table *****
def table_set(x,m):
    y=x
    refarray = [[0 for i in range(2)] for j in range(100)]
    refarray[0][0] = 0
    refarray[0][1] = y[0]
    refarray[1][0] = 6000
    refarray[1][1] = y[0]
    refarray[2][0] = 6000+0.0000001
    refarray[2][1] = y[1]
    refarray[3][0] = 6000+Tc1
    refarray[3][1] = y[1]
    refarray[4][0] = 6000+Tc1+0.0000001
    refarray[4][1] = y[2]
    refarray[5][0] = 6000+Tc1*2
    refarray[5][1] = y[2]
    refarray[6][0] = 6000+0.0000001+Tc1*2
    refarray[6][1] = y[3]
    refarray[7][0] = 6000+Tc1*3
    refarray[7][1] = y[3]
    refarray[8][0] = 6000+0.0000001+Tc1*3
    refarray[8][1] = y[4]
    refarray[9][0] = 6000+Tc1*4
    refarray[9][1] = y[4]
    refarray[10][0] = 6000+0.0000001+Tc1*4
    refarray[10][1] = y[5]
    refarray[11][0] = 6000+Tc1*5
    refarray[11][1] = y[5]
    refarray[12][0] = 6000+0.0000001+Tc1*5
    refarray[12][1] = y[6]
    refarray[13][0] = 6000+Tc1*6
    refarray[13][1] = y[6]
    refarray[14][0] = 6000+0.0000001+Tc1*6
    refarray[14][1] = y[7]
    refarray[15][0] = 6000+Tc1*7
    refarray[15][1] = y[7]
    refarray[16][0] = 6000+0.0000001+Tc1*7
    refarray[16][1] = y[8]
    refarray[17][0] = 6000+Tc1*8
    refarray[17][1] = y[8]
    refarray[18][0] = 6000+0.0000001+Tc1*8
    refarray[18][1] = y[9]
    refarray[19][0] = 6000+Tc1*9
    refarray[19][1] = y[9]
    refarray[20][0] = 6000+0.0000001+Tc1*9
```

```
refarray[20][1] = y[10]
refarray[21][0] = 6000+Tc1*10
refarray[21][1] = y[10]
refarray[22][0] = 6000+0.0000001+Tc1*10
refarray[22][1] = y[11]
refarray[23][0] = 6000+Tc1*11
refarray[23][1] = y[11]
refarray[24][0] = 6000+0.0000001+Tc1*11
refarray[24][1] = y[12]
refarray[25][0] = 6000+Tc1*12
refarray[25][1] = y[12]
refarray[26][0] = 6000+0.0000001+Tc1*12
refarray[26][1] = y[13]
refarray[27][0] = 6000+Tc1*13
refarray[27][1] = y[13]
refarray[28][0] = 6000+0.0000001+Tc1*13
refarray[28][1] = y[14]
refarray[29][0] = 6000+Tc1*14
refarray[29][1] = y[14]
refarray[30][0] = 6000+0.0000001+Tc1*14
refarray[30][1] = y[15]
refarray[31][0] = 6000+Tc1*15
refarray[31][1] = y[15]
refarray[32][0] = 6000+0.0000001+Tc1*15
refarray[32][1] = y[16]
refarray[33][0] = 6000+Tc1*16
refarray[33][1] = y[16]
refarray[34][0] = 6000+0.0000001+Tc1*16
refarray[34][1] = y[17]
refarray[35][0] = 6000+Tc1*17
refarray[35][1] = y[17]
refarray[36][0] = 6000+0.0000001+Tc1*17
refarray[36][1] = y[18]
refarray[37][0] = 6000+Tc1*18
refarray[37][1] = y[18]
refarray[38][0] = 6000+0.0000001+Tc1*18
refarray[38][1] = y[19]
refarray[39][0] = 6000+Tc1*19
refarray[39][1] = y[19]
refarray[40][0] = 6000+0.0000001+Tc1*19
refarray[40][1] = y[20]
refarray[41][0] = 6000+Tc1*20
refarray[41][1] = y[20]
refarray[42][0] = 6000+0.0000001+Tc1*20
refarray[42][1] = y[21]
refarray[43][0] = 6000+Tc1*21
refarray[43][1] = y[21]
refarray[44][0] = 6000+0.0000001+Tc1*21
refarray[44][1] = y[22]
refarray[45][0] = 6000+Tc1*22
refarray[45][1] = y[22]
refarray[46][0] = 6000+0.0000001+Tc1*22
refarray[46][1] = y[23]
refarray[47][0] = 6000+Tc1*23
refarray[47][1] = y[23]
refarray[48][0] = 6000+0.0000001+Tc1*23
refarray[48][1] = y[24]
refarray[49][0] = 6000+Tc1*24
```

```
refarray[49][1] = y[24]
refarray[50][0] = 6000+0.0000001+Tc1*24
refarray[50][1] = y[25]
refarray[51][0] = 6000+Tc1*25
refarray[51][1] = y[25]
refarray[52][0] = 6000+0.0000001+Tc1*25
refarray[52][1] = y[26]
refarray[53][0] = 6000+Tc1*26
refarray[53][1] = y[26]
refarray[54][0] = 6000+0.0000001+Tc1*26
refarray[54][1] = y[27]
refarray[55][0] = 6000+Tc1*27
refarray[55][1] = y[27]
refarray[56][0] = 6000+0.0000001+Tc1*27
refarray[56][1] = y[28]
refarray[57][0] = 6000+Tc1*28
refarray[57][1] = y[28]
refarray[58][0] = 6000+0.0000001+Tc1*28
refarray[58][1] = y[29]
refarray[59][0] = 6000+Tc1*29
refarray[59][1] = y[29]
refarray[60][0] = 6000+0.0000001+Tc1*29
refarray[60][1] = y[30]
refarray[61][0] = 6000+Tc1*30
refarray[61][1] = y[30]
refarray[62][0] = 6000+0.0000001+Tc1*30
refarray[62][1] = y[31]
refarray[63][0] = 6000+Tc1*30+Tc2
refarray[63][1] = y[31]
refarray[64][0] = 6000+0.0000001+Tc2+Tc1*30
refarray[64][1] = y[32]
refarray[65][0] = 6000+Tc2*2+Tc1*30
refarray[65][1] = y[32]
refarray[66][0] = 6000+0.0000001+Tc2*2+Tc1*30
refarray[66][1] = y[33]
refarray[67][0] = 6000+Tc2*3+Tc1*30
refarray[67][1] = y[33]
refarray[68][0] = 6000+0.0000001+Tc2*3+Tc1*30
refarray[68][1] = y[34]
refarray[69][0] = 6000+Tc2*4+Tc1*30
refarray[69][1] = y[34]
refarray[70][0] = 6000+0.0000001+Tc2*4+Tc1*30
refarray[70][1] = y[35]
refarray[71][0] = 6000+Tc2*5+Tc1*30
refarray[71][1] = y[35]
refarray[72][0] = 6000+0.0000001+Tc2*5+Tc1*30
refarray[72][1] = y[36]
refarray[73][0] = 6000+Tc2*6+Tc1*30
refarray[73][1] = y[36]
refarray[74][0] = 6000+0.0000001+Tc2*6+Tc1*30
refarray[74][1] = y[37]
refarray[75][0] = 6000+Tc2*7+Tc1*30
refarray[75][1] = y[37]
refarray[76][0] = 6000+0.0000001+Tc2*7+Tc1*30
refarray[76][1] = y[38]
refarray[77][0] = 6000+Tc2*8+Tc1*30
refarray[77][1] = y[38]
refarray[78][0] = 6000+0.0000001+Tc2*8+Tc1*30
```

```

refarray[78][1] = y[39]
refarray[79][0] = 6000+Tc2*9+Tc1*30
refarray[79][1] = y[39]
refarray[80][0] = 6000+0.0000001+Tc2*9+Tc1*30
refarray[80][1] = y[40]
refarray[81][0] = 6000+Tc2*10+Tc1*30
refarray[81][1] = y[40]
refarray[82][0] = 6000+0.0000001+Tc2*10+Tc1*30
refarray[82][1] = y[41]
refarray[83][0] = 6000+Tc2*11+Tc1*30
refarray[83][1] = y[41]
refarray[84][0] = 6000+0.0000001+Tc2*11+Tc1*30
refarray[84][1] = y[42]
refarray[85][0] = 6000+Tc2*12+Tc1*30
refarray[85][1] = y[42]
refarray[86][0] = 6000+0.0000001+Tc2*12+Tc1*30
refarray[86][1] = y[43]
refarray[87][0] = 6000+Tc2*13+Tc1*30
refarray[87][1] = y[43]
refarray[88][0] = 6000+0.0000001+Tc2*13+Tc1*30
refarray[88][1] = y[44]
refarray[89][0] = 6000+Tc2*14+Tc1*30
refarray[89][1] = y[44]
refarray[90][0] = 6000+0.0000001+Tc2*14+Tc1*30
refarray[90][1] = y[45]
refarray[91][0] = 6000+Tc2*15+Tc1*30
refarray[91][1] = y[45]
refarray[92][0] = 6000+0.0000001+Tc2*15+Tc1*30
refarray[92][1] = y[46]
refarray[93][0] = 6000+Tc2*16+Tc1*30
refarray[93][1] = y[46]
refarray[94][0] = 6000+0.0000001+Tc2*16+Tc1*30
refarray[94][1] = y[47]
refarray[95][0] = 6000+Tc2*17+Tc1*30
refarray[95][1] = y[47]
refarray[96][0] = 6000+0.0000001+Tc2*17+Tc1*30
refarray[96][1] = y[48]
refarray[97][0] = 6000+Tc2*18+Tc1*30
refarray[97][1] = y[48]
refarray[98][0] = 6000+0.0000001+Tc2*18+Tc1*30
refarray[98][1] = y[49]
refarray[99][0] = 6000+Tc2*19+Tc1*30
refarray[99][1] = y[49]
app.GetDataManager().GetDataSet(m).SetTable(refarray)
***** Parameter definition under initial (healthy) condition*****
Ts=0.04 #two periods per magnetic analysis
Tc1=2.0 #Time constant in first 30 steps used in thermal
Tc2=40.0 #Time constant in last 18 steps used in thermal
Ibf=84.8 #RMS value of turn fault current
IA=84.8 #RMS value of phase A
IC=84.8 #RMS value of phase C
IB=84.8 #RMS value of phase B
ID=IE=IF=IG=IH=II=84.8 #RMS value of phase D, E, F, G, H, I
n=80
T_ewA4=[0 for i in range(int(n))]
T_ewA3=[0 for i in range(int(n))]
T_ewA2=[0 for i in range(int(n))]
T_ewA1=[0 for i in range(int(n))]

```

```
T_phA=[0 for i in range(int(n))]  
T_ewC4=[0 for i in range(int(n))]  
T_ewC3=[0 for i in range(int(n))]  
T_ewC2=[0 for i in range(int(n))]  
T_ewC1=[0 for i in range(int(n))]  
T_phC=[0 for i in range(int(n))]  
T_ewB2F=[0 for i in range(int(n))]  
T_ewB4F=[0 for i in range(int(n))]  
T_phBF=[0 for i in range(int(n))]  
T_ewB1=[0 for i in range(int(n))]  
T_ewB3=[0 for i in range(int(n))]  
T_phB1=[0 for i in range(int(n))]  
T_ewB2_3=[0 for i in range(int(n))]  
T_ewB4_3=[0 for i in range(int(n))]  
T_phB2_3=[0 for i in range(int(n))]  
T_ewB2_4=[0 for i in range(int(n))]  
T_ewB4_4=[0 for i in range(int(n))]  
T_phB2_4=[0 for i in range(int(n))]  
T_ewD4=[0 for i in range(int(n))]  
T_ewD3=[0 for i in range(int(n))]  
T_ewD2=[0 for i in range(int(n))]  
T_ewD1=[0 for i in range(int(n))]  
T_phD=[0 for i in range(int(n))]  
T_ewF4=[0 for i in range(int(n))]  
T_ewF3=[0 for i in range(int(n))]  
T_ewF2=[0 for i in range(int(n))]  
T_ewF1=[0 for i in range(int(n))]  
T_phF=[0 for i in range(int(n))]  
T_ewG4=[0 for i in range(int(n))]  
T_ewG3=[0 for i in range(int(n))]  
T_ewG2=[0 for i in range(int(n))]  
T_ewG1=[0 for i in range(int(n))]  
T_phG=[0 for i in range(int(n))]  
T_ewI4=[0 for i in range(int(n))]  
T_ewI3=[0 for i in range(int(n))]  
T_ewI2=[0 for i in range(int(n))]  
T_ewI1=[0 for i in range(int(n))]  
T_phI=[0 for i in range(int(n))]  
T_ewE4=[0 for i in range(int(n))]  
T_ewE3=[0 for i in range(int(n))]  
T_ewE2=[0 for i in range(int(n))]  
T_ewE1=[0 for i in range(int(n))]  
T_phE=[0 for i in range(int(n))]  
T_ewH4=[0 for i in range(int(n))]  
T_ewH3=[0 for i in range(int(n))]  
T_ewH2=[0 for i in range(int(n))]  
T_ewH1=[0 for i in range(int(n))]  
T_phH=[0 for i in range(int(n))]  
T_BF=[0 for i in range(int(n))]  
P_ewA4=[0 for i in range(int(n))]  
P_ewA3=[0 for i in range(int(n))]  
P_ewA2=[0 for i in range(int(n))]  
P_ewA1=[0 for i in range(int(n))]  
P_phA=[0 for i in range(int(n))]  
P_ewC4=[0 for i in range(int(n))]  
P_ewC3=[0 for i in range(int(n))]  
P_ewC2=[0 for i in range(int(n))]  
P_ewC1=[0 for i in range(int(n))]
```

```
P_phC=[0 for i in range(int(n))]  
P_ewB2F=[0 for i in range(int(n))]  
P_ewB4F=[0 for i in range(int(n))]  
P_phBF=[0 for i in range(int(n))]  
P_ewB1=[0 for i in range(int(n))]  
P_ewB3=[0 for i in range(int(n))]  
P_phB1=[0 for i in range(int(n))]  
P_ewB2_3=[0 for i in range(int(n))]  
P_ewB4_3=[0 for i in range(int(n))]  
P_phB2_3=[0 for i in range(int(n))]  
P_ewB2_4=[0 for i in range(int(n))]  
P_ewB4_4=[0 for i in range(int(n))]  
P_phB2_4=[0 for i in range(int(n))]  
P_ewD4=[0 for i in range(int(n))]  
P_ewD3=[0 for i in range(int(n))]  
P_ewD2=[0 for i in range(int(n))]  
P_ewD1=[0 for i in range(int(n))]  
P_phD=[0 for i in range(int(n))]  
P_ewF4=[0 for i in range(int(n))]  
P_ewF3=[0 for i in range(int(n))]  
P_ewF2=[0 for i in range(int(n))]  
P_ewF1=[0 for i in range(int(n))]  
P_phF=[0 for i in range(int(n))]  
P_ewG4=[0 for i in range(int(n))]  
P_ewG3=[0 for i in range(int(n))]  
P_ewG2=[0 for i in range(int(n))]  
P_ewG1=[0 for i in range(int(n))]  
P_phG=[0 for i in range(int(n))]  
P_ewI4=[0 for i in range(int(n))]  
P_ewI3=[0 for i in range(int(n))]  
P_ewI2=[0 for i in range(int(n))]  
P_ewI1=[0 for i in range(int(n))]  
P_phI=[0 for i in range(int(n))]  
P_ewE4=[0 for i in range(int(n))]  
P_ewE3=[0 for i in range(int(n))]  
P_ewE2=[0 for i in range(int(n))]  
P_ewE1=[0 for i in range(int(n))]  
P_phE=[0 for i in range(int(n))]  
P_ewH4=[0 for i in range(int(n))]  
P_ewH3=[0 for i in range(int(n))]  
P_ewH2=[0 for i in range(int(n))]  
P_ewH1=[0 for i in range(int(n))]  
P_phH=[0 for i in range(int(n))]  
I_BF=[0 for i in range(int(n))]
```

```
I_BF[0]=Ibf  
TewA4=190  
TewA3=190  
TewA2=190  
TewA1=190  
TphA=190  
TewC4=190  
TewC3=190  
TewC2=190  
TewC1=190  
TphC=190  
TewB2F=190  
TewB4F=190
```

TphBF=190
TewB1=190
TewB3=190
TphB1=190
TewB2_3=190
TewB4_3=190
TphB2_3=190
TewB2_4=190
TewB4_4=190
TphB2_4=190
TewD4=190
TewD3=190
TewD2=190
TewD1=190
TphD=190
TewF4=190
TewF3=190
TewF2=190
TewF1=190
TphF=190
TewG4=190
TewG3=190
TewG2=190
TewG1=190
TphG=190
TewI4=190
TewI3=190
TewI2=190
TewI1=190
TphI=190
TewE4=190
TewE3=190
TewE2=190
TewE1=190
TphE=190
TewH4=190
TewH3=190
TewH2=190
TewH1=190
TphH=190

PewA4=(1+0.00395*TewA4)*0.04044/3*IA*IA*1.4*0.2592*5/14
PewA3=(1+0.00395*TewA3)*0.04044/3*IA*IA*1.4*0.2592*6/14
PewA2=(1+0.00395*TewA2)*0.04044/3*IA*IA*1.4*0.2592*2/14
PewA1=(1+0.00395*TewA1)*0.04044/3*IA*IA*1.4*0.2592*1/14
PphA=(1+0.00395*TphA)*0.04044/3*IA*IA*1.4*0.2408
PewC4=(1+0.00395*TewC4)*0.04044/3*IC*IC*1.4*0.2592*3/14
PewC3=(1+0.00395*TewC3)*0.04044/3*IC*IC*1.4*0.2592*4/14
PewC2=(1+0.00395*TewC2)*0.04044/3*IC*IC*1.4*0.2592*4/14
PewC1=(1+0.00395*TewC1)*0.04044/3*IC*IC*1.4*0.2592*3/14
PphC=(1+0.00395*TphC)*0.04044/3*IC*IC*1.4*0.2408/2
PewB2F=(1+0.00395*TewB2F)*0.04044/3*Ibf*Ibf*1.4*0.2592*6/14/8*1.28
PewB4F=(1+0.00395*TewB4F)*0.04044/3*Ibf*Ibf*1.4*0.2592*1/14/8*1.25
PphBF=(1+0.00395*TphBF)*0.04044/3/16*Ibf*Ibf*1.4*0.2408*1.28
PewB1=(1+0.00395*TewB1)*0.04044/3*IB*IB*1.4*0.2592*5/14
PewB3=(1+0.00395*TewB3)*0.04044/3*IB*IB*1.4*0.2592*2/14
PphB1=(1+0.00395*TphB1)*0.04044/3*IB*IB*1.4*0.2408*8/16
PewB2_3=(1+0.00395*TewB2_3)*0.04044/3*IB*IB*1.4*0.2592*6/14*3/8

```

PewB4_3 = (1+0.00395*TewB4_3)*0.04044/3*IB*IB*1.4*0.2592*1/14*3/8
PphB2_3 = (1+0.00395*TphB2_3)*0.04044/3*IB*IB*1.4*0.2408*3/16
PewB2_4 = (1+0.00395*TewB2_4)*0.04044/3*IB*IB*1.4*0.2592*6/14*4/8
PewB4_4 = (1+0.00395*TewB4_4)*0.04044/3*IB*IB*1.4*0.2592*1/14*4/8
PphB2_4 = (1+0.00395*TphB2_4)*0.04044/3*IB*IB*1.4*0.2408*4/16
PewD4=(1+0.00395*TewD4)*0.04044/3*ID*ID*1.4*0.2592*5/14
PewD3=(1+0.00395*TewD3)*0.04044/3*ID*ID*1.4*0.2592*6/14
PewD2=(1+0.00395*TewD2)*0.04044/3*ID*ID*1.4*0.2592*2/14
PewD1=(1+0.00395*TewD1)*0.04044/3*ID*ID*1.4*0.2592*1/14
PphD=(1+0.00395*TphD)*0.04044/3*ID*ID*1.4*0.2408
PewF4=(1+0.00395*TewF4)*0.04044/3*IF*IF*1.4*0.2592*3/14
PewF3=(1+0.00395*TewF3)*0.04044/3*IF*IF*1.4*0.2592*4/14
PewF2=(1+0.00395*TewF2)*0.04044/3*IF*IF*1.4*0.2592*4/14
PewF1=(1+0.00395*TewF1)*0.04044/3*IF*IF*1.4*0.2592*3/14
PphF=(1+0.00395*TphF)*0.04044/3*IF*IF*1.4*0.2408
PewG4=(1+0.00395*TewG4)*0.04044/3*IG*IG*1.4*0.2592*5/14
PewG3=(1+0.00395*TewG3)*0.04044/3*IG*IG*1.4*0.2592*6/14
PewG2=(1+0.00395*TewG2)*0.04044/3*IG*IG*1.4*0.2592*2/14
PewG1=(1+0.00395*TewG1)*0.04044/3*IG*IG*1.4*0.2592*1/14
PphG=(1+0.00395*TphG)*0.04044/3*IG*IG*1.4*0.2408
PewI4=(1+0.00395*TewI4)*0.04044/3*II*II*1.4*0.2592*3/14
PewI3=(1+0.00395*TewI3)*0.04044/3*II*II*1.4*0.2592*4/14
PewI2=(1+0.00395*TewI2)*0.04044/3*II*II*1.4*0.2592*4/14
PewI1=(1+0.00395*TewI1)*0.04044/3*II*II*1.4*0.2592*3/14
PphI=(1+0.00395*TphI)*0.04044/3*II*II*1.4*0.2408
PewE1=(1+0.00395*TewE1)*0.04044/3*IE*IE*1.4*0.2592*5/14
PewE2=(1+0.00395*TewE2)*0.04044/3*IE*IE*1.4*0.2592*6/14
PewE3=(1+0.00395*TewE3)*0.04044/3*IE*IE*1.4*0.2592*2/14
PewE4=(1+0.00395*TewE4)*0.04044/3*IE*IE*1.4*0.2592*1/14
PphE=(1+0.00395*TphE)*0.04044/3*IE*IE*1.4*0.2408
PewH1=(1+0.00395*TewH1)*0.04044/3*IH*IH*1.4*0.2592*5/14
PewH2=(1+0.00395*TewH2)*0.04044/3*IH*IH*1.4*0.2592*6/14
PewH3=(1+0.00395*TewH3)*0.04044/3*IH*IH*1.4*0.2592*2/14
PewH4=(1+0.00395*TewH4)*0.04044/3*IH*IH*1.4*0.2592*1/14
PphH=(1+0.00395*TphH)*0.04044/3*IH*IH*1.4*0.2408

```

```

P_ewA4[0]=PewA4
P_ewA3[0]=PewA3
P_ewA2[0]=PewA2
P_ewA1[0]=PewA1
P_phA[0]=PphA
P_ewC4[0]=PewC4
P_ewC3[0]=PewC3
P_ewC2[0]=PewC2
P_ewC1[0]=PewC1
P_phC[0]=PphC
P_ewB2F[0]=PewB2F
P_ewB4F[0]=PewB4F
P_phBF[0]=PphBF
P_ewB1[0]=PewB1
P_ewB3[0]=PewB3
P_phB1[0]=PphB1
P_ewB2_3[0]=PewB2_3
P_ewB4_3[0]=PewB4_3
P_phB2_3[0]=PphB2_3
P_ewB2_4[0]=PewB2_4
P_ewB4_4[0]=PewB4_4
P_phB2_4[0]=PphB2_4

```

```
P_ewD4[0]=PewD4
P_ewD3[0]=PewD3
P_ewD2[0]=PewD2
P_ewD1[0]=PewD1
P_phD[0]=PphD
P_ewF4[0]=PewF4
P_ewF3[0]=PewF3
P_ewF2[0]=PewF2
P_ewF1[0]=PewF1
P_phF[0]=PphF
P_ewG4[0]=PewG4
P_ewG3[0]=PewG3
P_ewG2[0]=PewG2
P_ewG1[0]=PewG1
P_phG[0]=PphG
P_ewI4[0]=PewI4
P_ewI3[0]=PewI3
P_ewI2[0]=PewI2
P_ewI1[0]=PewI1
P_phI[0]=PphI
P_ewE4[0]=PewE4
P_ewE3[0]=PewE3
P_ewE2[0]=PewE2
P_ewE1[0]=PewE1
P_phE[0]=PphE
P_ewH4[0]=PewH4
P_ewH3[0]=PewH3
P_ewH2[0]=PewH2
P_ewH1[0]=PewH1
P_phH[0]=PphH

table_set(P_ewA4,"EW A4")
table_set(P_ewA3,"EW A3")
table_set(P_ewA2,"EW A2")
table_set(P_ewA1,"EW A1")
table_set(P_phA,"phase A")
table_set(P_ewC4,"EW C4")
table_set(P_ewC3,"EW C3")
table_set(P_ewC2,"EW C2")
table_set(P_ewC1,"EW C1")
table_set(P_phC,"phase C")
table_set(P_ewB2F,"EW B2F")
table_set(P_ewB4F,"EW B4F")
table_set(P_phBF,"phase BF")
table_set(P_ewB1,"EW B1")
table_set(P_ewB3,"EW B3")
table_set(P_phB1,"phase B1")
table_set(P_ewB2_3,"EW B2_3")
table_set(P_ewB4_3,"EW B4_3")
table_set(P_phB2_3,"phase B2_3")
table_set(P_ewB2_4,"EW B2_4")
table_set(P_ewB4_4,"EW B4_4")
table_set(P_phB2_4,"phase B2_4")
table_set(P_ewD4,"EW D4")
table_set(P_ewD3,"EW D3")
table_set(P_ewD2,"EW D2")
table_set(P_ewD1,"EW D1")
table_set(P_phD,"phase D")
```

```
table_set(P_ewF4,"EW F4")
table_set(P_ewF3,"EW F3")
table_set(P_ewF2,"EW F2")
table_set(P_ewF1,"EW F1")
table_set(P_phF,"phase F")
table_set(P_ewG4,"EW G4")
table_set(P_ewG3,"EW G3")
table_set(P_ewG2,"EW G2")
table_set(P_ewG1,"EW G1")
table_set(P_phG,"phase G")
table_set(P_ewI4,"EW I4")
table_set(P_ewI3,"EW I3")
table_set(P_ewI2,"EW I2")
table_set(P_ewI1,"EW I1")
table_set(P_phI,"phase I")
table_set(P_ewE4,"EW E4")
table_set(P_ewE3,"EW E3")
table_set(P_ewE2,"EW E2")
table_set(P_ewE1,"EW E1")
table_set(P_phE,"phase E")
table_set(P_ewH4,"EW H4")
table_set(P_ewH3,"EW H3")
table_set(P_ewH2,"EW H2")
table_set(P_ewH1,"EW H1")
table_set(P_phH,"phase H")
```

```
T_ewA4[0]=TewA4
T_ewA3[0]=TewA3
T_ewA2[0]=TewA2
T_ewA1[0]=TewA1
T_phA[0]=TphA
T_ewC4[0]=TewC4
T_ewC3[0]=TewC3
T_ewC2[0]=TewC2
T_ewC1[0]=TewC1
T_phC[0]=TphC
T_ewB2F[0]=TewB2F
T_ewB4F[0]=TewB4F
T_phBF[0]=TphBF
T_ewB1[0]=TewB1
T_ewB3[0]=TewB3
T_phB1[0]=TphB1
T_ewB2_3[0]=TewB2_3
T_ewB4_3[0]=TewB4_3
T_phB2_3[0]=TphB2_3
T_ewB2_4[0]=TewB2_4
T_ewB4_4[0]=TewB4_4
T_phB2_4[0]=TphB2_4
T_ewD4[0]=TewD4
T_ewD3[0]=TewD3
T_ewD2[0]=TewD2
T_ewD1[0]=TewD1
T_phD[0]=TphD
T_ewF4[0]=TewF4
T_ewF3[0]=TewF3
T_ewF2[0]=TewF2
T_ewF1[0]=TewF1
T_phF[0]=TphF
```

```

T_ewG4[0]=TewG4
T_ewG3[0]=TewG3
T_ewG2[0]=TewG2
T_ewG1[0]=TewG1
T_phG[0]=TphG
T_ewI4[0]=TewI4
T_ewI3[0]=TewI3
T_ewI2[0]=TewI2
T_ewI1[0]=TewI1
T_phI[0]=TphI
T_ewE4[0]=TewE4
T_ewE3[0]=TewE3
T_ewE2[0]=TewE2
T_ewE1[0]=TewE1
T_phE[0]=TphE
T_ewH4[0]=TewH4
T_ewH3[0]=TewH3
T_ewH2[0]=TewH2
T_ewH1[0]=TewH1
T_phH[0]=TphH

St=[0 for i in range(int(n))]*31
S=[0 for i in range(int(n))]*31
Pj=[0 for i in range(int(n))]

nm=31+10*60;
refarray = [[0 for i in range(1)] for j in range(int(nm))]
for j in range(int(nm)):
    if j<31:
        refarray[j][0] =200*j
    elif j<331:
        refarray[j][0] = 6000.0+Tc1/10*(j-30)
    else:
        refarray[j][0] = 6000.0+Tc2/10*(j-330)+Tc1/10*(330-30)
app.GetDataManager().GetDataSet(u"Time table 1").SetTable(refarray)
for k in range(48):
    z=k+1
    app.SetCurrentStudy(u"2D PM_motor_load_turnfault couple")
    app.View().SetCurrentCase(1)
    app.SetCurrentStudy(u"2D PM_motor_load_turnfault couple")

    T_BF[k]=((TewB2F+TewB4F)/2*57+TphBF*55)/(57+55)
    app.GetModel(u"6P36S_turn").GetStudy(u"2D PM_motor_load_turnfault
couple").GetCircuit().GetComponent(u"NB2_F").SetValue(u"Temperature", T_BF[k])
    app.GetModel(u"6P36S_turn").GetStudy(u"2D PM_motor_load_turnfault
couple").GetCircuit().GetComponent(u"PB2_F ").SetValue(u"Temperature", T_BF[k])

    app.SetCurrentStudy(u"2D PM_motor_load_turnfault couple")
    app.GetModel(u"6P36S_turn").GetStudy(u"2D PM_motor_load_turnfault
couple").GetStep().SetValue(u"Step", 61)
    app.GetModel(u"6P36S_turn").GetStudy(u"2D PM_motor_load_turnfault couple").Run()

    Current_variable_Ibf="IBf"
    caseID=0
    CircuitCurrent_DataSet=app.GetStudy(u"2D PM_motor_load_turnfault
couple").GetDataSet(u"Circuit Current", 1)
    parameter = app.CreateResponseDataParameter("Circuit Current")

```

```

parameter.SetCalculationType("RMS")
parameter.SetStartValue("31")
parameter.SetEndValue("61")
parameter.SetUnit("Step")
parameter.SetVariable(Current_variable_Ibf)
parameter.SetAllLine(False)
parameter.SetCaseRangeType(1)
parameter.SetLine("PB2_F ")
app.GetDataManager().CreateParametricDataWithParameter(CircuitCurrent_DataSet,
parameter)
Ibf1 = app.GetModel(u"6P36S_turn").GetStudy(u"2D PM_motor_load_turnfault
couple").GetResponseVariable(Current_variable_Ibf, int(caseID))
Ibf=Ibf1
I_BF[z]=Ibf
app.GetModel(u"6P36S_turn").GetStudy(u"2D PM_motor_load_turnfault
couple").DeleteParametricData(u" Circuit Current")

PewA4=(1+0.00395*TewA4)*0.04044/3*IA*IA*1.4*0.2592*5/14
PewA3=(1+0.00395*TewA3)*0.04044/3*IA*IA*1.4*0.2592*6/14
PewA2=(1+0.00395*TewA2)*0.04044/3*IA*IA*1.4*0.2592*2/14
PewA1=(1+0.00395*TewA1)*0.04044/3*IA*IA*1.4*0.2592*1/14
PphA=(1+0.00395*TphA)*0.04044/3*IA*IA*1.4*0.2408
PewC4=(1+0.00395*TewC4)*0.04044/3*IC*IC*1.4*0.2592*3/14
PewC3=(1+0.00395*TewC3)*0.04044/3*IC*IC*1.4*0.2592*4/14
PewC2=(1+0.00395*TewC2)*0.04044/3*IC*IC*1.4*0.2592*4/14
PewC1=(1+0.00395*TewC1)*0.04044/3*IC*IC*1.4*0.2592*3/14
PphC=(1+0.00395*TphC)*0.04044/3*IC*IC*1.4*0.2408/2
PewB2F=(1+0.00395*TewB2F)*0.04044/3*Ibf*Ibf*1.4*0.2592*6/14/8*1.28
PewB4F=(1+0.00395*TewB4F)*0.04044/3*Ibf*Ibf*1.4*0.2592*1/14/8*1.25
PphBF=(1+0.00395*TphBF)*0.04044/3/16*Ibf*Ibf*1.4*0.2408*1.28
PewB1 = (1+0.00395*TewB1)*0.04044/3*IB*IB*1.4*0.2592*5/14
PewB3 = (1+0.00395*TewB3)*0.04044/3*IB*IB*1.4*0.2592*2/14
PphB1 = (1+0.00395*TphB1)*0.04044/3*IB*IB*1.4*0.2408*8/16
PewB2_3 = (1+0.00395*TewB2_3)*0.04044/3*IB*IB*1.4*0.2592*6/14*3/8
PewB4_3 = (1+0.00395*TewB4_3)*0.04044/3*IB*IB*1.4*0.2592*1/14*3/8
PphB2_3 = (1+0.00395*TphB2_3)*0.04044/3*IB*IB*1.4*0.2408*3/16
PewB2_4 = (1+0.00395*TewB2_4)*0.04044/3*IB*IB*1.4*0.2592*6/14*4/8
PewB4_4 = (1+0.00395*TewB4_4)*0.04044/3*IB*IB*1.4*0.2592*1/14*4/8
PphB2_4 = (1+0.00395*TphB2_4)*0.04044/3*IB*IB*1.4*0.2408*4/16
PewD4=(1+0.00395*TewD4)*0.04044/3*ID*ID*1.4*0.2592*5/14
PewD3=(1+0.00395*TewD3)*0.04044/3*ID*ID*1.4*0.2592*6/14
PewD2=(1+0.00395*TewD2)*0.04044/3*ID*ID*1.4*0.2592*2/14
PewD1=(1+0.00395*TewD1)*0.04044/3*ID*ID*1.4*0.2592*1/14
PphD=(1+0.00395*TphD)*0.04044/3*ID*ID*1.4*0.2408
PewF4=(1+0.00395*TewF4)*0.04044/3*IF*IF*1.4*0.2592*3/14
PewF3=(1+0.00395*TewF3)*0.04044/3*IF*IF*1.4*0.2592*4/14
PewF2=(1+0.00395*TewF2)*0.04044/3*IF*IF*1.4*0.2592*4/14
PewF1=(1+0.00395*TewF1)*0.04044/3*IF*IF*1.4*0.2592*3/14
PphF=(1+0.00395*TphF)*0.04044/3*IF*IF*1.4*0.2408
PewG4=(1+0.00395*TewG4)*0.04044/3*IG*IG*1.4*0.2592*5/14
PewG3=(1+0.00395*TewG3)*0.04044/3*IG*IG*1.4*0.2592*6/14
PewG2=(1+0.00395*TewG2)*0.04044/3*IG*IG*1.4*0.2592*2/14
PewG1=(1+0.00395*TewG1)*0.04044/3*IG*IG*1.4*0.2592*1/14
PphG=(1+0.00395*TphG)*0.04044/3*IG*IG*1.4*0.2408
PewI4=(1+0.00395*TewI4)*0.04044/3*II*II*1.4*0.2592*3/14
PewI3=(1+0.00395*TewI3)*0.04044/3*II*II*1.4*0.2592*4/14
PewI2=(1+0.00395*TewI2)*0.04044/3*II*II*1.4*0.2592*4/14
PewI1=(1+0.00395*TewI1)*0.04044/3*II*II*1.4*0.2592*3/14

```

```
PphI=(1+0.00395*TphI)*0.04044/3*II*II*1.4*0.2408
PewE1=(1+0.00395*TewE1)*0.04044/3*IE*IE*1.4*0.2592*5/14
PewE2=(1+0.00395*TewE2)*0.04044/3*IE*IE*1.4*0.2592*6/14
PewE3=(1+0.00395*TewE3)*0.04044/3*IE*IE*1.4*0.2592*2/14
PewE4=(1+0.00395*TewE4)*0.04044/3*IE*IE*1.4*0.2592*1/14
PphE=(1+0.00395*TphE)*0.04044/3*IE*IE*1.4*0.2408
PewH1=(1+0.00395*TewH1)*0.04044/3*IH*IH*1.4*0.2592*5/14
PewH2=(1+0.00395*TewH2)*0.04044/3*IH*IH*1.4*0.2592*6/14
PewH3=(1+0.00395*TewH3)*0.04044/3*IH*IH*1.4*0.2592*2/14
PewH4=(1+0.00395*TewH4)*0.04044/3*IH*IH*1.4*0.2592*1/14
PphH=(1+0.00395*TphH)*0.04044/3*IH*IH*1.4*0.2408
```

```
P_ewA4[z]=PewA4
P_ewA3[z]=PewA3
P_ewA2[z]=PewA2
P_ewA1[z]=PewA1
P_phA[z]=PphA
P_ewC4[z]=PewC4
P_ewC3[z]=PewC3
P_ewC2[z]=PewC2
P_ewC1[z]=PewC1
P_phC[z]=PphC
P_ewB2F[z]=PewB2F
P_ewB4F[z]=PewB4F
P_phBF[z]=PphBF
P_ewB1[z]=PewB1
P_ewB3[z]=PewB3
P_phB1[z]=PphB1
P_ewB2_3[z]=PewB2_3
P_ewB4_3[z]=PewB4_3
P_phB2_3[z]=PphB2_3
P_ewB2_4[z]=PewB2_4
P_ewB4_4[z]=PewB4_4
P_phB2_4[z]=PphB2_4
P_ewD4[z]=PewD4
P_ewD3[z]=PewD3
P_ewD2[z]=PewD2
P_ewD1[z]=PewD1
P_phD[z]=PphD
P_ewF4[z]=PewF4
P_ewF3[z]=PewF3
P_ewF2[z]=PewF2
P_ewF1[z]=PewF1
P_phF[z]=PphF
P_ewG4[z]=PewG4
P_ewG3[z]=PewG3
P_ewG2[z]=PewG2
P_ewG1[z]=PewG1
P_phG[z]=PphG
P_ewI4[z]=PewI4
P_ewI3[z]=PewI3
P_ewI2[z]=PewI2
P_ewI1[z]=PewI1
P_phI[z]=PphI
P_ewE4[z]=PewE4
P_ewE3[z]=PewE3
P_ewE2[z]=PewE2
P_ewE1[z]=PewE1
```

```
P_phE[z]=PphE
P_ewH4[z]=PewH4
P_ewH3[z]=PewH3
P_ewH2[z]=PewH2
P_ewH1[z]=PewH1
P_phH[z]=PphH
app.SetCurrentStudy(u"2D PM_motor_load_turnfault couple")
app.GetModel(u"6P36S_turn").GetStudy(u"2D PM_motor_load_turnfault
couple").DeleteResultCurrentCase()
```

```
app.SetCurrentStudy(u"transient turnfault")
table_set(P_ewA4,"EW A4")
table_set(P_ewA3,"EW A3")
table_set(P_ewA2,"EW A2")
table_set(P_ewA1,"EW A1")
table_set(P_phA,"phase A")
table_set(P_ewC4,"EW C4")
table_set(P_ewC3,"EW C3")
table_set(P_ewC2,"EW C2")
table_set(P_ewC1,"EW C1")
table_set(P_phC,"phase C")
table_set(P_ewB2F,"EW B2F")
table_set(P_ewB4F,"EW B4F")
table_set(P_phBF,"phase BF")
table_set(P_ewB1,"EW B1")
table_set(P_ewB3,"EW B3")
table_set(P_phB1,"phase B1")
table_set(P_ewB2_3,"EW B2_3")
table_set(P_ewB4_3,"EW B4_3")
table_set(P_phB2_3,"phase B2_3")
table_set(P_ewB2_4,"EW B2_4")
table_set(P_ewB4_4,"EW B4_4")
table_set(P_phB2_4,"phase B2_4")
table_set(P_ewD4,"EW D4")
table_set(P_ewD3,"EW D3")
table_set(P_ewD2,"EW D2")
table_set(P_ewD1,"EW D1")
table_set(P_phD,"phase D")
table_set(P_ewF4,"EW F4")
table_set(P_ewF3,"EW F3")
table_set(P_ewF2,"EW F2")
table_set(P_ewF1,"EW F1")
table_set(P_phF,"phase F")
table_set(P_ewG4,"EW G4")
table_set(P_ewG3,"EW G3")
table_set(P_ewG2,"EW G2")
table_set(P_ewG1,"EW G1")
table_set(P_phG,"phase G")
table_set(P_ewI4,"EW I4")
table_set(P_ewI3,"EW I3")
table_set(P_ewI2,"EW I2")
table_set(P_ewI1,"EW I1")
table_set(P_phI,"phase I")
table_set(P_ewE4,"EW E4")
table_set(P_ewE3,"EW E3")
table_set(P_ewE2,"EW E2")
table_set(P_ewE1,"EW E1")
table_set(P_phE,"phase E")
```

```

table_set(P_ewH4,"EW H4")
table_set(P_ewH3,"EW H3")
table_set(P_ewH2,"EW H2")
table_set(P_ewH1,"EW H1")
table_set(P_phH,"phase H")
S[k]=10*k+40 #Every time constant has 10 steps and first 6000s has 30 steps
app.View().SetCurrentCase(1)
app.SetCurrentStudy(u"transient turnfault")
app.GetModel(u"6P36S_part_model_thermal_couple_4").GetStudy(u"transient
turnfault").GetStep().SetValue(u"Step", S[k])
app.GetModel(u"6P36S_part_model_thermal_couple_4").GetStudy(u"transient turnfault").Run()
row=S[k]
Temperature_table =
app.GetModel(u"6P36S_part_model_thermal_couple_4").GetStudy(u"transient
turnfault").GetResultTable().GetData(u"AverageTemperature")
Column="EW_A4"
TewA4=Temperature_table.GetValue(int(row), Column)
Column="EW_A3"
TewA3=Temperature_table.GetValue(int(row), Column)
Column="EW_A2"
TewA2=Temperature_table.GetValue(int(row), Column)
Column="EW_A1"
TewA1=Temperature_table.GetValue(int(row), Column)
Column="PHASE_A"
TphA=Temperature_table.GetValue(int(row), Column)
Column="EW_C4"
TewC4=Temperature_table.GetValue(int(row), Column)
Column="EW_C3"
TewC3=Temperature_table.GetValue(int(row), Column)
Column="EW_C2"
TewC2=Temperature_table.GetValue(int(row), Column)
Column="EW_C1"
TewC1=Temperature_table.GetValue(int(row), Column)
Column="PHASE_C"
TphC=Temperature_table.GetValue(int(row), Column)
Column="EW_B2F"
TewB2F=Temperature_table.GetValue(int(row), Column)
Column="EW_B4F"
TewB4F=Temperature_table.GetValue(int(row), Column)
Column="PHASE_B2F"
TphBF=Temperature_table.GetValue(int(row), Column)
Column="EW_B1"
TewB1=Temperature_table.GetValue(int(row), Column)
Column="EW_B3"
TewB3=Temperature_table.GetValue(int(row), Column)
Column="PHASE_B1"
TphB1=Temperature_table.GetValue(int(row), Column)
Column="EW_B2_3"
TewB2_3=Temperature_table.GetValue(int(row), Column)
Column="EW_B4_3"
TewB4_3=Temperature_table.GetValue(int(row), Column)
Column="PHASE_B2_3"
TphB2_3=Temperature_table.GetValue(int(row), Column)
Column="EW_B2_4"
TewB2_4=Temperature_table.GetValue(int(row), Column)
Column="EW_B4_4"
TewB4_4=Temperature_table.GetValue(int(row), Column)
Column="PHASE_B2_4"

```

```
TphB2_4=Temperature_table.GetValue(int(row), Column)
Column="EW_D4"
TewD4=Temperature_table.GetValue(int(row), Column)
Column="EW_D3"
TewD3=Temperature_table.GetValue(int(row), Column)
Column="EW_D2"
TewD2=Temperature_table.GetValue(int(row), Column)
Column="EW_D1"
TewD1=Temperature_table.GetValue(int(row), Column)
Column="PHASE_D"
TphD=Temperature_table.GetValue(int(row), Column)
Column="EW_F4"
TewF4=Temperature_table.GetValue(int(row), Column)
Column="EW_F3"
TewF3=Temperature_table.GetValue(int(row), Column)
Column="EW_F2"
TewF2=Temperature_table.GetValue(int(row), Column)
Column="EW_F1"
TewF1=Temperature_table.GetValue(int(row), Column)
Column="PHASE_F"
TphF=Temperature_table.GetValue(int(row), Column)
Column="EW_G4"
TewG4=Temperature_table.GetValue(int(row), Column)
Column="EW_G3"
TewG3=Temperature_table.GetValue(int(row), Column)
Column="EW_G2"
TewG2=Temperature_table.GetValue(int(row), Column)
Column="EW_G1"
TewG1=Temperature_table.GetValue(int(row), Column)
Column="PHASE_G"
TphG=Temperature_table.GetValue(int(row), Column)
Column="EW_I4"
TewI4=Temperature_table.GetValue(int(row), Column)
Column="EW_I3"
TewI3=Temperature_table.GetValue(int(row), Column)
Column="EW_I2"
TewI2=Temperature_table.GetValue(int(row), Column)
Column="EW_I1"
TewI1=Temperature_table.GetValue(int(row), Column)
Column="PHASE_I"
TphI=Temperature_table.GetValue(int(row), Column)
Column="EW_E4"
TewE4=Temperature_table.GetValue(int(row), Column)
Column="EW_E3"
TewE3=Temperature_table.GetValue(int(row), Column)
Column="EW_E2"
TewE2=Temperature_table.GetValue(int(row), Column)
Column="EW_E1"
TewE1=Temperature_table.GetValue(int(row), Column)
Column="PHASE_E"
TphE=Temperature_table.GetValue(int(row), Column)
Column="EW_H4"
TewH4=Temperature_table.GetValue(int(row), Column)
Column="EW_H3"
TewH3=Temperature_table.GetValue(int(row), Column)
Column="EW_H2"
TewH2=Temperature_table.GetValue(int(row), Column)
Column="EW_H1"
```

```
TewH1=Temperature_table.GetValue(int(row), Column)
Column="PHASE_H"
TphH=Temperature_table.GetValue(int(row), Column)
T_ewA4[z]=TewA4
T_ewA3[z]=TewA3
T_ewA2[z]=TewA2
T_ewA1[z]=TewA1
T_phA[z]=TphA
T_ewC4[z]=TewC4
T_ewC3[z]=TewC3
T_ewC2[z]=TewC2
T_ewC1[z]=TewC1
T_phC[z]=TphC
T_ewB2F[z]=TewB2F
T_ewB4F[z]=TewB4F
T_phBF[z]=TphBF
T_ewB1[z]=TewB1
T_ewB3[z]=TewB3
T_phB1[z]=TphB1
T_ewB2_3[z]=TewB2_3
T_ewB4_3[z]=TewB4_3
T_phB2_3[z]=TphB2_3
T_ewB2_4[z]=TewB2_4
T_ewB4_4[z]=TewB4_4
T_phB2_4[z]=TphB2_4
T_ewD4[z]=TewD4
T_ewD3[z]=TewD3
T_ewD2[z]=TewD2
T_ewD1[z]=TewD1
T_phD[z]=TphD
T_ewF4[z]=TewF4
T_ewF3[z]=TewF3
T_ewF2[z]=TewF2
T_ewF1[z]=TewF1
T_phF[z]=TphF
T_ewG4[z]=TewG4
T_ewG3[z]=TewG3
T_ewG2[z]=TewG2
T_ewG1[z]=TewG1
T_phG[z]=TphG
T_ewI4[z]=TewI4
T_ewI3[z]=TewI3
T_ewI2[z]=TewI2
T_ewI1[z]=TewI1
T_phI[z]=TphI
T_ewE4[z]=TewE4
T_ewE3[z]=TewE3
T_ewE2[z]=TewE2
T_ewE1[z]=TewE1
T_phE[z]=TphE
T_ewH4[z]=TewH4
T_ewH3[z]=TewH3
T_ewH2[z]=TewH2
T_ewH1[z]=TewH1
T_phH[z]=TphH

app.GetModel(u"6P36S_part_model_thermal_couple_4").GetStudy(u"transient
turnfault").DeleteResultCurrentCase()
```

```
app.Save()
```

```
print(T_ewA4)
print(T_ewA3)
print(T_ewA2)
print(T_ewA1)
print(T_phA)
print(T_ewC4)
print(T_ewC3)
print(T_ewC2)
print(T_ewC1)
print(T_phC)
print(T_ewB2F)
print(T_ewB4F)
print(T_phBF)
print(T_ewB1)
print(T_ewB3)
print(T_phB1)
print(T_ewB2_3)
print(T_ewB4_3)
print(T_phB2_3)
print(T_ewB2_4)
print(T_ewB4_4)
print(T_phB2_4)
print(T_ewD4)
print(T_ewD3)
print(T_ewD2)
print(T_ewD1)
print(T_phD)
print(T_ewF4)
print(T_ewF3)
print(T_ewF2)
print(T_ewF1)
print(T_phF)
print(T_ewG4)
print(T_ewG3)
print(T_ewG2)
print(T_ewG1)
print(T_phG)
print(T_ewI4)
print(T_ewI3)
print(T_ewI2)
print(T_ewI1)
print(T_phI)
print(T_ewE4)
print(T_ewE3)
print(T_ewE2)
print(T_ewE1)
print(T_phE)
print(T_ewH4)
print(T_ewH3)
print(T_ewH2)
print(T_ewH1)
print(T_phH)
print(P_ewA4)
print(P_ewA3)
print(P_ewA2)
print(P_ewA1)
```

```
print(P_phA)
print(P_ewC4)
print(P_ewC3)
print(P_ewC2)
print(P_ewC1)
print(P_phC)
print(P_ewB2F)
print(P_ewB4F)
print(P_phBF)
print(P_ewB1)
print(P_ewB3)
print(P_phB1)
print(P_ewB2_3)
print(P_ewB4_3)
print(P_phB2_3)
print(P_ewB2_4)
print(P_ewB4_4)
print(P_phB2_4)
print(P_ewD4)
print(P_ewD3)
print(P_ewD2)
print(P_ewD1)
print(P_phD)
print(P_ewF4)
print(P_ewF3)
print(P_ewF2)
print(P_ewF1)
print(P_phF)
print(P_ewG4)
print(P_ewG3)
print(P_ewG2)
print(P_ewG1)
print(P_phG)
print(P_ewI4)
print(P_ewI3)
print(P_ewI2)
print(P_ewI1)
print(P_phI)
print(P_ewE4)
print(P_ewE3)
print(P_ewE2)
print(P_ewE1)
print(P_phE)
print(P_ewH4)
print(P_ewH3)
print(P_ewH2)
print(P_ewH1)
print(P_phH)
print(I_BF)
```